Tailored nitrogen-containing polyaromatics - from surfaces to stacks

Submitted by

Colm Delaney B.A. (Mod) MSc.

Trinity College Dublin, Ireland

A thesis submitted to the University of Dublin, Trinity College for the degree of

Doctor of Philosophy

University of Dublin, Trinity College *2016*

Declaration

I declare that this thesis has not been submitted as an exercise for a degree at this or any other university and it is entirely my own work.

I agree to deposit this thesis in the University's open access institutional repository or allow the library to do so on my behalf, subject to Irish Copyright Legislation and Trinity College Library conditions of use and acknowledgement.

Summary

Chapter 1: This chapter gives a broad introduction to the subjects of graphene and nanographenes, which are discussed in subsequent chapters. Common methodologies for the synthesis of substituted polyphenylenes and hexabenzocoronenes are discussed. These prove an important preface to the concepts in the following chapters. An introduction to heteroatom substitution is also given, with particular emphasis placed on the influence of nitrogen atoms in the aromatic platform.

Chapter 2: This chapter begins with an introduction to common modes of cyclodehydrogenation, used in both all-carbon and heteroatom-containing polyphenylenes, taking examples from a broad range of published research. The main body of the chapter then introduces a novel bond-forming phenomenon which is seen for nitrogen-containing polyphenylenes in the presence of Br_2. C-C bond formation of this nature has never been documented before. This reaction is repeated, confirmed and tested through a range of varying conditions.

The synthesis of a library of compounds allows for analysis of the limitations of this reaction and subsequent evaluation of potential mechanisms. The use of *in situ* NMR studies, combined with X-ray crystallography allowed for assignment of the reaction pathway and full characterisation of the final products, which possessed 2N, 4N and 6N substitution.

Chapter 3: Chapter 3 begins with an exhaustive review of fuel cells and their constituent parts. In particular, this is focussed on the role which heteroatom-doped carbon frameworks can play in both catalytic and support materials. The review finishes with selected data from recent years, relating to the growth of nanographenes from single-molecule precursors.

The second part of this chapter focuses on designing analogous nitrogen-substituted molecules with peripheral halogenation. These compounds can be used under a range of stimuli to induce different forms of intermolecular growth. Using electron-beam irradiation, incident light and thermally induced polymerisation, the viability of such reactions is determined. The ability to monitor the effect of such stimuli *in situ* allows for determination of the resulting structures using transmitting electron microscopy, mass spectrometry and scanning tunnelling microscopy. The final part of this section focuses

on the initial results from preliminary electrochemical studies to analyse any possible catalytic behaviour from such molecules.

Chapter 4: This chapter outlines early work which was carried out in the project, in which a generic method for the formation of discotic liquid crystals is developed. The precursor compounds were synthesised with ease, but subsequent alkyl coupling reactions proved problematic. Although hampered by low-yielding synthesis, this route is used to synthesise a fully-fused discotic-liquid crystal. Using small-angle neutron scattering, information could be gleaned pertaining to the long-range behaviour of the molecule. A preliminary polarising optical microscopy study of the compound also allows for investigation of the phases at varied temperature.

Chapter 5: This chapter gives a full account of the experimental work which was carried out within this research.

Acknowledgements

I would like to extend a sincere thank you to my supervisor, Prof. Sylvia Draper, for the help and support she has offered me since I started with the group. I must also thank Prof. Sarath Perera who encouraged us all, both academically and personally. Thank you to Drs. John O' Brien and Manuel Ruther for all the thorough NMR analysis and to Drs. Martin Feeney and Gary Hessmann for mass spectrometry. I thank Dr. Brendan Twamley for his patience, enthusiasm and crystallographic help.

I would also like to take this opportunity to thank all the Draper group members, both past and present. To Colin, Belen, Buddhie, Deanne, Dilwyn, Fran and Niamh, thank you for welcoming me to the group with such open arms. To the current members, Rob, Yue, Lankani, Eugene, Bryan, Junsi and Nitheen, thank you for being so supportive. I also owe a lot of thanks to my former undergraduate students. To Gearoid, I thank you sincerely for the help and friendship which kept things going throughout.

To my family, all of this is thanks to you.

'Though we live in a world that dreams of ending

that always seems about to give in

something that will not acknowledge conclusion

insists that we forever begin.'

-Brendan Kennelly

Table of Contents

List of Figures

List of Schemes

List of Tables

Abbreviations

1D	one-dimensional
2D	two-dimensional
Å	angstrom
Ar	aryl
a.u.	arbitrary units
B^-	generic base
bpy	2,2'-bipridine
Bu	butyl
C	Celsius
cm	centimeter
COSY	correlation spectroscopy
CVD	chemical vapour deposition
d	doublet
dd	doublet of doublets
DER	distributed energy resource
DEPT	distortionless enhancement by polarisation transfer
DFT	density functional theory
DLC	discotic liquid crystal
DMF	dimethylformamide
DMPD	1,4-dimethylpiperazine-2,3-dione
DMSO	dimethylsulfoxide
e^-	electron
EPR	electron paramagnetic resonance
em	emission
ESI-MS	electrospray ionisation mass spectrometry
FET	field effect transistor

FTIR	Fourier transform infrared spectroscopy
g	gram
GNR	graphene nanoribbon
HBC	hexa-peri-hexabenzocoronene
HMBC	heteronuclear multiple-bond correlation
HMQC	heteronuclear multiple-quantum correlation
HOMO	highest occupied molecular orbital
HPLC	high-performance liquid chromatography
hr	hour
Hz	hertz
i	current
i	iso
IR	infrared
J	coupling constant
K	Kelvin
kJ	kilojoule
L	ligand
LUMO	lowest unoccupied molecular orbital
m	multiplet
M	molarity
min	minute
mol	mole
m.p.	melting point
m.u.	mass units
m/z	mass to charge ratio
MALDI-TOF MS	matrix-assisted laser desorption/ionisation – time of flight mass spectrometry
max	maximum

Me	methyl
mg	milligram
MHz	megahertz
mL	millilitre
mmol	millimole
mol	mole
MS	mass spectrometry
mV	millivolt
N-½HSB	half-cyclised nitrogen-heterosuperbenzene
N-HSB	nitrogen-heterosuperbenzene
nm	nanometer
NMR	nuclear magnetic resonance
nOe	nuclear Overhauser effect
ns	nanoseconds
Nu^-	nucleophile
OFET	organic field-effect transistor
OLED	organic light emitting diode
OPV	organic photovoltaic
ORR	oxygen reduction reaction
PAH	polycyclic aromatic hydrocarbon
PEMFC	proton exchange membrane fuel cell
Ph	phenyl
POM	polarising optical microscopy
ppm	parts per million
PVD	photovoltaic device
RT	room temperature
s	singlet
SANS	small angle neutron scattering

SCE	saturated calomel electrode
STM	scanning tunnelling microscopy
sec	second
solv.	solvent
t	triplet
t* or *tert	tertiary
THF	tetrahydrofuran
TLC	thin layer chromatography
TMS	tetramethylsilane
TOCSY	total correlation spectroscopy
UHV	ultra-high vacuum
UV/Vis	ultraviolet-visible
V	volt
vs.	versus
XPS	X-ray photoelectron spectroscopy
°	degrees
δ	chemical shift
Δ	heat
ε	molar absorption coefficient
λ	wavelength
μs	microsecond
τ	half life
%	percentage

1 Introduction

1.1 The Future of Energy

Over the next 100 years it is expected that the global population will increase to 11 billion people.[1] The current global energy demand of 1.4×10^5 TWh[2] is expected to double within the next fifty years.[3] World oil reserves currently total 1,687.9 billion barrels which, with current growth factored in, would satisfy only 53.3 more years of global production.[4] It is not surprising therefore, in a world where annual oil usage grows by 1.1 million barrels per day,[4] that a significant and imminent energy crisis is forecast. Even those with a more short-term and insular view cannot refute the fact that the Organisation of Petroleum Exporting Countries (OPEC) currently produce 71.9% of all oil globally, yet half of total consumption is attributed to a much smaller number of countries.[4] Stepping aside from energy supply and geo-political motivations, there still remains an immediate environmental concern. The International Energy Agency's '*World Energy Outlook 2014*' report predicts CO_2 emissions to rise by 20% over the next 30 years and a global temperature rise of 3.6 °C.[5] This has been strongly supported by recent 'Intergovernmental Panel on Climate Change' reports which state that there is only a short time by which to reduce carbon emissions before the 'observed impacts of climate change are widespread and consequential'.[6] With only 5.3% of current energy demands being met by renewable sources, there is an enormous potential market share which can be filled with clean, efficient and renewable alternatives. Predictions expect biofuel use to triple to 4.6 million barrel of oil equivalents over the next few decades.[4] Alternatives such as algae-generated fuels, bio-diesel and even carbon-neutral fuels such as methane still fail to address the majority of environmental issues.[4] Also, moving away from biomass fuel sources offers the possibility of leaving behind historical legacies of large electrical generation facilities being located near natural resources and supplying bulk amounts of power through the grid. This offers the possibility of strategic, cleaner and more efficient energy production and supply.

1.1.1 Fuel Cells and Renewable Energy Sources

Whether scientists can address the impending issues directly through energy-generation, or indirectly *via* the harnessing of natural resources, it is clear that the fields of chemistry and material-science have a lot to offer. Energy experts are predicting that the future may lie in the concept of energy generation and storage being carried out by a variety of small devices connected to the grid; known as distributed generation. The devices, known as distributed energy resources (DERs) could provide energy to a discrete location without the reliance on centralised power-plants. This offers the potential for more reliable

methods of energy generation, in ways which are not limited by the need for large kilowatt production. DERs can be supplied using hydro, wind or solar power. In addition, a method of cogeneration can also be used to provide electricity from steam turbines, natural gas or various forms of fuel cells. They can also provide a direct solution to the annual production losses from downtime in electricity production, caused by faults on the electrical grid.

Solar energy from one day's irradiation at the Earth's surface could satisfy the global demand for almost two decades. With 120 petawatts of energy from the sun being incident on the earth, there is no doubt that the ability to harness even a fraction of this energy would drastically change the energy outlook for the immediate future. Total energy production by photovoltaics has grown year on year and appears as one of the few possibilities to match the ever-increasing demand. This is best appreciated in a 2009 report by The Worldwatch Institute which projected growth in the various renewable energy sectors over a 40-year period, shown in Figure 1.1. It is believed that solar energy will be a significant contributor and will enable energy production to match projections for demand into the future.[7]

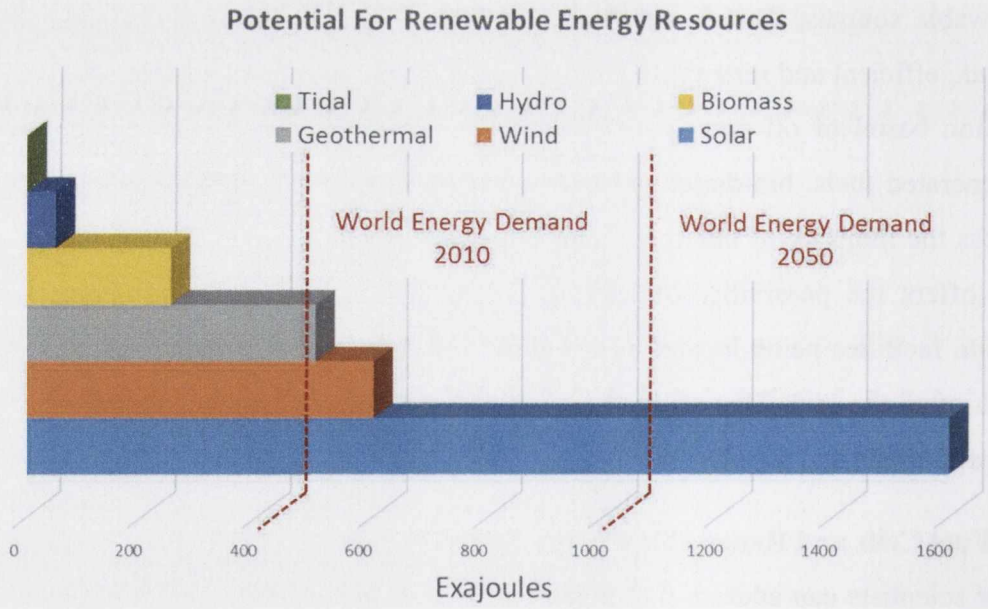

Figure 1.1: Predictions for world energy demand and supply by renewable natural resources; 'State of the World 2009', Worldwatch Institute.[7]

With the entry of large multinationals to the photovoltaic market, solar energy modules are very quickly approaching mainstream use. The introduction of technology and powertrain companies such as Tesla to the industry, means that the application of these

technologies moves ever closer to the end user. Rather than seeing this development as a means to an end, such exciting developments in application can be seen as a springboard to encourage more fundamental development in this area. To fully understand where this technology has progressed from, it is worth focusing briefly on the milestones in the development of photovoltaic research to this point.

The field of organic devices continues to grow exponentially, yielding a wide-range of applications, such as Photovoltaic Devices (PVDs) and Fuel Cells.[8] These drive an ever-increasing need, in academia and industry alike, for the innovative design of new compounds that can act as highly-functional and efficient semiconducting materials. There has been a paradigm shift from conventional conjugated materials, such as linear oligomers and polymers to low cost manufacturing alternatives. As the price of energy continues to soar, doubts surrounding the availability of precious metals become ever more common. The push to increase the efficiency and lower the cost of environmentally-friendly alternatives provides an eternal challenge for the chemist. This market was forecast to be worth $30 billion by 2015.[9] Further benefits of organic compounds with promising electronic properties result from their potential in large-area processing and in a host of different lightweight and flexible electronic devices, as outlined in Chapter 3. Techniques which make use of low-cost and simple fabrication methods, combined with cheap substrates such as glass and plastic, have resulted in the commercial production of some highly-advanced organic-electronic systems. Many successful attempts to synthesise organic compounds to this end, focus on the use of graphene sheets and fragments, with various different functionalities.[10] To fully appreciate how this can be achieved, it is necessary to focus some attention on the material itself and the manner in which it can be altered.

1.2 Graphene

Graphene was first isolated by Geim and Novoselov *via* mechanical cleavage in 2004.[11] It comprises a two-dimensional layer of sp^2 hybridised carbon atoms (shown in Figure 1.2) and exhibits extremely high thermal and electrical conductivity, owed to its unusual physical properties. The intriguing electrical,[12,13] optical[14] and mechanical properties[15] of graphene have also resulted in it being heralded as one the most promising material of the 21st century. For optoelectronic applications, the ability of graphene to self-assemble *via* π-stacking, into highly-ordered supramolecular assemblies, has attracted much positive attention. Micromechanical cleavage and sonication from graphite flakes represent two of

the most common means for isolation of a graphene crystallite, while epitaxial growth on metal substrates remains one of the more promising methods for device fabrication. Ensuring well defined shape and size of crystallites, as seen in Figure 1.2, is integral to the formation of a band gap and the successful use of graphene in devices. Despite the exponential rate of development of graphene production, there exists but a few research groups undertaking the laborious task of progressing feasible routes to its bottom-up synthesis.

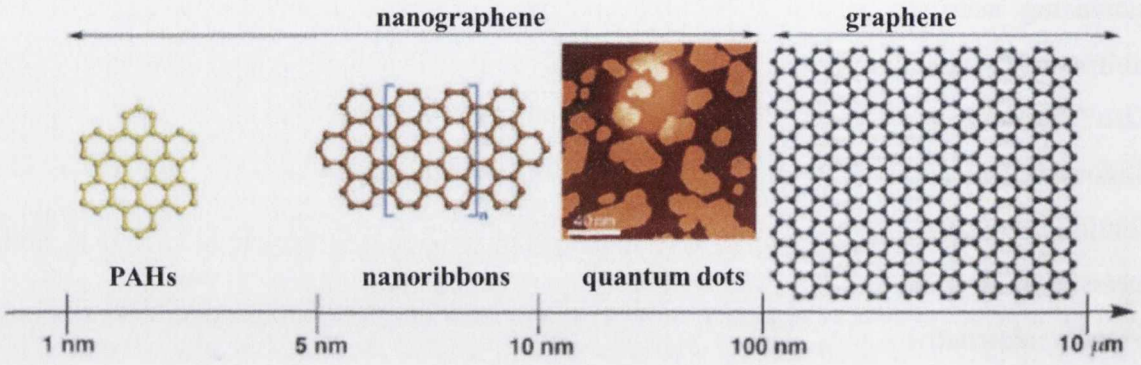

Figure 1.2: Classification of graphene and graphene fragments with respect to relative size. Reproduced with edits from Mullen et al.[16]

A small subset of bottom-up research focuses on the much sought-after doped graphenes, which offer control of the highest-occupied molecular orbital (HOMO)-lowest unoccupied molecular orbital (LUMO) gaps.[17] By exploiting the size of this band gap and tuning it to energies within the visible range, direct applications may be found for these compounds without compromising their widely publicised optical and physical attributes.[18] While pristine graphene has a significantly higher electron mobility than silicon, a fundamental limitation to its application is caused as a result of its lack of band-gap. The inability to switch off the conduction in a graphene sheet would limit any future application. This can be remedied by the introduction of heteroatoms to the graphene platform. This work has resulted in a race to successfully introduce dopants into graphene sheets and thereby tune the Fermi levels. In a fashion similar to that seen in carbon nanotubes, doping began with the use of gas adsorption such as O_2 and NO_2 molecules.[19] More recently N,[20] S,[21] and P[22] atoms have been introduced using various methods, and in the past four years there has been an upsurge in publications and patents pertaining to these experimental methods.

Current routes to achieve doped graphene fragments use: (i) thermal annealing[23] (ii) arc-discharge[24] and (iii) chemical vapour deposition (CVD)[25] methods. Such energy-intensive processes often result in an unsatisfactory distribution of nitrogen atoms and low percentage doping in the resulting material. The nature of nitrogen substitution introduced by these methods can take many forms, some examples are shown in Figure 1.3, such as graphitic, pyridinic, pyrimidinic and pyrrolic substitution. Nitrogen atoms at each of these positions can result in dramatically different electronic properties in the sheet. The effect of heteroatom dopants in the form of pyridinic and graphitic nitrogen has also been seen to introduce catalytic activity to graphene-based materials. It has been proposed that the presence of a heteroatom alters the electrochemical behavior of adjacent carbon atoms, which has an effect on the chemisorption of an oxygen molecule. Such a phenomenon has been exploited for its effect on the Oxygen Reduction Reaction (ORR), integral to the operation of Proton Exchange Membrane Fuel Cells (PEMFCs).[17] This has been another driving force for the development of viable routes to emerging N-doped materials and will be discussed in more detail in Chapter 3.

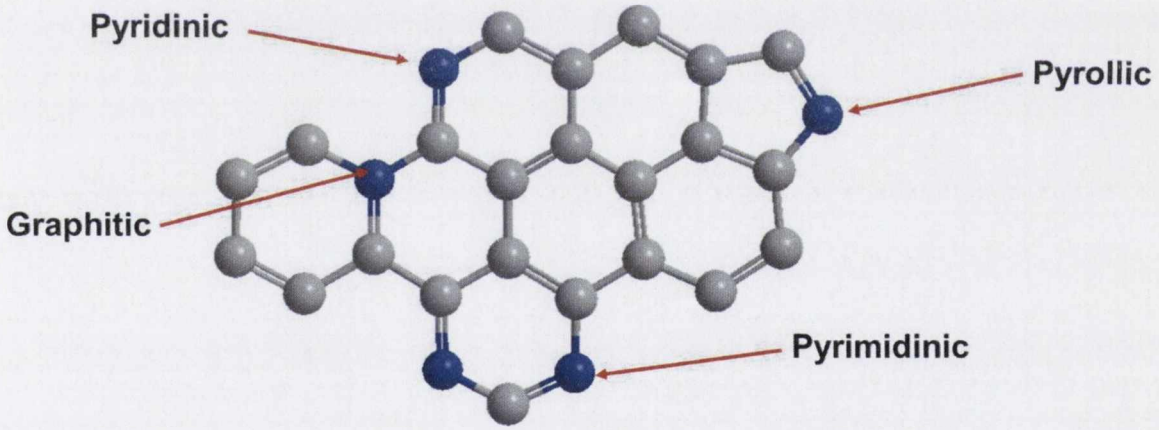

Figure 1.3: Schematic representation of nitrogen substitution within a graphitic framework. Nitrogen atoms are represented by blue spheres.

In a similar fashion to all-carbon nanographenes, bottom-up synthesis has also been successfully used to introduce dopant atoms in a measured and precise manner. One such recent example can be seen in the synthesis of graphene nanoribbons (GNRs), as discussed in Section 1.6.1. Fasel *et al.* have shown that by using heteroatom single-molecule precursors it is possible to grow selectively-substituted GNRs in a calculated and predictable manner using surface chemistry, on reactive metallic crystal faces. This method, as for the all-carbon analogues, exploits nitrogen-substituted PAH precursors as small repeating units to form larger 2D structures. To appreciate the role PAHs can play

in the directed formation of graphene fragments with predefined properties it is important to understand the nature of the single-molecule precursor.

1.3 Polycyclic Aromatic Hydrocarbons (PAHs)

Since their discovery in coal and tar deposits in the 19th century, polycyclic aromatic hydrocarbons (PAHs) have remained at the core of many industrial discoveries. Perceived formally as two-dimensional segments of a larger graphite structure and comprised solely of sp^2 hybridised carbon atoms, these intriguing compounds have seen a dramatic resurgence since the pioneering work of luminaries such as Scholl and Clar.[26] Theoretically it is suggested that approximately 20,600 possible structures sized between 4-10 aromatic rings exist, some examples of which are shown in Figure 1.4.[27] Correlations between the size of the framework, chemical reactivity and thermal stability have also warranted much research.

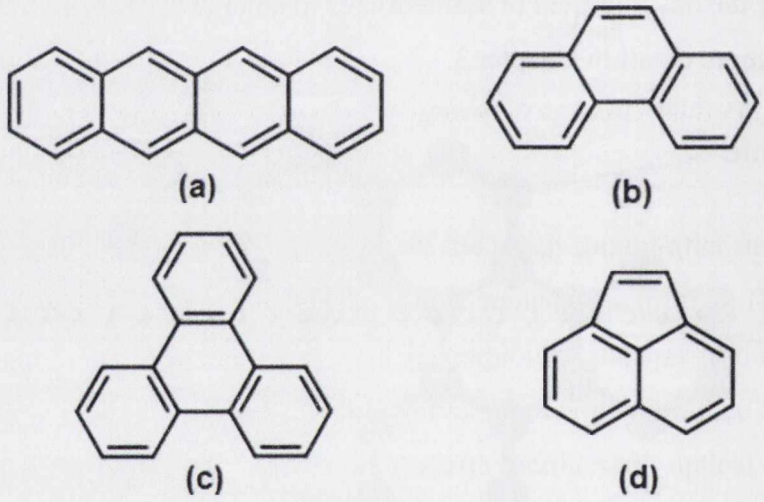

Figure 1.4: Some examples of naturally occurring PAHs: (a) tetracene; (b) phenanthrene; (c) triphenylene; (d) fluoranthene.

All benzenoid PAHs in particular have attracted much scientific interest, mainly due to their innate aromaticity, as described by Clar's aromatic sextet model. While garnering much research interest, they only represent a minute fraction of all possible PAHs. All benzenoid molecules can be differentiated from other PAHs because of their benzene-like character. By subdividing π-electrons and assigning them to specific C_6 rings, the analysis aims to create the largest number of units with π-electron sextets. Figure 1.5 shows the 4 possible mesomeric structures obtained for the tetracene compound shown in Figure 1.4 (a).

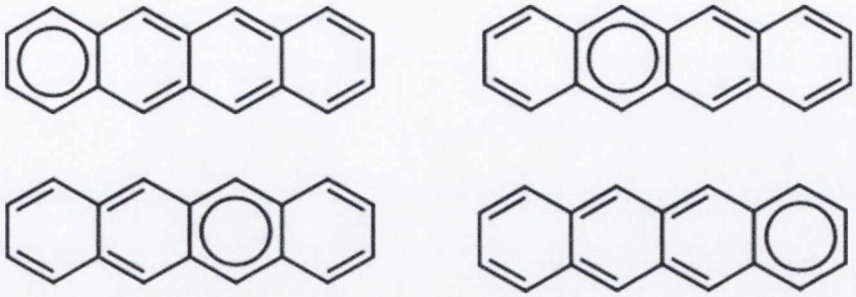

Figure 1.5: Four of Clar's aromatic sextet structures of tetracene.

Compounds such as triphenylene however, shown in Figure 1.4 (c), can only exhibit one Clar formula and are therefore referred to as all benzenoid. These compounds exhibit considerably reduced reactivity and higher thermodynamic stability. For example, when compared with its *kata* condensed C_{18} isomers, triphenylene shows the highest first ionisation energy and largest HOMO-LUMO gap. It is for this reason that all-benzenoid PAHs display significantly lower rate constants for Diels-Alder reactions than their *kata* condensed isomers.

1.3.1 Superbenzenes

Larger arrangements of benzenoid PAHs are classified by the orientation of their rings; linear (acene), angular (phene) and macrocyclic (circulene). Macrocyclic molecules, examples of which are shown in Figure 1.6, are referred to as superbenzenes because of the hexagonal nature of their cores, which are centred on the coronene moiety. The processability of these materials is strongly governed by the substitution at the periphery. Initial attempts at synthesising PAHs in a controlled manner used extremely inefficient and harsh conditions. Recent synthetic methodologies, spearheaded in the 1990s by Mullen *et al.*,[28,29,30] can provide a host of highly substituted polycyclic aromatic motifs which can be converted to fully fused products, such as those shown in Figure 1.6. The insolubility encountered with large PAHs warranted the need for innovative substitution on the periphery, with moieties such as *tertiary*-butyl groups. The presence of long alkyl chains can also confer increased solubility and even liquid-crystalline behaviour in certain cases.[31] These compounds show wonderful potential in OLED[32] and solar-cell[33] applications in which they behave as accurate analogues of graphene.

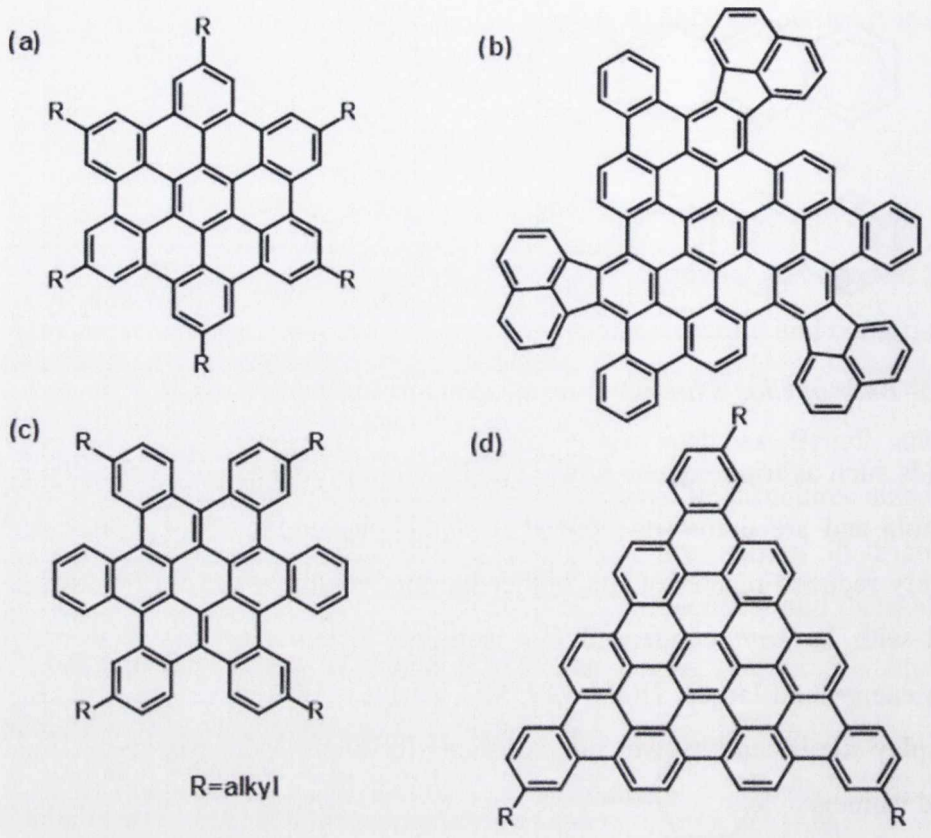

Figure 1.6: Examples of different size superbenzene cores: (a) hexabenzocoronene (C_{42}); (b) acenapthaobenzovalene (C_{90}); (c) hexa-cata-hexabenzocoronene (C_{48}); (d) benzo bistriphenylenovalene (C_{60}).

1.4 Synthesis of Polycyclic Aromatic Hydrocarbons

Achieving complete control in the synthesis of substituted graphene fragments, meant abandoning traditional routes *via* hexahalobenzene.[34] To successfully synthesise superbenzenes of this type, with selective functionalization on the periphery, the molecules are achieved using a polyphenylene precursor. In the case of hexabenzocoronene (HBC)-like molecules this precursor is hexaphenylbenzene. The two most successful routes to substituted hexaphenylbenzenes, as described by Mullen *et al.* are represented in Scheme 1.1. Route (i) shows the dicobaltoctacarbonyl-catalysed cyclotrimerisation of a substituted 1,2-diphenylethyne to yield the high symmetry polyphenylene. The limitations of route (i) arise from the required uniform functionalisation of all six pendant phenyl rings (*vide infra*). Route (ii) however, in which 1,2-diphenylethyne undergoes a [2+4] Diels-Alder cycloaddition reaction with substituted tetraphenylcyclopentadienones, can yield a range of suitably functionalised hexaphenylbenzenes. This second strategy has been adopted by Draper *et al.*[35,36] to

incorporate heteroatoms on to the periphery of hexaphenylbenzenes, in a controlled manner. Due to the varied nature of substitution possible at the periphery of such hexaphenylbenzenes, their uses have been broad and diverse. Polyphenylenes have found application in organometallic frameworks,[37] host-guest systems[38] and even in dithienylethene switches.[39] The nature of the substitution at the perimeter of hexaphenylbenzene is reliant on the manner in which the molecule is assembled, either *via* a cyclotrimerisation or cycloaddition.

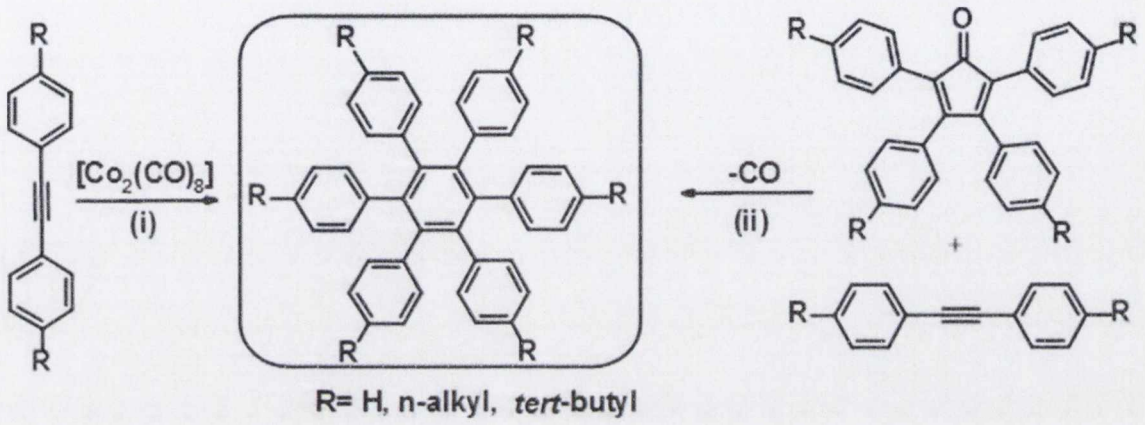

Scheme 1.1: Two routes for the synthesis of substituted hexaphenylbenzenes: (i) cyclotrimerisation of symmetric arylacetylenes; (ii) Diels-Alder [2+4] cycloaddition.

1.4.1 Cyclotrimerisation

The thermal cyclisation of acetylene was first reported by Bertholet in 1866. Metal catalysed trimerisations, as we know them today were introduced in 1948 by Reppe *et al.*[40] in the form of [2+2+2] cycloaddition reactions. This type of reaction may be catalysed by a range of different transition-metals, the most common being dicobaltoctacarbonyl which was realised by Vollhardt.[41] It is proposed that two alkyne moieties coordinate to a metal centre to form a metallacyclopentadiene which in turn coordinates to a third alkyne molecule. Formation of a metallacycle which undergoes reductive elimination at the metal eventually results in the formation of a 6-member ring.

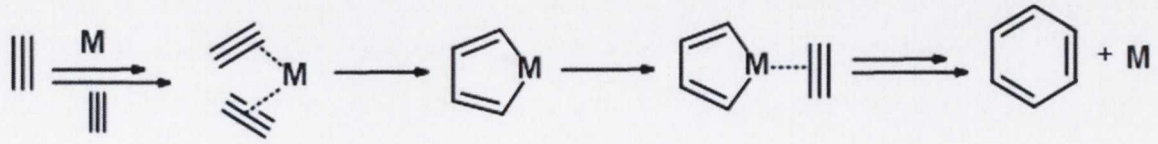

Scheme 1.2: Proposed steps for alkyne cyclotrimerisation.

Reacting arylacetylenes *via* cyclotrimerisation results in substitution at all 6 positions of the ring. This type of reaction can be used to synthesise polyphenylenes of different sizes and with various substituents, through the cyclotrimerisation of symmetric or asymmetric diarylacetylenes. As seen from Scheme 1.3, trimerisations of a symmetric arylacetylene would result in a single molecule with D_6 symmetry. When $R_1 \neq R_2$, cyclotrimerisation of the resulting asymmetric arylacetylene gives rise to both a symmetric and asymmetric product. Statistically, a ratio of 1:3 usually exists between abundances of symmetric and asymmetric polypheylenes. Depending on the substituents, separation of the isomers can be successfully achieved using column chromatography.

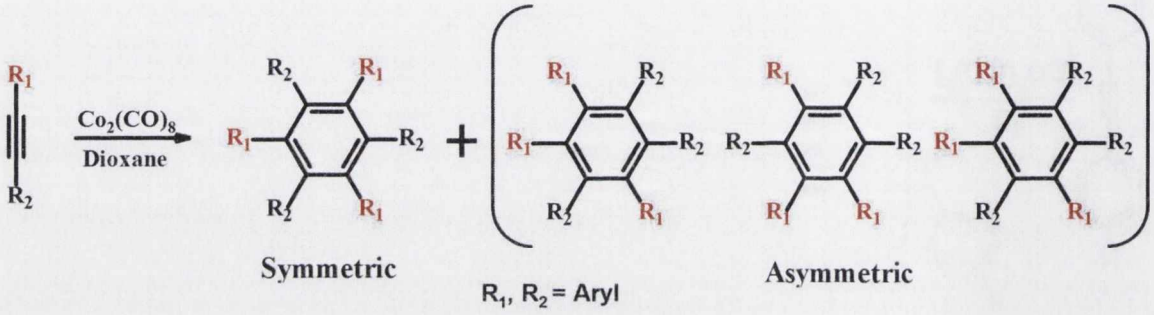

Scheme 1.3: Schematic representation of the dicobaltoctacarbonyl-catalysed cyclotrimerisation of an asymmetric arylacetylene.

Through the use of nitrogen-substituted arylacetylene molecules or terminal acetylenes it is possible to introduce heteroatom substitution to the central ring or peripheral rings of hexaaryl benzenes. In a similar manner, this reaction methodology can be used to introduce solubilising moieties to the periphery of larger polyphenylenes. Although this reaction scheme offers much potential, it is ultimately limited by the imposed symmetry generated by the trimerisation and hindered by the onerous task of separating the resulting isomers. The second possible route outlined in Scheme 1.1 using Diels-Alder cycloaddition offers a slightly more adaptable method of polyphenylene formation.

1.4.2 Diels-Alder Cycloaddition

Diels-Alder reactions are an extremely common method for the generation of peripheral or heteroatom-substituted 6-member rings. From its inception in the 1950s, this [2+4] pericyclic cycloaddition reaction between a diene and dienophile has garnered much attention because of its high stereochemical control. The [2+4] Diels-Alder reaction shown in Scheme 1.1 (ii) involves the generation of a polyphenylene from the stereospecific addition of a dienophile (arylacetylene) to the 1 and 4 positions of a conjugated diene (substituted tetraphenylcyclopentadienone). The generation of a new

ring is achieved *via* the formation of two new C-C bonds with the evolution of carbon monoxide, by heating both reactants in a non-polar solvent. Diels-Alder reactions are governed by the HOMO-LUMO pair which are closest in energy. Adhering to the Woodward-Hoffmann rules, regarding regiochemistry and stereochemistry, ensures that products from these reactions are highly predictable. Figure 1.7 shows a typical example of a 'neutral electron demand' case, for the cycloaddition of 1,3 butadiene and ethene. A 'normal electron demand' case occurs when electron-withdrawing substituents on the dienophile and electron-donating groups on the diene serve to reduce the $HOMO_{diene}$-$LUMO_{dienophile}$ separation as shown in Figure 1.7, thereby facilitating the reaction.

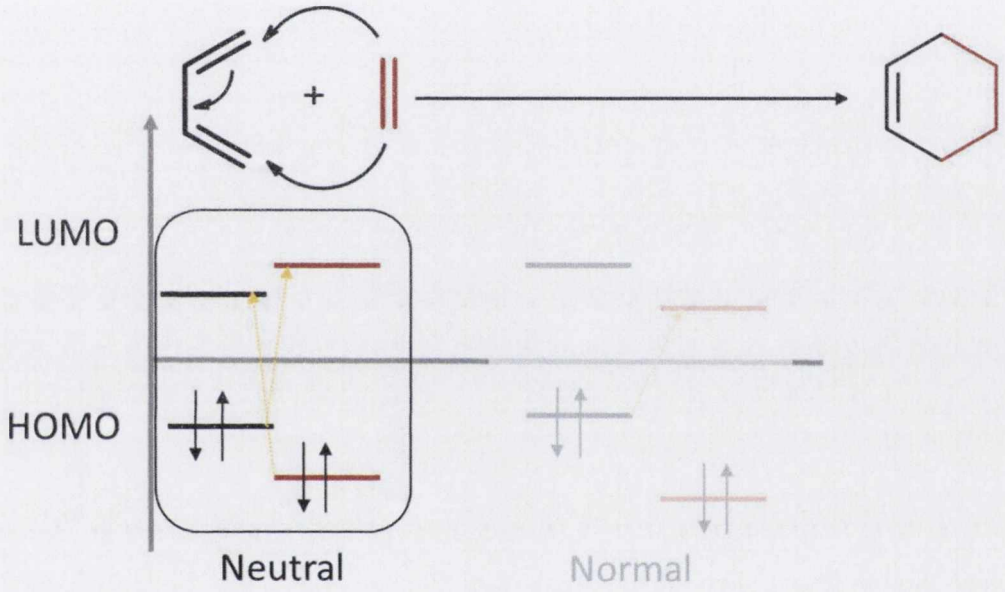

Figure 1.7: Schematic showing orbital interactions between the diene (black) and dienophile (red) in a Diels-Alder reaction. 'Normal' case shows the effect of adding electron-donating groups (diene) and electron withdrawing groups (dienophile) on the orbital interactions.

Using this route to generate hexaphenylbenzenes has a range of advantages over the cyclotrimerisation alternative. Scheme 1.4 shows the manner in which substitution can be introduced to the resulting polyphenylene, through its three constituent parts. Synthesis of the precursor cyclopentadienone *via* a two-fold Knoevenagel condensation introduces two varying types of substitution in a symmetric manner. [2+4] Diels-Alder cycloaddition with the arylacetylene can then be used as a means to situate two other types of substituents onto the resulting hexaphenylbenzene.

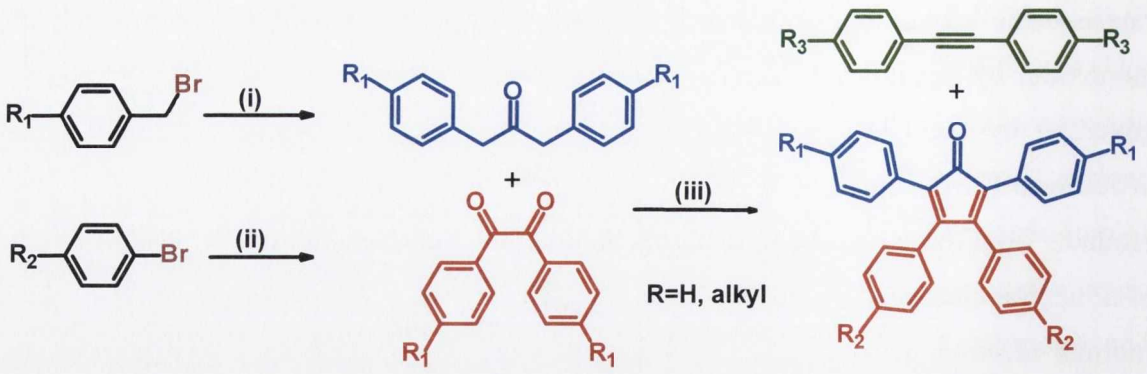

Scheme 1.4: Synthetic route for the formation of substituted hexaphenylbenzenes, divided into constituent parts: (i) procedure of des Abbayes[42] *to synthesise 1,3-diarylpropanones (blue); (ii) procedure of Mueller-Westerhoff* [43] *for the synthesis of 1,2-diketones (red); (iii) two-fold Knoevenagel reaction for the synthesis of tetraphenylcyclopentadienones.*

Mullen *et al.* have used Diels-Alder reactions to great effect for the synthesis of large dendritic polyphenylenes.[44] By changing the nature of the acetylene, the highly-efficient reaction can be used to synthesise large all-benzenoid oligophenylenes. Using trisubstituted benzenes as a synthetic template it is possible to prepare large dendritic polyaromatics *via* a series of [2+4] Diels-Alder iterations, as seen in Scheme 1.5.

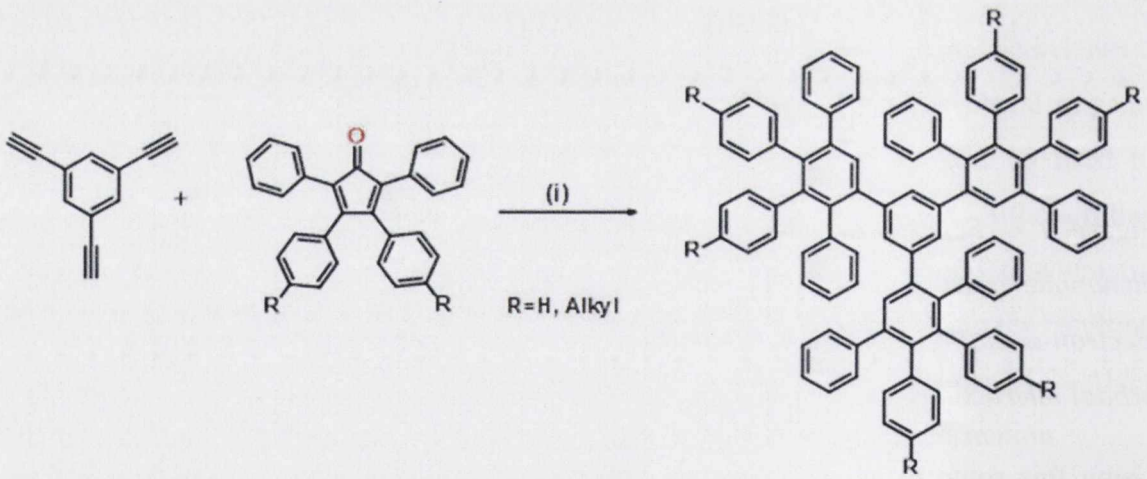

Scheme 1.5: A common Diels-Alder synthesis employed by Mullen et al. for the generation of large dendritic polyphenylenes; (i) o-xylene, 175 °C, 14 h, 95%.[44]

Cycloadditions of this nature serve as a suitable method for the generation of dendritic species, as they display high-yielding synthetic procedures with the limited generation of side-products. Additionally, because of the formation of new aromatic rings at each site the reaction equilibrium is energetically favoured towards the formation of products. The

pioneering work shown to generate polyphenylenes with varied substitution is only made possible by the ability to synthesise both precursors with predictable substitution patterns. While substitution on the cyclopentadienone is limited by the symmetry of its constituent parts, the substituted arylacetylene offers a greater degree of controllability in its synthesis. For the introduction of varied peripheral substitution or heteroatom inclusion, the ability to develop high-yielding steps for the formation of substituted arylacetylenes is integral to varied polyphenylene formation.

1.4.3 Sonagashira Coupling

Whether prepared *via* cyclotrimerisation or cycloaddition routes, the control of substitution on the resulting polyphenylene is reliant on the successful high-yielding synthesis of an arylacetylene precursor. For the most part, such an alkyne can be generated *via* the sp-sp^2 bond formation between a terminal alkyne and an aryl halide, as outlined in Scheme 1.6. Normally, this reaction can be achieved using a palladium catalyst in the presence of a copper salt, and is known as Sonogashira Cross Coupling. In the presence of a strong base, such as an amine the reduction of the Pd^{II} catalyst is made possible.

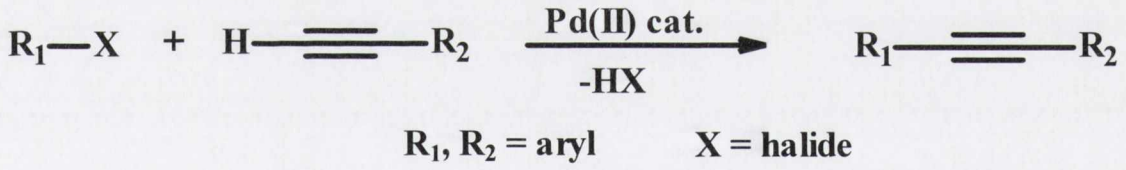

Scheme 1.6: Synthetic procedure to generate a diarylaceylene via a Sonagashira cross-coupling reaction.

In recent years, microwave organic synthesis has amassed much interest, particularly in the field of cross-coupling reactions, such as Stille,[45] Suzuki,[46] Negishi[47] and Heck[48] couplings. Gourdon *et al.* have pioneered research in the field of microwave driven Sonogashira coupling to yield pyrimidyl substituted aryl acetylenes.[49] With yields in excess of 93% and reaction times decreased from 24 hours under conventional methods to 30 minutes, this method has much proven success. It is believed that as microwave irradiation is not reliant on the thermal conduction of the reaction vessel, instantaneous superheating occurs as the microwave energy results in molecular rotation.

1.4.4 Cyclodehydrogenation

Intramolecular cyclodehydrogenation is a key step in creating extremely planarised systems from substituted hexaphenyl benzenes. To form a condensed PAH from a polyphenylene it is necessary to induce a series of C-C bond formations between the pendant phenyl rings. For over a century the desire to form fused cyclic systems has garnered considerable attention, in both research and industry alike. In 1910 Scholl *et al.* first used aluminium (III) chloride in the fusion of biaryls. Recently, the Scholl mechanism has been modelled by King *et al.*[50,51] with particular consideration given to hexaphenylbenzene. This study proposed two possible mechanisms: a) a radical cation based mechanism, shown in Scheme 1.7 for *ortho*-terphenyl and b) an arenium cation based mechanism, introduced in Section 1.6.1. For all-carbon systems it is postulated that the reaction proceeds *via* a radical cation mechanism. From DFT studies it was seen that each subsequent step lowered the energy required for the next, in a cascade mechanism - 'the slippery slope'. Mullen *et al.* have optimised the reaction conditions of oxidative cyclodehydrogenation of all-carbon PAHs, while avoiding partial cyclodehydrogenation or dimerization.

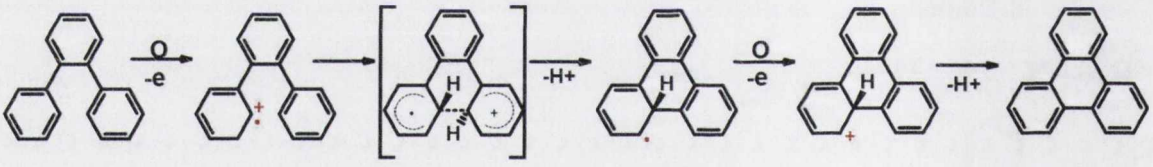

Scheme 1.7: Main steps for the cyclodehydrogenation of ortho-terphenyl via a radical cation mechanism, (O = Oxidant).

1.5 Applications of PAHs

The substitution of nanographene precursors in a symmetric or asymmetric fashion allows for the introduction of a range of different moieties. Intramolecular bond closure, achieved *via* cyclodehydrogenation, yields condensed PAHs with peripheral substitution which can confer different properties onto the fused core. *Tertiary*-butyl substitution for example has been shown to increase solubility by hindering inter-disc associations, while alkoxy substituents have been shown to influence the shape of the HBC molecule, leading to a twisted conformation in the solid state. An enormous body of work has been carried out on alkyl substituted HBC molecules, which show fascinating self-assembly on the microscale. By introducing long alkyl or alkoxy substitution it is possible to tailor these molecules to applications. These solution-processable HBC derivatives behave like

discotic liquid crystals and can be solution-cast directly on PTFE substrates. Their preference to form columnar mesophases mean that larger molecules of this nature form overlapped molecular wires which can be influenced by temperature changes. The past decade has seen many developments on the inclusion of PAHs into organic devices. Mullen *et al.* used zone-casting techniques,[52] (shown in Figure 1.8) for the successful deposition of C_{12}-HBC in ordered layers, for use in a field-effect transistor. Substituted HBCs, such as those shown in Figure 1.8 (b) or porphyrin-HBC-porphyrin triads studied by Holmes *et al.* have been used to great effect in photovoltaic devices.[53]

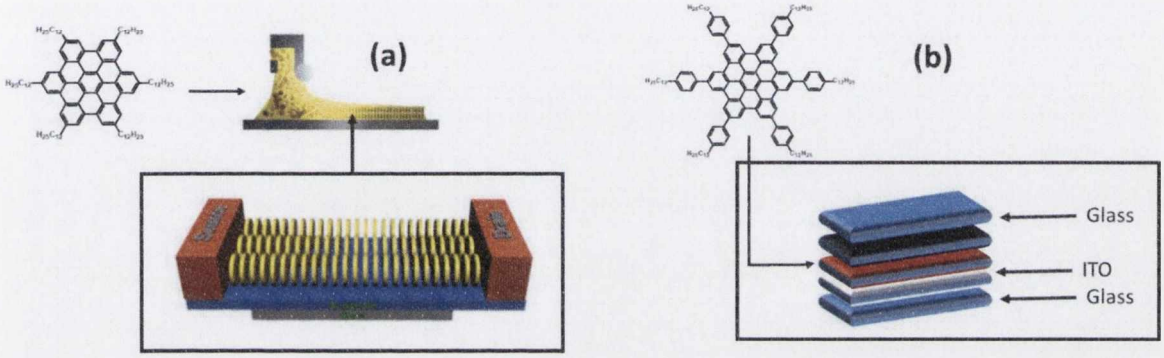

Figure 1.8: Examples of the integration of HBC derivatives into device architectures: (a) zone-casting of C_{12}HBC for application in a FET;[52] *(b) C_{12}Ph-HBC as a donor layer in a PVD.*[53]

Ultimately, the application of nanographenes in organic photovoltaics is torn between a necessity for substitution to alter electronic properties and the need to retain alkyl substitution for solubility and processability. The low solubility of coronene or hexabenzocoronene has restricted their potential in device manufacture, favouring compounds with complete peripheral substitution. However, the inclusion of atoms such as oxygen, nitrogen, phosphorus, boron or sulphur directly to the core of nanographenes can also be used to alter solubility, electronic and opto-electronic properties

1.6 Heteroatom PAHs

While heteroatom doping of graphene sheets has received great interest in the past decade, tuning electronic behaviour in a similar fashion for smaller PAH analogues has only recently seen a surge in growth. Until the work of Draper *et al.*, changing the chemical behaviour of small nanographenes was achieved either through altering the degree of π-conjugation or introducing peripheral substitution, in the form of electron-donating or electron-withdrawing groups. It is now known that the insertion of heteroatoms directly into the PAH scaffold can allow the molecule to retain planarity and

symmetry, while altering its electronic properties and aiding self-organisation behaviour. It is possible to achieve all the methods of substitution outlined for doped graphene sheets, but in a directed and controlled manner. The simplest types of substitution of PAHs can be achieved with heteroatom equivalents of triphenylene, pyrene, dibenzo chrysene and tribenzotetraphene, some examples of which are shown in Figure 1.9. These molecules show examples of peripheral nitrogen substitution which are commonly used for coordination to bidentate metal centres.

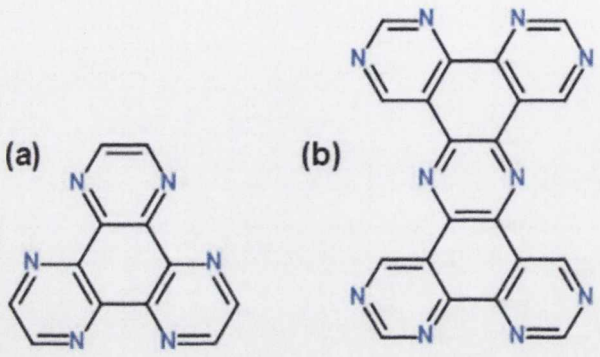

Figure 1.9: Two examples of peripheral nitrogen substitution in PAHs: (a) pyrazino pyrimidoquinazoline; (b) tetrapyrimido phenazine.

In a manner analogous to substitution in a graphene framework, it is also possible to achieve varied types of heteroatoms which show interesting potential applications. Heteroatom substitution can also be achieved for charged species, as demonstrated by Wu *et al.* in the synthesis of heteroatom PAH cations.[54] These fused compounds, derived from acridinium, xanthylium or thioxanthylium precursors show considerable control of their photophysical properties from the long-lived charge transfer state, which is dependent on the type of heteroatom substituted at the periphery. Inclusion of additional alkyl substitution, as in the case of HBC, can be used to confer self-assembling properties on to the fused molecules, as for Figure 1.10 (b). Furthermore, the organisation of the tridodecyl-substituted xanthylium salt results in the formation of liquid-crystalline phases which can aid incorporation in potential applications.

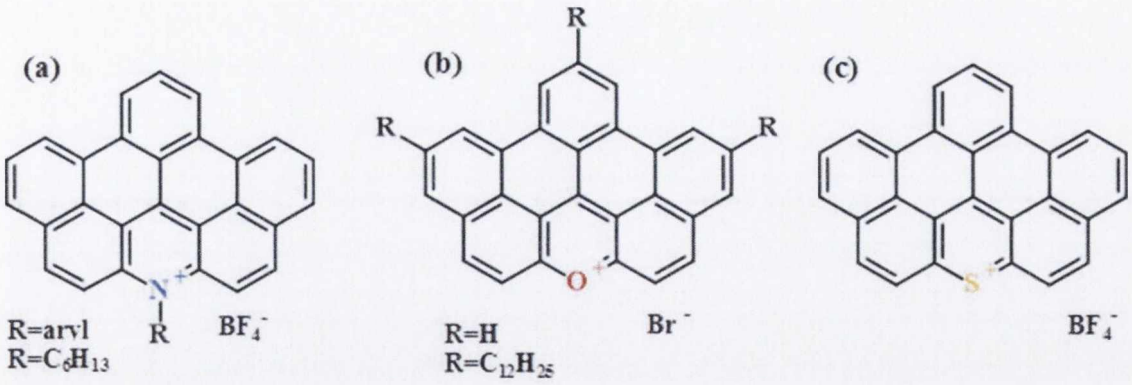

Figure 1.10: Three examples of heteroatom substituted PAHs: (a) dibenzonapthothebenidium (b) benzonapthacenoxanthylium; (c) benzonapthacenothioxanthylium.[54]

Substitution with heteroatoms at internal positions in condensed PAHs has also been a much sought-after characteristic. Figure 1.11 (a) depicts one of the simplest examples of dual internal substitution, in the form of aza-borapyrene.[55] This has recently been extended upon by Saito *et al.* to yield sulphur-containing platforms.[56] Larger scaffolds with internal substitution have always been a significant synthetic hurdle. Takase and co-workers have recently succeeded in achieving pyrollitic substitution in a fully-cyclised PAH (Figure 1.11 (b)).[57]

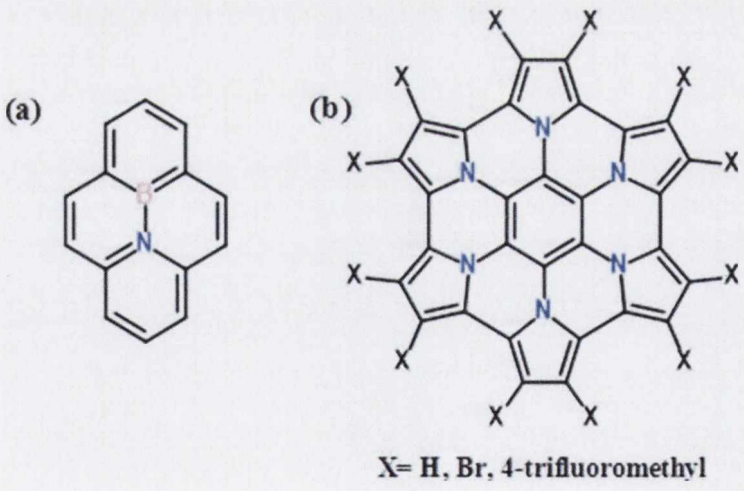

Figure 1.11: Examples of heteroatom PAHs with interior substitution: (a) 10a-aza-10b-borapyrene;[55] *(b) hexapyrrolohexaazacoronene.*[57]

By coupling substituted pyrolles to a benzene core Takase has shown it was possible to synthesise a hexapyrollobenzene which, upon cyclodehydrogenation, closed around the periphery. This form of substitution offers intriguing charge-carrier properties attributed

to its reversible redox behaviour. Another family of molecule which constitutes a large part of hetero-nanographene research is the nitrogen-substituted heterosuperbenzene.

1.6.1 Nitrogen-heterosuperbenzene (NHSB)

Nitrogen-containing heterosuperbenzenes are an intriguing class of molecule, first synthesised by Draper *et al.* in 2002.[36] The inclusion of nitrogen atoms into the heterosuperbenzene framework confers ligand functionality, greater solubility and increased electron-accepting ability. These functionalities can be introduced as in Scheme 1.8, using nitrogen substituted acetylenes, either through Diels-Alder or cyclotrimerisation reactions, to yield any of the three polyphenylenes outlined.

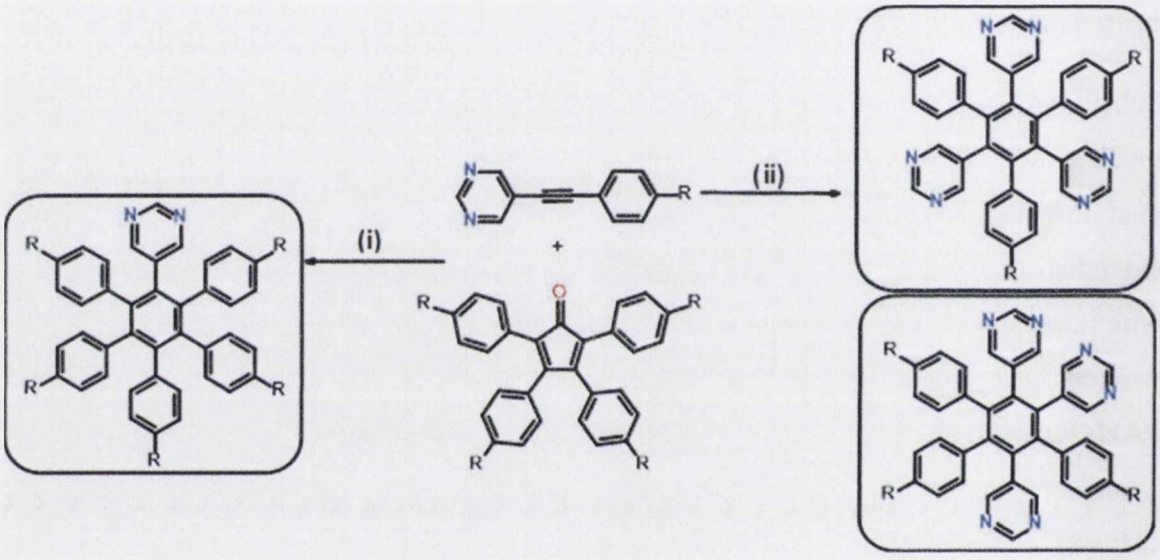

Scheme 1.8: Synthetic procedure for the generation of nitrogen-substituted polyphenylenes: (i) Diels-Alder cycloaddition; (ii) dicobaltoctacarbonyl catalysed cyclotrimerisation.

Oxidative cyclodehydrogenation of the polyphenylene precursors to synthesise NHSB has attracted a lot of interest. Conditions which result in high yields of full cyclisation (>80%) for all-carbon analogues have been seen to return different variants of cyclodehydrogenation in the presence of nitrogen substitution. As discussed in depth in Chapter 2, it is likely that in the presence of nitrogen atoms that cyclodehydrogenation progresses *via* an Arenium Cation mechanism, as outlined for the triphenylene sample case in Scheme 1.9. Protonation appears to occur at C5, thereby placing a positive charge on C6. Electrophilic attack then results in bond formation between contiguous phenyl rings.

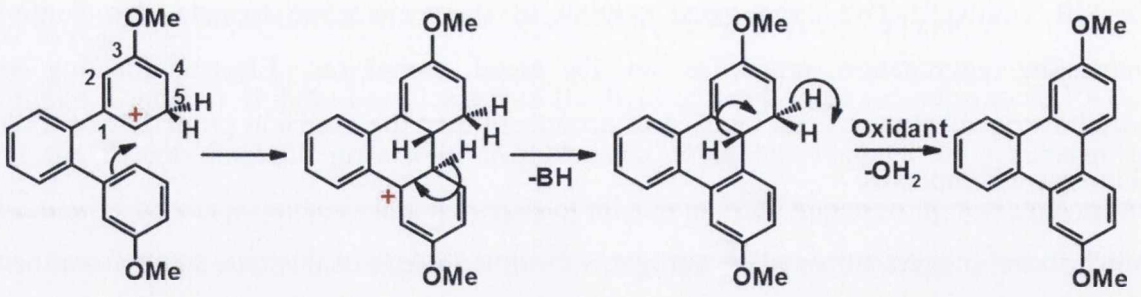

Scheme 1.9: Main steps in the cationic Scholl mechanism for the cyclodehydrogenation of a substituted ortho-terphenyl (BH= Lewis Acid).

The presence of peripheral nitrogen atoms has a direct influence on the degree and relative abundance of partially cyclodehydrogenated products. For systems which contain heteroatoms on the periphery, such as those presented by Draper *et al.*, the possibility of forming a family of partially cyclised compounds is considerably increased.[58,59] Scheme 1.10 shows three of the products isolated from the cyclodehydrogenation of nitrogen substituted polyphenylenes. Respectively they show 3 C-C, 4 C-C and 6 C-C bond formations, to yield from half-cyclised to fully-cyclised products. The partially-cyclised products in Scheme 1.10 (a) and (b) do not undergo any subsequent bond formation to yield products with higher degrees of fusion.

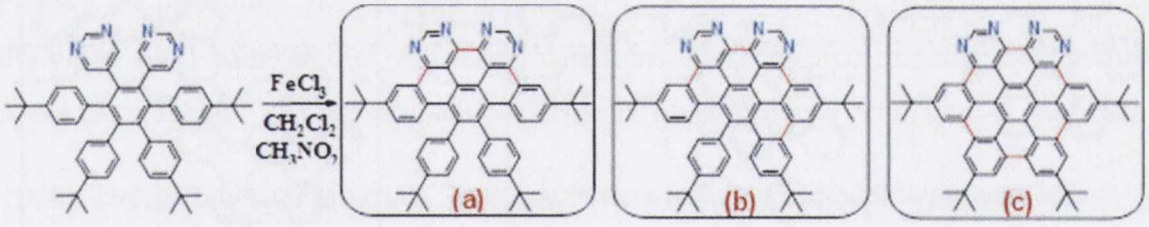

Scheme 1.10: Cyclodehydrogenation of 5,5'-(4,4''-di-tert-butyl-5',6'-bis(4-(tert-butyl)phenyl)-[1,1':2',1''-terphenyl]-3',4'-diyl)dipyrimidine using $FeCl_3$ to yield three major products. Isolated yields of (a) 20% (b) 20% and (c) 45% were achieved.[60]

To counteract the propensity to form partially fused products, directed activation at the *para*-positions of the arenium cations has been achieved through resonance stabilisation using methoxy groups, thereby increasing the chances of complete cyclisation. Upon cyclodehydrogenation these fused PAHs exhibit phenanthroline (N-N) and phenylpyridine (C-N) type coordination environments. With such an adaptable platform, this wide-ranging family of ligands can be used to form complexes with varying optical and electrochemical properties. Most notably, the low-lying π^* orbital of fully-cyclised NHSB forms a complex with Ru(II) which is both a wide-range 'black' absorber and

near-IR emitter.[35] The large fused portion of these bidentate ligands also confers interesting aggregation properties on its metal complexes. Electron-donating or withdrawing substituents can be used to accurately tune the emission properties of these fluorescent complexes.

Much recent interest surrounding nitrogen-substituted PAHs of this type stems from their potential use as feedstocks for graphene nanoribbons (GNRs). As a means to circumvent issues of solubility and limited reactivity towards solution-based cyclodehydrogenation agents, this route may well yield interesting architectures for molecular electronics applications. An example by Sinitskii *et al.*, shown in Scheme 1.11 can subsequently be used to promote intermolecular C-C coupling.[61] The varied chemistry possible from growing nanographenes in this manner is realised through the well-documented synthetic control of the monomers, previously achieved for nitrogen-substituted PAHs by Draper *et al.* Controlling nitrogen motifs and halogen substitution at the single-molecule level has a profound effect on the shape, size and substitution seen in the resulting ribbon. This method holds much potential for the creation of well-defined nanostructures in a controllable manner.

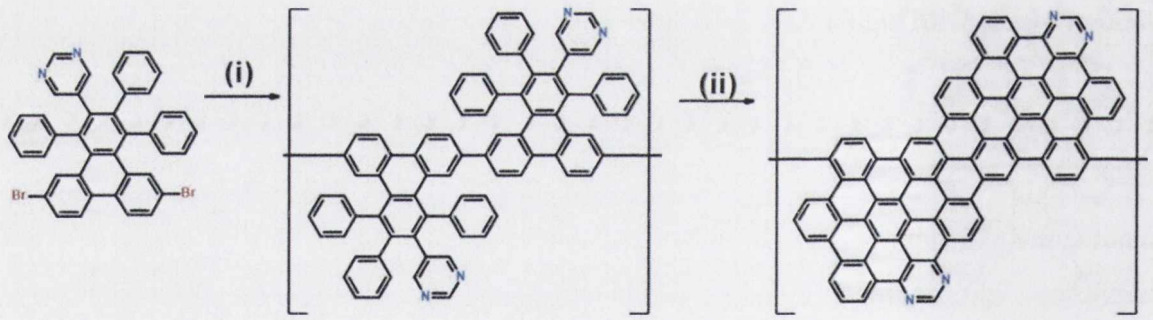

Scheme 1.11: Example of nanoribbon formation from a nitrogen-substituted polyphenylene: (i) Yamamoto coupling using bis(cyclooctadiene)nickel(0); (ii) cyclodehydrogenation using $FeCl_3$.[61]

1.7 Aims

This work aims to approach three distinct and disparate problems, which span from synthetic organic chemistry to materials application. The current growth in nitrogen-substituted PAH research has stimulated recent interest in the field, yet there still remains a drastic need to:

- Develop an understanding of novel methods for cyclodehydrogenation.
- Synthesise a library of novel compounds suitable for materials development.

- Explore the synthesis and characterisation of discotic liquid crystals.

To date, Draper *et al.* have been leaders in the field of small, nitrogen-substituted PAHs, yet the recent dramatic growth in this research topic has resulted in a substantial disconnect between synthesis and materials-application. The Draper group remains one of the few groups with the expertise to develop an all-encompassing plan for the advancement of such synthesis and to relay information from initial materials studies back to molecular design. The following three chapters aim to outline the synthesis of a library of novel compounds which has been tailored over several years to offer efficient synthesis, effective preparation and purification methods and potential scale up. The work aims to fully characterise these compounds in a thorough manner using NMR, mass spectrometry, X-ray crystallography and elemental analysis. This preliminary data on the road to application will be used to feed back into synthetic methodologies and to tailor future materials. This information loop is vital in developing bespoke materials towards application. This ambition would serve to try and rectify the disconnection between synthesis and further application.

1.7.1 Chapter 2

This chapter aims to investigate novel modes for cyclodehydrogenation. It was hoped that probing the limitations and mode of operation of this reaction could be made possible by designing a set of molecules which might individually help piece together information about the scope of C-C bond formation. This work attempts to:

- Design molecules to study the scope of new forms of cyclodehydrogenation.
- Use the information gleaned to propose a mechanism for reaction.
- Extrapolate the findings to explore conditions for bond formation in nitrogen-substituted PAHs.

1.7.2 Chapter 3

This chapter aims to investigate a new potential route for the formation of substituted PAHs. Such a target might allow for the development of a wide-ranging synthesis to yield nanographene feedstocks. It is intended to test the capabilities of such molecules for the formation of new scaffolds. This work will aim to take research from an embryonic stage, by working to:

- Develop a new synthetic procedure for substituted PAH formation.
- Synthesise appropriate molecules for the formation of superstructures.

- Evaluate new routes towards polymerisation.
- Begin preliminary testing of potential catalytic-activity.

1.7.3 Chapter 4

This chapter aims to deal with a new medley of compounds which combine nitrogen substitution with peripheral alkyl substitution. By developing on current synthetic routes for all-carbon analogues, in addition to attempting new routes for a more general synthesis, it is hoped that a collection of potential liquid-crystal molecules may be achieved. Through the use of common techniques for the appraisal of self-assembling potential it is hoped that identification of key-indicators of strategic design may be identified. This works aims to:

- Adapt current routes for discotic liquid-crystal synthesis to N-PAHs.
- Expand synthetic procedures to evaluate an adaptable route.
- Determine potential liquid-crystal ability using common techniques such as Polarising Optical Microscopy (POM) and Small Angle Neutron Scattering (SANS).

1.8 References

(1) Gerland, P.; Raftery, A. E.; Sevcikova, H.; Li, N.; Gu, D.; Spoorenberg, T.; Alkema, L.; Fosdick, B. K.; Chunn, J.; Lalic, N.; Bay, G.; Buettner, T.; Heilig, G. K.; Wilmoth, J. *Science* **2014**, *346*, 234–237.

(2) International Energy Statistics - EIA http://www.eia.gov/cfapps/ipdbproject/iedindex3.cfm?tid=44&pid=44&aid=2&cid=ww, &syid=2004&eyid=2007&unit=QBTU (accessed Feb 1, 2015).

(3) International Energy Outlook 2014 - Energy Information Administration http://www.eia.gov/forecasts/ieo/ (accessed Feb 1, 2015).

(4) BP. BP Statistical Review of World Energy 2013 http://www.bp.com/energyeconomics (accessed Feb 11, 2015).

(5) Birol, F. *World Energy Outlook*; 2014.

(6) IPCC. *Intergovernmental Panel on Climate Change*; 2014.

(7) Worldwatch Institute. *State of the World: Into a Warming World*; 2009.

(8) Schmidt-Mende, L.; Fechtenkötter, A.; Müllen, K.; Moons, E.; Friend, R. H.; MacKenzie, J. D. *Science* **2001**, *293*, 1119–1122.

(9) Harrop P., D. R. Organic Electronics Forecasts, Players & Opportunities: IDTechEx http://www.idtechex.com/research/reports/organic_electronics_forecasts_players_and_opportunities_000117.asp (accessed Jan 4, 2013).

(10) Fiori, G.; Bonaccorso, F.; Iannaccone, G.; Palacios, T.; Neumaier, D.; Seabaugh, A.; Banerjee, S. K.; Colombo, L. *Nat. Nanotechnol.* **2014**, *9*, 768–779.

(11) Novoselov, K. S.; Geim, A. K.; Morozov, S. V; Jiang, D.; Zhang, Y.; Dubonos, S. V; Grigorieva, I. V; Firsov, A. A. *Science* **2004**, *306*, 666–669.

(12) Gao, M.; Pan, Y.; Zhang, C.; Hu, H.; Yang, R.; Lu, H.; Cai, J.; Du, S.; Liu, F.; Gao, H.-J. *Appl. Phys. Lett.* **2010**, *96*, 053109.

(13) Ouyang, Y.; Guo, J. *Appl. Phys. Lett.* **2009**, *94*, 263107.

(14) Balog, R.; Jørgensen, B.; Nilsson, L.; Andersen, M.; Rienks, E.; Bianchi, M.; Fanetti, M.; Laegsgaard, E.; Baraldi, A.; Lizzit, S.; Sljivancanin, Z.; Besenbacher, F.; Hammer, B.; Pedersen, T. G.; Hofmann, P.; Hornekaer, L. *Nat. Mater.* **2010**, *9*, 315–319.

(15) Chen, H.; Müller, M. B.; Gilmore, K. J.; Wallace, G. G.; Li, D. *Adv. Mater.* **2008**, *20*, 3557–3561.

(16) Chen, L.; Hernandez, Y.; Feng, X.; Müllen, K. *Angew. Chem. Int. Ed. Engl.* **2012**, *51*, 7640–7654.

(17) Zhang, L.; Xia, Z. *J. Phys. Chem. C* **2011**, *115*, 11170–11176.

(18) Zhang, Y.; Tang, T.-T.; Girit, C.; Hao, Z.; Martin, M. C.; Zettl, A.; Crommie, M. F.; Shen, Y. R.; Wang, F. *Nature* **2009**, *459*, 820–823.

(19) Zhang, Y.-H.; Chen, Y.-B.; Zhou, K.-G.; Liu, C.-H.; Zeng, J.; Zhang, H.-L.; Peng, Y. *Nanotechnology* **2009**, *20*, 185504.

(20) Zhang, C.; Fu, L.; Liu, N.; Liu, M.; Wang, Y.; Liu, Z. *Adv. Mater.* **2011**, *23*, 1020–1024.

(21) Zhang, L.; Niu, J.; Li, M.; Xia, Z. *J. Phys. Chem. C* **2014**, *118*, 3545–3553.

(22) Song, J.; Yu, Z.; Gordin, M. L.; Hu, S.; Yi, R.; Tang, D.; Walter, T.; Regula, M.; Choi, D.; Li, X.; Manivannan, A.; Wang, D. *Nano Lett.* **2014**, *14*, 6329–6335.

(23) Li, X.; Wang, H.; Robinson, J. T.; Sanchez, H.; Diankov, G.; Dai, H. *J. Am. Chem. Soc.* **2009**, *131*, 15939–15944.

(24) Li, N.; Wang, Z.; Zhao, K.; Shi, Z.; Gu, Z.; Xu, S. *Carbon N. Y.* **2010**, *48*, 255–259.

(25) Wei, D.; Liu, Y.; Wang, Y.; Zhang, H.; Huang, L.; Yu, G. *Nano Lett.* **2009**, *9*, 1752–1758.

(26) King, B. T.; Kroulík, J.; Robertson, C. R.; Rempala, P.; Hilton, C. L.; Korinek, J. D.; Gortari, L. M. *J. Org. Chem.* **2007**, *72*, 2279–2288.

(27) Gutman, I.; Cyvin, S. J. *Introduction to the Theory of Benzenoid Hydrocarbons*; Springer: Berlin, Heidelberg, 1989.

(28) Craats, A. M. van de; Warman, J. M.; Fechtenkötter, A.; Brand, J. D.; Harbison, M. A.; Müllen, K. *Adv. Mater.* **1999**, *11*, 1469–1472.

(29) Iyer, V. S.; Yoshimura, K.; Enkelmann, V.; Epsch, R.; Rabe, J. P.; Müllen, K. *Angew. Chemie-International Ed.* **1998**, *37*, 2696–2699.

(30) Thuneman, A. F.; Ruppelt, D.; Ito, S.; Müllen, K. *J. Mater. Chem.* **1999**, *9*, 1055–1057.

(31) Herwig, P.; Kayser, C. W.; Müllen, K.; Spiess, H. W. *Adv. Mater.* **1996**, *8*, 510 – &.

(32) Jarikov, V. V. *J. Appl. Phys.* **2006**, *100*, 014901.

(33) Dong, Q.; Zhou, Y.; Pei, J.; Liu, Z.; Li, Y.; Yao, S.; Zhang, J.; Tian, W. *Org. Electron.* **2010**, *11*, 1327–1331.

(34) Berresheim, A. J.; Müller, M.; Müllen, K. *Chem. Rev.* **1999**, *99*, 1747–1786.

(35) Gregg, D. J.; Bothe, E.; Höfer, P.; Passaniti, P.; Draper, S. M. *Inorg. Chem.* **2005**, *44*, 5654–5660.

(36) Draper, S. M.; Gregg, D. J.; Madathil, R. *J. Am. Chem. Soc.* **2002**, *124*, 3486–3487.

(37) Waybright, S. M.; McAlpine, K.; Laskoski, M.; Smith, M. D.; Bunz, U. H. F. *J. Am. Chem. Soc.* **2002**, *124*, 8661–8666.

(38) Bauer, R. E.; Clark Jr., C. G.; Müllen, K. *New J. Chem.* **2007**, *31*, 1275–1282.

(39) Ó Máille, G. M. PhD Thesis, 2013.

(40) Reppe, W.; Schweckendiek, W. J. *Justus Liebigs Ann. Chem.* **1948**, *560*, 104–116.

(41) Vollhardt, K. P. C. *Acc. Chem. Res.* **1977**, *10*, 1–8.

(42) Tanguy, G.; Weinberger, B.; des Abbayes, H. *Tetrahedron Lett.* **1984**, *25*, 5529–5532.

(43) Muellerwesterhoff, U. T.; Zhou, M. *J. Org. Chem.* **1994**, *59*, 4988–4992.

(44) Carbone, P.; Calabretta, A.; Stefano, M. Di; Negri, F.; Müllen, K. **2006**.

(45) Villemin, D.; Caillot, F. *Tetrahedron Lett.* **2001**, *42*, 639–642.

(46) Wang, J.-X.; Wei, B.; Hu, Y.; Liu, Z.; Yang, Y. *Synth. Commun.* **2001**, *31*, 3885–3890.

(47) Ohberg, L.; Westman, J. *Synlett* **2001**, *2001*, 1893,1896.

(48) Vallin, K. S. A.; Emilsson, P.; Larhed, M.; Hallberg, A. *J. Org. Chem.* **2002**, *67*, 6243–6246.

(49) Nagarajan, S.; Barthes, C.; Gourdon, A. *Tetrahedron* **2009**, *65*, 3767–3772.

(50) Rempala, P.; Kroulík, J.; King, B. T. *J. Org. Chem.* **2006**, *71*, 5067–5081.

(51) Rempala, P.; Kroulik, J.; King, B. T. *J. Am. Chem. Soc.* **2004**, *126*, 15002–15003.

(52) Tracz, A.; Jeszka, J. K.; Watson, M. D.; Pisula, W.; Müllen, K.; Pakula, T. *J. Am. Chem. Soc.* **2003**, *125*, 1682–1683.

(53) Wong, W. W. H.; Khoury, T.; Vak, D.; Yan, C.; Jones, D. J.; Crossley, M. J.; Holmes, A. B. *J. Mater. Chem.* **2010**, *20*, 7005.

(54) Wu, D.; Pisula, W.; Haberecht, M. C.; Feng, X.; Müllen, K. *Org. Lett.* **2009**, *11*, 5686–5689.

(55) Bosdet, M. J. D.; Piers, W. E.; Sorensen, T. S.; Parvez, M. *Angew. Chem. Int. Ed. Engl.* **2007**, *46*, 4940–4943.

(56) Dou, C.; Saito, S.; Matsuo, K.; Hisaki, I.; Yamaguchi, S. *Angew. Chem. Int. Ed. Engl.* **2012**, *51*, 12206–12210.

(57) Takase, M.; Narita, T.; Fujita, W.; Asano, M. S.; Nishinaga, T.; Benten, H.; Yoza, K.; Müllen, K. *J. Am. Chem. Soc.* **2013**, *135*, 8031–8040.

(58) Wijesinghe, L.; Draper, S. M. *Unpublished Results*; Trinity College Dublin.

(59) Lankage, B. S.; Draper, S. M. *Unpublished Results*; Trinity College Dublin.

(60) Gregg, D. J.; Bothe, E.; Hofer, P.; Passaniti, P.; Draper, S. M. *Inorg. Chem.* **2005**, *44*, 5654–5660.

(61) Vo, T. H.; Shekhirev, M.; Kunkel, D. a; Orange, F.; Guinel, M. J.-F.; Enders, A.; Sinitskii, A. *Chem. Commun. (Camb).* **2014**, *50*, 4172–4174.

2 Bromine as a Cyclodehydrogenation agent

2.1 Oxidative Cyclodehydrogenation

At its simplest, oxidative aromatic coupling involves the formation of inter- or intramolecular C-C bonds between aromatic compounds. The generation of an electrophilic centre promotes attack at an adjacent electron rich site, resulting in the formation of a new bond. The historical roots of this reaction lie as far back as 1871 when Löwe first demonstrated oxidative dimerization for the formation of ellalic acid from gallic acid, mediated by either H_3AsO_4 or Ag_2O. 1873 saw Von Richter and co-workers use $FeCl_3$ to dimerise 2-napthol in 90% yield.[1] In 1910, Roland and Scholl showed the ability of molten $AlCl_3$ to generate poly(*p*-phenylene) from benzene. Subsequently, intramolecular oxidative cyclodehydrogenation found use in the synthesis of anthraquinone dyes and subsequently in the formation of polycyclic aromatic hydrocarbons (PAHs). The various methodologies for aryl-aryl bond formation can be broadly categorised into six categories:

a) Lewis-acid catalysed
b) Oxidant
c) Base catalysed
d) Oxidative photocyclisation (Mallory Reaction)
e) Melting under vacuum
f) Heterogeneous (surface assisted)

Initially used in the fusion of biaryls, as seen in Figure 2.1 (a), non-oxidising Lewis acids such as $AlCl_3$ required the use of an oxidant, usually molecular oxygen. In 1961 Kovacic and Kyriakis introduced the $AlCl_3/CuCl_2$ system in which copper chloride replaced molecular oxygen as the oxidant for the cyclodehydrogenation of polyphenylenes.[2] Subsequently a range of different systems, including $MoCl_5$,[3] $SbCl_5$,[4] and $Tl(O_2CCF_3)_3$ in CF_3COOH[5] have all been used. Aromatic coupling in the presence of an oxidant is today considered in tandem with Lewis acid coupling, but historically of course these were two separate methodologies. Potassium metal could be used to generate intramolecular bond formation in yields >95% for the generation of perylene and similar fused PAHs.[6] The reaction of aromatic molecules in the presence of Lewis acids began to include reagents which could also behave as 1-electron oxidants, such as $FeCl_3$ and $MoCl_5$.[7] Today, by convention this methodology is referred to as the Scholl reaction. These systems have been the stalwart of intramolecular cyclodehydrogenation for PAHs for the past 50 years and will be discussed in further detail in Section 2.2.

Historically, base catalysed aryl-aryl bond formation has always played an important role in synthetic and industrial chemistry. The possibility of ring formation coupled with proton loss was first observed by Kardos in 1913.[8] Using molten KOH in the presence of air he successfully synthesised perylene diimide, shown in Figure 2.1 (c). This synthesis has been used to great effect for the synthesis of rylene-like dyes.[9] In conjunction with Yamamoto coupling, it is possible to couple two molecules and subsequently cyclodehydrogenate to form diimide dyes. This yields fully condensed oligomers which exhibit altered absorption and emission properties. For substituted electron-deficient molecules of this nature, it has been shown that other oxidative systems prove unsuccessful in bond formation or result in cleavage of alky substituents.

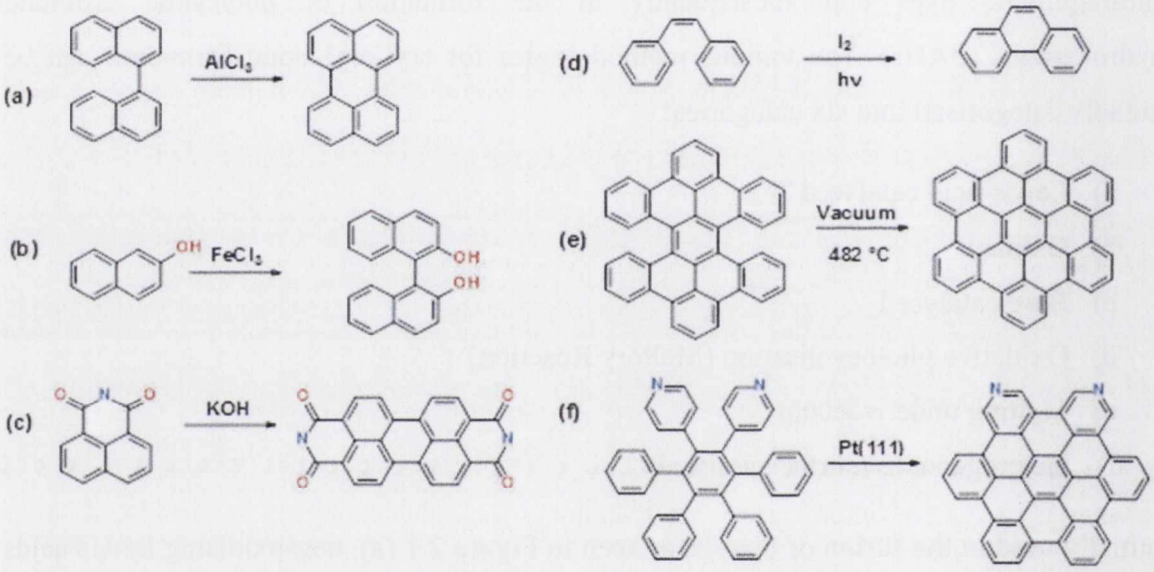

Figure 2.1: Common methodologies for oxidative bond formation: (a) $AlCl_3$ coupling of binaphthalene; (b) oxidation of 2-naphtol; (c) base-catalysed coupling of 1,8-naphthalenedicarboximide;[9] (d) Mallory reaction to cyclise stilbenes;[12] (e) vacuum driven dehydrogenation, outlined by Clar and Ironside;[10] (f) surface-assisted cyclodehydrogenation by Pinardi et al.[11]

Although the use of photochemical isomerization had been studied for some time, its existence as a practical synthetic tool only became possible in 1964 with Mallory's discovery that iodine could be used to catalyse the isomerisation of stilbenes.[12] Mechanistically, it is believed that iodine is photochemically cleaved, thereby generating radicals which perform the oxidation. Cyclisation of the *cis*-stilbene, shown in Figure 2.1 (d) represents reversible conrotatory cyclisation ($_{\pi}6$), though the speed of cis/trans isomerisation allows either isomer to result in successful bond formation. Subsequent

trapping of hydrogen iodide with propylene oxide inhibits any reduction of the double bonds. The use of thermal bond formation is also worthy of brief note, as it has existed for more than 100 years but only came to prominence in 2002 when it was exploited in thermal cyclodehydrogenation to form C_{60}. More recently the use of vacuum flash photolysis has aided cyclodehydrogenation of fluoranthenes, stilbenes and substituted perylenes, as shown in Figure 2.1 (e).[13]

Heterogeneous catalysis for intramolecular bond formation was first demonstrated for simple triphenylenes using a Pd-Pt-charcoal catalyst, achieving yields of greater than 60%. Subsequently this was applied to a range of other systems such as napthenes, fluoranthenes and even hexabenzocoronene. It paved the way for the use of modern-day heterogeneous catalysis systems which have become commonplace in the past ten years. Most notably, the watershed case occurred in 1999 when Echavarren and co-workers formed a crushed fullerene by cyclodehydrogenation, using $Pd(OAc)_2$ as catalyst.[14] The subsequent development of high-vacuum systems, twinned with the ease of production of highly-reactive crystalline faces of transition metals, has generated extensive research on the subject of on-surface bond formation. Single molecule cyclodehydrogenation of hexaphenylbenzene has been successfully performed by Mullen *et al.* on a Cu(111) substrate.[15] Inclusion of heteroatoms has also successfully been achieved for complete cyclodehydrogenation of dipyridyl polyphenylenes, as shown in Figure 2.1 (f). These methodologies have also been extended to the formation of pristine and doped graphene nanoribbons. They present a useful way of circumventing the regioselectivity problems found in solution-based bond formation, which would result in incomplete cyclisations. It has been seen that such reactions can also be catalyzed by Au(111)[16] and Pt(111)[17] crystal faces.[18–20] These processes offer low energy routes to N-doped graphene nanoribbons and nano-fragments, *via* single-source precursors and will be discussed in greater detail in Chapter 3.[18,19,21]

2.2 The Scholl Reaction

Named after the Swiss chemist Roland Scholl who pioneered the synthesis of coronene, the Scholl reaction was originally defined by Balaban and Nenitzescu as a reaction involving 'the elimination of two aryl-bound hydrogens accompanied by the formation of an aryl-aryl bond', under the influence of Friedel-Crafts catalysts. In essence, this definition has only developed marginally in the time since. Academic convention now defines a wide variety of dehydrogenative coupling methodologies as Scholl reactions.

However, it is not with these semantics, but rather the contentious issue of a reaction mechanism that the research lies truly divided. As this methodology forms such an integral part of PAH formation, it is worthy of much attention. The mechanism for the Scholl reaction has been proposed to operate *via* one of two opposing mechanisms: a radical cation mechanism, first proposed by Rooney and Pink[22] and an arenium cation mechanism, proposed by Baddeley in 1950, which progresses *via* the formation of a σ-complex.[23]

2.2.1 Radical Cation Mechanism

The radical cation mechanism involves the formation of a radical cation by one-electron oxidation, which behaves as the rate-determining step in the reaction. Support for this mechanism has come in the form of experimental work by Hammerick and Parker[24] and more recently in the form of a computational study performed by Negri and coworkers.[25] After the initial formation of a radical cation, a new C-C bond is generated by electrophilic attack to a second aromatic ring. The elimination of one hydrogen then results in aromatisation of one ring. For full aromatisation and higher degrees of cyclisation it is necessary for a second radical cation to be generated. Experimental observation makes it difficult to find definitive answers, as commonly used Lewis acids such as $FeCl_3$ or $MoCl_5$ also behave as oxidants. A compound such as $K_3[Fe(CN)_6]$ (which behaves only as an oxidant and not a Lewis acid) could prove as a useful insight into understanding the mechanism. Unfortunately, $K_3[Fe(CN)_6]$ exhibits a significantly lower oxidation potential than either of the other two reagents and therefore cannot be used to directly compare mechanisms.

The ability to perform cyclodehydrogenation electrochemically adds support to the possibility of the radical cation pathway. The likely generation of radicals however does not necessarily result in the generation of productive intermediates for further reaction, especially for compounds which are unable to stabilise long lived radicals. Rathore and co-workers have recently used 2,3-dichloro-5,6-dicyano-1,4-benzoquinone (DDQ) in the presence of acid to perform oxidative cyclodehydrogenation on fused aromatics, such as naphthalene and anthracene, with oxidation potentials up to 1.7 V.[4] Interestingly, through observation and radical trapping using hydroquinone, the authors were able to confirm that the reaction proceeds *via* a radical-based mechanism in yields up to 97%, for isoalkyl substituted HBCs.

A useful comparator for these reactions is the smallest of the polyaromatic family; triphenylene, first studied by Allen and Pingert in 1942. Several kinetic and computational studies present the mechanism of its cyclodehydrogenation as shown in Scheme 2.1, with the rate determining step believed to be the formation of the radical cation intermediate, upon removal of an electron from the reactant. Negri and co-workers have recently published a very comprehensive Density Functional Theory (DFT) analysis for triphenylene using the B3LYP/3-21G function.[25] By optimising geometries of the *ortho*-terphenyl ($C_{18}H_{14}$) precursor molecule and subsequent intermediates, an analysis of the cyclodehydrogenation is performed, paying particular attention to steric factors, spin and charge distribution. They found that the cation radical $C_{18}H_{14}^{\bullet+}$ exhibits dihedral angles between the pendant phenyls and central ring which are reduced by more than 20% from the neutral starting material. Additionally, the distance between carbon atoms at the *ortho* positions on these pendant phenyls decrease from 3.331 Å in *o*-terphenyl to 2.949 Å in the intermediate. Both of these rearrangements would result in considerably stronger interactions between adjacent rings. Analysis of spin and charge density distributions show that both *ortho* carbons behave as feasible centres for bond formation and that subsequent formation of a σ-bond between phenyl rings is likely. The release of the second proton to produce the fully aromatised triphenylene requires the removal of another electron. This is calculated to require a lower energy than for the generation of $C_{18}H_{14}^{\bullet+}$ as it is associated with a singly occupied molecular orbital.

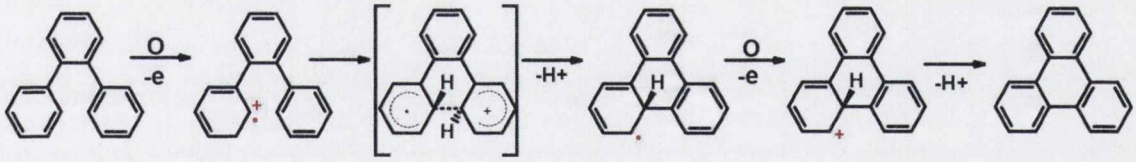

Scheme 2.1: Radical cation mechanism for the cyclodehydrogenation of o-terphenyl, as outlined by Negri and coworkers (O = Oxidant).[25]

2.2.2 Arenium Cation Mechanism

King *et al.* have been leaders in the converse argument, favouring the formation of an arenium cation intermediate which is supported by experimental and computational studies.[3] This route requires the formation of an electrophilic σ-complex between the proton/Lewis acid and the organic substrate. Attack of this electrophilic species to an adjacent aromatic ring, generates C-C bond formation, which is proceeded by hydrogen elimination, to generate the new aromatised compound. This would mean that any acid, Brønsted or Lewis could be used to generate the diamagnetic arenium intermediate. It has

been seen, as a result of this, that the generation of two equivalents of acid per bond formed leads to an accelerated reaction. Baddeley and co-workers have observed that the presence of HCl is integral to the formation of C-C bonds in the synthesis of benzanthrone. They propose that after the protonation of the aromatic compound a σ-complex is formed, which in turn reacts with another aromatic molecule to generate the C-C bond. The increasing concentration of acid is said to increase the speed of the subsequent reactions.[23]

Fortuitously, King and co-workers have also focused their attentions on the cyclisation of *o*-terphenyl. They argue that the cyclized Wheland intermediate formed *via* the radical cation mechanism is much higher in energy than its arenium cation analogue. As these intermediates influence the rate-determining proton transfer mechanism and subsequent barriers to oxidation, they propose that this adds support for the mechanism shown in Scheme 2.2.

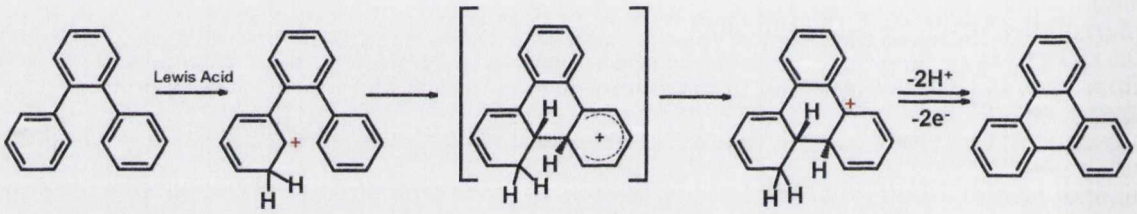

Scheme 2.2: Arenium Cation mechanism as applied to the cyclodehydrogenation of o-terphenyl, proposed by King et al.[3]

Increasing the size of the polyphenylene precursor and taking cis/trans orientations into account, it still remains clear that C-C bond formation *via* a radical cation results in substantially higher energy barriers than observed even in the highest energy scenarios for arenium cation formation. By considering the final result, i.e. complete cyclodehydrogenation by either mechanism as energetically degenerative states, they conclude that a radical cation mechanism becomes less favoured as the size of the platform grows. They also postulate that in acidic media, which do not promote radical formation, it is much more likely for cyclodehydrogenation to proceed *via* an arenium cation mechanism.

2.2.3 Application to Hexaphenylbenzene

Both Negri and King have embraced the laborious task of using computational models coupled with practical observations, to shine light on the cyclodehydrogenation of the more complex PAH system, namely hexaphenylbenzene (HPB). Not only do they

evaluate the likelihood of potential mechanisms but they also present useful predictions for the formation of partially fused products, which have been supported by synthetic observations. As in the case for *o*-terphenyl, Negri assesses the formation of the cationic radical and computationally shows that the symmetry of the intermediate is lowered to different degrees around the molecule. In accordance with the Jahn-Teller effect, this results in two adjacent phenyl rings being brought into close proximity. Calculation of the electrochemical nature of the radical-generating reaction shows a low oxidation potential and therefore gives support to the thesis of a radical cation route.[25] Consideration of the locality of charge shows that this reaction exhibits a less dramatic geometry change than for small PAH analogues. Factoring-in solvent effects for this first step points to the reaction being exothermic in solution. After aromatisation is restored to generate Scheme 2.3 (**1**), there exists three possible isomers for the subsequent bond formation. Again, investigation of their electronic distribution and spin density, in conjunction with an analysis of subsequent radical cations was enlightening. Shown in Scheme 2.3 are the various endothermic changes calculated for the radical-cation intermediate states generated from **1**.

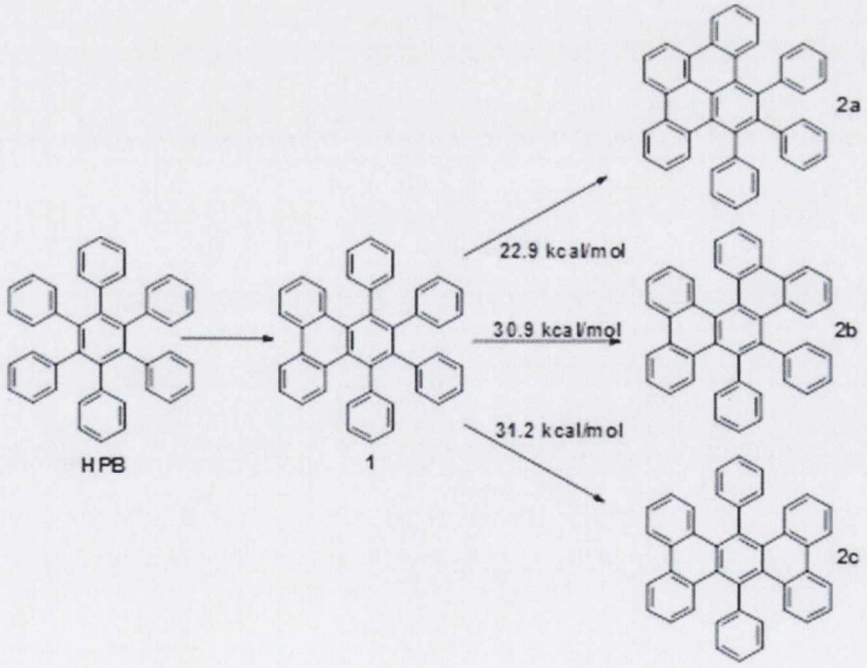

*Scheme 2.3: Potential routes of subsequent cyclodehydrogenation from $C_{42}H_{28}$ (**1**) as modelled using DFT.*[25]

This is supported by spin and charge distribution calculations. Interestingly, the generation of stable stationary points, other than **2a**, with any additional C-C bond

formation was shown not to be viable. This eliminates the possibility of simultaneous bond formation starting from the same radical cation.

King and co-workers propose that the first C-C bond formation is the rate determining step, with all subsequent cyclisations happening faster than the previous.[3] Energetically, they also find that the ability for greater electron delocalisation in increasingly larger fused systems means that subsequent bond formations become more favourable. This, they conclude, means that intermediates cannot be accumulated during the course of this reaction but are rather consumed at a greater rate than they are formed. The Hammond postulate, which states that 'a transition state for an endothermic reaction bears greater resemblance to the products' means that each new cyclisation will occur faster than the last. This, the authors term 'The Slippery Slope' and it is schematically represented in Scheme 2.4.

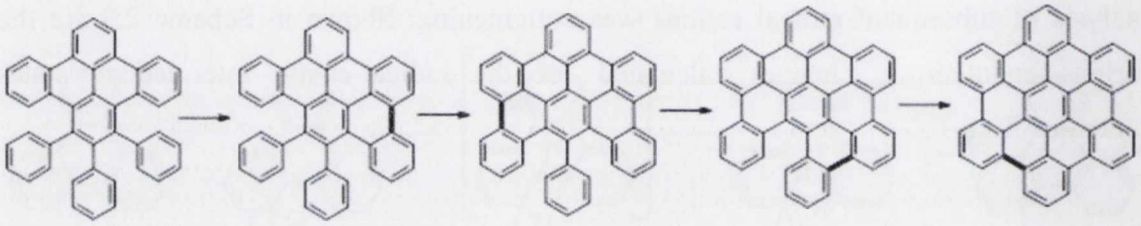

Scheme 2.4: Order of bond formation as predicted by Rempala et al. for the 'Slippery Slope' mechanism in hexaphenylbenzene, starting from the $C_{42}H_{24}$ intermediate.[3]

Although starting from the same intermediate (**2a** in Scheme 2.3) predicted by Negri *et al.*, their claim that subsequent intermediates cannot be accumulated flies in the face of the synthetic observations made by Mullen *et al.*[26] With fully characterised intermediates published in the literature, the shortcomings of the methodologies used by Rempala *et al.* are brought into question. In particular the model of $CuCl_2$ as a homogeneous mixture in carbon disulphide is fundamentally flawed. This could potentially be the source of error for the inability to predict partially cyclised compounds.

The energetic changes observed upon introducing heteroatoms or electron withdrawing or donating groups all have a very tangible effect on the nature and degree of cyclisation. This does little however to help propose one mechanism over another as the differences could be as a result of alterations in the electrophilic nature of the arenium cation or variation in the radical stability of the radical cation. There is no unequivocal proof of a mechanism by either route. In reality, one or both mechanisms could play a significant

role depending upon reaction conditions, reagent phase, precursor size, electronic distribution, spin distribution or steric repulsion. This is most evident in the work of Rathore and Kochi in which they compare catalytic activity induced by proton transfer versus that initiated by the transfer of an electron.[27] In essence, the transfer of a proton to an organic donor amounts to two $1e^-$ electron oxidations. Catalytic activity *via* proton transfer is dependent on the increased electrophilic reactivity of the cation adduct, while for an electron transfer pathway it is reliant on the likelihood of homolysis for the cation radical intermediate. This latter scenario forms the basis of Pinacol and Claisen reactions. As both possibilities occur on a very short timescale and progress through the formation of transient intermediates, it is likely that the clear differentiation made between both pathways may not be as well defined as previously thought. Rathore and Kochi have used electron paramagnetic resonance (EPR) to study the generation of cation radicals in fused aromatic systems, in the presence of acid. Using a range of aromatic donors (D) they explored the various possibilities (outlined in Scheme 2.5) for cation to radical-cation interconversions in the presence of acids such as HBF_4 and CF_3SO_3H. [27]

$$D + H^+ \rightleftharpoons DH^+$$

$$DH^+ + D \rightleftharpoons D^{+\bullet} + DH^{\bullet}$$

$$DH^{\bullet} + H^+ \rightleftharpoons DH_2^{+\bullet}$$

$$DH_2^{+\bullet} + D \rightleftharpoons D^{+\bullet} + DH_2$$

Scheme 2.5: Proposed interconversion from cation to radical cation in the presence of acid, (D = aromatic donor).[27]

The ability to generate the radical cation form $D^{\bullet+}$ can be increased to almost quantitative yields in the presence of an oxidant, such as a quinone. These quinone-mediated oxidative conversion reactions, using tetrachloro-*p*-benzoquinone or dichlorodicyano-*p*-benzoquinone in the presence of acid, can be proven by the quantitative isolation of analogous hydroquinones (Scheme 2.6). This has been used to good effect for the oxidative cyclodehydrogenation of countless Scholl products. Most notably it has been used on compounds with altered electronic distribution (arising through substitution or heteroatom inclusion) which had proven unreactive by more traditional Scholl methods.

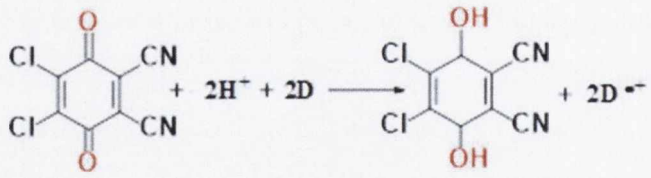

Scheme 2.6: Generation of an organic radical cation using DDQ in the presence of acid.

To fully appreciate the need for an oxidative cyclodehydrogenation system, which could deal with a more varied electronic distribution, it is necessary to establish the effect that a move away from all carbon systems may have on bond closure and to detail the hurdles encountered with previous systems.

2.3 Electronic Effects on Cyclodehydrogenation

The varied oxidation potentials of organic molecules, as influenced by substituent effects, have long been a consideration in choosing the most appropriate cyclodehydrogenating agent. As the radical cation mechanism is extremely sensitive to the spread of electrons across a molecule, bond closure may be directed to the positions at which electron density is maximised. Inclusion of electron donating *o*, *p*-directors such as methoxy substituents can be used to direct bond closure through resonance, and can result in high yields of cyclisation (seen in Scheme 2.7 (a)).

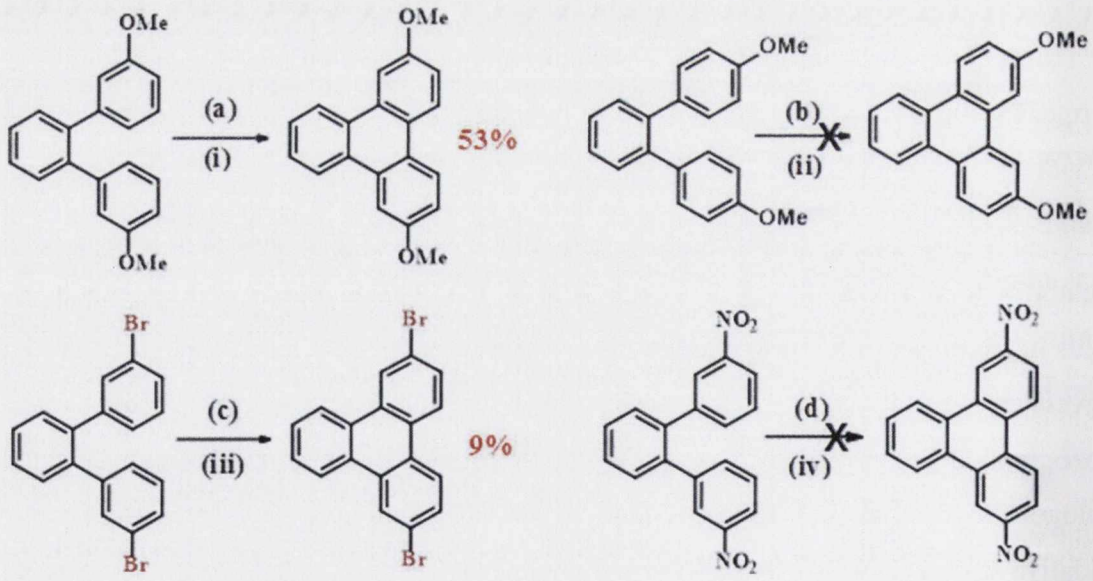

Scheme 2.7: Effect of electron donating and withdrawing substituents on the cyclisation of o-terphenyl using common cyclodehydrogenating agents: (i) $MoCl_5$ in CH_2Cl_2; (ii) $MoCl_5$ or $PIFA/BF_3Et_2O$; (iii) $MoCl_5$; (iv) $MoCl_5$ or $PIFA/BF_3Et_2O$.

A *para* substitution with methoxy substituents can completely inhibit bond formation in an *o*-terphenyl molecule, even under the various reactions conditions seen in Scheme 2.7 (b). These effects have been modelled computationally by King *et al.* through calculating the relative proton affinities of positions on the substituted rings. For the substitution pattern seen in Scheme 2.7 (a) protonation *ortho* to the bond-forming site appears most likely and will indeed promote bond formation. This has been supported computationally and empirically by others, including Wijesinghe *et al.*[28] Substitution with bromine atoms[28] also serves to direct *o*, *p* substitution, but its deactivating nature is seen to decrease the likelihood of bond formation, resulting in the poor yield observed in Scheme 2.7 (c). In the most dramatic of cases, nitro substitution, which would result in deactivated *m*-directing substitution, fully inhibits the progression of the Scholl reaction. The effect of electron withdrawing groups on the oxidative cyclodehydrogenation of PAHs has caused many obstacles which are not encountered in more electron-rich analogues. Following $FeCl_3$ treatment, brominated hexaphenylbenzenes only show trace amounts of cyclisation. Less electron deficient counterparts, such as iodo-hexaphenylbenzene have been seen to fully cyclodehydrogenate however.[29] As many Lewis acid catalysts have been shown to result in ether or alkyl cleavage, a route which could be used to build up an aromatic platform with halogen substituents in place, holds much potential for the synthesis of alkyl-substituted PAHs. Jones *et al.* have recently discovered that DDQ in the presence of methane sulfonic acid, as discussed previously, gives unprecedented success for complete cyclisation of hexaphenylbenzenes substituted with Br, F and CF_3, represented by the structures in Figure 2.2.

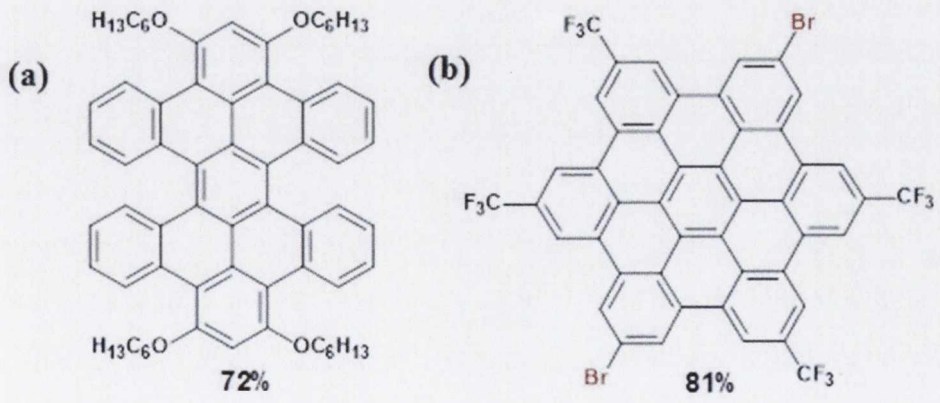

Figure 2.2: Structures resulting from the cyclodehydrogenation of substituted hexaphenyl benzenes using DDQ, with (a) electron donating o,p directing alkoxy substituents and (b) electron-withdrawing deactivating Br and CF_3 moieties.

This methodology was also applied to synthesise tetrabenzocoronene derivatives, substituted with chlorine and fluorine groups at the periphery. It is clear that electronic distribution has an influence on the ability of polyaromatic molecules to generate reactive cations and to subsequently promote cyclodehydrogenation. This is most evident upon the inclusion of heteroatoms into the aromatic platform. It is therefore necessary to focus some attention on previous attempts to cyclodehydrogenate in the presence of internal heteroatoms substitution.

2.4 The Effect of Heteroatoms on Cyclodehydrogenation

Just as the effects of peripheral substitution can be seen to change activation towards cyclodehydrogenation, so too can the inclusion of heteroatoms within an aromatic ring. Historically, harsh conditions using molten $AlCl_3$ achieved successful bond formation in compounds such as coumarin and *N*-acylurea. For more precise methodologies however, the varied reactivity originating from the addition of a heteroatom can yield different levels of success and different degrees of bond closure. This is outlined very effectively by Gryko and co-workers for the synthesis of 1-azaperylene in Scheme 2.8.[30]

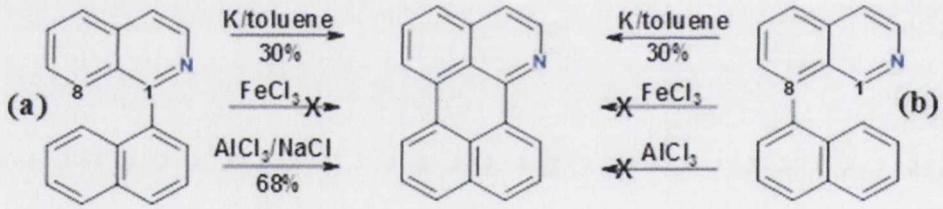

Scheme 2.8: Various routes attempted for the synthesis of 1-azaperylene from (a) 1-(naphthalene-1-yl) isoquinoline and (b) 8-(naphthalene-1-yl) isoquinoline.[30]

Fusion at the 8 position of the isoquinoline moiety seen in 1-(naphthalene-1-yl) isoquinoline shows the likelihood of attack at a more electron rich centre, as is commonly seen in electrophilic aromatic substitution reactions of isoquinolines. This manifests itself in a yield of 68% for a strong Lewis acid system. Conversely, 8-(naphthalene-1-yl) isoquinoline shown in Scheme 2.8 (b) shows that C-C bond formation at the much more electron-poor 1 position can only be achieved in the harshest K/toluene system. As seen with peripheral substitution, the altered aromaticity, the ability to generate cations and the manner in which the substitution directs electrophilic attack, all influence the ease and success of cyclodehydrogenation. This is most apparent in the attempted cyclodehydrogenation performed by Wu *et al.* on the compounds shown in Figure 2.3.[31] Pyridine exhibits a pK_a of 5.2, in a similar range to to that of isoquinoline (pK_a= 5.4) and

consideration of the canonical resonance forms show that the generation of a reactive cation at the 3, 5 positions of a pyridine ring is highly unlikely. This would preclude any chance of bond formation between rings in a system such as Figure 2.3 (a). Although the 3, 5 positions on a pyridine ring are activated for attack, as in Figure 2.3 (b), bond formation is not seen to occur. It is likely also that substitution at the 3 position, as seen in Figure 2.3 (c) (d), deactivates these positions and reduces the chance of attack. For other electron deficient systems such as pyrimidyl substitution (pK_a = 1.3) the resonance forms depict a much more likely situation of bond formation at the 4,6 positions of the pyrimidyl ring.

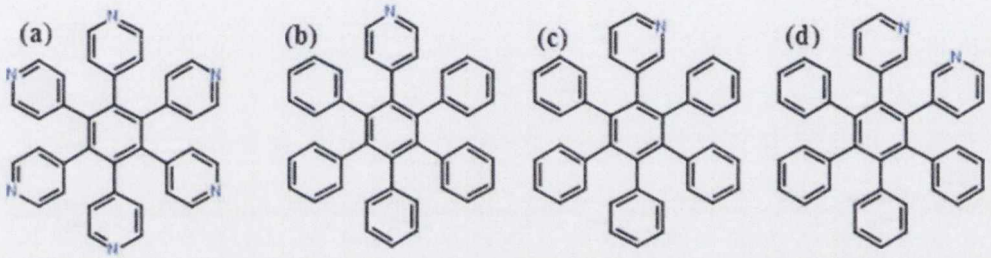

Figure 2.3: Various examples of pyridyl substituted polyphenylenes synthesised by Mullen et al. which proved unreactive to cyclodehydrogenation under standard Lewis acid conditions.[31]

The inclusion of nitrogen atoms in more aromatic platforms was first attempted by Lazerges *et al.* for hexapyrollylbenzene. With the expectation of the trivial generation of radical cations to yield bond formation, as is commonly seen in the synthesis of pyrolle based organic conducting polymers, systems such as iron perchlorate were attempted without yielding full cyclisation. Takase and coworkers, upon using $FeCl_3$, showed the potential for full cyclodehydrogenation, as shown in Scheme 2.9.[32]

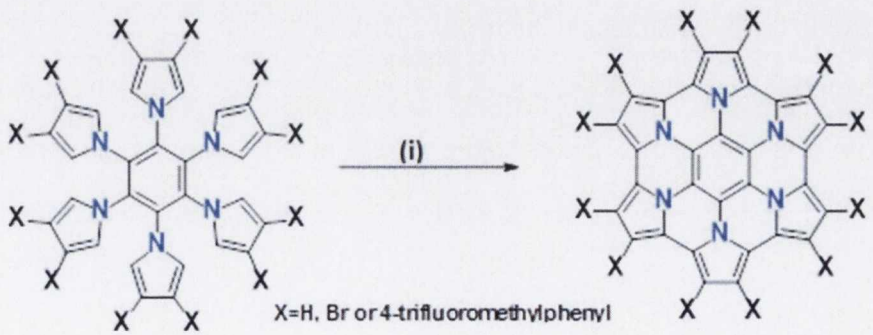

Scheme 2.9: Cyclodehydrogenation of hexapyrrolylbenzene for the formation of hexapyrrolohexaazacoronenes: (i) $FeCl_3$, CH_2Cl_2, CH_3NO_2.[32]

In particular, by substituting with electron withdrawing groups in both β positions, the more electron deficient pyrolles were seen to fully cyclodehydrogenate in very high yields. A planar molecule was achieved, in stark contrast to the DFT calculations which predicted a bowl-shaped molecule. Using flash photolysis and electrochemical measurements it was confirmed that one-electron transfer, followed by very fast bond formation results in the cyclodehydrogenation. Previously the cyclodehydrogenation of other heteroatom compounds, such as phosphorus and oxygen-containing molecules has been achieved photolytically. More recently however, cyclodehydrogenation with other heteroatoms has also been made possible using various Lewis acid conditions. Swager *et al.* have recently synthesised dibenzo[3,4:5,6]anthra[1,2-b:8,7-b']dithiophene and its substituted derivatives *via* $FeCl_3$-catalysed oxidative cyclodehydrogenation in yields as high as 75%, as shown in Figure 2.4 (a).[33] In a similar fashion, Yamaguchi and coworkers were able to induce a selective cyclisation in 6,13-dihydro-6,13-diborapentacene using $FeCl_3$ in CH_3NO_2 and CH_2Cl_2.[34] Using mesityloxy substitution at the 4,5 positions of the anthracyl moieties it was possible to induce cyclodehydrogenation (Figure 2.4 (b)).

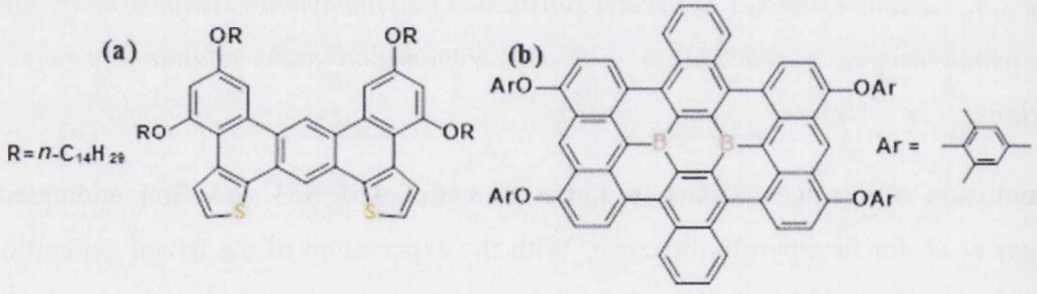

Figure 2.4: Heteroatom-containing molecules generated from cyclodehydrogenation using $FeCl_3$: (a) dibenzo[3,4:5,6]anthra[1,2-b:8,7-b']dithiophene;[33] *(b) boron-doped nanographene.*[34]

2.5 Synthesis and Characterisation

2.5.1 Diaza Polyphenylene Synthesis

Section 2.4 highlighted the difficulties experienced in carrying out C-C bond closures in the presence of heteroatoms such as nitrogen. With this in mind, it was decided to revisit some earlier findings within the group, which had also been seen by Gourdon *et al.* surrounding the cyclodehydrogenation of the simplest 2N containing fragments: diaza-substituted polyphenylenes.[35] This work had shown that cyclodehydrogenation using $AlCl_3/CuCl_2$ or $MoCl_5$ gave rise to insoluble polychlorinated products and had led the authors to conclude that para unsubstituted pendant phenyl rings cause uncontrolled

oligomerisation. Over the past 5 years a push to synthesise partially fused nitrogen doped fragments, either as oligomers or nanoribbons in the absence of metal catalysts, has garnered much attention. As discussed in Chapter 3 the ability to synthesise polyphenylene precursors to this end would offer much potential in the field of electrocatalysis, with the possibility of exploitation for oxygen reduction in fuel cell technologies. Discovery of a new route to cyclisation for these systems, offering directed and controllable synthesis is highly desirable. For a diaza-substituted polyphenylene, changes can be made to the five peripheral phenyl rings. As outlined in Chapter 1 this is done by reacting a substituted cyclopentadienone with an arylacetylene. Substitution can be introduced to the cyclopentadienone in a symmetric fashion across the four pendant phenyl rings. Substitution on the arylacetylene can be achieved in an asymmetric fashion. This was done most effectively by synthesising a phenyl pyrimidyl acetylene, with a substitution pattern conferred upon the final product from the ethynyl benzene starting material, as shown in Scheme 2.10. This was be achieved using a Pd(II) catalyst in the presence of CuI, modified from Gourdon, using microwave synthesis in diethylamine/DMF or using traditional Schlenk techniques in trimethylamine/DMF.[35] The crystalline nature of the products added to the ease of purification with isolation of the product being achieved in high yields. This resulted in three asymmetric arylacetylenes with varying degrees of electron donating and withdrawing ability. Incorporating this substitution into polyphenylene frameworks is achieved by reaction with tetraphenylcyclopentadienones.

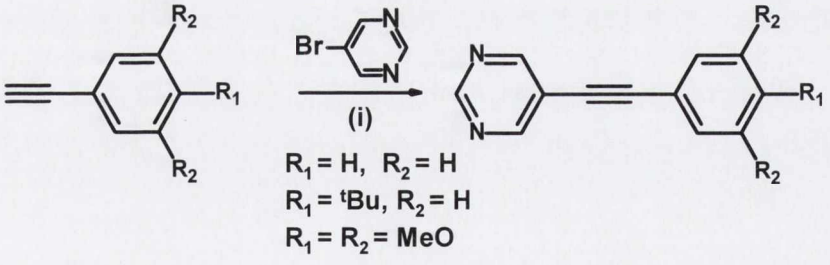

Scheme 2.10: Synthetic route to substituted 5-(phenylethynyl)pyrimidines: (i) $Pd(PPh_3)_2Cl_2$, CuI, Et_3N, μλ, 125 °C, 50 min (63%).

As shown in Chapter 1, the synthesis of such substituted tetraphenylcyclopentadienones was achieved by a Knoevenagel condensation between a substituted diphenylpropanone and a substituted 1, 2 dione *via* a reflux under basic conditions, as shown in Scheme 2.11 (iii). A Diels-Alder reaction, using benzophenone as solvent, produced the

polyphenylenes in yields up to 75%. Purification by column chromatography, followed by recrystallization from CH_2Cl_2/hexane or CH_2Cl_2/methanol, allowed for the synthesis to be increased to gram-scale quantities, while producing highly-pure white crystalline samples. Scheme 2.11 shows the three polyphenylenes which were synthesised in this manner and characterised using mass-spectrometry, elemental analysis, thermogravimetric analysis and IR.

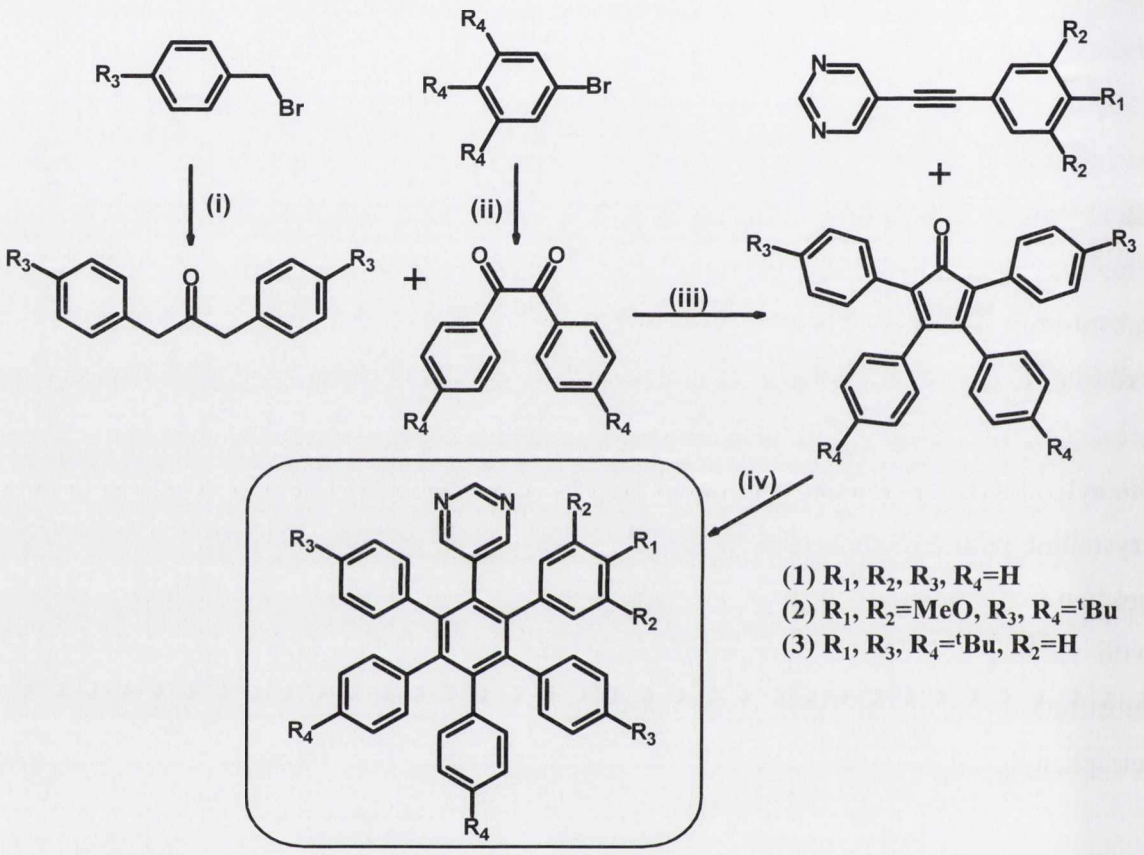

*Scheme 2.11: The synthetic route to polyphenylenes **1**, **2**, **3**: (i) $Fe(CO)_5$, Bu_4NHSO_4, $Ca(OH)_2$, reflux, 18 h; (ii) n-BuLi, THF, dimethylbenzene-1,4-diamine, -78 °C, 18 h; (iii) KOH, ethanol, reflux, 5-30 min; (iv) benzophenone, 250-300 °C.*

2.5.2 Cyclodehydrogenation

In the presence of bromine, these polyphenylenes (**1**, **2**, **3**) display a very intriguing reactivity. Previously, for all-carbon analogues neat bromine was successfully used to yield fully brominated polyphenylenes in almost quantitative yields. However, in the presence of heterosubstituted polyphenylenes the results were extraordinary; modification of the procedure yielded a methodology which could be used solely for the purpose of cyclodehydrogenation. When heated in the presence of excess bromine, under pressure-tube conditions with toluene as the solvent, cyclisation around the pyrimidyl ring is seen

to occur, as seen in Scheme 2.12. Collection of the precipitated product, followed by recrystallisation from CH_2Cl_2/CH_3OH gives **4** and **6** as pale yellow needles in yields from 70-90%. Initially, when pursuing purification by column chromatography, it was necessary to remove excess bromine by sodium thiosulfate or sodium carbonate washes. Once the correct conditions were achieved it was possible to crystallise the product directly from the reaction mixture. This eliminated yet another reaction step and ultimately led to the isolation of crystals of **4** which were suitable for single crystal (X-ray diffraction) XRD.

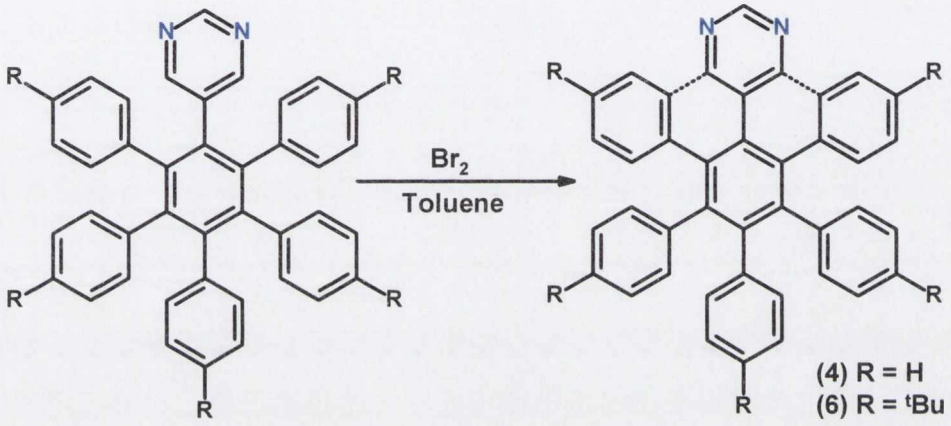

*Scheme 2.12: Procedure for the synthesis of **4** and **6**. Polyphenylene precursors were heated in a pressure-tube in the presence of toluene and bromine for 1 h.*

4 crystallized in the P-1 space group with two molecules per unit cell. Two toluene solvent molecules found in the voids could not be modelled to an acceptable level and therefore SQUEEZE was applied. As a result of the ring-closure, the fused phenyl and pyrimidine rings now form part of a significantly curved bowl-like structure, as seen in Figure 2.5. The strained nature of this pyrimidine section results in a curve of 20° at the extremities, relative to the plane of the central ring. The molecules pack in a head-to-tail fashion, with almost perfect overlap of the pyrimidine rings, exhibiting π-π interactions between the fused aromatic cores. This results in intermolecular distances of 3.538 Å between planes. In the absence of substitution at the newly fused platform, the lateral and horizontal curvature seen over the fused 6-ring moiety (tribenzoperimidine) appears to inhibit greater interaction or overlap.

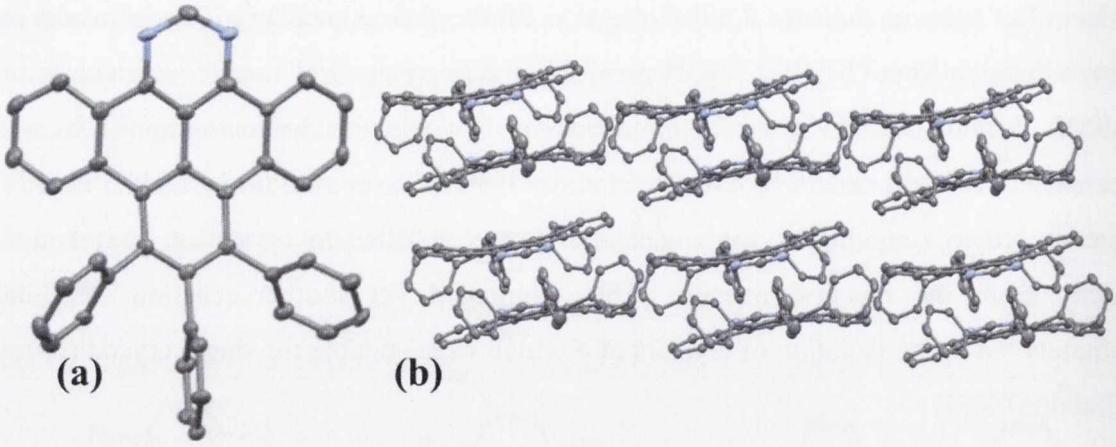

Figure 2.5: Representation of the asymmetric unit and packing motif seen in the crystal structure of ***4****. Thermal displacement ellipsoids shown at 50% with hydrogen atoms omitted for clarity.*

The C-C bond-forming reaction was studied by *in situ* ^{1}H NMR spectroscopy. Using a $1x10^{-8}$ M solution of polyphenylene in $CDCl_3$, with 100 equivalents of bromine, it was possible to gain interesting insights into the timescale of each step of the reaction. The spectroscopic study over the course of 25 minutes documented the fast nature of the cyclisation between the pyrimidine ring and its neighboring phenyl rings. Figure 2.6 shows the relevant iterations of the reaction at the pyrimidine ring, as characterized by ^{1}H NMR spectroscopy. The evolving spectra were rationalized with respect to time *via in situ* experiments. The information garnered from these ^{1}H NMR spectroscopic studies (Figure 2.6) meant that it was subsequently possible to separately vary the reaction time, temperature, solvent, vessel conditions (open or closed) and to optimize the formation of most of the products and thereby gain an opportunity to fully characterize them.

The most dramatic change in the spectrum of the unsubstituted (**1**) is seen upon initial cyclisation, where the resonance of H1 in the pyrimidine ring shifts from δ = 8.6 ppm to a singlet at δ = 9.1 ppm upon initial formation of **4**. The signal at δ = 8.2 ppm, appearing as a singlet (corresponding to both protons, alpha to nitrogen (2, 2') in the starting material) shifts to 8.7 ppm, integrating for 1H. This confirms the instantaneous formation of the C-C bond at one side of the molecule. Within 4 minutes proton H1 is observed to have shifted to a very broad singlet at δ = 10.6 ppm (observed in much better definition in Figure 2.7 at δ = 9.85 ppm). The decreasing concentration of the partially cyclised product, as quantified by periodic mass spectrometry analysis confirms that both bond forming events do not necessarily occur contemporaneously. The fusion also results in the

significant deshielding of H4, from δ = 6.9 ppm to δ = 9.5 ppm upon initial cyclisation, where it now appears as a doublet and exhibits ^{3}J coupling of 8 Hz. As with the more complicated systems discussed elsewhere in this thesis, the examination of HSQC spectra allowed for full assignment of the molecules.

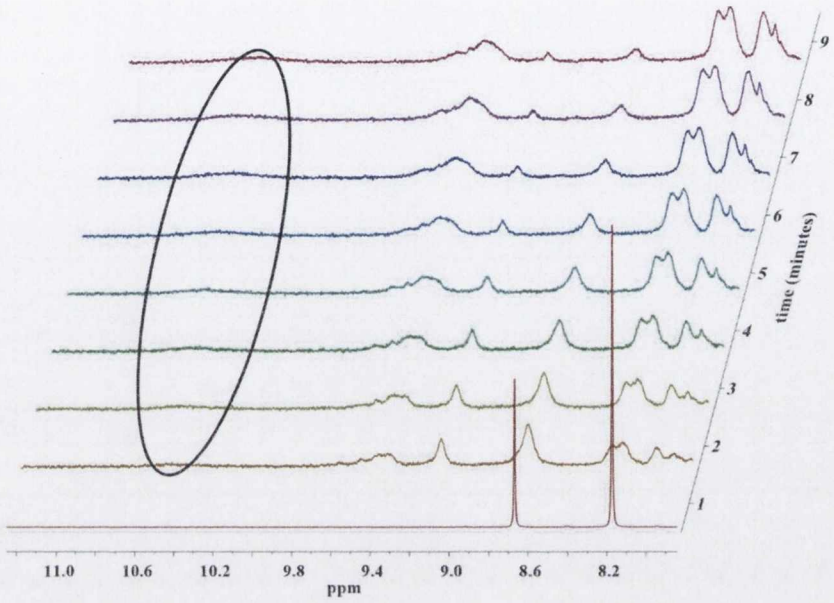

*Figure 2.6: In situ ^{1}H NMR in $CDCl_3$ at room temperature, showing the pyrimidyl resonances of **1** and the subsequent formation of **4** with respect to time. Encircled area highlights broad singlet at δ = 10.6 ppm.*

HMBC allows for the assignment of H7 to the doublet at δ = 7.74 ppm integrating for 2H. Through-space NOESY experiments can then be used to identify H7 on the adjacent phenyl ring and lead to the subsequent assignment of H8 and H9 respectively. The multiplet centred at δ = 6.95 ppm and integrating for 3H can therefore be attributed to H12/H13 and likewise the most upfield signal can accordingly be assigned to H11. To glean more information about the nature of this 1/3 cyclisation, two distinct routes were proposed to assess possible sources of influence on the cyclodehydrogenation; 1) variation of phenyl substituents and 2) modification of nitrogen substitution patterns. Substitution with electron withdrawing and electron donating groups could be used to qualitatively study the effect of electronic stabilisation on the first generated cation. Substitution with methoxy and *tertiary*-butyl moieties would satisfy these conditions, in addition to increasing the solubility of partially fused products. Methoxy substituents, as mentioned previously, have also been shown to directly influence cyclodehydrogenation through *ortho/para* activation. Their presence would test the possibility of inducing further bond closure throughout the molecule.

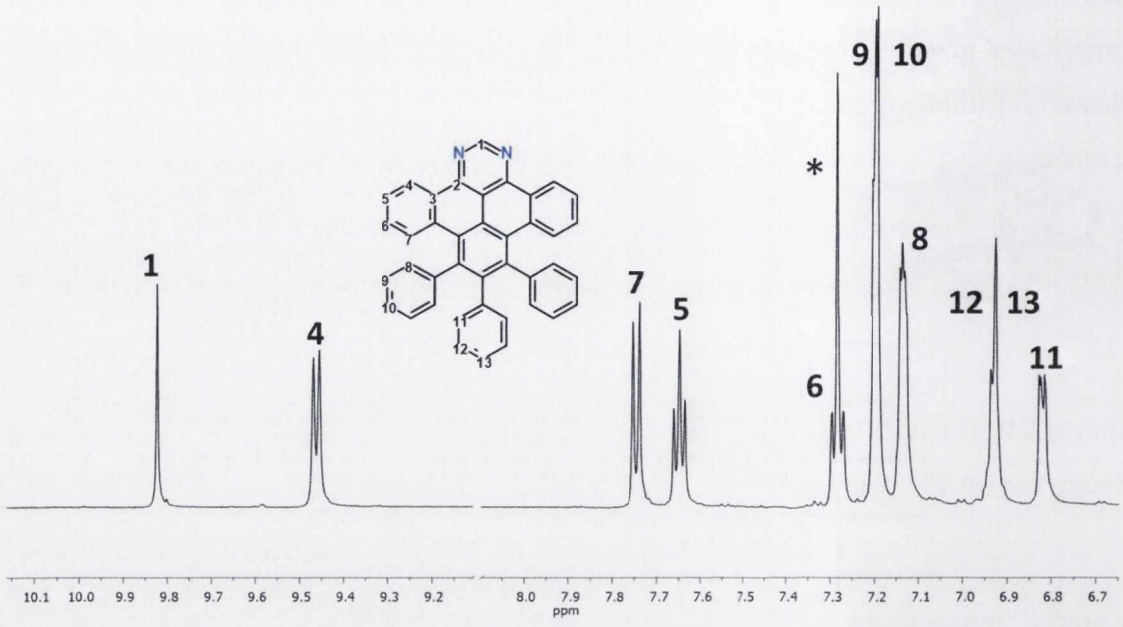

*Figure 2.7: Assignment of ^1H NMR signals of **4** in $CDCl_3$ at room temperature. Asterisk denotes $CDCl_3$ solvent peak.*

Cyclodehydrogenation of a methoxy substituted compound such as **2** using DDQ was found to only result in the formation of one bond. In the presence of bromine, however, cyclodehydrogenation resulted in the formation of two C-C bonds on the pyrimidine ring, to generate the 1/3 cyclised product in >90% yield. As before, no further purification was necessary. A side-reaction noted upon characterisation of the product was the apparent cleavage of one methoxy group, to yield an alcohol. Most likely, in the presence of large concentrations of generated HBr, cleavage of the ether from the *para* substituent is achieved in quantitative yields. Treatment of ether functionalities with strong acids is commonly seen to result in alcohols and alkyl halides, as outlined in Scheme 2.13, usually *via* an S_N2 pathway, when the ether is on a primary carbon.

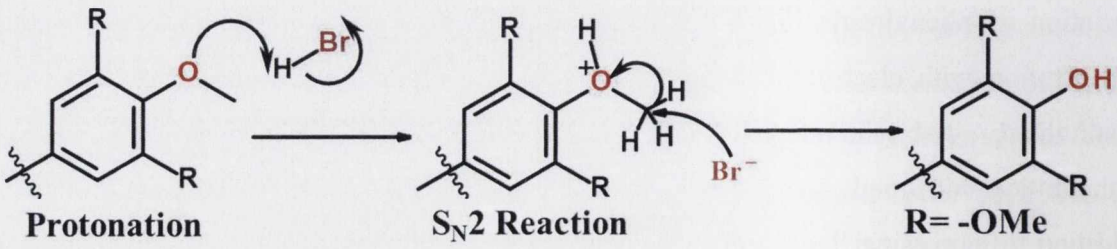

Scheme 2.13: Mechanism for the acid cleavage of an ether substituent by the attack of strong nucleophilic anions via an S_N2 mechanism.

The selectivity of the methoxy cleavage at the *para* position is most likely a result of either reduced reactivity of the ether groups at the *meta* positons or steric hindrance inhibiting backside attack by the incoming nucleophile. This steric hindrance may be caused by the orientation of both *meta* substituents (seen in the solid state, *via* single crystal XRD to be most sterically encumbered) or alternatively may be because ether cleavage is potentially preceded by bond closure. If bond closure were to occur first, it is likely that the accessibility of methoxy groups at both *meta* substituted positions would be even more limited than that at the *para* substitution. This would mean that nucleophilic attack would be much less likely to occur. This proposed order of reaction was supported by the rate of the relative steps and the enormous proportions of Br_2 relative to HBr, which will ultimately control the slowest rate-determining step of the alkyl cleavage. Full NMR assignment of **6**, shown in Figure 2.8, proves useful in this instance as the molecule no longer possesses the C_2 axis of symmetry seen in the more symmetrically substituted analogues.

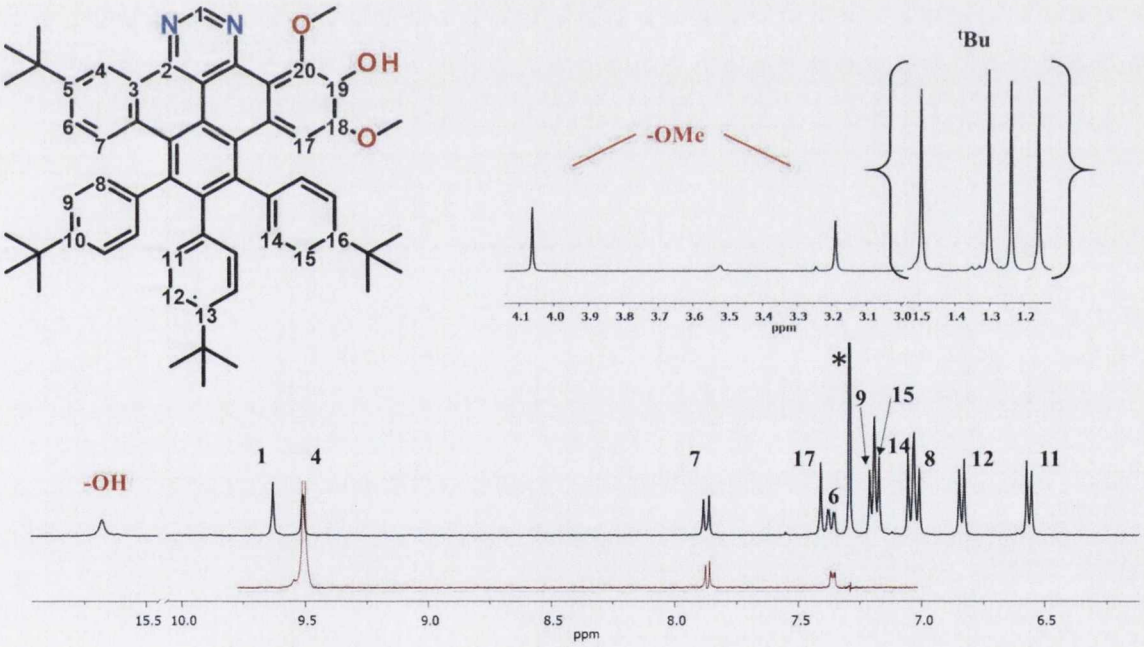

*Figure 2.8: ^{1}H NMR spectrum of **6**. Inset shows alkyl region and selective 1D TOCSY shown in red ($CDCl_3$, RT, 600 MHz). Asterisk denotes $CDCl_3$ solvent peak.*

The singlet, integrating for 1 proton and corresponding to H1 can be easily assigned in these fused systems by its characteristic downfield shift, seen here at δ = 9.62 ppm. From the HMBC, this can be seen to correlate to the most downfield carbon signal. Similarly, H4 moves downfield upon cyclisation and appears as a doublet with coupling constant J =

2.2 Hz, which is indicative of splitting of the spin by the *meta* proton (H6). H6 appears as a doublet of doublets with J = 9 Hz and J = 2.2 Hz, corresponding to coupling with the (H4) and (H7) respectively. The relationship of protons on this ring were confirmed by 2D or selective TOCSY experiment, an example of which is inset in red in Figure 2.8.

In suitable systems, a selective TOCSY experiment allows for direct irradiation of a certain signal's frequency, followed by observation of the response from other nuclei within the same spin system. In this case the selective TOCSY enables the unequivocal assignment of the H4-H6-H7 relationship. Selective irradiation of H7 can be used to accurately identify H8 and in a similar fashion, with a marginally longer relaxation time, H9. Likewise, the singlet at δ = 7.41 ppm, corresponding to H17, can be irradiated and used to identify H14 and H15. A selective TOCSY experiment can then be used to identify the AB system of the remaining phenyl ring. HMBC and HSQC experiments can be used to complete the assignment, by correlation of the carbon signals; they also offer support to the tentative assignment of the ring systems. This is most apparent in the correlation between the s-d-dd of an AMX system. Likewise for the assignment of quaternary carbons on the methoxy-substituted ring, the HMBC can be used to fully characterise the environment of H17 around the ring system.

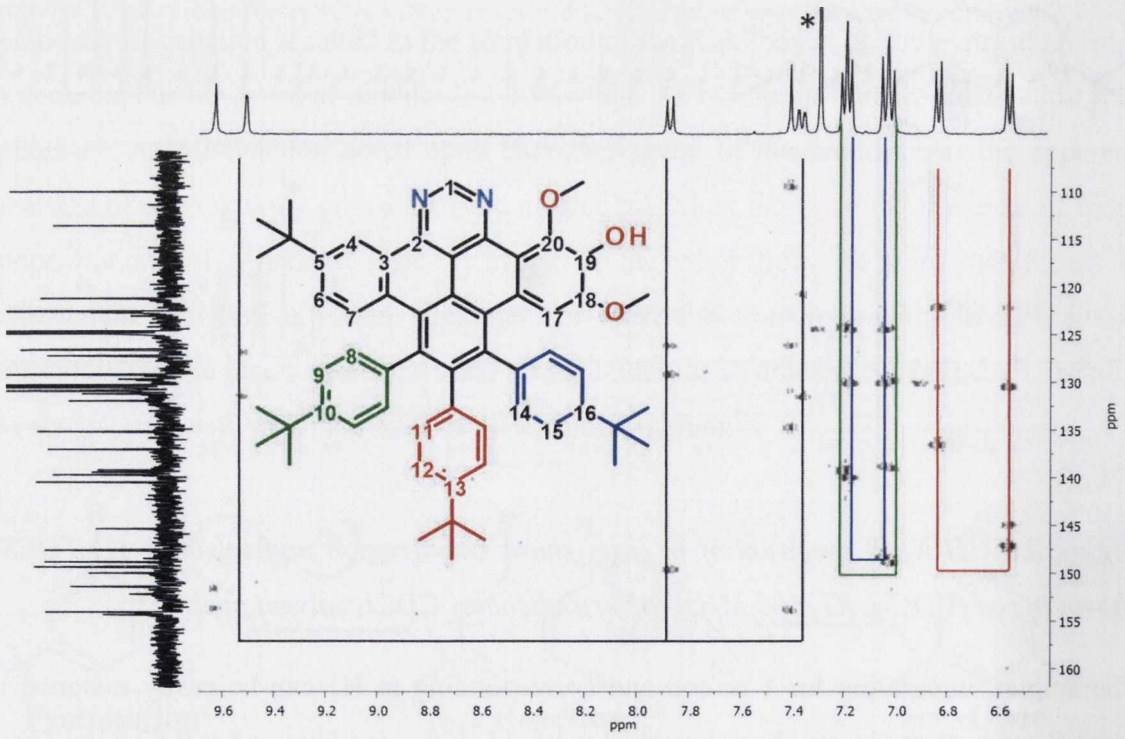

Figure 2.9: HMBC experiment for the aromatic region of ***6****. Colour-coding depicts three pendant phenyl ring systems ($CDCl_3$, RT, 600MHz). Asterisk denotes $CDCl_3$ solvent peak.*

Although showing an efficient route to alcohol substituted polyaromatics, coupled with contemporaneous cyclisation, the inclusion of methoxy substitution did not result in the expected outcome. It had been hoped that the trisubstituted methoxy ring would serve to potentially promote the formation of a new bond at the C17 position, after initial cyclisation had occurred. In reality, this activation failed to suffice. It was decided to replace the methoxy substitution pattern with that of a fifth *tertiary*-butyl moiety. This would serve to restore C_2 symmetry, in addition to increasing the solubility and propensity to form crystals suitable for XRD. The resulting penta-substituted **6** also served as a direct comparator for dipyrimidyl polyphenylenes common within the group.

For **6**, *tertiary*-butyl substitution is seen to have a very profound effect on the shape of the molecule and orientation of packing (observed in Figure 2.10 (b)). From a dichloromethane/methanol solution long fibrous crystals were grown. As in **4**, the disordered solvent molecules were removed using the SQUEEZE protocol included in PLATON.[36]

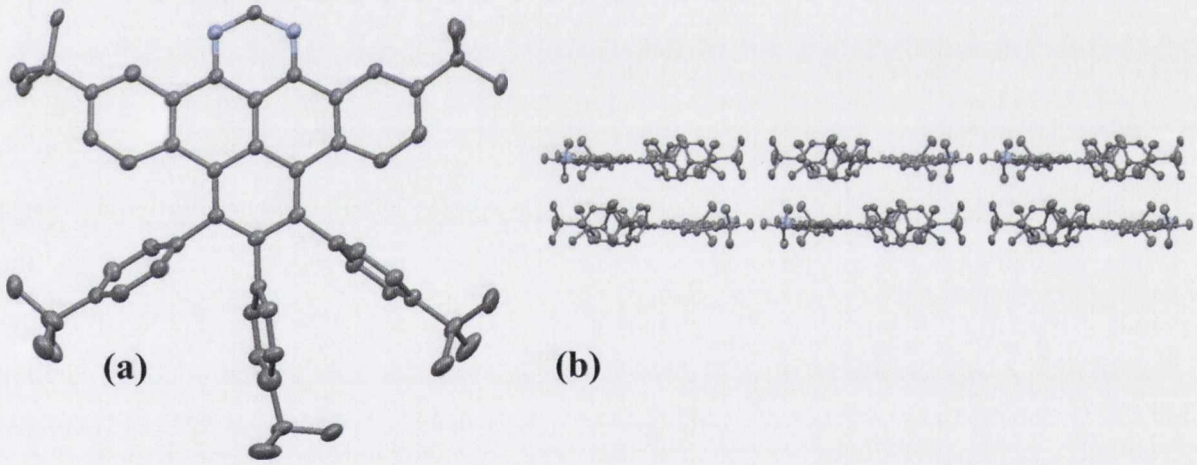

*Figure 2.10: Representation of the single-crystal structure of **6**: (a) asymmetric unit; (b) packing motif observed. Displacement ellipsoids shown at 50% and hydrogen atoms omitted for clarity.*

The *tertiary*-butyl substitution is seen to result in an almost perfectly flat molecule. The molecule does not deviate from the plane of the central ring. The head to tail stacking is much more pronounced in this molecule, with the pyrimidyl ring aligned with the central pendant phenyl of the next molecule in the lattice. As expected, the *tertiary*-butyl groups inhibit very close packing. Mass spectrometry data of the three diaza derivative cyclisations are concisely summarised in Table 2.1.

*Table 2.1: Summary of mass spectral analysis for diaza-substituted polyphenylenes **1**, **2**, **3** (red) and fused analogues **4**, **5**, **6** (black).*

Compound	Formula	Calculated $[M+H]^+$	m/z	Compound	Formula	Calculated $[M+H]^+$	m/z
1	$C_{40}H_{28}N_2$	537.2331	537.2324	**4**	$C_{40}H_{24}N_2$	533.2018	533.2015
2	$C_{58}H_{61}N_2O_3$	851.5152	851.5160	**5**	$C_{58}H_{60}N_2O_3$	833.4682	833.4615
3	$C_{60}H_{68}N_2$	817.5461	817.5463	**6**	$C_{60}H_{64}N_2$	813.5148	813.5149

In addition to offering the novel synthesis of these fully characterised products, this procedure is also a much higher-yielding alternative to $FeCl_3$. This method has been shown to offer full scalability to gram-scale quantities of diaza-substituted compounds. The absence of any chromatography step allows for facile scale-up. Fully exploiting nitrogen-containing compounds for coordination or nanoscale applications however would require for extension of this method to higher degrees of nitrogen substitution. In turn, varied nitrogen substitution patterns may provide a further insight into the manner in which this bond formation occurs.

2.5.3 Tetraaza Cyclodehydrogenation

To explore the generality of this new method, and to apply it to the more challenging 4N systems, the unsubstituted polyphenylene 5,5'-(3',6'-diphenyl-[1,1':2',1''-terphenyl]-4',5'-diyl)dipyrimidine was initially chosen. This precursor was selected not only for direct comparison with the substituted 2N system (**1**), but also as it gave potential for the formation of higher degrees of cyclodehydrogenation. The presence of two nitrogen-containing rings could, in theory, offer more than one site for generation of a reactive cation. If successful, tetraaza substitution could lead to a family of half-cyclised platforms. In reality, the unsubstituted dipyrimidyl polyphenylene was not seen to undergo intermolecular cyclodehydrogenation in a range of different Br_2 cyclodehydrogenating conditions, and bromine served only to substitute around the periphery, as seen in Scheme 2.14. It was expected, as seen in the synthesis of **4**, that a dipyrimidyl molecule such as this would undergo bond formation prior to electrophilic attack by bromine. The mass spectrum in Scheme 2.14 and further NMR studies show that this is not the case. Both phenyl rings adjacent to pyrimidine were more susceptible to halogenation than to C-C bond formation, in this case. This peculiarity is explored in greater detail through the use of *in situ* NMR studies for other tetraaza polyphenylenes (*vide infra*).

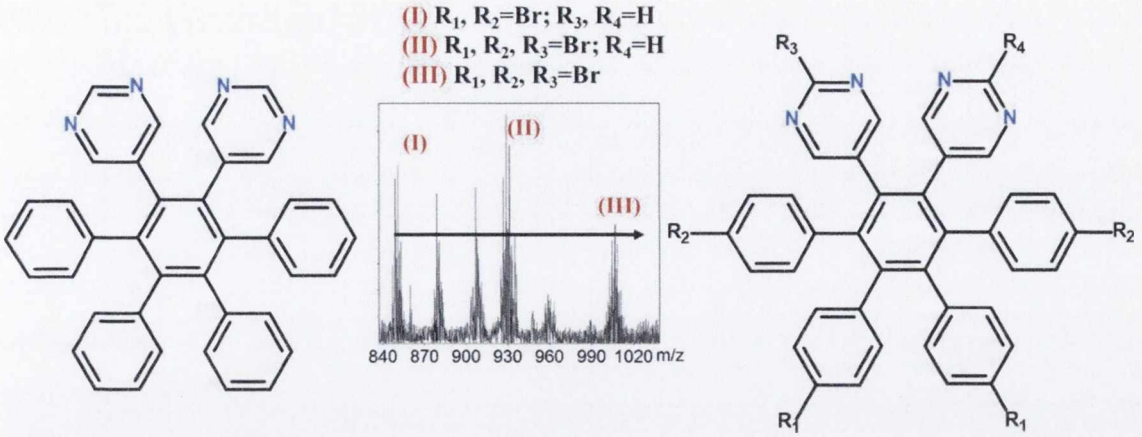

Scheme 2.14: Schematic showing the sequential bromination of 5,5'-(3',6'-diphenyl-[1,1':2',1''-terphenyl]-4',5'-diyl)dipyrimidine. Inset shows the mass spectrum and three most abundant species, which are observed as $[M+H]^+$ using MALDI.

Greater control of this reaction can be achieved by substituting two phenyl rings with *tertiary*-butyl groups. The *tertiary*-butyl groups block two of the *para* positions on the pendant phenyls. This provides a two-fold advantage: i) lessening the chances of substitution on these rings, which would inhibit fusion and ii) providing electron donation, which has been seen to promote bond formation at the necessary positions. The other pendant phenyl rings, which appear to play no role in cyclodehydrogenation around the pyrimidyl rings were left unsubstituted or functionalised with bromine substituents. On heating the dipyrimidyl polyphenylene precursor 1,2-dipyrimidyl-3,6-bis-(4-tert-butylphenyl)-4,5-bis-(4-bromo-phenyl)benzene) (**7**) in toluene with Br_2 for 45 minutes the half-cyclised product **8** was isolated in 70% yield, as shown in Scheme 2.15.

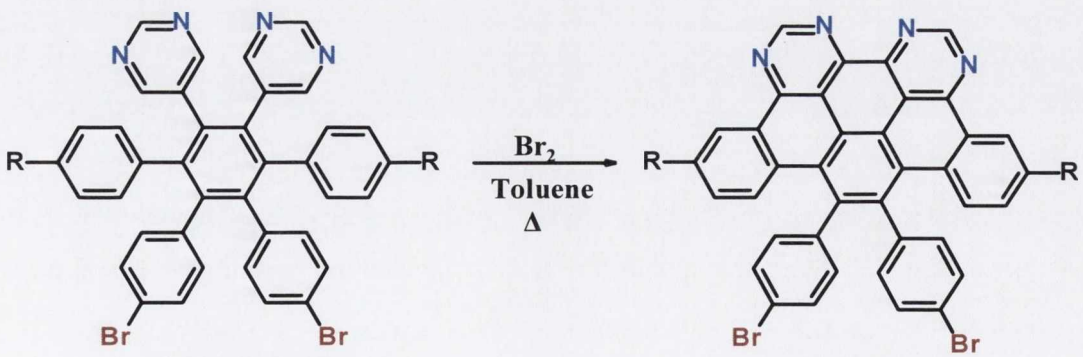

(7) R = *tert*-butyl
(9) R = H

(8) R = *tert*-butyl
(10) R = H

Scheme 2.15: Synthetic procedure for the cyclodehydrogenation of dipyrimidyl polyphenylenes at 90 °C in toluene using Br_2.

This was a significant improvement on the reported yields of any diaza analogues generated using $FeCl_3$. Recrystallisation of **8** from CH_2Cl_2/MeOH yielded the product as extremely thin yellow crystalline fibres, which were suitable for single crystal X-ray diffraction studies. The crystallographic data was refined as a 2-component twin using PLATON and HKLF 5 programmes and was successfully integrated using a triclinic unit cell. The structure confirmed C-C bond formation at both sides of the pyrimidine rings, to yield a half-cyclised product seen in Figure 2.11. The packing motif shows the head-to-tail stacking between the fused platforms of alternating molecules exhibiting interplanar distances of 3.365 Å and 3.349 Å respectively, as demonstrated in Figure 2.12 (b).

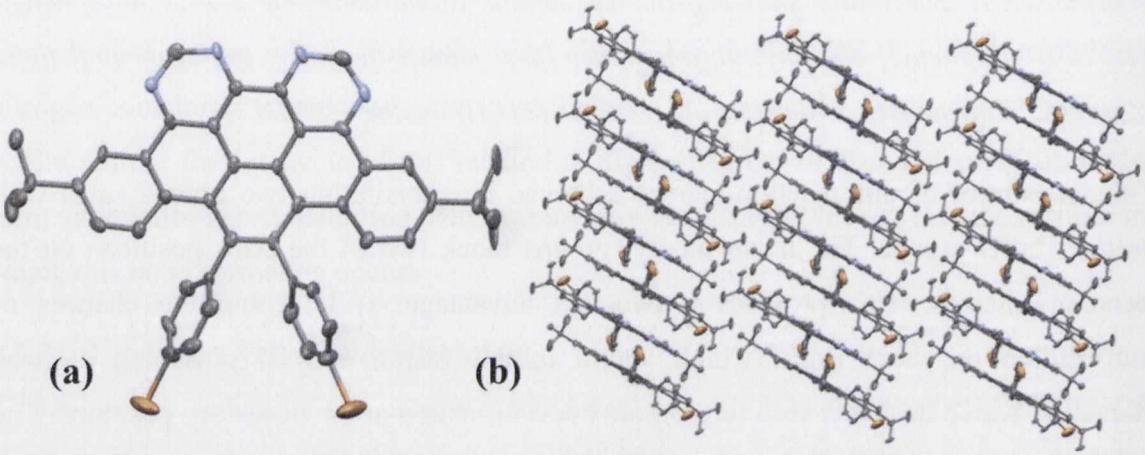

Figure 2.11: Representation of the single-crystal molecular structure of ***8****: (a) single molecule with ellipsoids at 50% probability; (b) packing structure in the crystal lattice along the b axis. Hydrogen atoms removed for clarity; N: blue; Br: orange.*

Such a small distance between planes is extremely rare for a compound of this nature. This close packing can be attributed to the head-to-tail nature in which the molecules align in the crystal form, and therefore result in the long thin fibres seen upon crystallisation. Almost perfect Bernal AB stacking is observed between pairs of molecules, shown in Figure 2.12. Bernal stacking, as observed in graphite, results in the corner of a benzene ring from one layer aligning to the middle of the ring below it. A third layer then repeats the sequence, as the corner of its hexagonal building blocks align with that of the original layer.

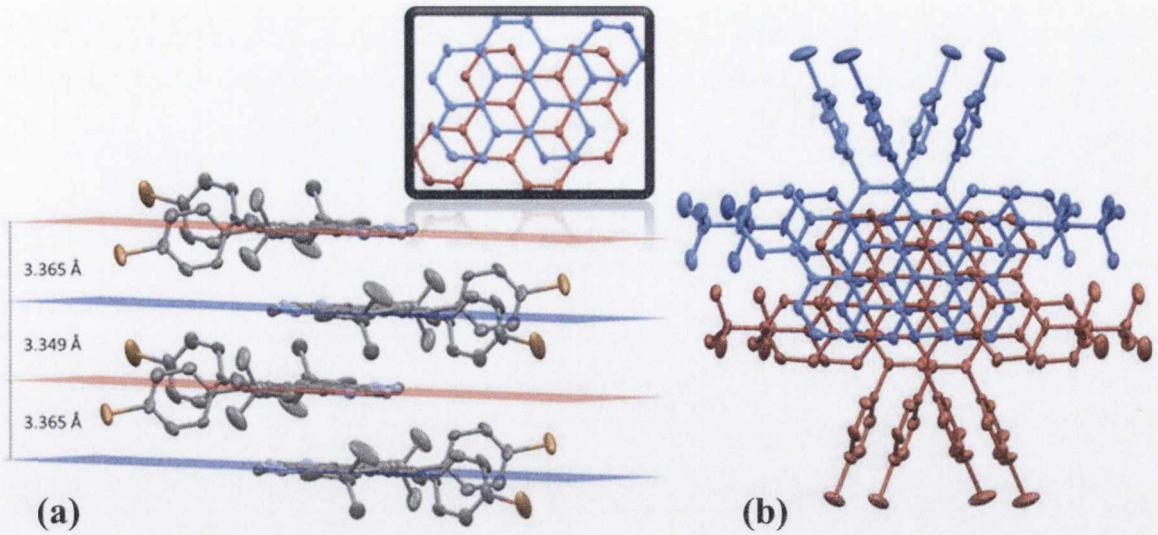

Figure 2.12: Representations of the crystal structure of ***8****: (a) intermolecular stacking as viewed along the b axis; (b) staggered overlap of adjacent molecules along the a axis. Inset shows a simplified graphic of observed overlap. Blue and red represent two alternating layers of molecules.*

A direct comparison can be made with the 3.350 Å spacing observed between the sheets of graphene, to form the graphite structure, shown in Figure 2.13 (a). It is believed that the close-packed nature of this ABA alignment results in the unique electrical conductivity observed for multiple layers of graphene, shown in Figure 2.13 (b). The presence of even a slight off-set to this alignment results in the dramatic shift to an insulating nature.

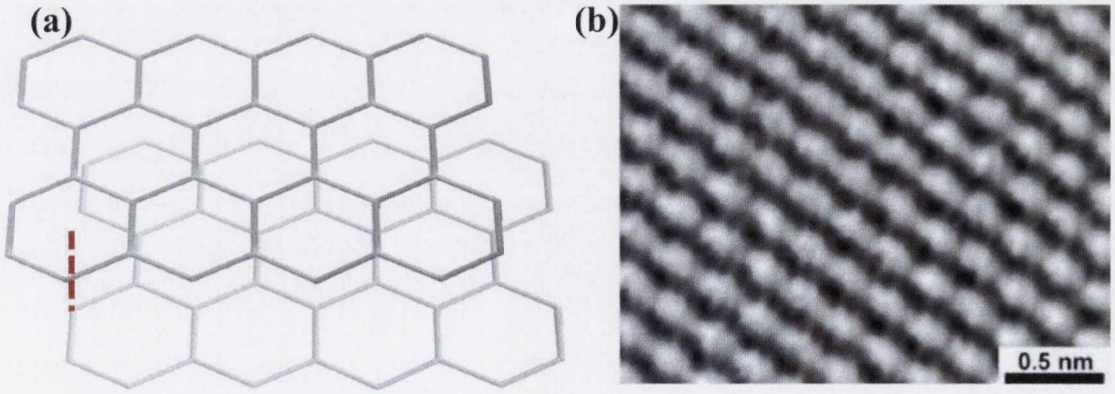

Figure 2.13: Representation of the packing seen in graphite: (a) schematic of the stacked planes with interplanar distance highlighted; (b) STM image of graphite.[37]

NMR spectroscopy proved useful in understanding the formation and characterisation of **8**. Most dramatic is the shift observed upon fusion around the pyrimidyl ring. The proton

H1 in the uncyclised compound is shifted by approximately 1.5 ppm. The removal of proton H2 upon cyclisation means that H4 now appears as a doublet, with a coupling constant of $J = 2$ Hz, most likely corresponding to coupling with proton H6, as previously observed in **6**.

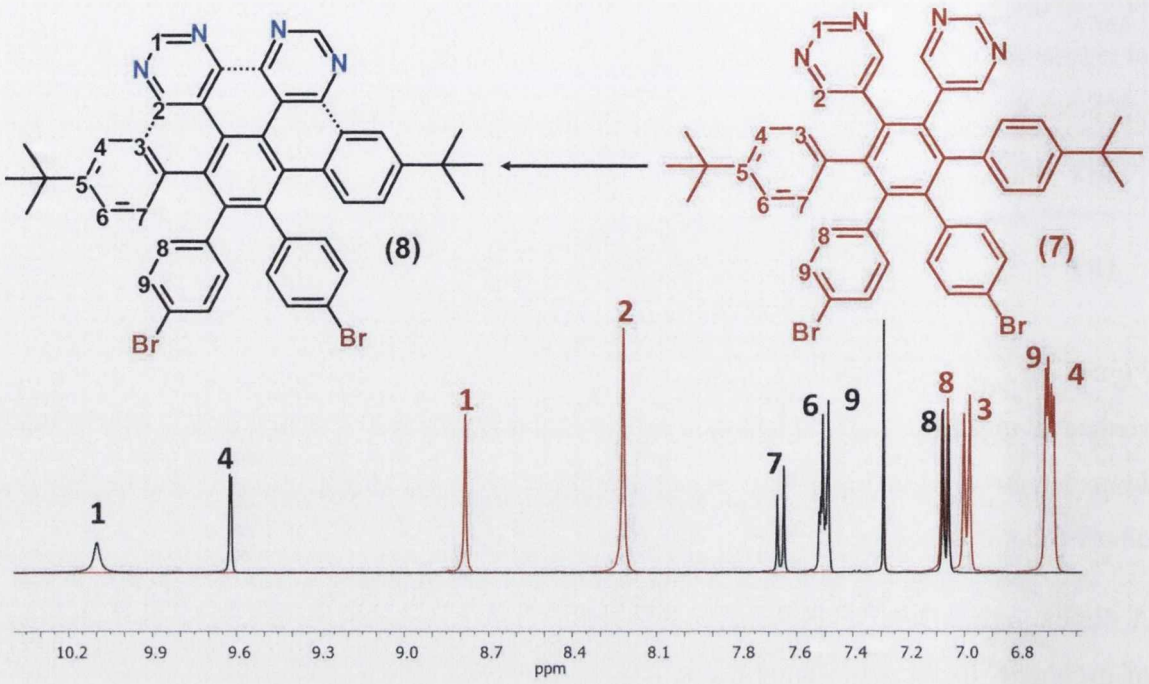

*Figure 2.14: ^1H NMR assignment of **7** (red) and **8** (black) ($CDCl_3$, RT, 600 MHz). Asterisk denotes $CDCl_3$ solvent peak.*

Interestingly, *in situ* NMR experiments also provided information about the rate and order of the ring closure for **7**. In contrast to the monopyrimidyl substituted system, which showed very fast conversion to the cyclised form with reaction times within minutes, the dipyrimidyl polyphenylene (**7**) shows a response in the region of days. Although unexpected, such a slow response proved quite fortuitous, as it allowed for the study of the intermediates in greater detail. Stimuli such as heating (*in situ*), irradiation with UV light and exposure to air showed no discernible effect on the reaction. Figure 2.15 shows NMR spectra following the addition of Br_2 in 100 equivalents. Upon sitting at room temperature for 48 hours, the reaction was eventually seen to begin. As observed for the 2N systems previously, the initial response upon reaction coincides with noticeable shifts in the ^1H NMR spectrum. The first is the downfield shift of the two pyrimidine ring singlets by 0.4 ppm and 0.65 ppm respectively. A second shift is observed in the free phenyl ring signals. The concomitant lowering of symmetry results in the appearance of two distinct *tertiary*-butyl peaks, integrating for 9H each.

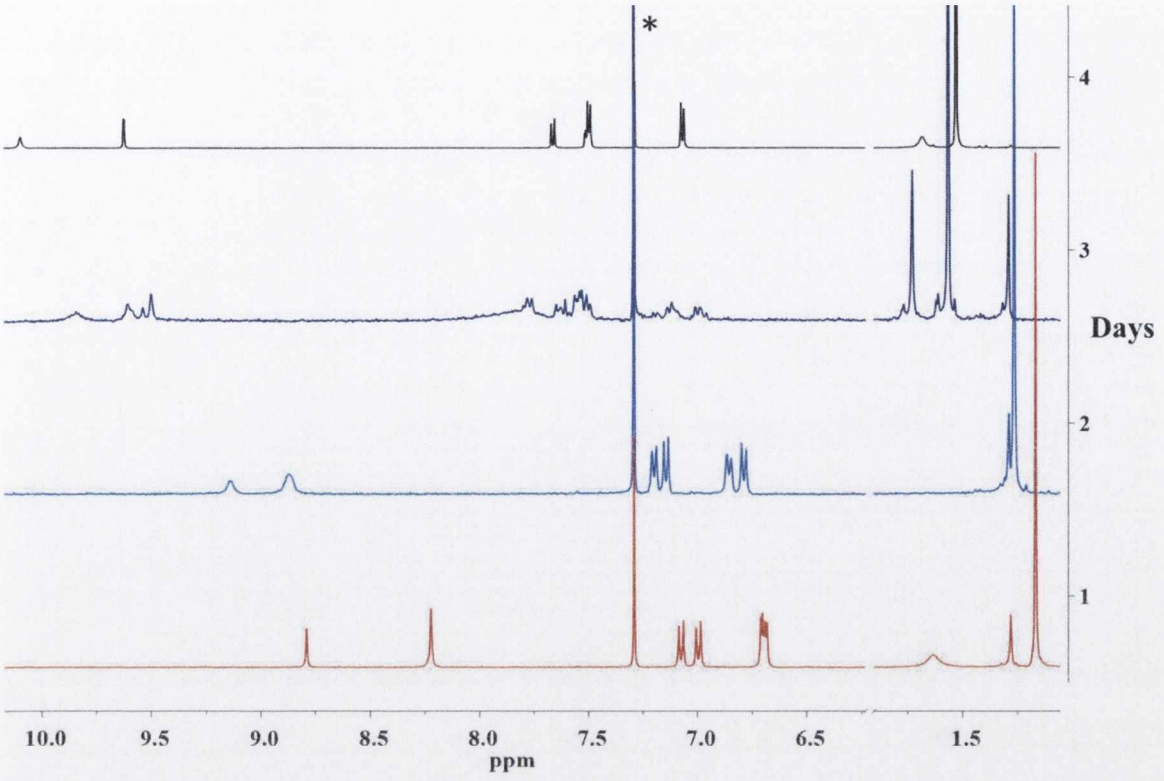

Figure 2.15: In situ ^{1}H NMR studies of 7 (red) with bromine (100 eq) showing progression over 96 h period. Black spectrum shows fully fused product **8**. *Asterisk denotes solvent peak ($CDCl_3$, RT, 400 MHz).*

Closer inspection, combined with the use of 2D experiments shows that the reduction of symmetry in the molecule results in 4 distinct singlet peaks in the downfield region of the spectrum. Selective TOCSY experiments confirm that these correspond to the proton signals from the pyrimidine rings and the singlet from the adjacent fused phenyl. This postulation was easily confirmed by selective investigation of both *tertiary*-butyl signals, which are seen to correspond to the fused portion and remaining free phenyl ring, respectively. Once cyclisation is finished, the four downfield singlets again become two and correspond to the H1 and H4 positions, as seen for **8**. As mentioned, such a slow reaction time also allows for the reaction mixture to be directly sampled from *in situ* NMR studies and monitored *via* mass spectrometry. These results also corroborate the aforementioned findings. Within the first 24 h period only uncyclised polyphenylene **7** is observed (shown in red in Figure 2.16 as $[M+H]^+$). From 48 h the dominant species corresponds to the 1/3 cyclised intermediate **8-a**, with no remaining trace of any uncyclised starting material. After 72 h only the half-cyclised molecule exists (shown in black in Figure 2.16 as $M+H^+$). Mass spectrometry is also a useful tool to confirm the absence of any other bromination occurring.

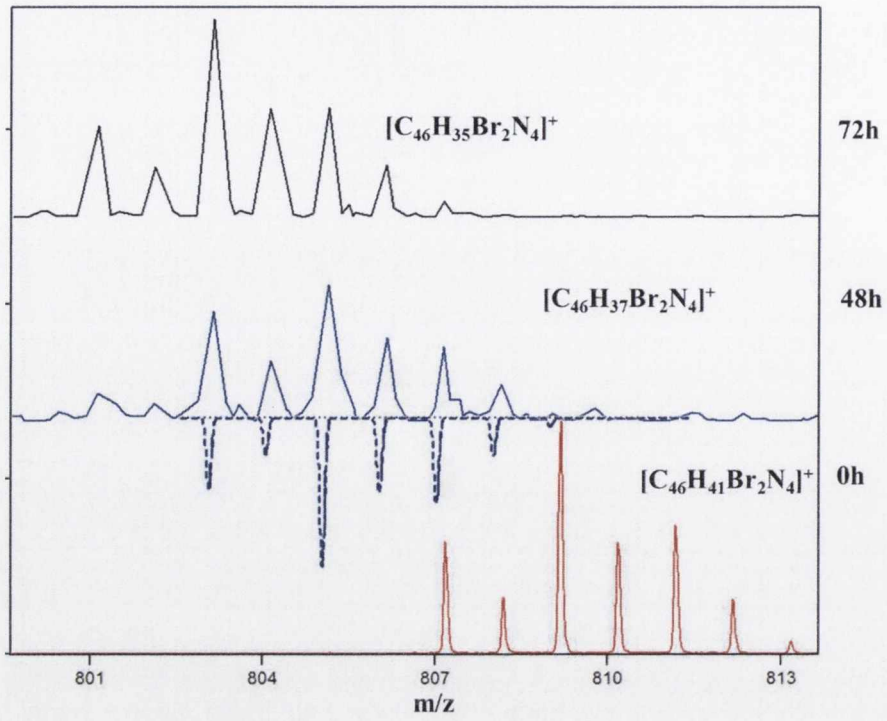

*Figure 2.16: Mass spectrometry analysis of the NMR samples, showing progression of the cyclodehydrogenation reaction: red (7); blue (**8-a**); black (**8**). For the 1/3 cyclised intermediate (**8-a**), the dashed line depicts the isotopic model.*

These results call into question previous assumptions regarding this reaction, which suggested contemporaneous reaction at both symmetrically equivalent sites. In reality, it seems much more likely that ½ cyclisation of the dipyrimidyl polyphenylene occurs in at least three distinct parts; i) generation of an initial cation and attack to a phenyl ring ii) bond closure between both pyrimidine rings and finally iii) bond formation between another pendant phenyl and the partially fused portion. The fortuitous nature of the slow reaction rate allowed for the use of 2D NMR and mass spectrometry for characterisation of the intermediates.

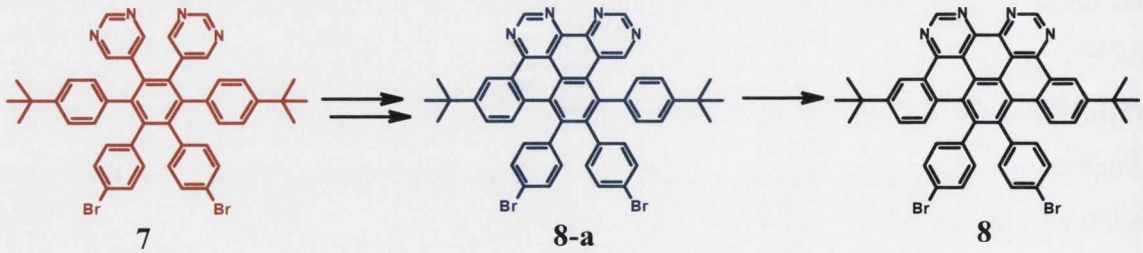

Scheme 2.16: Proposed pathway for the cyclodehydrogenation of 7.

Adaptation of this cyclodehydrogenation methodology to other dipyrimidyl systems holds much potential for use in the synthesis of molecules which are inaccessible by common

Lewis Acid-oxidant mixtures. One such system which has been extensively studied by Mullen *et al.* and within the Draper group is substituted tetraphenylfluoranthene.

2.5.4 Diaza Fluoranthene Synthesis

The use of substituted fluoranthenes in the formation of hole-transport and emissive layers for OLEDs has been widely documented in recent years, due to their high stability and extremely efficient fluorescence quantum yields.[38] Fluoranthenes incorporate a fused five-member ring into their PAH skeleton and have been used as precursors to fullerenes and corranulenes, due to their curved orientation upon cyclodehydrogenation. The geometry and reactive nature of the fluroanthene moiety means that intramolecular cyclodehydrogenation has proven rather elusive and intermolecular oxidative coupling tends to take precedence, leading to complex extended polyaromatic systems. From 2001 Mullen and co-workers studied 7,8,9,10-tetraphenylfluoranthene and its derivatives.[39] They found that, irrespective of substitution pattern, intramolecular cyclodehydrogenation was not possible on the monomeric precursor shown in Scheme 2.17. Using $FeCl_3$ it was only possible to dimerise the molecules to form a periflanthene like molecule. In the presence of alkyl substitution, a subsequent intramolecular reaction then succeeded in cyclodehydrogenating the dimeric species. Similarly, for nitrogen-containing compounds, Draper *et al.* found that intramolecular coupling alone could not be achieved using a range of different cyclodehydrogenation conditions. Upon coupling of two compounds through the fluoranthene-base using $FeCl_3$ it was then possible to perform partial bond closure, but only in extremely low yields.

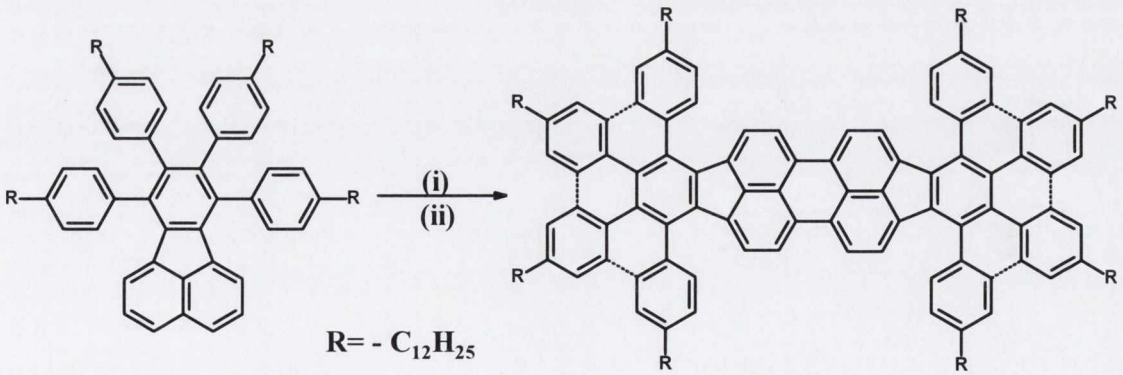

Scheme 2.17: Synthetic pathway to substituted periflanthene: (i)(ii) $FeCl_3/CH_3NO_2$.[39]

An adaptation of the bromine-driven cyclodehydrogenation presented here however can offer two significant benefits: i) the ability to perform full cyclodehydrogenation on the monomeric species and ii) one-pot cyclisation and monobromination to form a fused

periflanthene. In the presence of Br_2 and toluene, cyclodehydrogenation was performed on the polyphenylene precursor (**11**), this time with an added bonus: it was possible to isolate the monobrominated species in very high yield and purity. *In situ* NMR studies, shown in Figure 2.17, proved to be a useful tool for gleaning an understanding of the mode and completion of the reaction. As with the dipyrimidyl species mentioned previously, the propensity to cyclodehydrogenate is hampered by the inability of the rings to efficiently generate a reactive intermediate which would lead to bond formation. Due to this, it was possible to follow the reaction progress and ascertain that the monobromination occurs as the initial step. Full assignment of the ^{1}H-NMR spectrum of the uncyclised precursor allows for identification of the fluoranthene protons. These can be accurately used to monitor the progress of the reaction, in particular by the disappearance of H9. The bromination, as expected, corresponds to a desymmetrisation of the fused fluoranthene segment and results in five signals which exhibit a marginal shift due to the electronegative effect of the halogen substitution.

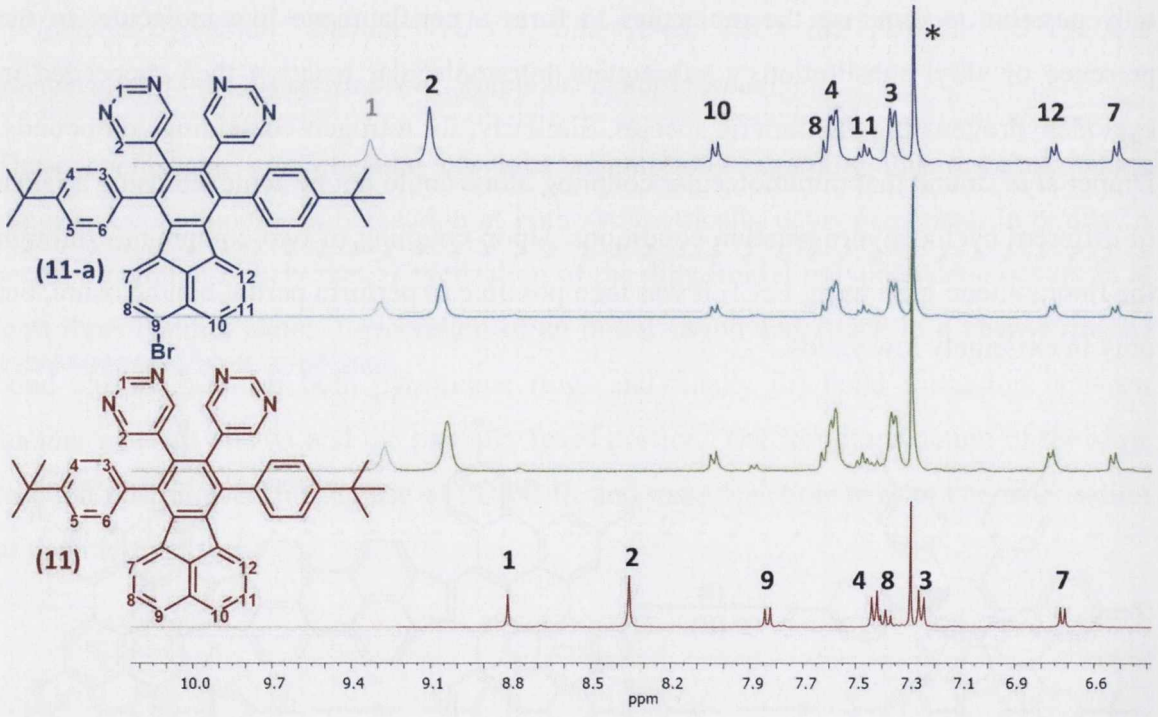

Figure 2.17: In situ NMR studies of ***11*** *($CDCl_3$, RT, 400 MHz). Colours represent spectra taken every 5 minutes: 0 min (red); 20 min (blue). Asterisk denotes $CDCl_3$ peak.*

The pendant phenyl and pyrimidyl rings, while displaying a small deshielded effect, still appear as a single set of signals, however. Monobromination occurs in a short space of time and was easily confirmed by mass spectrometry. It is likely that no further

bromination occurs at this point due to steric restrictions, hindering any further attack. *In situ* NMR could be used to observe the initiation of bond closure, but as seen in the aforementioned analogues efficient cyclodehydrogenation around the dipyrimidyl moieties occurs over a much longer timeframe and under harsher conditions, which are not favourable to *in situ* NMR studies. Complete conversion can be achieved much more successfully in a pressure tube at 70 °C. Recrystallisation from the reaction mixture yielded the cyclised product (**12**) as dark red crystals. The first single-crystal XRD structure of a fused fluoranthene of this kind showed the Br atom was disordered over two positions, with an occupancy of 72:28 and a dichloromethane molecule which was disordered over two positions (50:50). The orientation of the molecule showed the highly-strained nature evident in Figure 2.18. From the plane of the central 6-membered ring the pendant phenyl rings, which now form part of the fused core are raised from the plane by 21.58°.

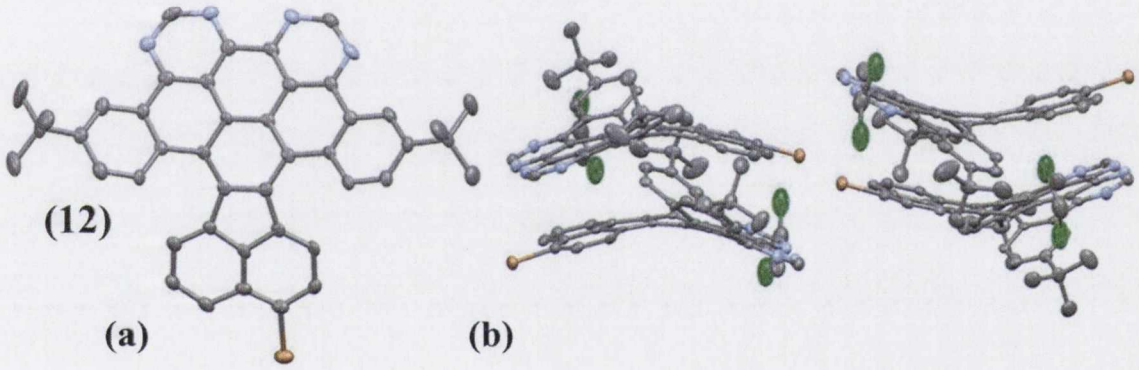

Figure 2.18: Representation of the crystal structure of ***12****, as determined by single-crystal XRD studies: (a) molecular structure with solvent molecules removed for clarity; (b) packing observed between the contorted molecules, along the a axis, showing dichloromethane solvent molecules in the voids. Ellipsoids shown at 50% probability and hydrogen atoms removed for clarity, N: blue; Br: orange, Cl: green.*

The new fused 7-ring portion now forms an angle of 40.69° with the fluoranthene moiety, with all the twist appearing to be focused on the central 6-member ring. Interactions between the pyrimidyl nitrogen atoms and the dichloromethane solvent molecules, and Br-Br interactions (distance 3.515 Å) are seen within the crystal lattice. The twisted nature of the molecule means that the phenyl rings have been raised from the plane to such an extent that the closest carbon atom to the fluoranthene moiety now resides 3.121 Å away. This, combined with the contorted shape of the molecule, makes further bond closure unlikely.

Further bromination at the remaining available site on the fluoranthene base does not occur, under a range of different conditions. However, coupling of two monobrominated species, in an end to end fashion, has been shown to offer an extremely efficient route to substituted periflanthenes. In a method analogous to that of Clar and Ironsides, used in the coupling of dibenzoperinaphthalene to form tetrazbenzoperopyrene, it would be possible to couple two equivalents of such a monobrominated in a similar manner.[10] This method offers much higher yielding steps by avoiding the pitfalls of the plethora of partially-fused derivatives, resulting from the use of $FeCl_3$.

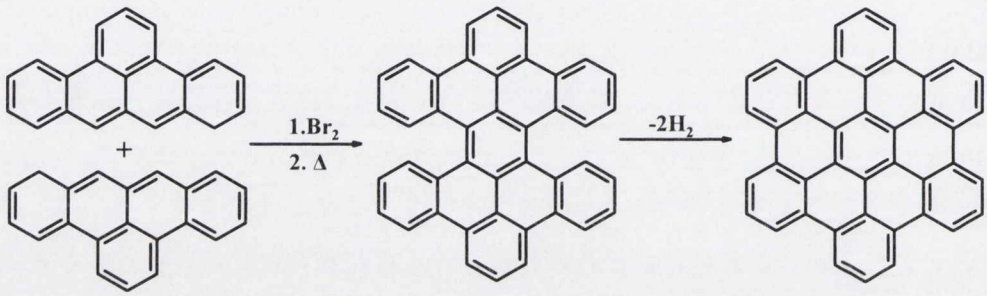

Scheme 2.18: Coupling of dibenzoperinaphthalene and subsequent thermally-driven cyclodehydrogenation.[10]

Table 2.2 shows that in a similar manner to monopyrimidyl substituted nitrogen compounds, high resolution mass spectrometry can be a very beneficial tool in the identification of fused 4N products. The table collates data to aid comparison between unfused polyphenylenes and cyclised counterparts. In all cases the major peak corresponds to the $[M+H]^+$ molecular ion, and shows excellent agreement with the theoretical values.

Table 2.2: Summary of mass spectral analysis for tetra-aza substituted polyphenylenes ***7, 9, 11*** *(red) and their fused analogues* ***8, 10, 12*** *(black).*

Compound	Formula	Calculated $[M+H]^+$	m/z	Compound	Formula	Calculated $[M+H]^+$	m/z
7	$C_{46}H_{40}N_4Br_2$	807.1692	807.1697	**8**	$C_{46}H_{34}N_4$	801.1228	801.1239
9	$C_{38}H_{24}N_4Br_2$	695.0446	695.0447	**10**	$C_{38}H_{18}N_4Br_2$	688.9976	688.9971
11	$C_{44}H_{38}N_4$	623.3175	623.3179	**12**	$C_{44}H_{31}N_2Br$	695.1810	695.1823

2.5.5 Varied Nitrogen Substitution Patterns

To truly understand the efficacy of this method of bond formation it is necessary to widen the range of attempted systems and strengthen any postulations about potential routes.

With this in mind, a range of different pyridyl platforms were chosen to crudely assess any potential capability of using these novel conditions to induce bond formation; two examples of contrasting systems are presented. The first system (**13**) had already been synthesised within the Draper group, and served as a direct comparator to the *tertiary*-butyl substituted compounds **6** and **8**. It was hoped that this substitution pattern, known to withstand cyclodehydrogenation *via* traditional means, would provide additional information about the mode of cyclisation.

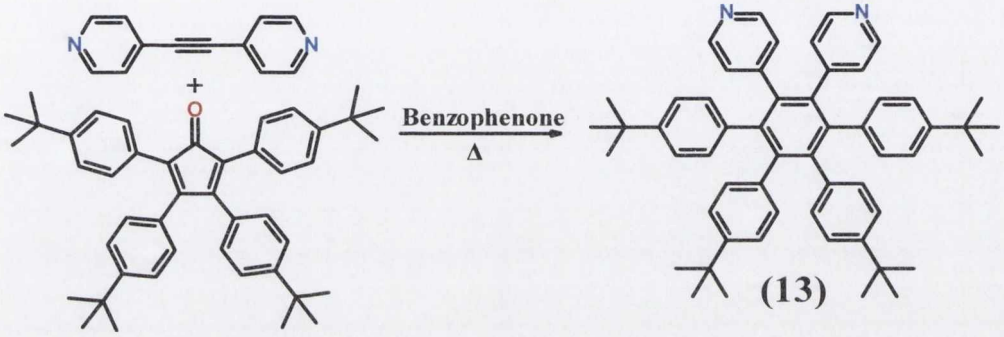

*Scheme 2.19: Synthetic procedure for the formation of **13**.*

Under a range of different reaction conditions using molecular bromine **13** was recovered unreacted. A similar response was also seen under more traditional $FeCl_3$ or DDQ conditions. In a bid to try and glean additional information about the inability to promote C-C bond formation between substituted pyridines and phenyl rings, slight adjustments were made in the design, to yield **14** (outlined in Scheme 2.20).

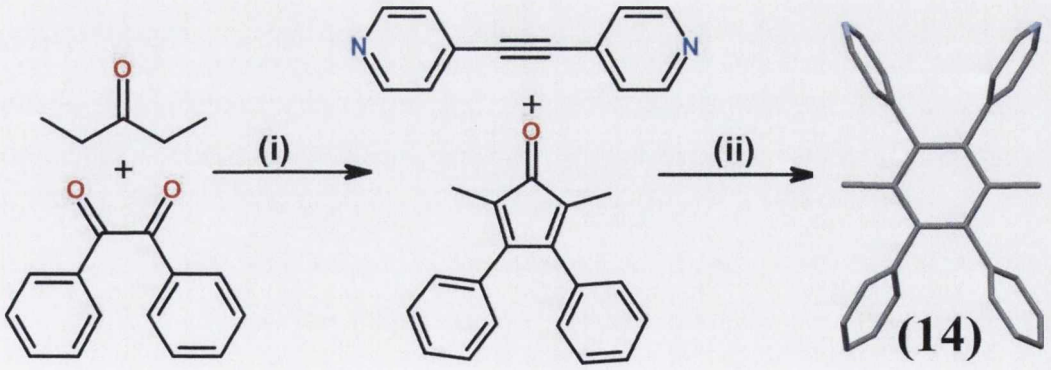

*Scheme 2.20: Synthetic procedure for the formation of **14**: (i) KOH, ethanol, reflux 30 min; (ii) benzophenone, 280 °C, 5h.*

This molecular layout was chosen in a bid to eliminate any potential sources of steric hindrance and rule out the formation of other potential cationic species which may behave in a competitive nature with the formation of a reactive cation at the 3, 5 positions of the

pyridyl rings. Worthy of brief note is the crystal structure of **14** which crystallised in the orthorhombic space group P 2_1 2_1 2_1, uncommon for polyphenylene systems such as these. The flat nature of the molecule, coupled with the large voids around the methyl moieties results in a head-to-tail packing arrangement between neighbouring molecules. Interactions between the alpha protons on the pyridyl rings and the central benzene ring of its closest neighbour gave dimeric packing in an alternating zig-zag fashion at approximately 43° to each other, as represented by the red and blue lines in Figure 2.19 (b).

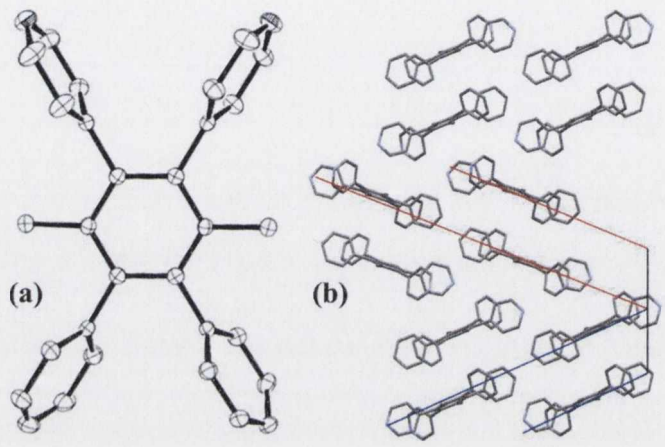

*Figure 2.19: Structure of **14** as determined by single-crystal XRD: (a) ORTEP representation with ellipsoids at 50% probability; (b) packing observed in the crystal lattice along the a axis. Blue and red lines represent alternating planes. Hydrogen atoms removed for clarity.*

In a similar manner to **13**, the use of Br_2 under a range of reaction conditions served no purpose but the return of unreacted starting material of the polyphenylene. Any attempt to further the reaction by means of stimuli such as increasing pressure, temperature or irradiation all proved fruitless. With each varied system, a knowledge of the scope of the reaction could be pieced together. To extrapolate information about any potential reactivity it was necessary to study some other pertinent systems.

2.5.6 New Motifs with Higher Degrees of Substitution

To extend the application of this methodology it was of benefit to explore other areas in which traditional systems had previously failed to result in cyclodehydrogenation. Success in this regard would allow for the synthesis of new systems with varied degrees of nitrogen substitution. The first platform chosen was one which incorporates both pyrimidyl and phenanthroline units. Such a molecule proves of much interest from both

an application and synthetic viewpoint. Molecules which combine N^N and C^N coordination are sought-after as bridging ligands, as they demonstrate the ability to promote charge transfer between metal centres. These molecules find use in catalytic assemblies due to their potential to capture light energy which can then be transferred to catalytic metal centres.[40] For the creation of such potential coordination sites it is often necessary to have two rigid portions in the molecule, which lend themselves to metal coordination. In the presence of metal-based cyclodehydrogenating agents this results in an inability to induce cyclisation, caused by the apparent coordination of the cyclodehydrogenation agent to the phenanthroline site.[41] The synthesis of **15** was achieved in a similar manner to previous polyphenylenes, but in this case using the phenanthroline cyclopentadienone precursor shown in Scheme 2.21. As is common for cyclopentadienones of this nature, it exists only at elevated temperatures, tending to remain as the more stable hydroxy-substituted analogue at room temperature. Upon the addition of heat, the expulsion of a water molecule generates the dienone which can undergo Diels-Alder cycloaddition. **15** is isolated as an off-white solid which can be precipitated directly from the reaction mixture. As before, under pressure tube conditions in the presence of bromine it was possible to cyclise around the pyrimidine ring, to yield **16** as a maroon-coloured crystalline solid.

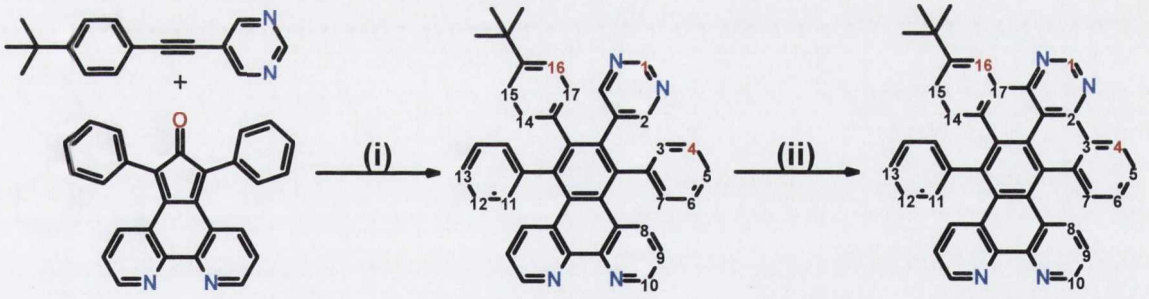

*Scheme 2.21: Synthetic route and numbering system for ^{1}H NMR assignment of **16**: (i) benzophenone, 290 °C, 3 h ; (ii) Br_2, toluene, 90 °C, pressure tube.*

Highlighted in Table 2.3 are the most significant changes to the ^{1}H-NMR spectrum observed upon cyclisation of the polyphenylene. In line with other trends demonstrated to this point, the most dramatic shift is observed at the two rings which become part of the dibenzoperimidine core, notably H16 and H4. H1 is also seen to shift upon cyclisation by approximately 1.2 ppm. A deshielding effect is also noticed for the phenathroline moiety, which still appears as a single set of signals in the ^{1}H NMR spectrum. Similarly for the

tertiary-butyl signal, a shift of approximately 0.3 ppm is observed as it becomes part of the fused six-ring platform. Applying this methodology as a metal-free solution to current cyclodehydrogenation hurdles offers much potential, as will be discussed in Chapter 3.

*Table 2.3: Notable ^1H NMR shifts of **16** and precursor (**15**) ($CDCl_3$, RT, 600 MHz).*

Proton	H1	H2	H3,5	H4	H8	H9	H10	H16
15 (ppm)	8.78	8.09	7.25	7.25	7.86	7.25	8.95	7.00
16 (ppm)	10.03	-	-	9.72	8.88	8.5	9.45	9.64

Given the recurrent theme of pyrimidine to phenyl ring-closure, systems with higher degrees of nitrogen substitution (shown to reduce the propensity for metal-based ring closures) were devised. Cyclotrimerisation of asymmetric acetylenes has been pioneered within the Draper group. Drawing from procedures used previously by Mullen *et al.* for all carbon analogues the inclusion of a nitrogen bearing ring can give rise to two possible isomers, each with a different arrangement of three pyrimidine rings. Adaptation of the synthetic practice, combined with careful manipulation of purification was used to generate the novel symmetric (**17**) and asymmetric (**18**) isomers shown in Scheme 2.22.

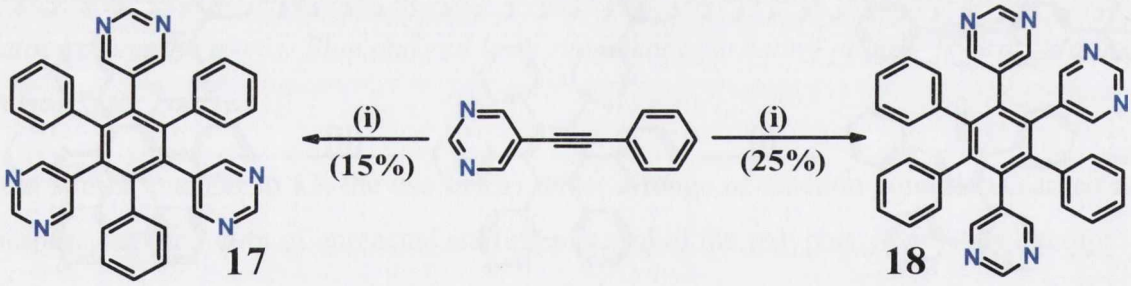

*Scheme 2.22: Cyclotrimerisation conditions of 5-(phenylethynyl)pyrimidine to yield both symmetric (**17**) and asymmetric (**18**) isomers: (i) $Co(CO)_8$, dioxane, 115 °C, 24 h, under N_2.*

Use of column chromatography followed by subsequent preparative-plate purification gave both isomers in high purity with high-resolution mass spectrometry showing a measured value of 541.2130 for $[M+H]^+$ with a calculated value of 541.2135. Differentiation between both isomers was readily achieved by ^1H NMR from the different environment of the pyrimidyl signals. Figure 2.20 shows the ^1H NMR assignment of isomer **17** which possesses C_3 symmetry. The inset HSQC, combined with selective

TOCSY experiments allowed for the full assignment of the ^{1}H and ^{13}C NMR spectra, using the proton signal at $\delta = 8.27$ ppm as a convenient point of reference.

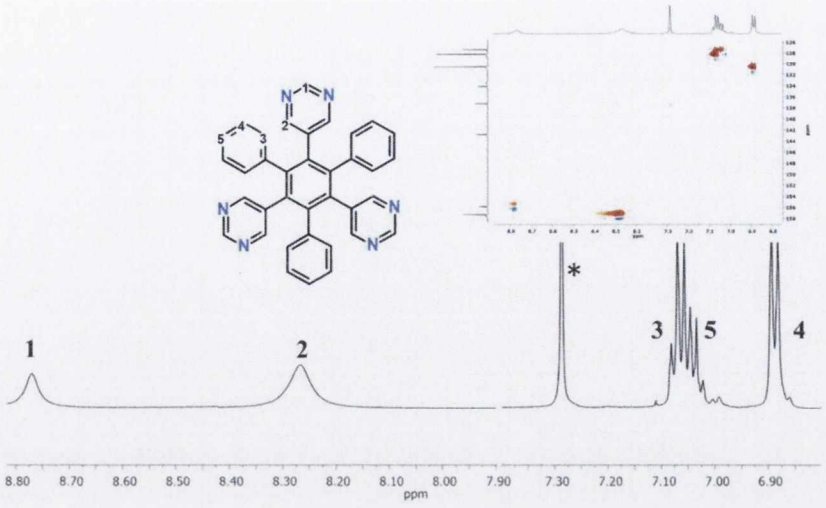

*Figure 2.20: Full assignment for ^{1}H NMR of **17**. Asterisk denotes solvent peak ($CDCl_3$, RT, 600 MHz). Inset shows HSQC spectrum.*

Characterisation of the asymmetric isomer (**18**) proved more complex, owing to the more convoluted nature of its signals. Through the use of NOE experiments it was possible to identify through space interactions from the α-protons on the three pyrimidine rings.

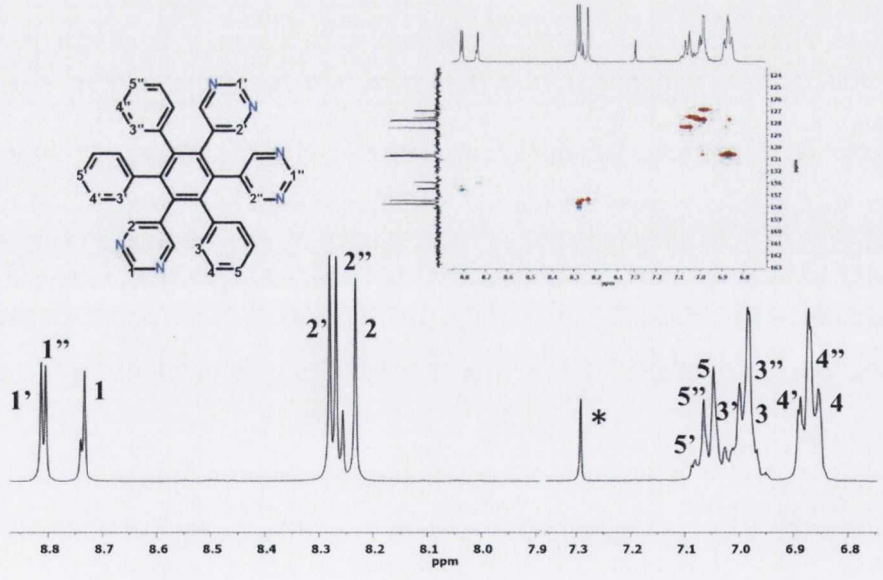

*Figure 2.21: Full assignment of ^{1}H NMR spectrum of **18**. Asterisk denotes solvent peak ($CDCl_3$, RT, 600 MHz). Inset shows HSQC spectrum.*

2D TOCSY experiments then allowed for subsequent assignment of the proton signals. When coupled with the HSQC spectrum, inset in Figure 2.21, it was possible to assign all of the carbons signals.

The successful synthesis of **17** and **18** was the first example of a symmetric unsubstituted polyphenylene of this nature. Other variants with electron withdrawing and donating substituents have also been synthesised, some of which are presented in Chapter 4. The presence of a pyrimidyl ring, straddled by two pendant phenyls, as seen in **17** directs a higher degree of cyclisation around these areas and, depending on the reaction conditions, can yield a range of potential structures. After subjecting the symmetric polyphenylene (**17**) to elemental bromine at high temperature in a pressure tube the resulting dark red product was filtered and washed with cold toluene. Mass spectrometry indicated was formation of 4 new bonds, arising from the four possible structures shown in Figure 2.22.

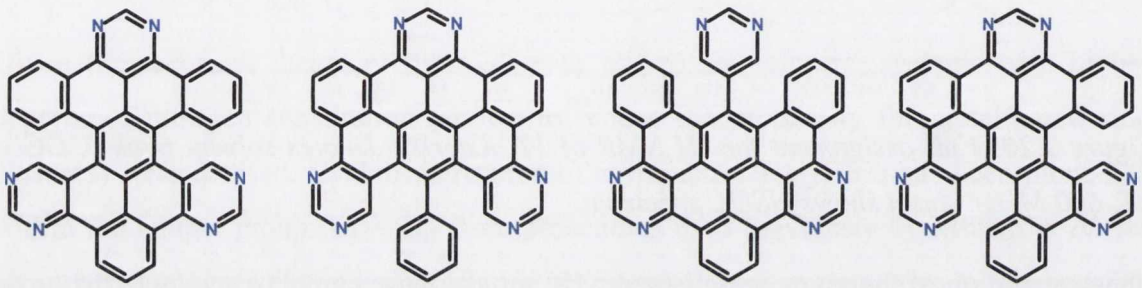

*Figure 2.22 Four possible isomers created upon cyclodehydrogenation of 4-bonds in **17**.*

At first glance, options **I-III** offer possibilities with a C2 axis of symmetry present in the molecule, thereby potentially simplifying NMR characterisation. In reality, much synthetic work has been carried out by the Draper group to show the steric effects of heteroatoms on partially fused aromatics such as these. The energetic drive towards cyclisation can result in highly contorted structures, thereby reducing symmetry and locking pendant phenyl rings by inhibiting free rotation. This has been observed from single-crystal XRD data and is supported by DFT and temperature dependent NMR studies. This will be discussed in greater details and with respect to the barrier to free phenyl rotation in Chapter 4. Given the need to characterise the materials unequivocally, it is necessary for the possible products to be readily distinguishable *via* common techniques, such as mass spectrometry and NMR.

With this in mind, it was thought to turn to the asymmetric isomer (**18**). It was hoped that the adjacent dipyrimidyl substitution as before, would invoke initial cyclisation across three bonds, thereby limiting possible outcomes and simplifying full characterisation.

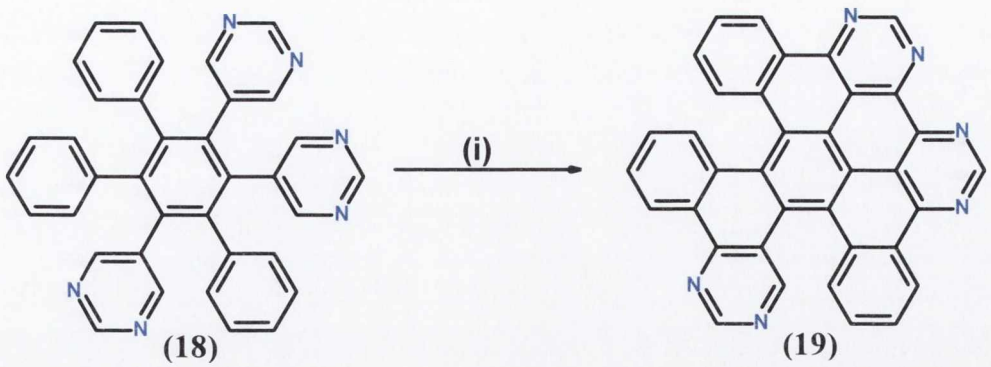

*Scheme 2.23: Procedure for the formation of **19**: (i) Br_2, toluene, 90 °C, pressure tube.*

Treatment of the polyphenylene (**18**) in bromine and toluene (Scheme 2.23) resulted in the precipitation of an orange solid, which mass spectrometry confirmed to be a pure sample, corresponding to only a 4-bond closure. ^{1}H-NMR while complex in nature did in fact show the presence of one single isomer. A 2D TOCSY experiment, shown in Figure 2.23, proved a useful tool for first assessing the nature of the systems.

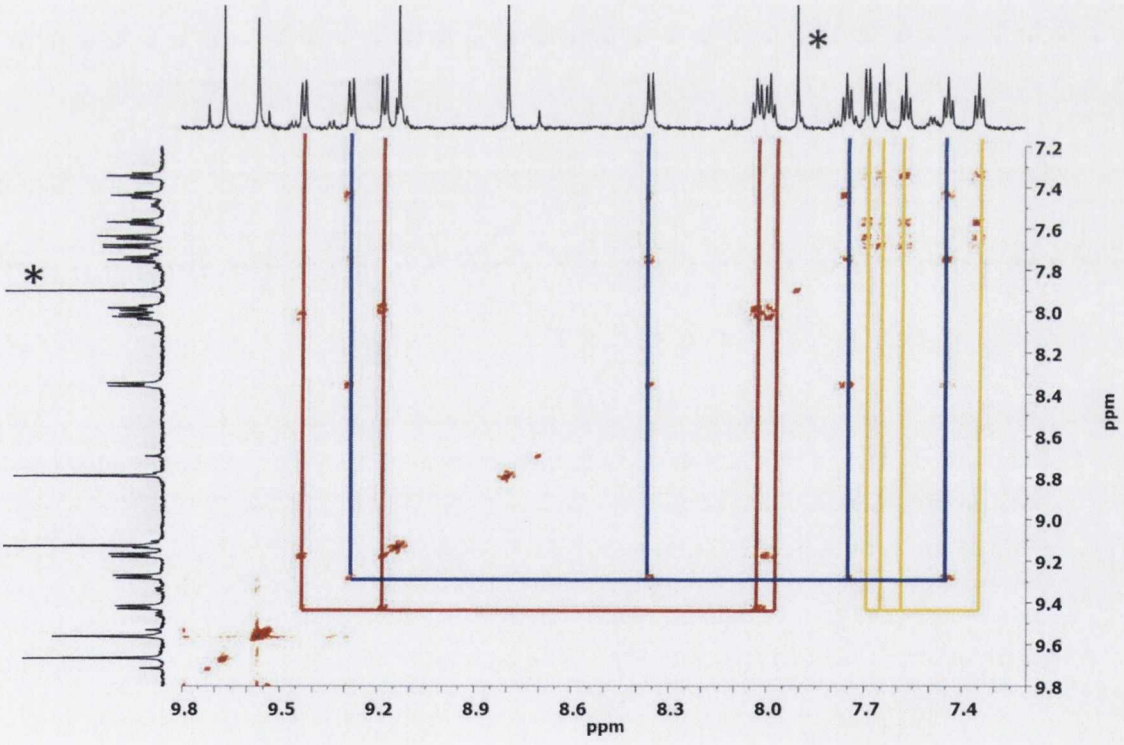

*Figure 2.23: Global TOCSY analysis of **19**: colours represent three different 4-spin systems. Asterisk denotes residual $CDCl_3$ solvent peak (CD_3OD, RT, 600 MHz).*

Three 4-spin systems can be easily identified with their characteristic d-t-t-d multiplicity, pointing to three distinct phenyl rings with fusion on one side only. Additionally, four downfield singlets, integrating for one proton each can be identified; three with significant downfield shifts, most likely corresponding to the proton at the 2 position of a fused or

partially-fused pyrimidine ring. The nature of the shifts and integrations of these four singlets suggest two fused pyrimidine rings in a similar environment, with the third in a significantly less deshielded position. NOE experiments from these four singlets allowed for identification of the single α-proton at δ = 9.57 ppm. This signal showed an NOE response from the heavily deshielded doublet (J = 8.2 Hz) and allowed for the assignment of H1, H2 and H3, as shown in Figure 2.24. The other three singlets and three downfield doublets all showed negligible through-space interactions. This confirmed their existence as protons at the 1 position of the pyrimidine rings and the protons adjacent to nitrogen atoms on fused phenyls respectively. Using HMBC and selective TOCSY experiments it was possible to assign signals H3, H4, H5 and H6 accordingly. In a similar fashion, selectively irradiating H7' at δ = 7.64 ppm, provided the first steps in assigning the ring shown in blue. HSQC analysis shown in Figure 2.24 proved a very accurate means of assigning all the carbon signals.

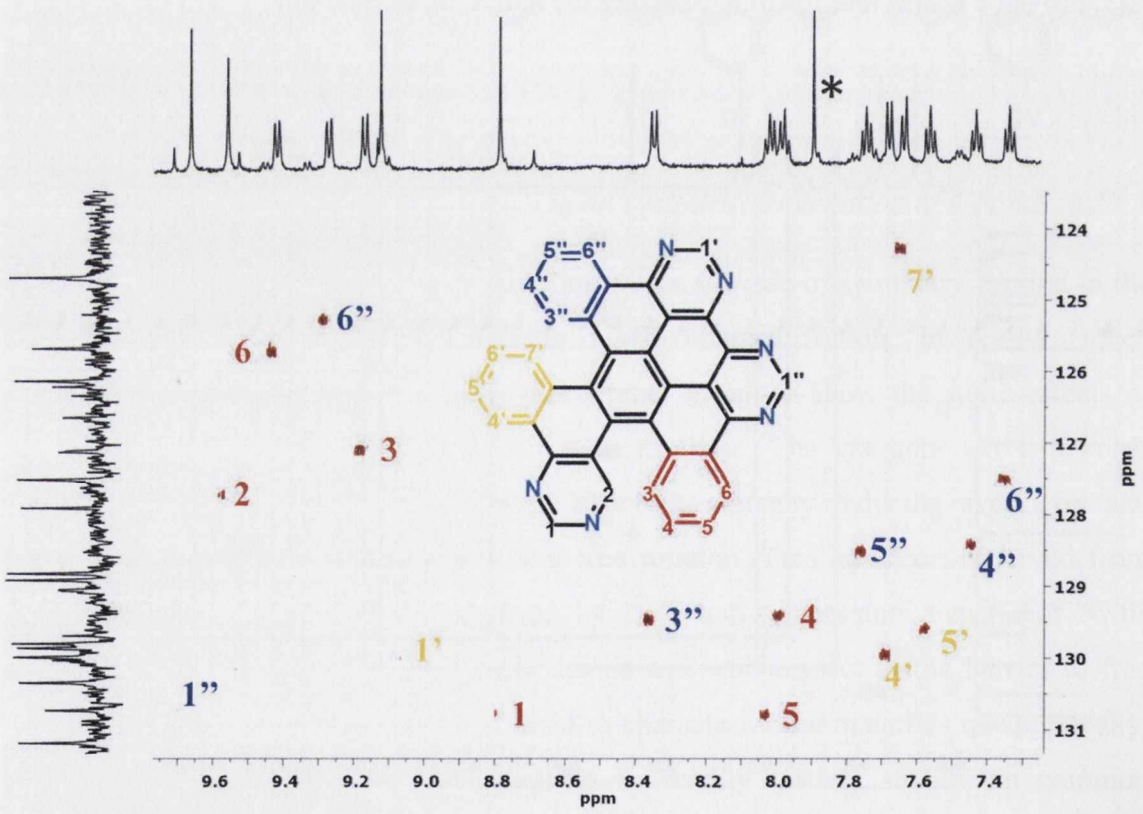

Figure 2.24: HSQC analysis of ***19*** *(600 MHz, CD_3OD, RT). Asterisk denotes residual $CDCl_3$ solvent peak.*

Previously, it has not been possible to cyclodehydrogenate unsubstituted polyphenylenes of this nature, due to the poor solubility of the starting material and increasing insolubility of the partially cyclised products. Using bromine to cyclodehydrogenate, combined with

raised temperatures and the use of toluene as solvent, made it possible to achieve 2/3 cyclisation; more than ever previously seen for an unsubstituted N-polyphenylene. While the asymmetric isomer, which is formed in threefold abundance, proved a convenient tool for assessing cyclodehydrogenation in this case, any higher degrees of C-C bond formation are hampered by the presence of two adjacent phenyl rings. To promote higher degrees of bond formation by this route it would be necessary for each phenyl ring to be straddled by alternating pyrimidyl rings, as seen in the symmetric **17**. As outlined in previous sections, the addition of *tertiary*-butyl substituents may improve the solubility of more cyclised products, while also inhibiting any peripheral bromination. This may prove a useful solution to forming the first fully cyclised hexaaza-NHSB by this method, if the highly strained nature of partially-cyclised intermediates does not serve to impede further C-C bond formation.

2.6 Conclusion and Future Work

In summary, herein we have demonstrated a gateway reaction that offers an unprecedented and efficient process to partially-fused polyaromatics. This methodology offers a one-step route to C-C bond formation in systems that were previously resistant to such reactions. Within a relatively short timeframe this new synthetic procedure has been used to generate a large number of fused, nitrogen-containing polyaromatic platforms. In addition to gleaning vital information about the scope of this strategy, a library of novel compounds with potentially interesting photophysical and coordination properties has been generated. Most interesting is the potential that this route offers chemists both as a synthetic tool and as a starting point to ascertain the mode of cyclisation in these systems.

Adaptation of the procedure in Scheme 2.24, yielded serendipitous reactions which lead us to question the mechanism of cyclisation in hetero-substituted compounds.[42] Careful refinement of the conditions has now resulted in quite a predictable and high yielding process which can be used to either cyclise, or cyclise and substitute, as demonstrated in Chapter 3. This chapter documents eighteen months of methodical adaptation of the initial discovery which has now resulted in an optimized strategy with predictable outcomes. It has resulted in a successful synthetic procedure, which can be used to form between 1-4 new C-C bonds in nitrogen-substituted polyphenylenes. The accumulation of control experiments and negative results has proven just as valuable in deducing potentially rewarding pathways. The following section provides some observations which were found on the way.

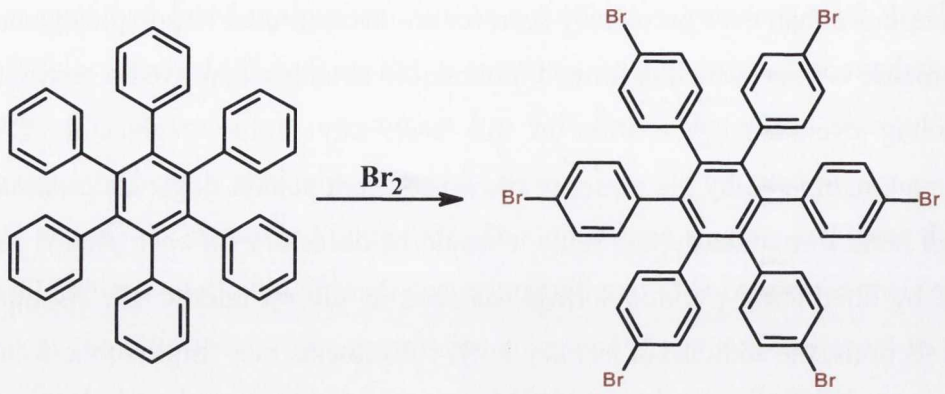

Scheme 2.24: Synthetic procedure for the synthesis of hexakis(4-bromophenyl)benzene.[42]

2.6.1 Observations

An all-compassing method for cyclodehydrogenation still does not exist. Methods using Lewis acids, such as $FeCl_3$ and $AlCl_3$ have been shown to fall short in the controlled cyclisation of polyphenylenes with heteroatom or electron-withdrawing substituents. Similarly, more recent systems such as the use of DDQ in acidic conditions, which successfully cyclise halogenated hexaphenylbenzenes, induce no response whatsoever for nitrogen substituted systems. Molecular bromine has been shown to be the first cyclodehydrogenating agent to successfully yield partially-cyclized brominated polyphenylenes. It has also demonstrated the highest yields, shortest reaction time, easiest purification and most predictability across a range of nitrogen-substituted precursors relative to any other cyclodehydrogenation system. Interestingly, this system has also be shown to eliminate the plethora of partially-fused intermediates that have become commonplace for other agents. To draw other conclusions about its ultimate efficacy needs a more in-depth description of the conditions needed.

As previously mentioned, in the embryonic stage of the development for this procedure, neat bromine was used at room temperature. Such conditions proved inefficient and ultimately posed problems for unsubstituted platforms. The modification of the procedure involved variation of solvent, temperature, reflux conditions and use of microwave synthesis. Most successful was the use of pressure tube conditions, with toluene as the solvent. The reasons for this are likely to be threefold;

i) A significant increase in temperature may potentially favour a thermodynamic product over bromination.

ii) Under pressure-tube conditions elevated temperature results in the evolution of bromine (b.p 58.8 °C), most likely leaving high concentrations of hydrobromic acid (b.p. 122 °C) *in situ*.

iii) Upon bond formation, a reduction in solubility means that precipitation of the product from the reaction mixture can occur.

The sluggish nature of the reaction is most evident for dipyrimidyl polyphenylenes, which fail to undergo cyclodehydrogenation at room temperature in any reasonable timeframe, as demonstrated by NMR studies. Even after the reaction had initiated, the slow progression allowed for progress to be quantified over 24 hour periods. Such observations may imply that the existence of unquenched Br_2 is superfluous to the whole reaction, thereby potentially indicating an arenium cation based mechanism. This could easily be rationalised by protonation at the '5' position of the pyrimidyl rings, thereby generating a cation at the adjacent carbon, *ortho* to both nitrogen atoms. Separate reactions have shown however that high a concentration of HBr, in the presence of various oxidising agents, is not sufficient to induce cyclodehydrogenation in any of these substrates. This may well show that a straightforward mechanism may not be forthcoming.

The presence of bromine always begs the question of homolytic fission of the weak halogen bond under UV irradiation. To this end, countless experiments were carried out in the dark and under UV irradiation, but no tangible influence could be ascertained. Similarly, radical scavengers such as TEMPO and hydroquinone were seen to have no impact on the progression of cyclodehydrogenation. This cannot be used to rule out a radical cation mechanism however as the possibility of a mechanism similar to that seen for the DDQ reaction could potentially take place in acidic conditions. The role of bromine as oxidant here may be used in a similar manner as DDQ, to speed up the oxidation and generation of a donor radical cation ($D^{\bullet+}$) shown in Scheme 2.25.

$$D + H^+ \rightleftharpoons DH^+$$

$$DH^+ + D \rightleftharpoons D^{+\bullet} + DH^{\bullet}$$

$$DH^{\bullet} + H^+ \rightleftharpoons DH_2^{+\bullet}$$

$$DH_2^{+\bullet} + D \rightleftharpoons D^{+\bullet} + DH_2$$

Scheme 2.25: Proposed interconversion from cation to radical cation in the presence of acid.[27]

2.6.2 Summary

A family of nitrogen-containing PAHs have been synthesised by a novel route, using molecular bromine. The yields of cyclodehydrogenation are at least on a par, and in most cases surpass yields ever seen for cyclisations of this kind. The methodology offers a completely metal-free alternative to C-C bond formation in these compounds. X-ray crystallography was used to complete an unequivocal characterisation of these compounds, combined with full NMR assignment and high resolution mass spectrometry analysis. *In situ* NMR studies were also used to garner information about the order and mode of bond formation. A directed synthetic approach was utilised to fully test plausible tactics for producing fused compounds and has therefore resulted in a quite robust methodology, based on empirical trends and a good knowledge of the limits of this reaction.

For all-carbon systems no cyclodehydrogenation is seen to occur by this route. All carbon hexaphenylbenzenes are seen to undergo *para* bromination, while precursors blocked at these sites show no response at all. Increasing the number of pyrimidine rings has a direct influence on the total number of C-C bond formations achieved. This can be limited ultimately at higher degrees of closure, at which point the twisted nature of the increasingly fused molecule inhibits any further attack. Already, this procedure has been shown to have a range of applications, some of which are currently in use, but to fully understand its capabilities a greater understanding of the order and mechanism of the reactions must be achieved.

2.6.3 Future Work

To fully address a mechanistic problem of this nature a multifaceted approach encompassing spectroscopy, computational studies and further direct synthesis is needed. The use of *in situ* electron paramagnetic resonance (EPR) studies could be used to give an indication of the mechanism of this reaction by assessing proton/one-electron transfer to the organic substrates. As previously seen for diphenylphenanthrenes, this would allow for a full analysis of the redox properties of the compounds and an assessment of the reversibility of oxidation as a function of substituent. The formation of organic radical cations *in situ* could easily be identified in this way. In a more indirect manner this could also be assessed by further studying the progression of the reaction in the presence of a radical spin trap, such as TEMPO. A nitroxyl radical of this nature would not only remove any organic radical cations which may be formed, but would also act as an

indirect manner in which EPR assignment could be more successfully made. Computational studies, in line with those mentioned previously by King *et al.* would prove invaluable in the prediction and justification of cyclodehydrogenated derivatives, especially those with higher degrees of nitrogen substitution. A theoretical study of energy-minimised structures for potential outcomes may provide an interesting insight into predicting the outcome of possible cyclisations caused by protonation at different sites. For hexaaza-substituted polyphenylenes, the presence of three pyrimidine rings offers multiple isomers that can prove indistinguishable by mass spectrometry or NMR spectroscopy. As steric factors and proximity play such an important role in subsequent electrophilic attack, a quantitative assessment of the various outcomes could be used to great effect in the design of molecules.

On a synthetic level, the findings outlined here hold the most potential. The Draper group has focused for several years on three connected synthetic pathways; cyclodehydrogenation, substitution to add subsequent functionality, and application. These three routes can be explored by this methodology with respect to the proposed compounds shown in Figure 2.25. Hexapyrollohexaazabenzenes, shown in Figure 2.25 (a), are an interesting class of molecule which until recently exhibited no successful route of cyclodehydrogenation. Recent endeavours still require substitution on the pendant pyrolle rings with highly electron-withdrawing groups. Assessing the viability of this bond closure with the use of Br_2 would prove an interesting challenge. The polyphenylene precursor to the molecule shown in Figure 2.25 (b) is discussed in greater detail in Chapter 4. The ability to combine this substitution and cyclodehydrogenation would prove of great interest for the formation of substituted ionomers for graphene surface growth or discotic liquid crystals. Figure 2.25 (c) depicts a potentially very exciting compound which is made possible by the fortuitous ether-cleavage and cyclodehydrogenation couple seen for **6**. For many years the Draper group have endeavoured to find a feasible route for the incorporation of anchor groups on to fused organic platforms. The addition of an –OH moiety can allow for strong interactions between the carboxylate moiety and metal surfaces such as copper. To this point however the cleavage of alkoxy substituents by relatively mild chemical or thermal reaction conditions has proven a significant in this regard. The ability to complete the majority of the synthetic procedure with trimethoxy substitution which could be concluded by cyclodehydrogenation, coupling with selective cleavage of the *para* methoxy substituent could be a very useful tool.

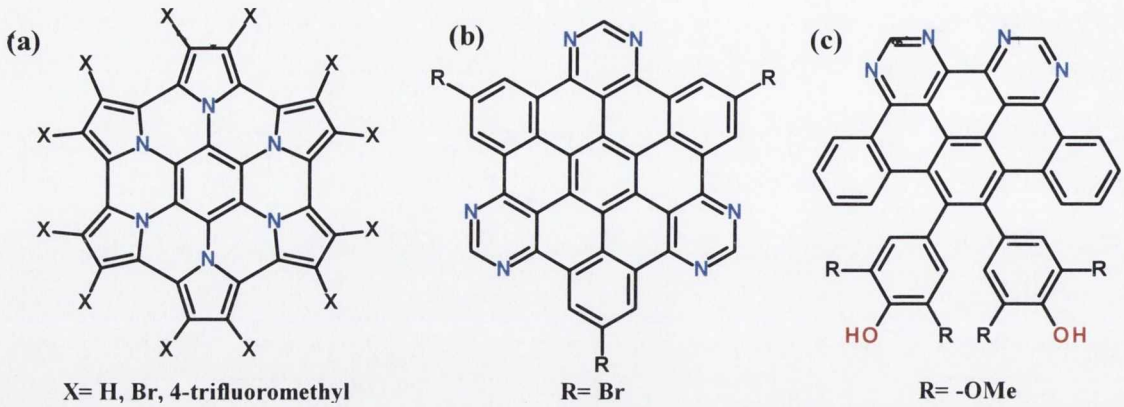

Figure 2.25: Three proposed structures made possible through the use of this novel route of cyclisation.

2.7 References

(1) Von Richter, V. *Ber. Dtsch. Chem. Ges.* **1873**, *6*, 1249–1260;

(2) Kovacic, P.; Kyriakis, A. *J. Am. Chem. Soc.* **1963**, *85*, 454–458.

(3) Rempala, P.; Kroulík, J.; King, B. T. *J. Org. Chem.* **2006**, *71*, 5067–5081.

(4) Rathore, R.; Kumar, A. S.; Lindeman, S. V.; Kochi, J. K. *J. Org. Chem.* **1998**, *63*, 5847–5856.

(5) McKillop, A.; Turrell, A. G.; Young, D. W.; Taylor, E. C. *J. Am. Chem. Soc.* **1980**, *102*, 6504–6512.

(6) Rickhaus, M.; Belanger, A. P.; Wegner, H. A.; Scott, L. T. *J. Org. Chem.* **2010**, *75*, 7358–7364.

(7) Pummerer, R.; Prell, E.; Rieche, A. *Berichte der Dtsch. Chem. Gesellschaft (A B Ser.* **1926**, *59*, 2159–2161.

(8) Kardos, M. Patent DE 276, 1913.

(9) Herbst, W.; Hunger, K. *Industrial Organic Pigments: Production, Properties, Applications*; John Wiley & Sons, 2006.

(10) Clar, E.; Ironside, C. T.; Zander, M. *J. Chem. Soc.* **1959**, 142.

(11) Pinardi, A. L.; Martin-gago, J. A. *ACS Nano* **2013**, 3676–3684.

(12) Mallory, F. B.; Wood, C. S.; Gordon, J. T.; Lindquist, L. C.; Savitz, M. L. *J. Am. Chem. Soc.* **1962**, *84*, 4361–4362.

(13) Tsefrikas, V. M.; Scott, L. T. *Chem. Rev.* **2006**, *106*, 4868–4884.

(14) Otero, G.; Biddau, G.; Sánchez-Sánchez, C.; Caillard, R.; López, M. F.; Rogero, C.; Palomares, F. J.; Cabello, N.; Basanta, M. A.; Ortega, J.; Méndez, J.; Echavarren, A. M.; Pérez, R.; Gómez-Lor, B.; Martín-Gago, J. A. *Nature* **2008**, *454*, 865–868.

(15) Treier, M.; Pignedoli, C. A.; Laino, T.; Rieger, R.; Müllen, K.; Passerone, D.; Fasel, R. *Nat. Chem.* **2011**, *3*, 61–67.

(16) Cai, J.; Ruffieux, P.; Jaafar, R.; Bieri, M.; Braun, T.; Blankenburg, S.; Muoth, M.; Seitsonen, A. P.; Saleh, M.; Feng, X.; Müllen, K.; Fasel, R. *Nature* **2010**, *466*, 470–473.

(17) Pinardi, A. L.; Otero-Irurueta, G.; Palacio, I.; Martinez, J. I.; Sanchez-Sanchez, C.; Tello, M.; Rogero, C.; Cossaro, A.; Preobrajenski, A.; Gómez-Lor, B.; Jancarik, A.; Stará, I. G.; Starý, I.; Lopez, M. F.; Méndez, J.; Martin-Gago, J. A. *ACS Nano* **2013**, *7*, 3676–3684.

(18) Bronner, C.; Stremlau, S.; Gille, M.; Brauße, F.; Haase, A.; Hecht, S.; Tegeder, P. *Angew. Chemie* **2013**, *52*, 4422–4425.

(19) Vo, T. H.; Shekhirev, M.; Kunkel, D. a; Orange, F.; Guinel, M. J.-F.; Enders, A.; Sinitskii, A. *Chem. Commun. (Camb).* **2014**, *50*, 4172–4174.

(20) Palma, C. *J. Am. Chem. Soc.* **2014**, *136*, 4651–4658.

(21) Linden, S.; Zhong, D.; Timmer, A.; Aghdassi, N.; Franke, J. H.; Zhang, H.; Feng, X.; Müllen, K.; Fuchs, H.; Chi, L.; Zacharias, H. *Phys. Rev. Lett.* **2012**, *108*, 216801.

(22) Rooney, J.; Pink, R. *Proc. Chem. Soc.* **1961**, 129.

(23) Baddeley, G. *J. Chem. Soc.* **1950**, 994.

(24) Hammerich, O.; Parker, V. D. *Adv. Phys. Org. Chem.* **1984**, *20*, 55–189.

(25) Di Stefano, M.; Negri, F.; Carbone, P.; Müllen, K. *Chem. Phys.* **2005**, *314*, 85–99.

(26) Ito, S.; Wehmeier, M.; Brand, J. D.; Kubel, C.; Epsch, R.; Rabe, J. P.; Müllen, K.; Kübel, C.; Epsch, R.; Rabe, J. P.; Müllen, K. *Chem. - A Eur. J.* **2000**, *6*, 4327–4342.

(27) Rathore, R.; Kochi, J. K. *Acta Chem. Scand.* **1998**, 114–130.

(28) Wijesinghe, L. P.; Lankage, B. S.; Ó Máille, G. M.; Perera, S. D.; Nolan, D.; Wang, L.; Draper, S. M. *Chem. Commun. (Camb).* **2014**, *50*, 10637–10640.

(29) Roberts, D. J.; Nolan, D.; Ó Máille, G. M.; Watson, G. W.; Singh, A.; Ledoux-Rak, I.; Draper, S. M. *Dalt. Trans.* **2012**, *41*, 8850.

(30) Grzybowski, M.; Skonieczny, K.; Butenschön, H.; Gryko, D. T. *Angew. Chem. Int. Ed. Engl.* **2013**, *52*, 9900–9930.

(31) Wu, D. PhD Thesis, Johannes Gutenberg University, 2008.

(32) Takase, M.; Narita, T.; Fujita, W.; Asano, M. S.; Nishinaga, T.; Benten, H.; Yoza, K.; Müllen, K. *J. Am. Chem. Soc.* **2013**, *135*, 8031–8040.

(33) Tovar, J. D.; Rose, A.; Swager, T. M. *J. Am. Chem. Soc.* **2002**, *124*, 7762–7769.

(34) Dou, C.; Saito, S.; Matsuo, K.; Hisaki, I.; Yamaguchi, S. *Angew. Chem. Int. Ed. Engl.* **2012**, *51*, 12206–12210.

(35) Nagarajan, S.; Barthes, C.; Gourdon, A. *Tetrahedron* **2009**, *65*, 3767–3772.

(36) Spek, A. L. *Acta Crystallogr. Sect. D* **2009**, *65*, 148–155.

(37) Trixler, F. Organic Semiconductor Group, Ludwig-Maximilians University, 2007.

(38) Kapoor, N.; Thomas, K. R. J. *New J. Chem.* **2010**, *34*, 2739.

(39) Wehmeier, M.; Wagner, M.; Müllen, K. *Chem. Eur. J.* **2001**, *7*, 2197–2205.

(40) Halpin, Y.; Pryce, M. T.; Rau, S.; Dini, D.; Vos, J. G. *Dalton Trans.* **2013**, *42*, 16243–16254.

(41) Tosonian, S.; Ruiz, C. J.; Rios, A.; Frias, E.; Eichler, J. F. *Open J. Inorg. Chem.* **2013**, *3*, 7–13.

(42) Rathore, R.; Fujimori, S. *Org. Synth.* **2005**, *82*, 30.

3 Probing Intermolecular Growth and Application

3.1 The Energy Production Market

Fuel cells are an alternative source of electricity which are not limited by fossil fuel availability, environmental restrictions or the logistics of distributed generation. Fuel cell revenue is predicted to increase almost 40-fold over the next 9 years, to an overall market of $40 billion.[1] The U.S. Government's 'self-generation incentive program' shown in Figure 3.1 (a) has directly contributed to the enormous year-on-year growth in fuel cell sales, outlined in Figure 3.1 (b).[2] Fuel cells offer an adaptable technology which can exhibit zero-emissions and the potential for off-grid power production and portable consumer devices. In addition, the generation of direct current through chemical reactions is unrestricted by Carnot limits, which describe the maximum efficiency possible in classic heat engines. To best appreciate the direction of fuel cell development going-forward it is necessary to re-familiarise with their progress over the past 150 years.

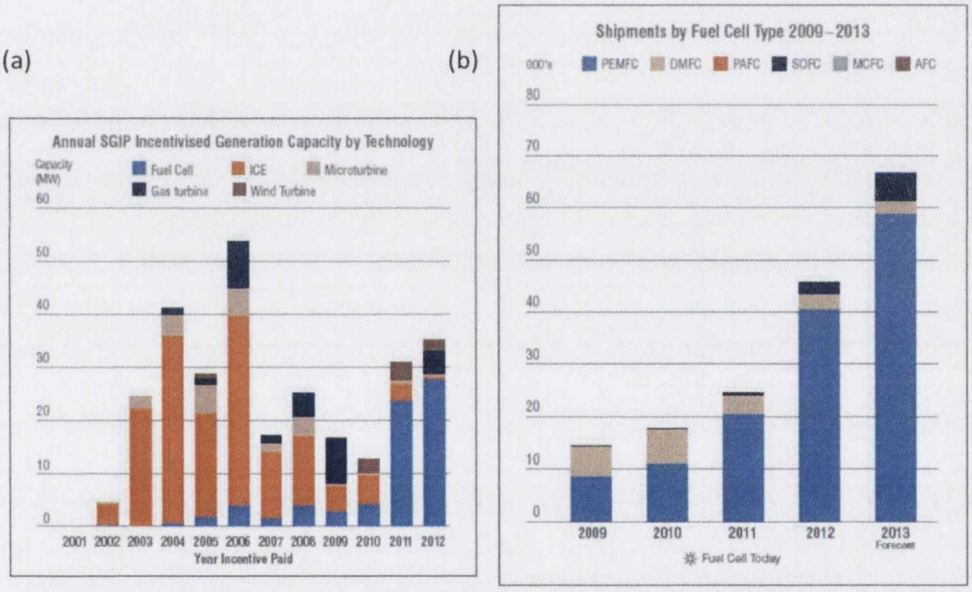

Figure 3.1: Growth in fuel cell technologies: (a) self-generation incentive programme provided by U.S Government providing rebates for distributed energy systems installed by customers;[2] (b) total global annual sales of fuel cell devices.[3]

3.2 Fuel Cell Development

The fuel cell was first discovered by Sir William Grove in 1839. Few inroads were made in the hundred years proceeding, until the introduction of General Electric to the market in the 1960s. The second-coming of fuel cells fortuitously coincided with the OAPEC oil embargo in the 1970s. Now, 40 years later the newest generation of fuel cells coincide with another period of political unrest and uncertainty about future oil availability. At a

fundamental level, fuel cells convert chemical energy into electrical energy. They comprise electrodes, electrolyte and a catalytic material. They are classified by the nature of their electrolyte into two families: liquid or solid. Examples of liquid-based electrolytes are found in alkaline fuel cells (AFCs), phosphoric acid fuel cells (PAFCs) and molten carbonate fuel cells (MCFCs). Common examples of solid-state electrolytes can be found in solid oxide full cells (SOFCs) and polymer electrode (proton exchange) membrane fuel cells (PEMFCs). Most liquid-phase electrolytes require extremely high operating temperatures, as outlined in Table 3.1, and as a result exhibit reduced durability. In spite of this, AFCs have been shown to maintain stable operation above 8000 hours and were used in the first U.S. Space Program. MCFCs, which operate at 650 °C have also been shown to have electrical, industrial and military applications.[4]

Table 3.1 Common types of fuel cell. Shading denotes liquid electrolytes.

Fuel Cell Type	Alkaline	Phosphoric Acid	Molten Carbonate	Solid-Oxide	Proton-Exchange Membrane
Electrolyte	KOH	H_3PO_4	Li_2/K_2CO_3	Y_2O_3 on ZrO_3	Nafion
Fuel	H_2	H_2	H_2, CH_4, CO	H_2, CH_4, CO	H_2, CH_3OH
Charge Carrier	H^+	H^+	CO_3^{2-}	O^{2-}	H^+
Electrode Catalyst	Platinum	Platinum	Nickel	Oxides, Nickel	Platinum
Temperature	90-260 °C	175-200 °C	650 °C	800-1000 °C	65-85 °C
Efficiency	40%	40%	60%	60%	40%
Contaminants	CO	CO	Sulfur	Sulfur	CO

Although probably the least exploited to this point, PEMFCs offer most potential for use in transport and stationary applications, by exhibiting high-durability and low operating temperatures, as shown in Table 3.1. Like most fuel cells, PEMFCs require a fuel (usually hydrogen) which is oxidised to protons and moves towards the cathode through the solid proton exchange membrane. Once at the cathode the protons react with the secondary fuel (in this case oxygen) to form water, as depicted in Figure 3.2. Direct methanol fuel cells (DMFCs) are another subclass of PEMFC, in which methanol is used as the fuel. DMFCs introduce a low concentration methanol solution into the cell and can operate at temperatures between 50-120 °C. The proton-exchange membrane must exhibit excellent proton conductivity, chemical and thermal stability and above all low gas permeability. The membrane must conduct protons as they move from the anode to cathode, at which point they recombine with electrons. This is usually done *via* a sulfonate group in which

the mobile proton is believed to hop from site to site, thereby allowing for the transport of protons, while forcing electrons around the conducting path, as seen in Figure 3.2.

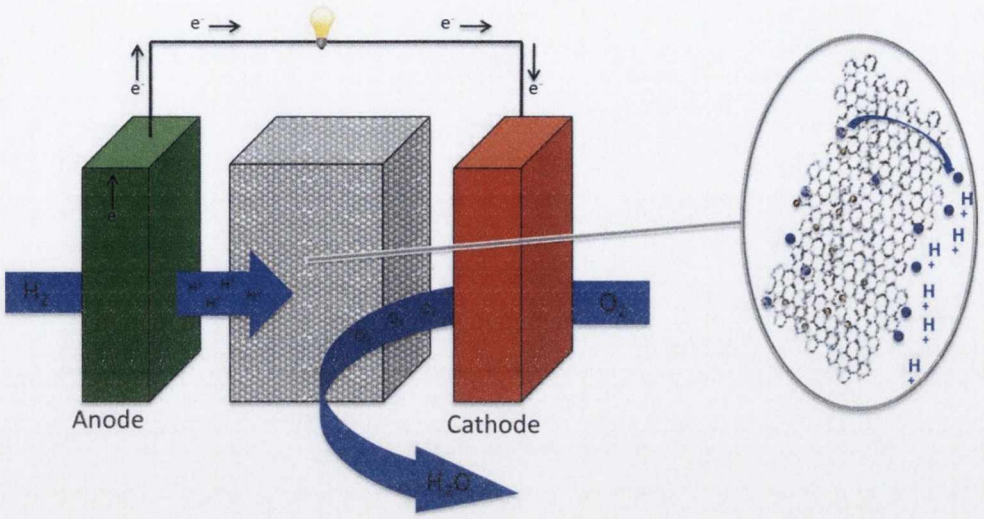

Figure 3.2: Graphic displaying simplified operation of a PEMFC. Inset depicts the transport of only H^+ ions across the proton exchange membrane, creating a potential for electron transport through an external circuit.

Low resistance of the membrane to proton transport proves extremely important to the efficiency of the fuel cell. Early membranes were first developed by Grubb and Niedrach of General Electric and were simple phenolic membranes, generated by the polymerisation of phenol-sulfonic acid using formaldehyde. Poor lifetimes (300-1000 h) and degradation ultimately lead to the development of sulfonated polystyrenes and 'D' Membranes. Low proton conductivity values for all of these materials resulted in power densities as low as 100 $mWcm^{-2}$. These membranes were eventually replaced in 1966 by a perfluorosulfonic acid developed by Du Pont and known as Nafion™. As a co-polymer of tetrafluoroethylene and sulfonyl fluoride it is semi-crystalline and shows stability in FCs up to 60,000 cycles, at temperatures between 43 °C - 82 °C.[5] Other analogous compounds, such as polyetherketones, polyimides and polyether sulfones have also been used with some success.[6]

3.3 Catalytic Materials

3.3.1 Traditional Catalysts

Historically platinum has been widely used to fabricate both anode and cathode, usually existing as small particles on the surface of significantly larger substrates, with coverages of between 0.2 mg/cm^3 and 28 mg/cm^3.[7] These substrates are gas diffusion layers (GDLs)

and serve as a physical support and current collector for the catalytic particles. They usually exhibit a micro-porous structure, hydrophobicity to avoid flooding, and are seen to enhance intimate electronic contact.[8] Most importantly they serve as high surface-area electrodes which can aid diffusion. They can also dissipate heat and compress to alleviate thermal expansion, a phenomenon commonly seen when the cells are fabricated into larger fuel-cell stacks.[9] The cost of platinum is a significant factor in limiting the commercialisation of PEMFCs. Platinum can be degraded by oxidation, corrosion and migration. Predictions state that current global platinum sources could sustain a 500 million unit fleet of cars for just 15 years.[10] At current costs, the precious metal alone in each car would prove more expensive for a 100 kW engine than that for a full combustion engine of the same power output. To create the power output of a common engine from fuel cells it is currently necessary to use between 50-100 g of Platinum metal. For research in this area to be truly successful, this value should be lowered to between 12-15 g.[11] A reduction in loading is currently achieved in two ways; 1) replacement of platinum with less noble metals or non-noble catalysts, in the form of transition metal alloys, carbides or macrocyclic compounds[12] or 2) deposition of a lower concentration of catalytic particles onto carbon blacks, diamonds, oxides or graphitised materials.[13] Very recent developments show that it is also possible to combine both of these modes of development to produce multifunctional materials that may operate as supports to metal catalysts, with the added bonus of low activity catalysis. A complete understanding of the mechanism of activity of platinum in fuel cells has remained elusive. It is generally accepted however that it occurs through the reduction of O_2 electrochemically either directly to water, with rate constant k_1 (4-electron process) or through adsorbed hydrogen peroxide ($H_2O_{2\ ADS}$) with rate constant k_2 (2-electron process).

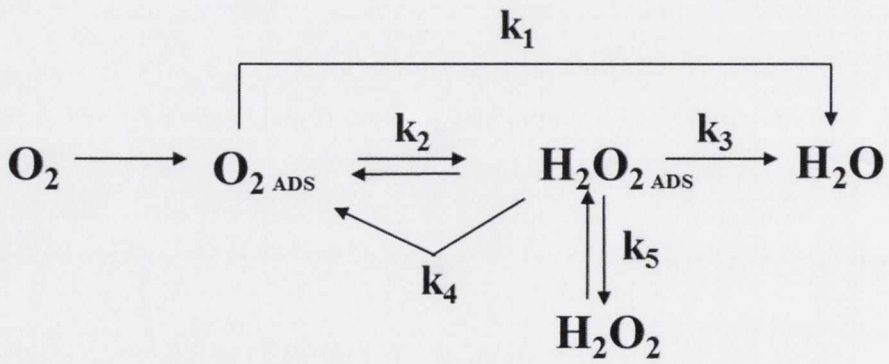

Figure 3.3: Oxygen reduction reaction (ORR) mechanism on platinum.[14]

Changes that are made to the catalytic material need to be mindful of the end use and the need to undertake *in situ* and *ex situ* testing. To make useful comparisons it is also worth noting that current state-of-the-art membrane-electrode assemblies (MEAs) exhibit loading of 0.4 mg/cm^2 with overpotentials of 400 mV and activity stability up to 5000 h. In addition, the nature of PEMFC devices mean that successful operation must occur at low temperatures and adhere to the need for thin electrodes (10-15 μm) which include 20-30 wt.% of PEM ionomer in the heterogeneous mix. Historically the introduction of a second, cheaper and more abundant metal has been successful for ORR. This can be done in a number of ways, most commonly *via* deposition of noble metals on single crystal surfaces of platinum, such as Cu on Pt(111) or Sn on polycrystalline Pt. These have been seen to be more active than Pt(111) or Pt/C alone, most likely due to the increased number of O_2 adsorption sites.

The greatest amount of recent progress however has been seen in the formation of Pt alloys with increased catalytic activity, most notably with metals such as Co, Ni, Cr or Fe. The process of alloying platinum with such transition metals can increase the d-band valency and in turn decrease the interatomic distances of metal particles. This has a profound effect on the observed catalytic activity. For use in PEMFCs, which can be very susceptible to contamination, alloying base metals must be done with care as any leaching of metals can lower the conductivity of the membrane and ultimately lead to its degradation. With regard to activity, leaching can be seen to increase resistance and lower the diffusion of oxygen. Although solutions have been found by reducing the excess of base metal and ensuring more complete alloying, base metal alloys are still inherently unstable under acidic conditions in PEMFCs. To assess the possibilities of developing a dual-functional material, which may serve as both an effective support and additional catalytic agent, we must first follow the progression of metal-containing and metal-free heterodoped compounds in the realm of catalysis.

3.3.2 Heteroatom Catalysts

Jasinski first discovered the ability of cobalt phthalocyanine (Figure 3.4 (a)) to catalyse ORR.[15] Since then, the existence of non-precious metal catalysts has broadened to include nitrogen-coordinated transition metal macromolecules, carbonitrides, conductive polymers (Figure 3.4 (b)) and more recently; doped graphitic materials.[16] In the decades after Jasinski's discovery, only marginal development was made in the field, through the use of metal-containing porpyhrins,[17] phthalocyanines,[18] pyrolysed carbon and nitrogen-

containing precursors[19]. The increased ORR activity seen in these systems is usually attributed to the presence of N-coordination to metals such as Fe, Co or Ni.[20,21] Bron *et al.* confirmed this theory for the pyrolysed Fe-containing phenathroline polymers, shown in Figure 3.4 (c). They showed the importance of pyridine-type coordination to transition metals in loading of 1-2%.[22]

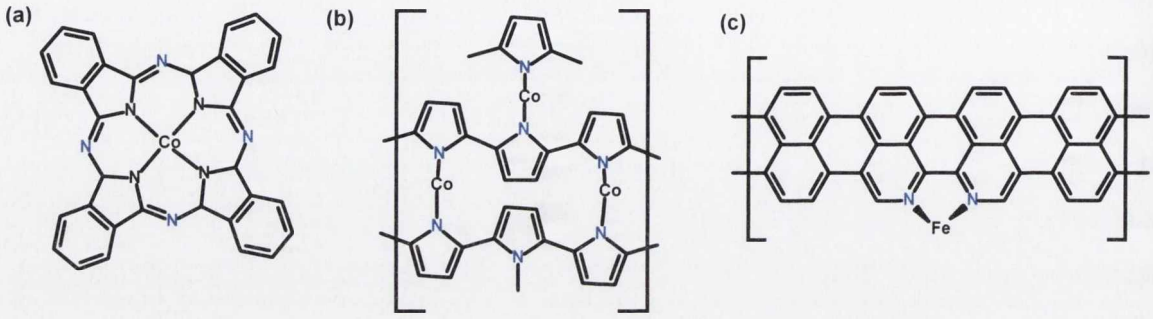

Figure 3.4: Examples of transition metal complexes which exhibit ORR catalytic activity: (a) cobalt phthalocyanine;[15] (b) cobalt polypyrrole composite by Bashyam et al.,[18] (c) iron containing phenanthroline polymers.[22]

Impregnation of carbon-black with uncoordinated phenanthroline confirmed that the activity had indeed emanated from the metal coordination sites. This system showed superior performance in electrochemistry analyses than iron acetate and also showed a low production of H_2O_2. In 2005 Mailayan *et al.* demonstrated the use of platinum particles on nitrogen-doped carbon nanotubes.[23] These were seen to increase the electron-withdrawing effect and ultimately facilitate the oxidation of methanol. 2006 saw Wang *et al.* introduce novel primary supports made from nitrogen-containing carbon nanotubes. The growth of these bamboo-like structures allowed for the deposition of small clusters of Pt-Ru with a mean size of 3.54 nm and showed considerably increased electrocatalytic activity relative to that seen in the absence of the nanotube array.[24] This finding demonstrated the first truly successful alternative to the more traditional method of incorporating nanotubes into existing mixes of electrocatalysts.

A current area of significant development surrounds the creation of highly-ordered doped mesoporous nanostructures with voids that prove more accessible to Nafion™ and thereby minimise the triple phase boundary between electrolyte, gas and catalyst.[25] These compounds have been heralded as efficient alternatives to more traditional systems, as they can exhibit better activity, stability and tolerance to poisoning for ORR in alkaline media. Even in conjunction with current metallic catalytic systems these compounds have

been shown to enhance the anchoring of the metal particles and lead to increased dispersion and stability. These doped carbon composite materials with non-noble metals (Fe, Co etc.) have shown enhanced activity in fuel cells.[18] Not until Xiong *et al.* reported ORR activity of vertically aligned nitrogen-doped carbon nanotubes (VA-NCNTs) formed from the pyrolysis of iron phthalocyanine had such behaviour been observed in a seemingly metal-free electrocatalyst.[26] By electrochemical purification this work showed the apparent removal of any residual Fe catalyst to yield VA-NCNTs, shown in Figure 3.5. These VA-NCNTs were shown to possess higher activity, lower overpotential and increased long-term stability relative to common commercially available Pt/carbon-black catalysts.

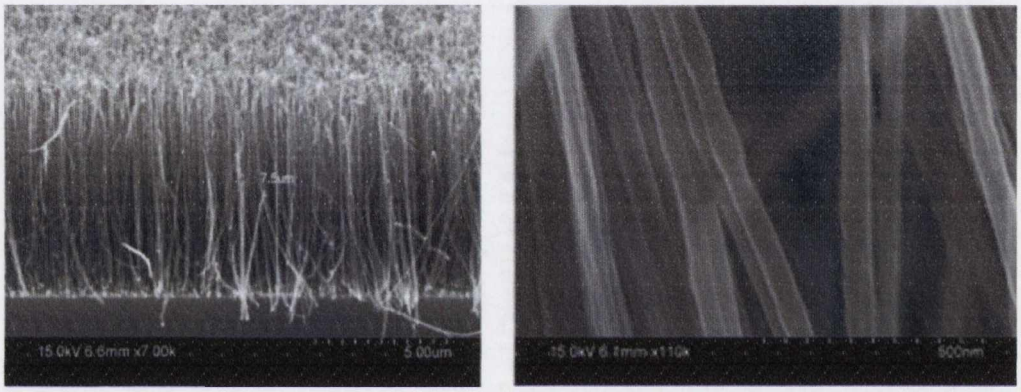

Figure 3.5: SEM images of nitrogen doped carbon nanotubes.[26]

This work has not gone without its detractors however, with controversy surrounding the mode of catalytic enhancement and the effect that any residual metal trapped within the graphite framework may have. Any residual impurities could have a potential effect on ORR activity. This ultimately left the need for a completely metal-free N-doped carbon material to address significant synthetic and practical reservations. This question was eventually addressed by the work of Liu *et al. via* nanocasting of nitrogen-containing dyes. They formed ordered graphitic arrays which reinforced Dai's work, showing significant ORR activity, which surpassed that of commercially available traditional Pt/C catalysts.[27] This existed as the watershed case, with a large body of work quickly following suit in the production of N-doped graphenes up to and including low-cost, large-scale synthesis from abundant nitrogen sources, such as melamine.[28] This allowed the study of catalytic behaviour to be assessed and directly attributed to the altered C-N environments, for compounds prepared in wholly metal-free environments.

3.3.3 Catalytic Supports

To better appreciate the development of dual-function catalytic materials it is necessary to understand the methods of electrode fabrication. There exists two specific categories of catalytic supports; primary conductive supports and secondary supports. The physical properties of a substrate can dramatically affect the stability and electrochemical efficiency of catalysts, especially in low-temperature fuel cells. The ability of a substrate to control a catalyst's morphology can lead to high surface-area and dispersion, and good crystallinity. This can ultimately facilitate better electron transfer. Supports can be immobilised *via* a range of different techniques including; impregnation, grafting, anchoring, deposition-precipitation or chemical vapour deposition (CVD). It is necessary that supports exhibit low combustive reactivity, combined with high conductivity and electrochemical stability. As decreasing the size of catalytic particles can lower specific activity, it is important to find high surface area substrates with good catalyst-support interactions.[29] Carbon supports are manufactured by the pyrolysis of hydrocarbons and offer a low cost and high availability solution. They were used almost exclusively up until the 1990s and have been shown to successfully control dispersions of platinum nanoparticles, thereby facilitating electron transfer between catalyst and electrode. They can result in increased metal dispersions and therefore raise electrocatalytic activity. Recent research has also shown that the functionalization of these materials can result in enhanced supports.[30] Although these current carbon based support systems can offer high conductivity and good specific interactions, there is much scope for improvement.

Heteroatom substitution can serve to drastically increase the binding energy of metal particles such as platinum on catalytic supports. For example, a two-fold increase in platinum-carbon binding energy is observed by incorporating adjacent nitrogen atoms into aromatic systems. This is attributed to the disruption of the double bond character and an increase in the contribution of the 2s orbital of the carbon atom and 6s orbital of the platinum in the carbon-metal bond.[31] Recent work by Wohlgemuth *et al.* describes nitrogen-containing carbon aerogels, synthesised using pyrrole-2-carboxaldehyde under hydrothermal carbonisation conditions. These provide high catalytic activity proportional to surface area, in the absence of any metal and show higher current densities and lower onset potentials than seen for traditional Pt systems.[32] The synthesis of doped, macroscopic carbon-based frameworks with high catalytic activity could offer architectures for noble/non-noble metal deposition with 3D electronic connectivity while, additionally providing an innate catalytic potential. To fully assess the influence that

heteroatoms, in particular nitrogen can have in such environments it is first necessary to understand the mode of their activity and the manner in which they can be introduced.

3.4 Nitrogen Doping

3.4.1 Nitrogen Doping for ORR

The chemical introduction of nitrogen atoms to a graphitic-like network can result in 'pyridinic', 'pyrolic' and 'graphitic' configurations, shown in Figure 3.6. Pyridinic refers to nitrogen atoms at graphene edges, pyrollic to atoms in five member rings, and graphitic to nitrogen atoms incorporated directly into the layer, replacing carbon atoms.

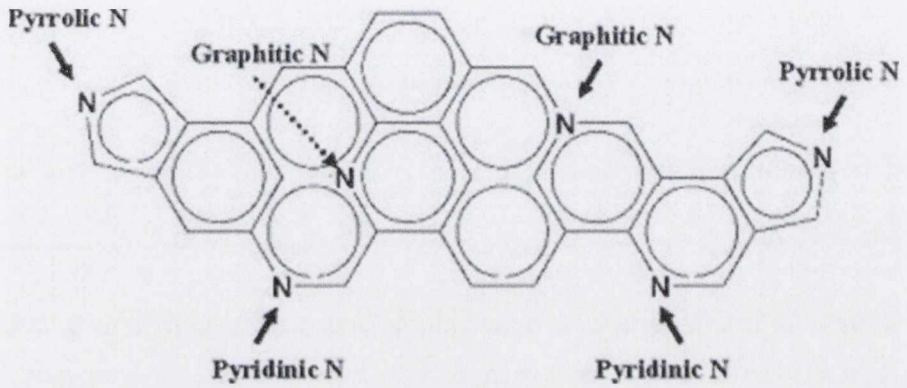

Figure 3.6: Potential nitrogen substitution positions in a graphitic structure.[33]

It is accepted that incorporation of nitrogen atoms into carbon materials will result in a change in the electronic structure, but it is important to establish the correlation between the position of the nitrogen atom and ORR performance. Initial B3LYP calculations by Aryanpour *et al.*[34] indicated that activity possibly originates from the high electron density on carbon atoms adjacent to the doped nitrogen atom. This would likely result in augmented O_2 adsorption, weakened oxygen bonding and would ultimately lead to direct reduction, generating OH^-. Nitrogen in a quaternary position for example appears to produce a new donor state near the Fermi level. This results in n-type conductivity. Irrespective of the type of substitution the presence of nitrogen in nanomaterials has been seen to increase the conductivity up to 325 S/cm at 4 wt.%, *via* a standard four-contact measurement.[35] Other publications show varying n-type character which in general results in a non-linear relationship observed between N% and conductivity, as shown in Table 3.2. A maximum of 15.4 S/cm has been seen for a nitrogen content of 3.1 wt.%.[36] Several caveats do exist for both methodology and morphology. The increase of nitrogen dopants may inevitably lead to greater defects within the material, which decrease conductivity. Therefore, the structure of a doped material should always be taken into account. Also,

the common methodology used to measure such conductivity is by the standard four-contact method. For 2-dimensional materials it can prove more than suitable, but for networks like nanotubes with a higher degree of dimensionality, measuring the conductivity of a pressed material may not be a genuine reflection of reality. While this data assesses the effect of heteroatoms on a macroscopic level, it is important to understand the source of such chemical activity, and the manner in which specific heteroatom substitution can be introduced.

Table 3.2: Conductivity of common bulk nitrogen-containing carbon nanomaterials, measured by the four-contact method.[37]

N-CNMs	N content (%)	[$\Omega^{-1} \cdot cm^{-1}$]
SWNTs	0.4	1800
	1.6	1000
N-CNT mats	0	258
	4	325
	5	123
	6.3	53
	7.4	60
N-mesoporous carbons	0	0.08
	4.3	0.43
	8.1	0.26
	11.9	0.04
N-CNFs	0	9.1
	1.7	11.0
	3.1	15.4
	8.2	6.1
N-CNTs	2.7	12.5

3.4.2 Activity in the Presence of Heteroatoms

A better understanding of the chemical nature of doping sites can be gleaned by assessing the steric and electronic changes introduced upon inclusion of a heteroatom. From first principles it can be determined that the incorporation of nitrogen atoms only changes the electronic bands to within 1 eV of the Fermi level, thereby retaining the properties of graphene. As the calculated bond lengths of C-C (1.42 Å) and C-N (1.41 Å) are similar in N-doped graphene,[38] only a minimal steric influence is exerted on the structure by pyridinic or graphitic substitutions. sp^3 hybridisation however would lead to a much more disrupted structure. Noting the electronegativities of N (3.04) and C (2.55) on the Pauling scale it is apparent that increasing polarization is induced into the network. This results in considerable changes in the electronic, magnetic and optical properties of graphene. Additionally, spin density and charge density prove extremely important in assessing ORR activity. Carbon atoms adjacent to nitrogen substitution exhibit high spin density and behave as the sites for OOH adsorption.[39] OOH adsorption is integral to ORR, hence the inability of pristine graphene to catalyse ORR. Due to the high dissociation barrier

exhibited by O_2, it is most likely that the mechanism for ORR in nitrogen doped materials is *via* the associative pathway for a 4-electron mechanism, which is outlined in Scheme 3.1. The removal of O_{ADS} serves as the limiting step in this pathway. The presence of water is essential to this mechanism. It is believed that the adsorption of O_2 is enhanced by the induced polarisation caused by H-bonding interactions with water. Zhang *et al.* have shown that the outlined 4-electron mechanism also applies in acidic environments.[39]

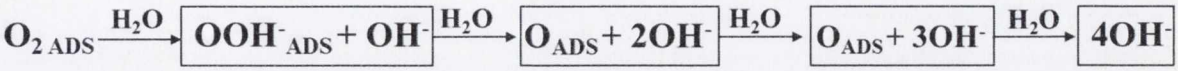

Scheme 3.1: Mechanism for ORR in N-doped graphitic material in an alkaline environment

Controversy does still exist about which specific properties of N-doped materials can be attributed to promote ORR activity, due to conflicting conclusions in several recent publications. Dai's previously discussed finding indicates increased oxygen adsorption occurs at the pyridinic N atom. Subsequently this has been supported by other research.[40,41] Lin *et al.* have shown, using primarily pyridinic N-doped materials, that such a substitution pattern may not be as catalytically active as previously thought.[25] Interestingly, as shown by Ruoff *et al.* substitution may play a significant role in the control of onset potential for ORR but is not only reliant on the percentage of nitrogen dopant present.[33]

3.4.3 Methods of Nitrogen Doping

To date, the synthesis of N-doped carbon materials has evolved in two directions: 1) post-treatment, such as the reduction of graphene oxide (GO), plasma or arc-discharge and photochemical reactions and 2) *in situ* doping, including chemical vapour deposition (CVD), ball milling and bottom-up synthesis. Concurrent reduction and doping of graphene can be achieved in post-treatment, either by thermal annealing or wet-chemical methods. Both of these methods involve the use of ammonia, yielding only pyridinic and pyrollic nitrogen. The efficacy of this methodology is made possible by the ability of NH_3 to act as a very effective reducing agent. Wet chemical methods also offer the possibility of using nitrogen-containing compounds such as urea or hydroxylamine to gradually release NH_3 *via* a hydrothermal process. These approaches can offer many benefits in the generation of catalytic membranes, as they have the potential to enhance nucleation of nanoparticles. A considerable drawback of these routes results from the laborious

procedures and harsh reaction conditions required, which ultimately results in relatively low yields.

Chemical Vapour deposition (CVD) has been used to great effect in the production of few-layer graphene for almost ten years. Using hydrocarbon sources such as methane, ethylene and ethyne deposited onto transition metal catalysts such as copper and nickel, CVD has been proven to be both a reliable and scalable approach to the production of large-domained graphene. By introducing nitrogen-containing precursors, such as 1,3,5-triazine on Cu foil,[42] or NH_3:CH_4:H_2:Ar on Cu[43] or Ni[44] substrates, CVD has been recently shown to yield nitrogen-doped graphene with N substitution from 0.25[43] - 5.6 at.%[42]. These methods, while performed at low pressures, require temperatures from 500-1000 °C and metal substrates. This makes them a less than ideal methodology for development or scale-up. The fundamental premise of this approach involves the dissociation of a nitrogen-containing precursor. Energetically the drawbacks of this dissociation are firstly the ultra-high vacuum (UHV) or very high temperature required to break the necessary bonds and secondly, the reformation of the constituent parts, which relies on the competing processes of C-C vs. C-N bond formation.

An adaptation of the CVD route for much lower-temperature deposition was achieved by Liu *et al.*, in a manner which avoided the pitfalls of increased defects, polycrystallinity and low device performance of previous methods.[45] Layers of single-crystal nitrogen-doped graphene were achieved through self-assembly of pyridine molecules on a Cu surface at 300 °C. This route resulted in 16.7 % doping by self-assembling the pyridine molecules at ambient pressure following a mechanism analogous to the competing nucleation and growth cycles well documented for simple CVD processes. Using a homologue of 1,3,5 triazine; cyanuric acid and trinitrophenol, a highly adaptable, low cost and easily accessible method was outlined. At lower temperatures and pressures, and in the absence of metal catalysts nitrogen doped graphene was synthesised in extremely high yields. By exploiting autoclave conditions at 320 °C, batches of 0.2 g could be prepared at a time, exhibiting synthetic yields of approximately 10%.[46] The doping conditions in this case were dominated by pyridinic and pyrollic nitrogen, with a lower proportion of graphitic nitrogen present, as confirmed by X-ray photoelectron spectroscopy (XPS) studies.

Other methods for highly-specific bottom-up syntheses of graphene sheets in milder conditions involve Wurtz-type reductive coupling, as demonstrated in Figure 3.7. This

procedure is based on the activation of alkyl halides using a metal catalyst primarily sodium, silver, zinc or potassium. The reaction of lithium nitride and CCl_4 for example at 120 °C for 12 h can produce the structure seen in Figure 3.7.[47] This follows the accepted mechanism of halogen removal, followed by coupling, assembly and subsequent polymerisation. Over the past few years a coming-together of synthetic and materials expertise has resulted in an interesting family of materials. Known as graphene nanoribbons (GNRs), these materials herald a departure from the simple CVD feedstocks presented hitherto. GNRs hold enormous potential from a molecular electronics and catalysis perspective. To fully understand the methodologies behind their generation it is necessary to focus on the development of on-surface material formation which serves as a foundation to the current work.

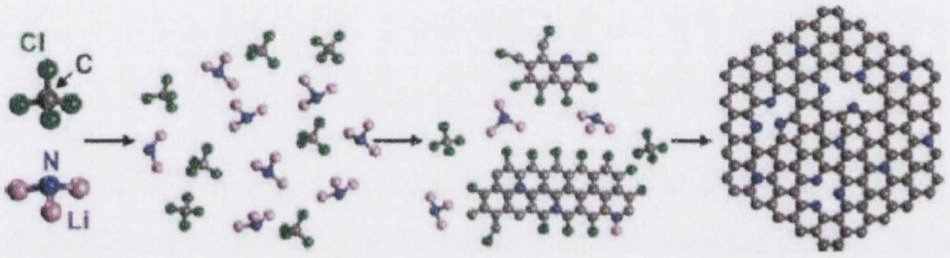

Figure 3.7: N-graphene synthesised via the reaction of CCl_4 and Li_3N.[47]

3.4.4 On-Surface Bond Formation

Although the synthesis of nanoribbons has recently been documented from a host of difference sources, *via* chemical, lithographical and the unzipping of nanotubes, there still remains a paucity of synthetic routes to highly-ordered and chemically defined doped nanoribbons. The past four years have addressed this need and have resulted in an exponential growth of publications in the field of surface-assisted polymerisation with subsequent cyclodehydrogenation, for a wide variety of carbon-based and heteroatom-doped precursors. These methods result in graphitic systems that boast atomic precision, defined width and topography, and are generated by specific polymerisation pathways which are governed by the choice of monomeric precursor. These routes offer enormous potential as low-cost alternatives, by using highly-reactive metallic faces to promote thermal dehalogenation and generate surface stabilised biradical species. Subsequent diffusion then leads to the formation of covalent C-C bonds and results in polymerisation. The desire to combine various monomeric building blocks and bottom-up synthesis has dominated nanofabrication research in recent years. In a bid to draw from developments in nanotechnology, the use of reactive surfaces has been found to offer a viable route to

custom-designed synthesis of well-defined motifs. The original inception of this class of oligomerisation began from much more primitive structures which were developed from Staudinger-type synthesis, with a view to creating 2D and 3D formations, which exhibited reactions at both areal and linear units.

Hawker and Sakamoto wondered if these platforms "could be used for the systematic construction of bulk materials in a true molecular-scale bottom-up approach".[48] Yokoyama *et al.* made inroads in this regard by tuning the surface-supported self-assembly of porphyrin molecules, shown in Figure 3.8 (a), to yield structures which were held together by tuneable non-covalent interactions. The adsorbed molecules were seen to form various length polymers which could be controlled by functionalization. By sublimation from a Knudsen cell in ultra-high vacuum (UHV) various substituted tetraphenylporphyrin molecules were deposited on a Au(111) surface and were seen by scanning tunnelling microscopy (STM) to form clusters, held in place by interactions between CN-NC moieties

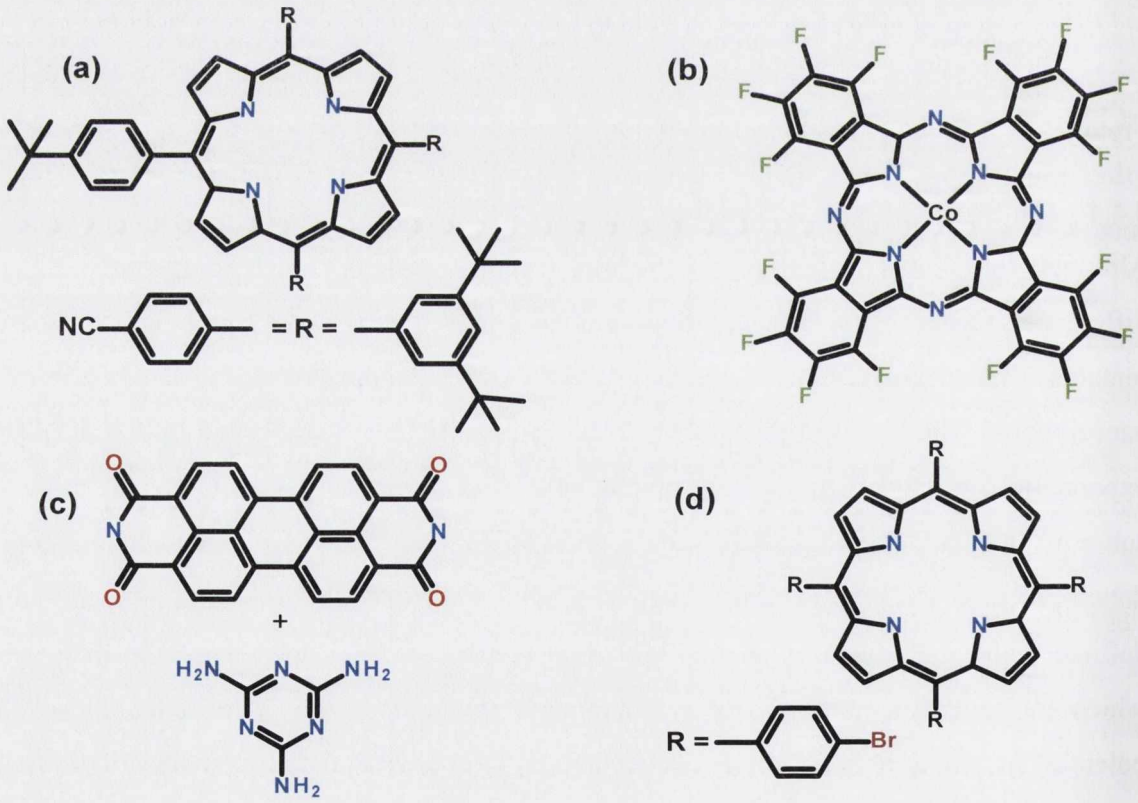

Figure 3.8: Various deposited molecules used as building blocks in the growth of on-surface nanostructures: (a) substituted tertiary-butyl phenylporphyrins used by Yokoyama et al.;[49] *(b) Co(II) hexadeca- fluoro-29H,31H-phthalocyanine;*[50] *(c) co-adsorbed tetracarboxylic acid and 1,3,5 triazine triamine;*[51] *(d) tetra(4-bromophenyl)porphyrin.*[52]

Similar behaviour was observed by Hipps *et al.* for analogous macrocycles such as the one shown in Figure 3.8 (b), which resulted in the growth of nanostructures, held together by long-range H-F interactions.[53] Such hydrogen bonding was also exploited in 2003 by Beton *et al.* in the surface assembly of co-adsorbed perylene tetra-carboxylic di-imide (PTCDI) and melamine which are shown in Figure 3.8 (c).[51] The geometries of these two molecules resulted in one molecule of melamine being surrounded by three PTCDI molecules. This structure was stabilised with multiple hydrogen bonding sites existing between the amino protons on the central molecule and the carboxylic groups of the outer three molecules.

The true potential of this route, as a method of GNR formation, was first predicted in a publication by Stefan Hecht wherein he assessed the various approaches that would need to be developed to offer feasibility to the methodology of surface-assisted synthesis.[54] The threefold approach he postulated would require: 1) a surface that could be activated by inducing a chemical change, 2) molecules that could self-organise on a surface and 3) a resulting network which was formally covalently bonded and adsorbed on the surface. In 2007 Hecht *et al.* returned with the seminal Nature publication which paved the way for the intelligent use of substituted molecules as building blocks for nanoscale architectures.[52] By using various brominated tetraphenylpoyphyrins (TPP), an example of which is shown in Figure 3.8 (d), it was seen that various methods of activation could be achieved by exploiting the lower energy cleavage of the carbon-halogen bond, to achieve dissociation. Different degrees of substitution at the various vertices of the TPP were observed by STM to have a profound effect on the geometrical nature of the subsequent networks formed. Lateral manipulation using STM was then able to differentiate between dimers, trimers and more substituted networks, according to the intermolecular/intramolecular forces observed. This heralded the arrival of true surface-enhanced oligomerisation. Rieder and co-workers subsequently found that on a reactive Cu(111) adaptation of a surface-based Ullmann reaction could induce a sufficient bias for the fission of a C-I bond which would result in a reactive phenyl radical.[55] Homocoupling of two of these molecules furnished a viable method for the synthesis of primitive nanostructures, albeit *via* a laborious molecule-by-molecule approach.

In 2008, Mullen *et al.* also entered the realm of 2D graphene nanoribbons with boronic acid substituted hexaphenylbenzenes. Using the novel method of Suzuki-Miyaura polymerisation, coupling could be achieved in 75% yield to yield nanoribbons of up to 12

nm wide. To create fully condensed and conjugated structures it was necessary to perform cyclodehydrogenation under the usual solution-based $FeCl_3$ conditions. SEM, TEM and STM studies could then be performed on these materials, an example of which is shown in Figure 3.9 once drop-cast onto substrates.[56]

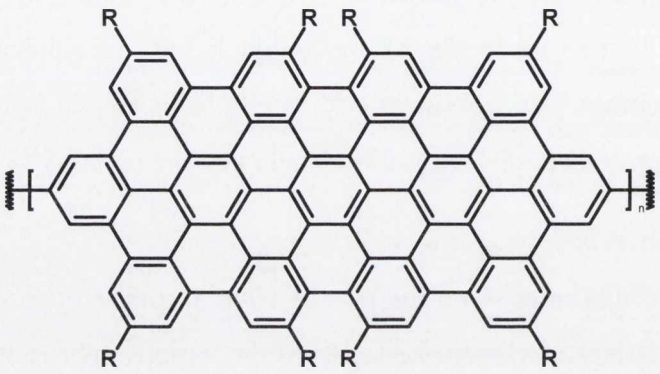

Figure 3.9: Fully conjugated ribbons generated by Mullen and coworkers.[56]

Developing this manner of coupling, Matena *et al.* investigated on-surface C-C bond formation, by studying the reactivity of tetraazaperylenes on Cu(111), as shown in Figure 3.10. They observed a two-step process: the first, at 150 °C saw the deposition of submonolayers to form molecular networks on the surface, with each monomer coordinating to the Cu layer through lone pairs on the nitrogen atoms. By increasing the temperature to 250 °C a second-step showed the formation of oligomeric and polymeric chains. These chains, represented in Figure 3.10 indicate that the reaction between monomers in a Wanzlick-like coupling could dominate over interactions with the metal surface.

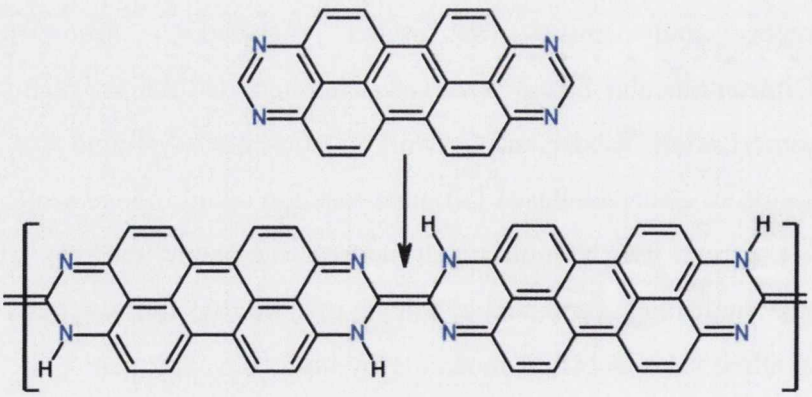

Figure 3.10: Double tautomerization of tetraazaperopyrene to form dimers and subsequent molecular networks.[57]

The materials shown in this section all displayed the intelligent adaptation of well-defined coupling reactions. The methodologies outlined laid the foundations for the exciting work which would follow. In early 2009, Rosei and Perepichka published an article in Science which accurately assessed and predicted the exponential growth in this area which would soon follow.[58] They assessed earlier methodologies using classical solution-based techniques and deemed the resulting rigid, planar organic polymers to be too insoluble for further processing or characterisation. They believed that the development of topological polymerisation held the key to successful formation of defect-free polymers. It was predicted that the adaptation of solution polymerization to surfaces would encounter two distinct challenges: 1) the ability to alter the reactivity of the deposited monomer and 2) the control of the propagated reactions by diffusion. Within twelve months of their publication, the scientific community had heeded such advice and followed suit with a constantly-developing stream of publications which used highly-reactive single-crystal metallic faces to catalyse the polymerisation of simple, symmetrical and derivitisable monomers *via* highly-documented modes of reticular synthesis.

3.4.5 On-Surface Polymerisation

In 2009, Lackinger *et al.* exploited the predicted conditions through the synthesis of 2D covalent organic frameworks of the triangular 1,3,5-tris(4-bromophenyl)benzene, shown in Figure 3.11.[59] Using ultra high vacuum (UHV) and a Cu catalytic substrate, as adapted from well documented solution chemistry, the monomers could be aligned to form protopolymers on the surface. Protopolymers are a family of materials which can align upon a surface, forming *quasi*-networks, without the generation of formal chemical bonds. At elevated temperatures, the phenyl-phenyl bond distance was seen to decrease in the order of 0.12 nm, corresponding to the likely formation of covalent linkages. The generation of radicals at slightly elevated temperatures result in three reactive sites at the apexes of the triangular building unit, leading to the formation of linear polymers in addition to pentagons, hexagons and heptagons. STM could then be used to provide information about the porous membranes formed. Interestingly, the activity of a single-crystal metal substrate was observed to play a very important role in the formation of polymers, due to its varied reactivity toward C-Br fission. The use of graphite crystal faces would result in an endothermic reaction for homolysis of physisorbed halides, thereby resulting in a highly unfavoured outcome. Also notable was the understanding gleaned about slightly less reactive substrates, such as Au(111) which require increased temperatures for thermal activation. Ultimately, for other systems, this can result in

activation occurring during sublimation, within the crucible. For 4-bromophenyl benzene however this was achieved after deposition, at temperatures between 140-160 °C, considerably lower than the quoted temperature of decomposition at 250 °C, as measured using TGA.

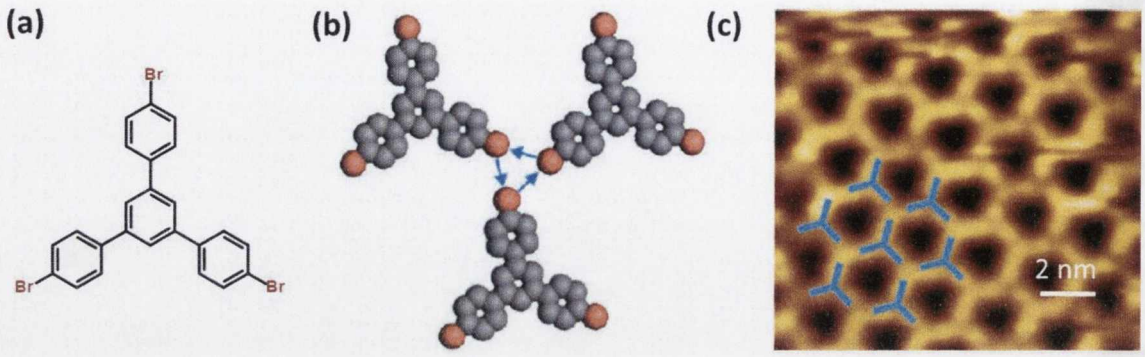

Figure 3.11: (a) deposition of 1,3,5-tris(4-bromophenyl)benzene; (b) formation of protopolymers on Cu(111) at 80 K; (c) self-assembly into a larger network, as imaged by STM.[60]

In a subsequent Journal of Physical Chemistry publication Lackinger *et al.* provided additional insights into the role of reactive substrates on the progression of the reaction.[60] Interestingly, they found that for face-centered cubic (FCC) metals, the potential energy surface is more highly corrugated on (110) than (111) surfaces. Therefore a Ag(110), which showed similar protopolymer formation as Cu(111) at room temperature, did not result in any supramolecular order at low temperature. It was concluded that thermally activated surface diffusion can be limited more easily on (110) surfaces. From this a general understanding can be deduced for the reactivity of planar π-conjugated adsorbates. It is believed that the new hybridised states are formed from the interaction of π electrons with the s- and d- sites of the catalytic metal. As frontier molecular orbitals are changed upon charge transfer between the aromatic and the transition metal surface, partial filling of the π* orbital occurs. As this alone could not yield C-Br homolysis, it is proposed by Lackinger *et al.* that an energy transfer from π* -α* facilitates the C-Br bond homolysis. Previous work by Kimura and Takamuku on aryl halides supports this deduction, justified by the transfer of an electron from the newly-occupied π* to the C-Br antibonding orbital.[61] This research was subsequently supported by Mullen *et al.*, predominantly for Cu(111) substrates, using *ab initio* calculations which predicted the order and mode of reaction for the six-step coupling observed for a cyclohexaphenylene molecule.[62]

3.4.6 Controlled Cyclisation

The polymerisation of substituted partially-fused polyaromatics had developed significantly over a short period of time. However, research which would prove integral to the formation of fused nanostructures had sat dormant for almost a decade. In 1999 Mullen *et al.* had published work on the cyclodehydrogenation and planarization of substituted hexaphenylbenzenes on metal surfaces. With limitations on scale, synthesis and characterisation the communication remained without any significant follow-up. Their work on adsorbed molecules on Cu(111) showed the possibility for thermally induced cyclodehydrogenation as a feasible route towards substituted condensed hexabenzocoronenes. In the years that followed, a greater understanding of on-surface polymerisation meant that the next rational step towards fully-condensed nanographenes would be to bridge the gap to include an all-encompassing procedure that resulted in deposition, polymerisation and complete cyclisation.

At the end of the last decade surface-catalysed cyclodehydrogenation saw a renaissance, supported greatly by advances in *in situ* methods of characterisation and moreover, the ability to successfully model reaction mechanisms for the single molecule and catalytic surface. Cai *et al.* published a watershed study on the bottom-up fabrication of nanoribbons.[63] This seminal work developed previous research surrounding the oligomerisation of small molecules and successfully yielded the deposition and subsequent polymerisation of significantly larger polyaromatics, namely dibromo bianthryl. The thermal dehalogenation of the deposited monomers, achieved at 250 °C resulted in species which diffused along the surface. Annealing the system for a second time at 400 °C resulted in completely aromatic ribbons of a finite width, which could be confirmed by Raman spectroscopy through examining the D (defect-derived) and G (graphitic structure-derived) bands. Most impressive in this work was the development of new polyphenylenes suitable for the generation of chevron-like ribbons. Deposition of dibromo tetraphenyltriphenylene resulted in similar colligation as seen in the linear molecules; however upon the formation of chains it was clear that the alternate molecules would have to flip to opposite orientations to accommodate steric requirements.

Using STM, XPS Martin-Gago *et al.* investigated thermally induced cyclisations on Pt(111) and Au(111) upon annealing triangular polyaromatics.[62] Most interestingly, it was observed from the author's computational simulations that dispersive interactions between the substrate and adsorbate allowed various inert surfaces to induce more planarised

conformations. The observations in both of these papers served to fill an important knowledge gap for surface-assisted methodologies. In addition, they served to open the floodgates to a stream of publications which now heralded the ability to produce fully condensed matter from surface assisted reactions, which had recently grown to include carbon oligomerization, Ullmann coupling and imidization.

3.5 Nitrogen-Containing Nanoribbons

It was fitting that the first report of monomer doping in the formation of precise graphene nanoribbons was again published by Hecht *et al.* in 2013.[64] By using pyridyl substituted phenanthrene-based polyphenylenes deposited on Au(111), they documented a two-step process involved in the generation of N-doped nanoribbons. The first step, which was initiated by heating to 250 °C, lead to desorption of monomers, followed by dehalogenation and coupling. The second step at 450 °C caused on-surface cyclodehydrogenation, resulting in fused chevron-shaped nitrogen doped nanoribbons. Using high-resolution electron energy loss spectroscopy (HREELS) it was possible to follow the fission of C-Br, the torsion induced by steric crowding of phenyl rings and to finally document the (C-H) bending modes and their subsequent disappearance as the pendant phenyls fuse to form part of the GNR. The total coverage of nanoribbons was estimated to be approximately 2/3 of a monolayer.

While some groups concentrated on the development of monomeric precursors, research pertaining to enhancing the reactivity of surfaces with a view to directing synthesis was being performed by Pinardi *et al.*, most evident in the ACS Nano publication from 2013.[65] Tailoring of on-surface dehydrogenation (either cyclodehydrogenation or dehydrogenative polymerisation) could be achieved by consideration of adsorbate-surface interactions. The strength of interaction between the adsorbate and metal surface proved most important in the direction of bond formation. As the processes appear to be strongly diffusion controlled, the nature of the coupling to single crystals such as Pt(111), Au(111), Cu(110) and Cu(111) determines the ease with which an adsorbed molecule may diffuse upon a surface. On Pt(111) diffusion is blocked, resulting in intermolecular cyclodehydrogenation. For the other metal faces however a combination of cyclodehydrogenation and polymerization both occur. In a follow-up publication, the possibility of even inducing formal C-Pt bonds on the periphery of fused cyclic polyaromatics was demonstrated. A combination of UHV-STM was used to follow the

intramolecular cyclodehydrogenation and subsequent metal surface bonding, resulting in a dome-shaped molecule, shown in Figure 3.12 (c).

Also noteworthy is the experimental and computational data pertaining to the order of cyclodehydrogenation. The energy to form an aza-benzene bond is seen to be less than that to form an arene-arene bond, therefore agreeing with previous observations in the solution phase. This means that cyclisation occurs away from the nitrogen containing rings (as shown in Figure 3.12), with the final bond closure occurring between both pyridine rings.

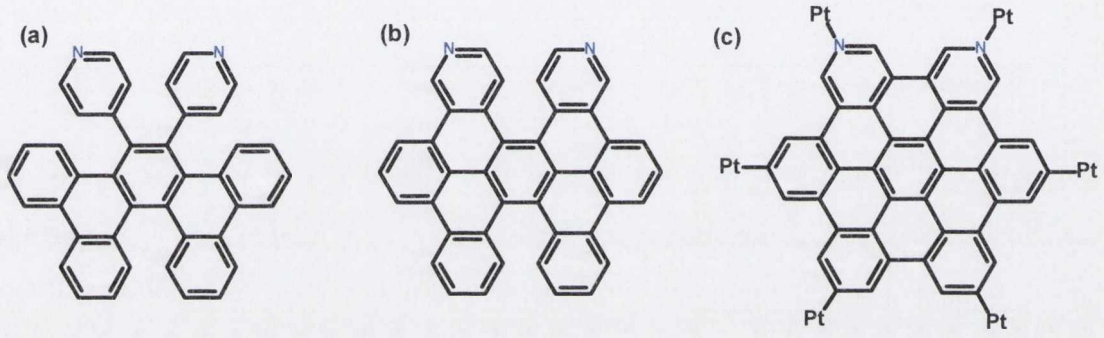

Figure 3.12: Various stages of cyclisation observed by Martin-Gago et al.[66] for 2,5 diazahexabenzocoronene: (a) demonstrates cyclisation beginning away from the nitrogen-containing rings; (b) 2/3 cyclised; (c) fully cyclised surface-bound molecule.

In 2014, interesting work by Cai *et al.* using 5,5'-(6,11-dibromo-1,4-diphenyltriphenylene-2,3-diyl) dipyrimidine, as shown in Figure 3.13, documented the introduction of pyrimidyl substitution to chevron-type GNRs.[67]

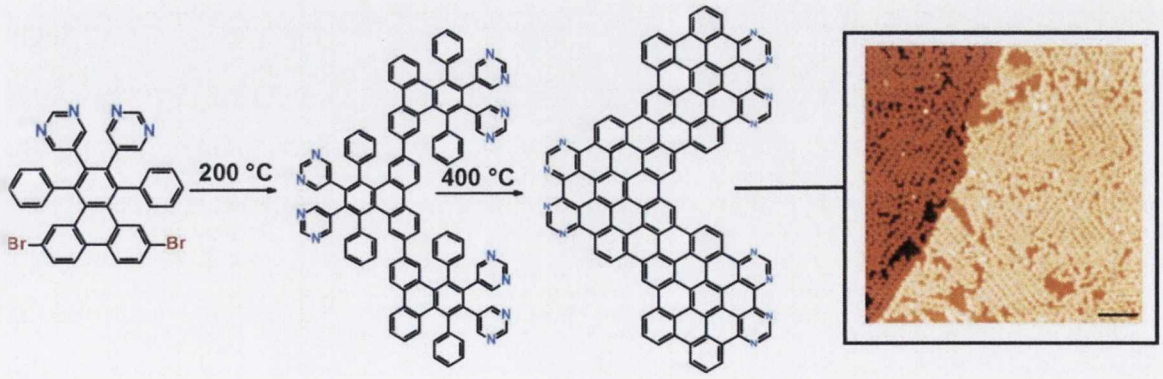

Figure 3.13: On surface polymerisation of 5,5'-(6,11-dibromo-1,4-diphenyltriphenylene-2,3-diyl) dipyrimidine to form covalent bonds upon dehalogenation at 200 °C which are fully condensed into GNRs at 400 °C. Inset shows STM image on Au(111) at T = 35 K (Scale bar 10 nm).[67]

This was the first publication which truly focused on the on-surface orientation of nitrogen-containing molecules. Using STM Cai *et al.* showed it was possible to assess the different packing caused by N-H interactions at the pyrimidine ring relative to pristine all-carbon GNRs. These interactions result in significantly increased aggregation at both high and low coverages and directly influence the manner in which adjacent ribbons align. This was addressed in much greater detail by Zhang *et al.* who provided a level of direct imaging and characterisation of electronic properties which had not been previously seen.[68] By evaporation of an analogous 6,11-dibromo-1,4-diphenyl-2,3-dipyridyltriphenylene compound at 180 °C onto Au(111) surface, it was possible to use Ullmann-like reactions to polymerise the precursor monomers. It was again possible to identify growth along the herringbone structure and thereby show preferential occupation of FCC regions and a complete lack of occupation of the lower-adsorption energy hexagonally-close-packed (HCP) sites. It was also possible to carryout full cyclodehydrogenation with an annealing process at 450 °C. What proved most interesting from this research was the observations made pertaining to increasing monomer surface-coverage; as coverage is increased the result is highly disordered alignment and very short oligomers. It appears that the high surface coverage serves to significantly limit diffusion and rotation of the monomers on the surface. As a monomer can therefore only couple with its nearest neighbours it is only possible to form much shorter oligomers.

The bulk syntheses of doped nanographenes began with large scale and poor control, predictability and reproducibility. The methodology of using tailored molecules with distinct functionalities to direct the synthesis has yielded new families of doped graphenes. These can be easily characterised by the defined nature imposed on them by their precursors. However most routes outlined still require the use of UHV, high-temperatures and highly-reactive single crystal faces as a requirement for C-C bond formation and subsequent dehydrogenation. Such conditions may ultimately limit the possibilities of application, unless it is possible to overcome the restrictions of prohibitive temperature, scale and 2-dimensional confinement constraints. If this can be achieved it would be possible to develop synthetic routes to reach gram-scale quantities of heteroatom-feedstocks. The following sections document the endeavours made in this body of work to generate novel structures which are suitable for this purpose. By developing new routes to bond formation, oligomerisation and polymerisation it will then be possible to try and extend the use of functionalised N-substituted polyaromatics, from materials fabrication to potential application.

3.6 Results and Discussion

3.6.1 Synthesis

For the realisation of nanostructure formation using pyrimidyl-substituted polyphenylenes it is necessary to synthesise molecules which possess a fused core, in addition to peripheral halogen substituents. The presence of partial cyclodehydrogenation serves to yield a more thermally and chemically stable molecule. The directed substitution on the pendant phenyl rings, as outlined in previous sections, offers positions at which other reactive molecules can be joined together in a molecular patchwork. All methods of cyclodehydrogenation have proved ineffective towards brominated polyphenylenes which possess nitrogen substitution. $AlCl_3$, $MoCl_5$ and $FeCl_3$ have all returned unreacted starting materials. However, using elemental bromine under controlled conditions, it was possible to demonstrate induced intramolecular bond formation, in addition to controlled bromination at the *para* positions of pendant unsubstituted phenyl rings. This resulted in a range of brominated pyrimidine-fused PAHs. Figure 3.14 shows the mass spectrum of the reaction mixture, comprising 1-pyrimidyl-2,3,4,5,6-pentaphenylbenzene and elemental bromine after 10 minutes. At room temperature no remaining uncyclised polyphenylene is observed after this reaction time.

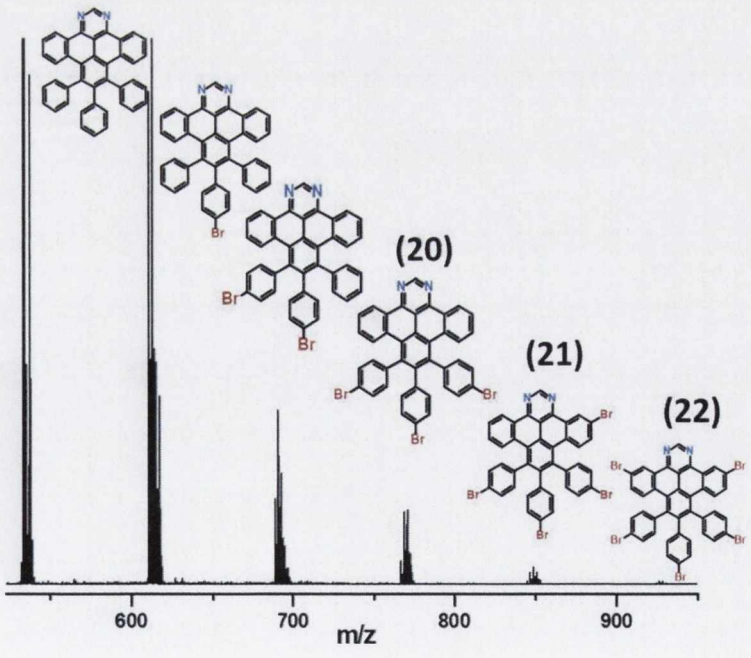

*Figure 3.14: Mass spectrum of 1-pyrimidyl-2,3,4,5,6-pentaphenylbenzene polyphenylene (**1**) and bromine after 10 minutes, in an open vessel at room temperature.*

In a similar fashion to the *in situ* characterisation used in Chapter 2 it was possible to perform NMR studies, which allow for the assessment of the time scale and reaction conditions necessary for the formation of brominated species. Figure 3.15 shows the relevant iterations of the reaction as characterized by ^{1}H NMR spectroscopy. Again, using a $1x10^{-8}$ M solution of 1-pyrimidyl-2,3,4,5,6-pentaphenylbenzene in $CDCl_3$ with 100 equivalents of bromine it was possible to extend the reaction time to cater for subsequent bromination around the periphery. This confirmed the presence of three dominant species over a period of 25 minutes. The first species, as presented in Chapter 2 is the 1/3 fused molecule, whose formation can be tracked from t=0 until t=9 minutes. Subsequent formation of the tribrominated (**20**) and pentabrominated (**22**) species is then observed.

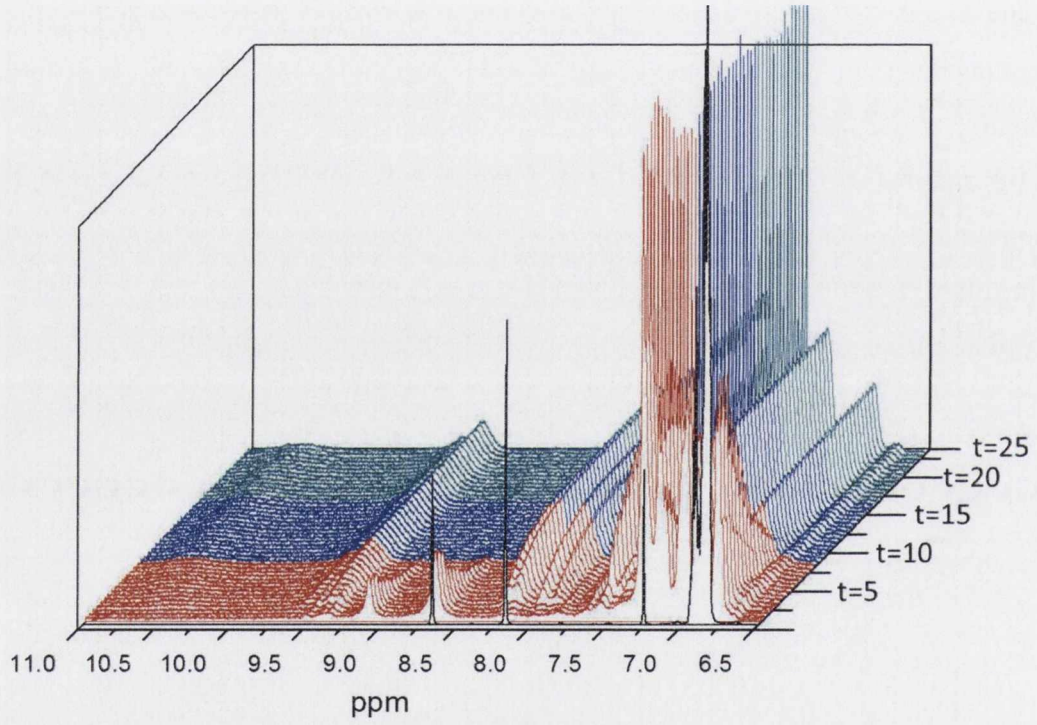

Figure 3.15: In-situ time-resolved ^{1}H NMR spectrum of a $1x10^{-8}$ M solution of 1-pyrimidyl-2,3,4,5,6-pentaphenylbenzene in $CDCl_3$, upon the addition of 100 equivalents of bromine.

3.6.2 Modification of Reaction Conditions

Returning to large scale it was then possible to control the experiment using either time or temperature to direct the formation of the main species. Isolation of the mono and dibrominated intermediates was also possible, albeit in extremely low yields. Chapter 2 outlined that in changing the reaction conditions (to increased pressure and temperature in toluene), only the formation of the fused product could be achieved. In a similar fashion,

the synthesis of the tri and pentasubstituted analogues could also be tailored here to dramatically increase their respective yields and eliminate the formation of side-products. Using neat bromine, with a reduced reaction time of 10-15 minutes it was possible to isolate **20**. Similarly, on changing the reaction conditions to reflux in chloroform, considerably higher proportions of **22** could be achieved, as outlined in Scheme 3.2

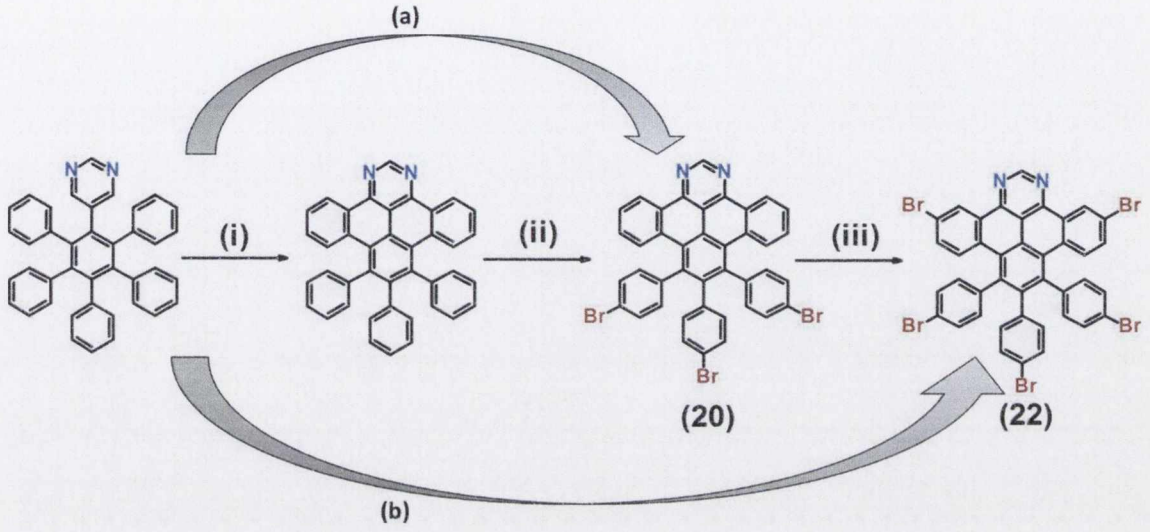

*Scheme 3.2: Synthetic scheme for the formation of **20** and **22**: (i) Br_2, RT, 10 mins, <5%; (ii) Br_2, RT, 20 mins,<10%; (iii) Br_2, >35mins, <10%. Direct routes: (a) Br_2, RT, 25 mins (80%); (b) Br_2, $CHCl_3$, reflux (50%).*

Figure 3.16 shows the individual ^1H NMR spectra of the isolated species, which are colour coded with respect to the *in situ* experiments in Figure 3.15. An overall downfield shift is seen in the *in situ* experiments, most likely as a result of high concentrations of HBr being formed. Overlaying the four spectra, as seen in Figure 3.16 therefore allows for direct comparison of the isolated products. The initial downfield shift upon cyclisation has been discussed previously. For **20** this is also coupled with a simplification of the spectrum caused by *para* bromination of the three pendant phenyl rings. Subsequent bromination of the dibenzoperimidine core to yield **22** results in an even more simplified spectrum. The doublet at δ = 9.4 ppm now appears again as a singlet, as bromination of the 4-spin system inhibits any long-range coupling. The aromatic region from δ = 6.0 - 7.5 ppm is consistent with this simplification, as the remaining signals appear as six doublets. Full NMR assignment is presented in Section 3.6.3.

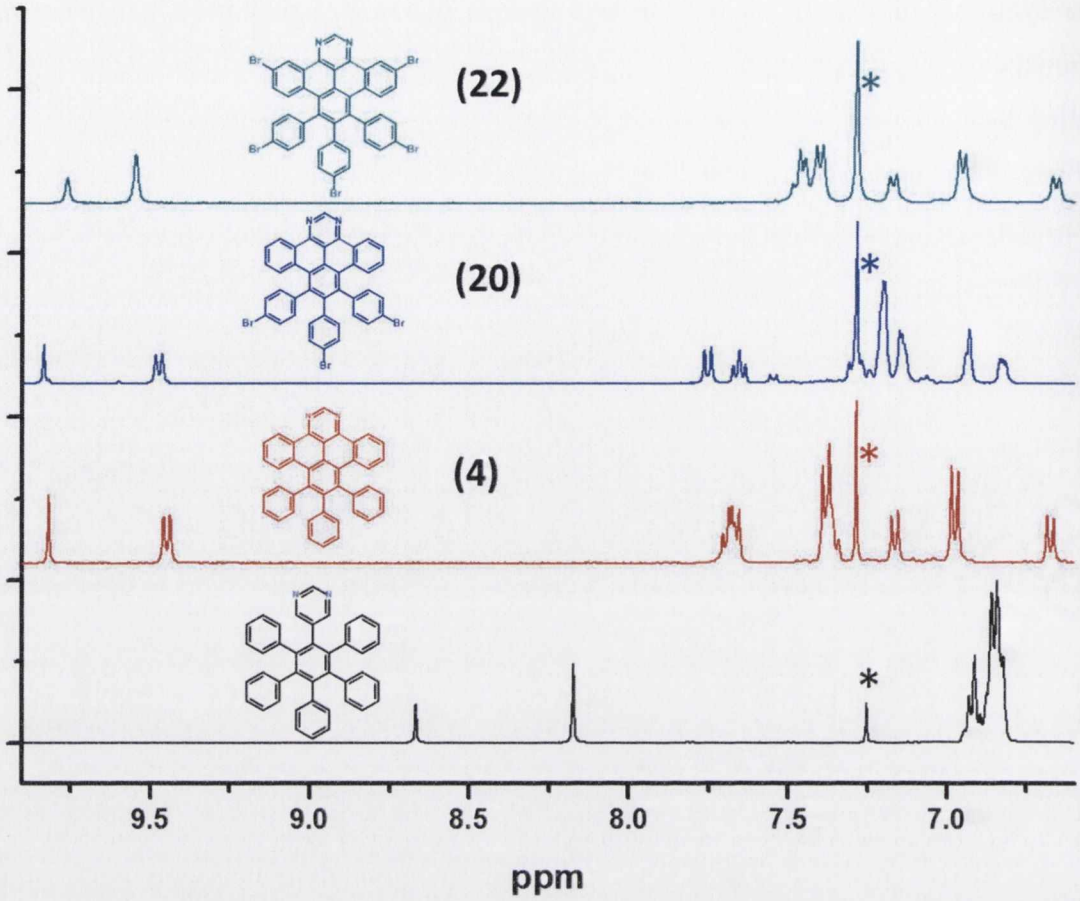

*Figure 3.16: ^1H NMR spectra of the isolated products **4**, **20**, **22** in $CDCl_3$ at room temperature. Asterisk denotes $CDCl_3$ solvent peak.*

Slow diffusion of **20** from deuterated chloroform or dichloromethane yielded two sets of crystals suitable for single-crystal X-ray Diffraction (XRD). Both sets crystallised in the triclinic $P\bar{1}$ space group, with Z = 2 and one dibenzoperimidine molecule per asymmetric unit, with a $CDCl_3$ or $CHCl_2$ solvent molecule in each. The first structure was solved and refined as $C_{41}H_{21}DBr_3Cl_3N_2$. The final anisotropic full-matrix least-squares refinement on F^2 with 458 variables converged at R1 = 3.86%, for the observed data and wR2 = 11.31% for all data. The goodness-of-fit was 1.092. Figure 3.17 (a) shows the ORTEP structure of **20** with thermal ellipsoids at 50% probability, confirming *para* substitution by the bromine atoms on the three pendant phenyl rings. Figure 3.17 (b) and (c) are shown along the b and c axes respectively and highlight the curved nature of the dibenzoperimidine moiety. Figure 3.17 (b) shows that, in a similar manner to the unsubstituted analogue, the pyrimidine ring is raised from the plane by approximately 20°. In a similar fashion, the dibenzo moieties are raised at the edges of the dibenzo-perimidine by 12°, seen clearly in Figure 3.17 (c).

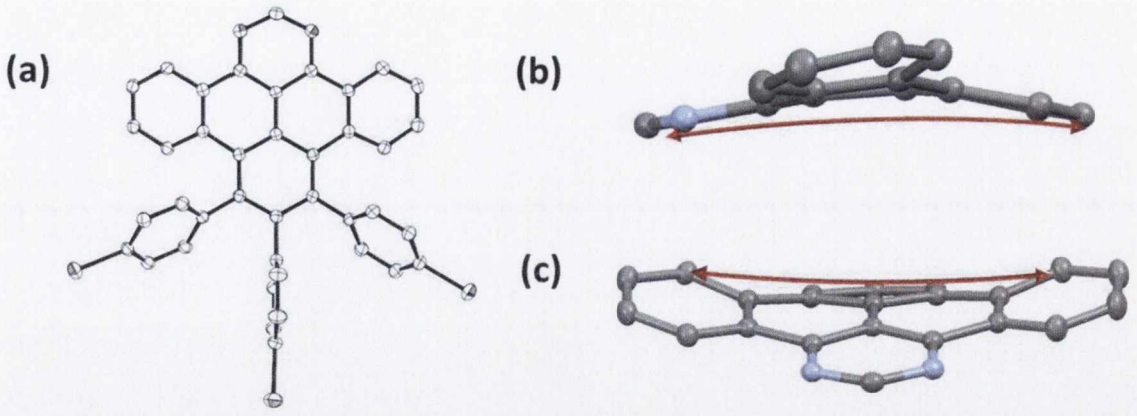

Figure 3.17: Representations of the single-crystal XRD structure of ***20****: (a) ORTEP representation of* ***20****, hydrogen atoms and solvent molecules removed for clarity; (b) and (c) are viewed along the b axis and c axis respectively, with hydrogen atoms and pendant phenyl rings removed for clarity. Thermal ellipsoids are shown at 50% probability. Blue represents nitrogen atoms.*

When crystallised with dichloromethane, molecules of **20** adopt a dimeric behaviour with head to tail stacking between adjacent rows, as seen in Figure 3.18 (a). Molecules overlap at the flat dibenzoperimidine moiety, with a distance of 4.101 Å between layers.

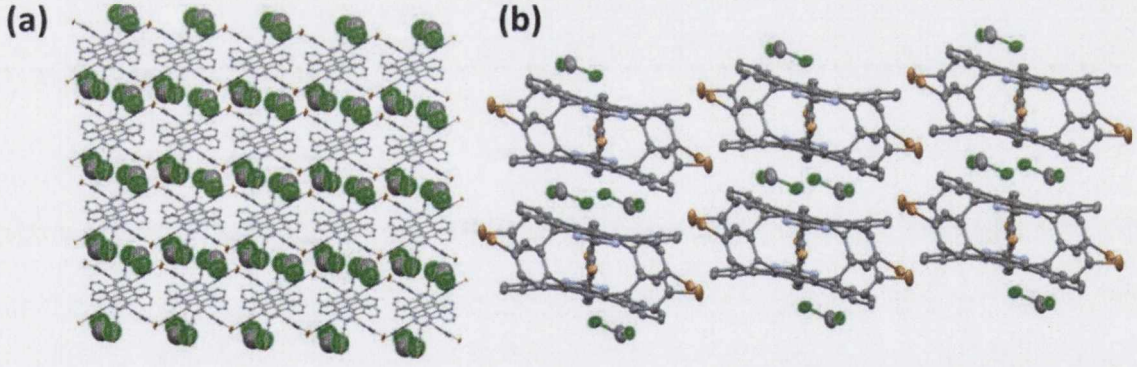

Figure 3.18: Crystal packing observed in ***20****: (a) along the a axis, with solvent molecules represented in space filling mode; (b) along the c axis. Thermal ellipsoids shown at 50% probability, orange: bromine, green: chlorine, blue: nitrogen.*

Weak H-H and N-H interactions from the pyrimidine ring to the central pendant phenyl of the next molecule play an important role in the crystal lattice. Solvent interactions between the chlorine atoms and bromine substituents on adjacent molecules ensure that the solvent remains in the curved void between the interacting pairs of molecules, as seen in Figure 3.18 (b).

Similarly, crystallisation of **22** from dichloromethane yielded crystals suitable for single-crystal XRD. **22** also crystallised in the Pī space group, with two pentabrominated molecules and a dichloromethane solvent molecule in the asymmetric unit. Bromination onto the dibenzoperimidine core serves to reduce the bend across the molecule. Interestingly, both molecules in the asymmetric unit adopt a perpendicular orientation to each other, which results in the classic herringbone packing motif exhibited in Figure 3.19 (b). Interactions between the central ring of one molecule and the central pendant phenyl ring of its perpendicular counterpart ensure that this orientation is maintained. Hydrogen bonding from the pyrimidyl nitrogen atoms to the protons on neighbouring phenyl rings results in head-to-tail packing, with an intermolecular distance of 3.867 Å between molecules in the central channel, which is highlighted in red in Figure 3.19 (b).

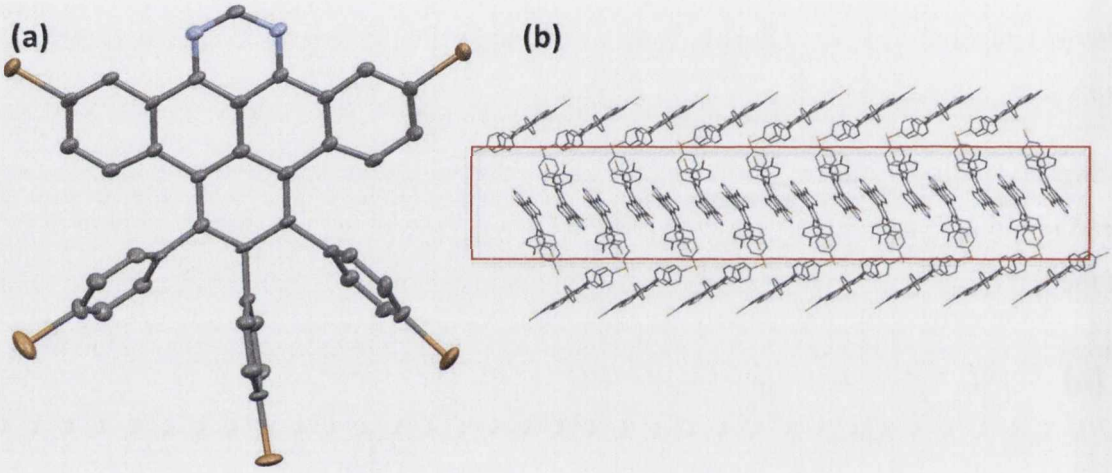

*Figure 3.19: Representations of the crystal structure of **22**: (a) thermal ellipsoids are shown at 50% probability; (b) expanded lattice viewed shown along the b axis. Hydrogen atoms and solvent molecules are removed for clarity; orange: bromine, blue: nitrogen.*

3.6.3 Full NMR Assignment

An illustration of the NMR assignment process is presented for **20** in Figure 3.20. It is indicative of both higher symmetry structures. Similar to its fused analogue (**4**), the assignment of the ^{1}H NMR signals for the dibenzoperimidine can be easily achieved using a 1D selective TOCSY experiment, based on interactions with the most downfield doublet at δ = 9.45 ppm which corresponds to H4. Accordingly, the doublet at δ = 7.69 ppm, integrating for 2H, with a coupling constant of J = 7.4 Hz can be assigned to H7. An NOE experiment from this signal can be used to assign signals at δ = 6.9 and 7.4 ppm, each integrating for 4 protons respectively. 2D HSQC and HMBC experiments then allow for easy identification of the ^{13}C signals. C10 and C13 can be assigned to signals at δ = 121.8

ppm and δ = 120.32 ppm and are characteristic of C-Br quaternary shifts. These can be used quite accurately to confirm the degree of bromination on these substrates.

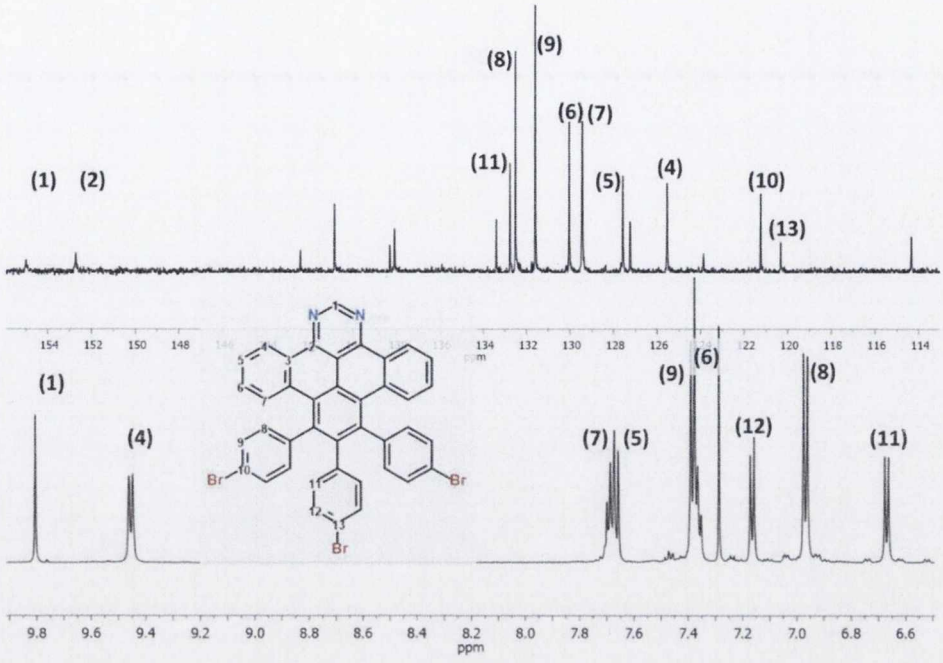

*Figure 3.20: ^{13}C NMR and ^{1}H NMR assignment of **20** ($CDCl_3$, RT, 151 MHz, 600 MHz).*

Full NMR assignment can also be achieved for the pentabrominated **22**. Table 3.3 shows a comparison between ^{1}H and ^{13}C signals for both compounds and their respective polyphenylene precursors.

*Table 3.3: ^{1}H NMR (blue) and ^{13}C NMR (grey) shifts of **20** and **22** ($CDCl_3$, RT, 600/151 MHz respectively). Most significant changes highlighted in red.*

Proton	H1	H4	H5	H6	H7	H8	H9	H11	H12
20 (ppm)	9.80	9.45	7.67	7.37	7.69	6.96	7.38	6.67	7.20
22 (ppm)	9.81	9.59	-	7.45	7.51	6.96	7.41	6.66	7.17
Carbon	**C1**	**C4**	**C5**	**C6**	**C7**	**C8**	**C9**	**C11**	**C12**
20 (ppm)	154.9	125.5	127.5	129.4	129.5	132.6	131.6	132.7	130.0
22 (ppm)	155.7	128.1	122.4	131.0	130.79	132.3	132.0	132.7	130.2

Decreasing the time of reflux can also be used to isolate the tetrabrominated (**21**) which was also characterised effectively using NMR. Although the molecule is asymmetric in nature, 1D selective TOCSY experiments can be used to easily assign the 3 and 4 spin

systems. H4 and H4' can be assigned accordingly, and are supported by the nature of coupling observed, exhibiting ^{3}J and ^{4}J coupling respectively. As before, through-space experiments from the peripheries of the dibenzoperimidine core can be used to assign signals from the 3 pendant phenyl rings.

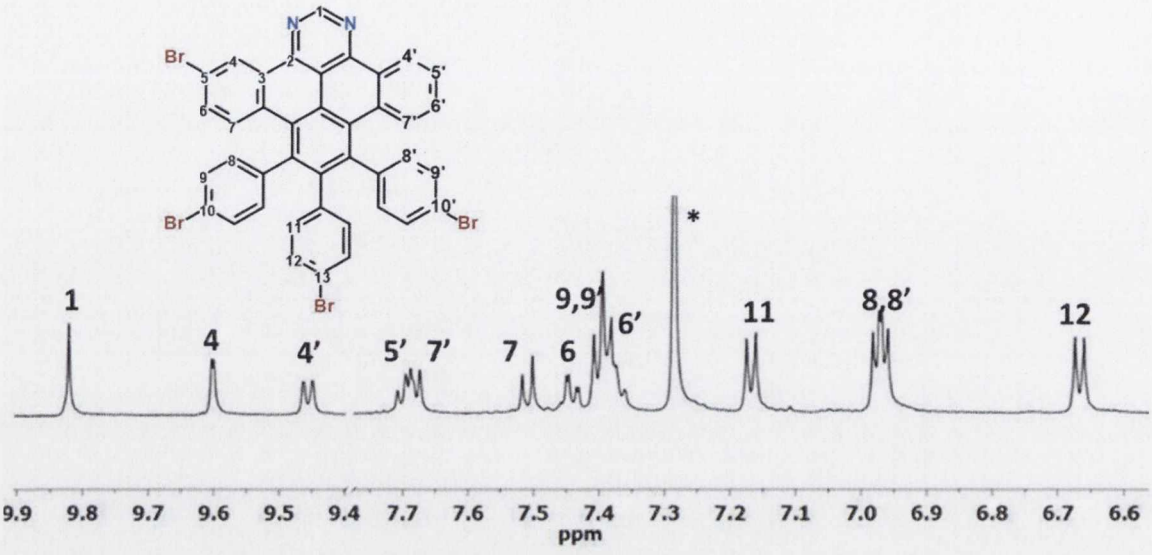

*Figure 3.21: ^{1}H NMR spectral assignment of **21** ($CDCl_3$, RT, 600 MHz). Asterisk denotes $CDCl_3$ solvent peak.*

Separation and purification of this product not only signifies isolation of stepwise bromination intermediates but also serves as interesting proof for the ability to tailor one reaction successfully to target different products. This demonstrates a gateway reaction that offers an unprecedented and one-step process to partially-fused and bromo-functionalized N-doped polyaromatics. These are suitable for chemical functionalization and/or further aromatization using existing routes. The work impacts on recent publications that mark the point of convergence between top-down and bottom-up synthetic routes to doped nanoribbons. The arrival of a metal-free reagent to form brominated precursors with precise substitution patterns provides new opportunities for the control of the symmetry and edge-characteristics of graphitic materials. This development could potentially broaden their application in electronic devices. Under the right conditions, such materials can be intermolecularly stitched together to form a patchwork, such as a holey graphene sheet or nanoribbon. The new selective fusion and bromination of highly aromatic di-aza and tetra-aza PAHs presented here also introduces a high-yielding methodology to deliver novel ligands. The systems isolated to date have been used to make orthometallated and N-coordinated transition metal complexes with

interesting photophysical applications.[69] These compounds serve as a perfect platform to undertake a materials study, to assess the potential that molecules of this nature may have in the growth of larger structures. Through the use of different stimuli and *in situ* techniques the first study of its kind on nitrogen-substituted polyaromatics, spanning from synthesis to application, was attempted.

3.7 Novel Modes of Material Development

3.7.1 Homolytic Fission

The past decade has seen an exponential growth in the use of microscopy to image single molecules. Scanning tunnelling microscopy (STM) and atomic force microscopy (AFM) in particular have proven useful in this regard but are of less assistance in surveying large areas. Transmitting electron microscopy (TEM) on the other hand is very useful in this regard, but has seen very few instances of single molecule imaging. Depending on the substrate surface, imaging of organic hexabenzocoronene-like molecules, or nitrogen-substituted analogues can prove extremely difficult, due to contrast issues between a carbon substrate and the organic molecule. Similarly, differentiating between cofacial aggregates and layers of single molecules can prove problematic. Fundamentally, we can consider the electron-nucleus cross section relationship either by Rutherford incoherent elastic scattering or by low-angle elastic scattering. The introduction of a heavy atom into such a molecule would increase the nucleus cross section, resulting in a higher intensity signal. This relationship also holds true for TEM, in which Z-imaging also relies on Rutherford scattering. The introduction of a significantly heavier atom to a HBC-type molecule could serve to increase contrast and could be used as a possible point of reference. Inadvertent success in this regard was achieved by Jones *et al.* in a study of nanomorphology of fluorinated HBC molecules used in heterojunction fullerene blends. Under the high energy conditions of electron-beam radiation the stability of the C-F bond makes it a perfect candidate for such a purpose.[70] The ability to image a polyaromatic of this nature would alone prove a very exciting progression. Additionally, the addition of halogen functionality holds added potential for intriguing results.

3.7.2 Probing Bonds with Irradiation

For weaker carbon-halogen bonds, the ability to induce bond fission under certain circumstances has long since been a staple of synthetic chemistry. Homolytic fission, often induced by irradiation or other stimuli can be used to generate a reactive carbocation and negative halide ion. As the energy of the carbon-halogen bond decreases down the

group, the ease with which fission can be achieved follows the order of I > Br > Cl > F. This behaviour has been the foundation of cross-linking polymers for decades. Recently however the use of electron beams as a high energy form of irradiation have been exploited to great effect for a wide range of cross-linking purposes.[71] The halogenated compounds presented in this thesis could serve as ideal platforms for exploitation in this regard. To begin, a less complex system was called for.

As a preliminary assessment of the reactivity of halogenated polyaromatics in this body of work, a natural starting point was found in an all carbon framework with a single site of halogen substitution; iodo-hexabenzocoronene (IHBC). Such a molecule, served as an accurate model for similar platforms, with substitution that can react under given stimuli. The crystal structure, as presented in Figure 3.22, shows that IHBC is an accurate comparator to *tertiary*-butyl substituted hexabenzocoronene. Its flat nature and small interatomic distances of 3.549 Å, between staggered head-to-tail stacks, show a similar behaviour to HBC in the crystalline state.

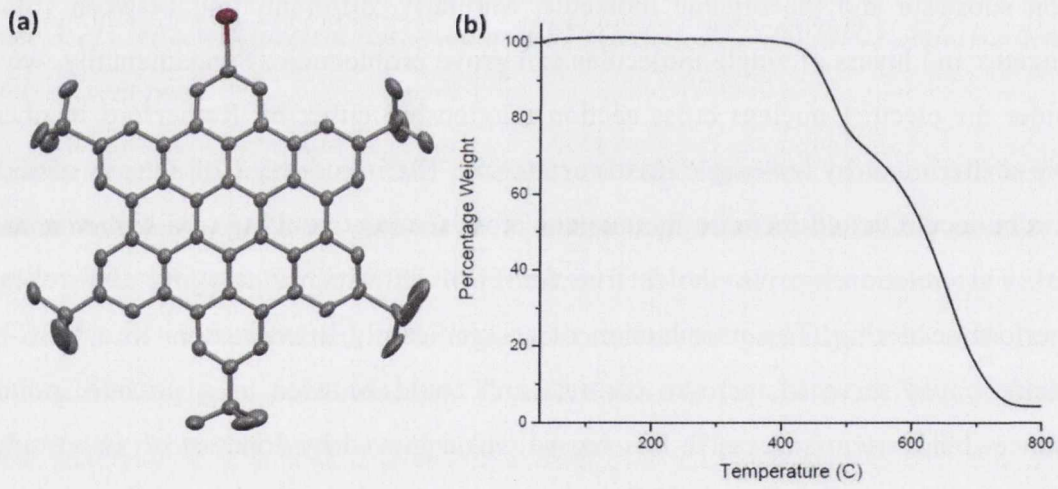

Figure 3.22: (a) Representation of the single-crystal XRD structure of IHBC with thermal ellipsoids at 50% probability. Hydrogen atoms are removed for clarity.[72] *(b) TGA analysis at 10 °C per minute under* N_2.

IHBC was found to exhibit high thermal stability, with the first onset of degradation seen just above 400 °C. The introduction of a halogen to the periphery of the molecule has no major effect on the solid state properties or stability of the molecule, but does offer different channels of reactivity which have remained untapped for some time. IHBC gave good coverage when drop-cast from dichloromethane onto an ultrathin carbon substrate (<3 nm) which was supported by a copper TEM grid and imaged using HRTEM (Figure

3.23 (a)). Within a short imaging window the formation of cubic crystals (circled in red) was observed; there also remained some hexagonal regions which increased in size from the original IHBC regions. These areas correspond to approximately 80 atoms (circled in white). This indicates that in certain regions the irradiation from the electron-beam appeared to induce a dimerization process between two IHBC molecules, most likely due to the scission of a C-I bond, followed by bond formation between two cores. After longer or higher intensity exposure all regions move to a cubic crystal lattice with 90° symmetry and lattice spacing of approximately 0.25 nm. For a 1 second exposure, in a window of this size, it is approximated that 1 x 10^4 $e^-/Å^2$ are incident. It is likely however that location and focussing of these areas would result in marginally higher doses of irradiation. Although such a high-energy method, which generates a large percentage of cubic crystalline structures, is far from a feasible route to generate controlled C-C bond formation, it holds promise that such reactions may be probed by similar, lower energy stimuli. The next step would be to attempt to induce a similar response using a lower energy electron beam coupled with *in situ* monitoring.

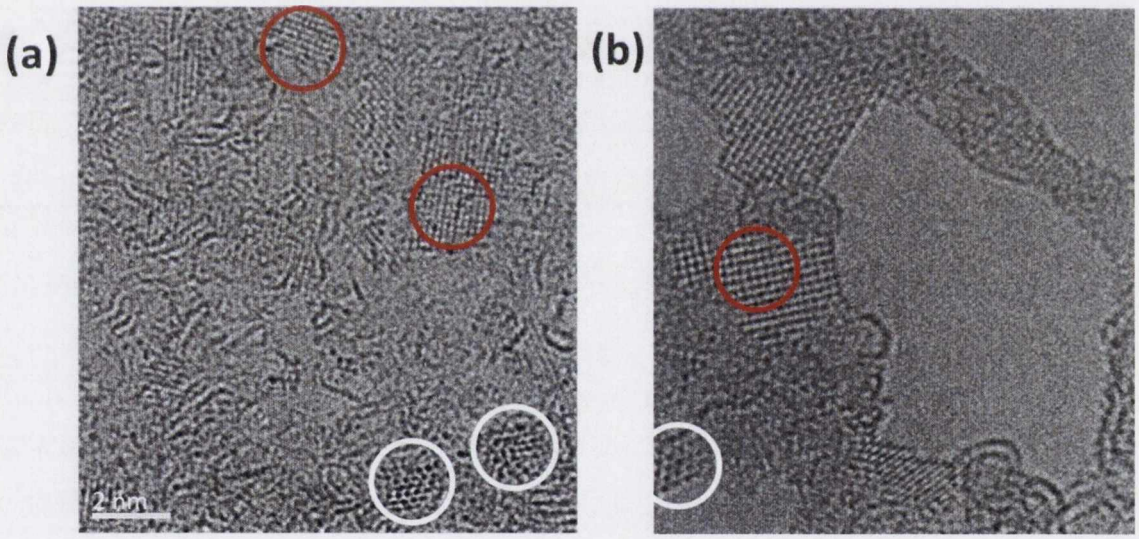

Figure 3.23: HRTEM images of IHBC as deposited by drop casting onto ultrathin amorphous carbon.

3.7.3 XPS Studies

3.7.3.1 General

X-ray Photoelectron Spectroscopy (XPS) is a very useful surface-sensitive technique, which has recently been used effectively in the study of nanoribbons and analogous structures, providing quantitative analysis of the elemental composition of materials. Usually performed under ultra-high vacuum (UHV), XPS serves to monitor the

interaction of X-rays with the core electrons of atoms within a surface, to a depth of approximately 100 Å. As core electrons are in close proximity to the nucleus their binding energies are indicative of particular elements. By monitoring these binding energies it is possible to glean chemical and electronic information about a compound. To date, single molecule precursors have not been studied by this method to a great extent. This is most likely due to the availability of more accessible techniques and the fact that the deposition of such molecules can lead to weakly bound films which do not efficiently transfer charge. This results in the stabilisation of positive charge on the molecules. This stabilisation of charge results in an overall shift in binding energies of approximately 1 eV. *In situ* charge neutralisation has been made possible by the use of a flood gun and transmission screen. These operate by passing a flux of low kinetic energy electrons (<10 eV) with a beam current in the μA range. For organic single crystals, such as coronene and substituted porphyrins, this method can be used very effectively to balance charge. This results in highly reproducible measurements, with respect to peak width and peak position as a function of flood gun beam energy.[73] For substituted single-molecule hexabenzocoronenes such charging is just as prevalent with shifts of approximately 2 eV observed for carbon 1s binding energies.[74]

3.7.3.2 Applying XPS to Halogenated Polyaromatics

As expected, the application of XPS studies to IHBC showed a considerable shift of the C 1s peak with respect to similar charged-neutralised nanographenes, irrespective of the efforts made to improve electrical connectivity to the spectrometer ground. Figure 3.24 shows the effect of applying charge neutralisation (5 eV flux) upon my IHBC sample, with the blue trace representing the binding energy of C-1s electrons. Interestingly, stopping the charge neutralisation flow still resulted in an overall shift of 0.5 eV (approximately the same value observed upon graphitisation of similar organic compounds).[75] This phenomenon is reproducible with pre-treated samples, confirming that this observation is not as a result of charge build-up on the substrate. To fully understand the effect that this low energy irradiation may have on the sample it was necessary to focus on the iodine XPS peaks, namely the I-$3d_{3/2}$ and I-$3d_{5/2}$ signals.

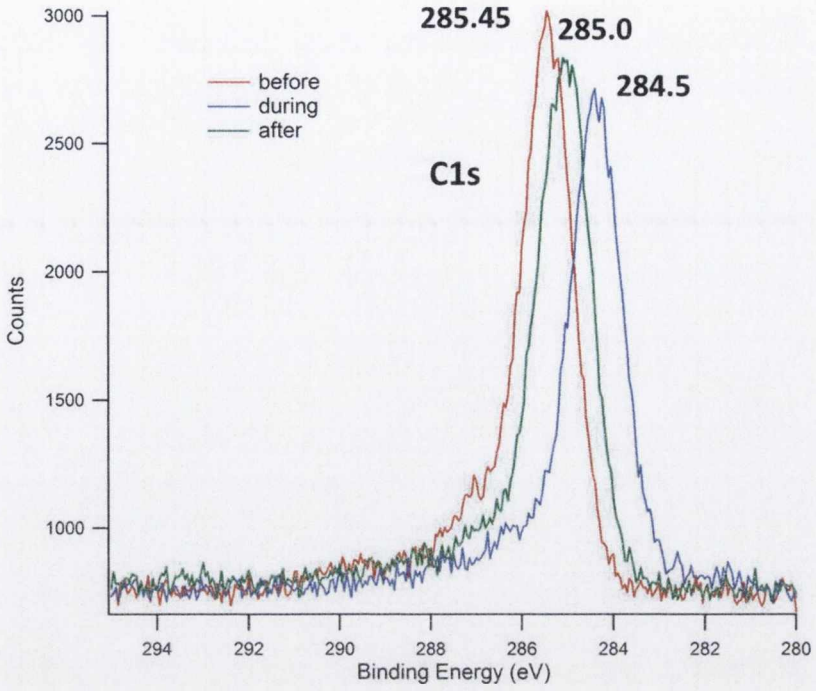

Figure 3.24: C(1s) photoelectron spectra of IHBC before, during and after flood gun irradiation.

Figure 3.25 shows the peaks as observed before and after treatment with the charge-neutralising gun. After treatment, it can be clearly seen in the green trace that peaks corresponding to the binding energies of iodine electrons in an aromatic framework no longer exist. This data appears to suggest that irradiation with a relatively low flux electron beam can serve to break the carbon-iodine bond. It can be ascertained from studies of iodobenzene that threshold electron energies of approximately 1.5 eV are required to break the C-I σ-bond, as determined using tunnelling electrons from a scanning tunnelling microscope tip at UHV.[71] It is also determined that disruption of the π bonds within the aromatic ring would require energy many multiples larger for a current of 1.2 nA.[55] It seems energetically plausible that an electron neutralisation gun can provide enough stimulus to remove a peripheral iodine atom from IHBC. However, it still remains to be seen if subsequent migration of generated cations, followed by reaction, could result in the formation of dimeric species in this instance, or moreover be a feasible route to the formation of larger polymeric domains. It is likely that the noted shift in C-1s binding energy may well correspond to the formation of a larger graphitic-like molecule.

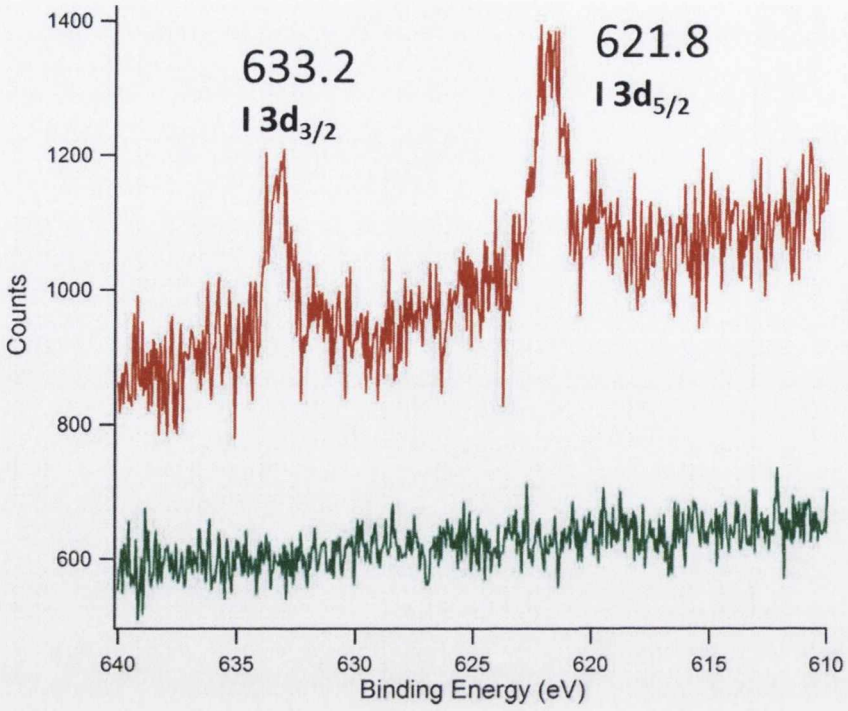

Figure 3.25: I-3d$_{3/2}$ and I-3d$_{5/2}$ photoelectron spectra before (red) and after (green) flood-gun irradiation.

These two interesting observations provide an insight into the behaviour of this halogenated polyaromatic molecule under different intensity electron irradiation. To try and fully ascertain the adaptability of this bond scission, as a means of material development, it was necessary to find other means of adding support to the observations seen. Finding a method to use less intense irradiation, coupled with an ability to probe any response would prove invaluable.

3.7.4 Light Irradiation

From a synthetic chemist's perspective, working on the single molecule scale, mass spectrometry always proves a rational route for the determination of superstructures. Matrix Assisted Laser Desorption Ionisation (MALDI) may indeed be a practical method for surveying the potential formation of larger structures. The nature of MALDI sample input allows for deposition directly on to sample plates. The ability to directly attach pre-treated substrates to this sample plate proved a novel means for a more traditional method of materials analysis. As this manner of sample introduction had not been previously utilised, there were numerous potential pitfalls. Using a Waters MALDI QTOF spectrometer, pre-treated samples from XPS measurements were directly attached to sample plates and with the application of a trans-2-[3-(4-tert-Butylphenyl)-2-methyl-2-propenylidene]malononitrile (DCTB) matrix were loaded to the spectrometer.

Interestingly, analysis showed that large proportions of the dimeric species were observed, thereby confirming the findings from XPS. Multiple control experiments with identical sample preparation, in the absence of electron gun irradiation also in the presence of DCTB show that only the single molecule precursor is observed intact. The use of high-resolution mass spectrometry to confirm on-surface reactions proved a very interesting marriage between the more abstract high-energy experimentation and traditional methodologies of the synthetic chemist.

The use of MALDI ionisation techniques to analyse samples, as outlined in Figure 3.26 involves the use of a laser source which directly excites an absorbing matrix above the sample. This subsequently results in desorption and ionisation of the molecules. On a regular MALDI sample plate, shown in the inset, hundreds of portioned sections give the ability to scan a large number of sections to monitor numerous reactions, without the need to purge previous samples or recalibrate between readings. It became apparent that the mode of operation of MALDI mass spectrometry might be an invaluable tool for probing and monitoring the reactivity of halogenated polyaromatics.

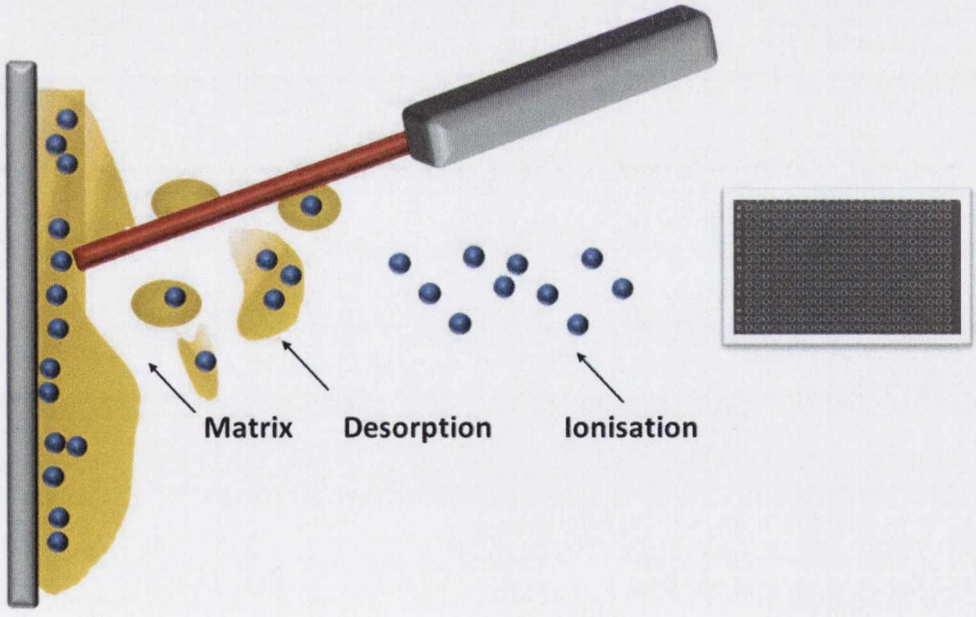

Figure 3.26: Simplified schematic of laser desorption as utilised in MALDI. Inset shows a typical MADLI sample plate.

With relatively low energy laser light, in the absence of a matrix, it was possible to directly excite these molecules. The high stability of hexabenzocoronene-like molecules of this nature, coupled with their relatively high absorption between 300-600 nm, made direct excitation in the absence of matrix a possibility. To begin with, various different

concentrations of IHBC were made and deposited directly on to the sample plate. A selection of different matrices were used to coat samples which were excited, as in Figure 3.26. Various other combinations were prepared in the absence of matrix, which resulted in the deposited IHBC crystalline material being excited directly by the laser source. Drop casting in this manner resulted in uneven formation of micro-aggregates. This was counteracted by selecting a large number of areas with which average findings could be calculated across each distinct sample. As expected, in the presence of a suitable matrix such as DCTB the IHBC molecule is detected as the $[M+H]^+$ species, shown in Figure 3.27 (a). Irrespective of the matrix used, the concentration of deposited sample or the intensity of incident laser light, the absorption by the sacrificial matrix removed enough energy to ensure that the IHBC was ionised completely intact. In the absence of matrix, under a range of conditions, it is seen that the light energy is more than sufficient to cleave the C-I bond. Depending on exposure-time it is possible to see the extent to which this C-I cleavage occurs, and the consequent extent of the dimeric species formed (Figure 3.27 (b)).

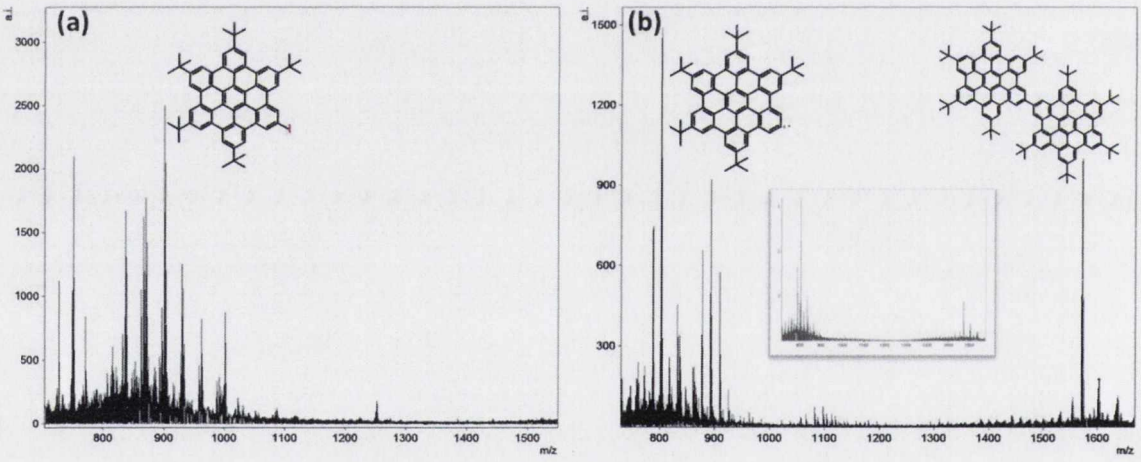

Figure 3.27: (a) MALDI Mass Spectrum of IHBC using DCTB matrix; (b) MALDI mass spectrum with direct excitation of IHBC. Inset shows increased abundance of $HBC^{+\bullet}$ upon higher intensity irradiation.

Initial studies show the relevant abundance of $M^{+\bullet}$ and M_2^+ species, which are seen at 802.4539 and 1602.8921 amu respectively, with respect to the decreasing levels of IHBC (seen at 928.3505 m/z). After each irradiation-sampling period the laser was moved to a visually unperturbed area. This ensured that some qualitative analysis could be performed at higher current intensity. Figure 3.27 (b) inset shows that with increasing intensity of laser irradiation the $M^{+\bullet}$ species is present in the largest abundance, with only trace

amounts of the IHBC precursor. The ability to generate this reactive cation under relatively low energy irradiation is of great interest. As a test case it confirms the accessible nature of C-I cleavage, while confirming the stability of the polyaromatic core with respect to irradiation.

The ability to generate and monitor the formation of a reactive charged species by this means is a novel route which paves the way for further study. To fully appreciate if a reaction of this nature could be used to form a larger patchwork of monomers it is necessary to focus attention on other analogous structures which offer similar stability with a higher degree of substitution. Additionally, pinpointing molecules which could be more synthetically challenging and which possess alternative halogen substitution may offer different shapes and substitution patterns. For the family of novel brominated species presented in Section 3.6.1 a systematic approach was taken with respect to laser desorption ionisation (LDI) irradiation. In a manner similar to that used for IHBC, a range of matrices and drop cast depositions were used across all precursors which yielded fascinating results. Presented here is one of the more exciting cases.

Compound **22** is an ideal candidate to outline higher degrees of intermolecular C-C bond formation which can be induced by relatively low irradiation. With a DCTB matrix applied in a regular fashion, **22** was detected as expected as $[M+H]^+$ at 926.7856 m/z, shown in Figure 3.28 (a). In a similar fashion to IHBC, in the absence of a matrix and with short irradiation time **22** showed the charged species shown in Figure 3.28 (b), which was created by the scission of one C-Br bond. Low energy irradiation coupled with longer irradiation time can be used to increase the relative abundance of this charged species.

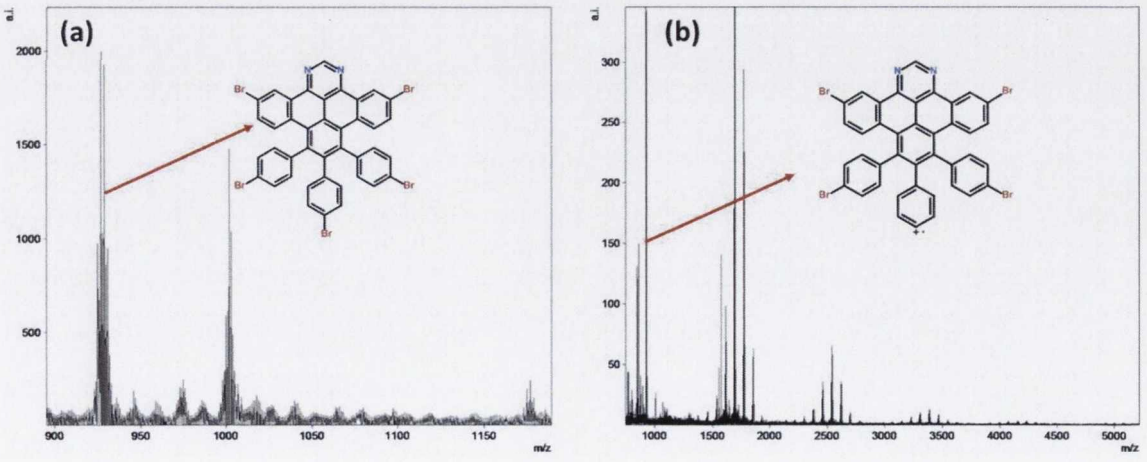

*Figure 3.28: MALDI Mass Spectra of **22**: (a) using a DCTB matrix; (b) in the absence of a matrix.*

Of considerably greater interest are the envelopes in the 1500-4500 m/z, shown in greater detail in Figure 3.29 with an overlay of isotopic models. The mass spectrum shows a very clear pattern of growth of molecular species from 1-5 molecular units, with the most abundant species for each envelope being depicted in each case.

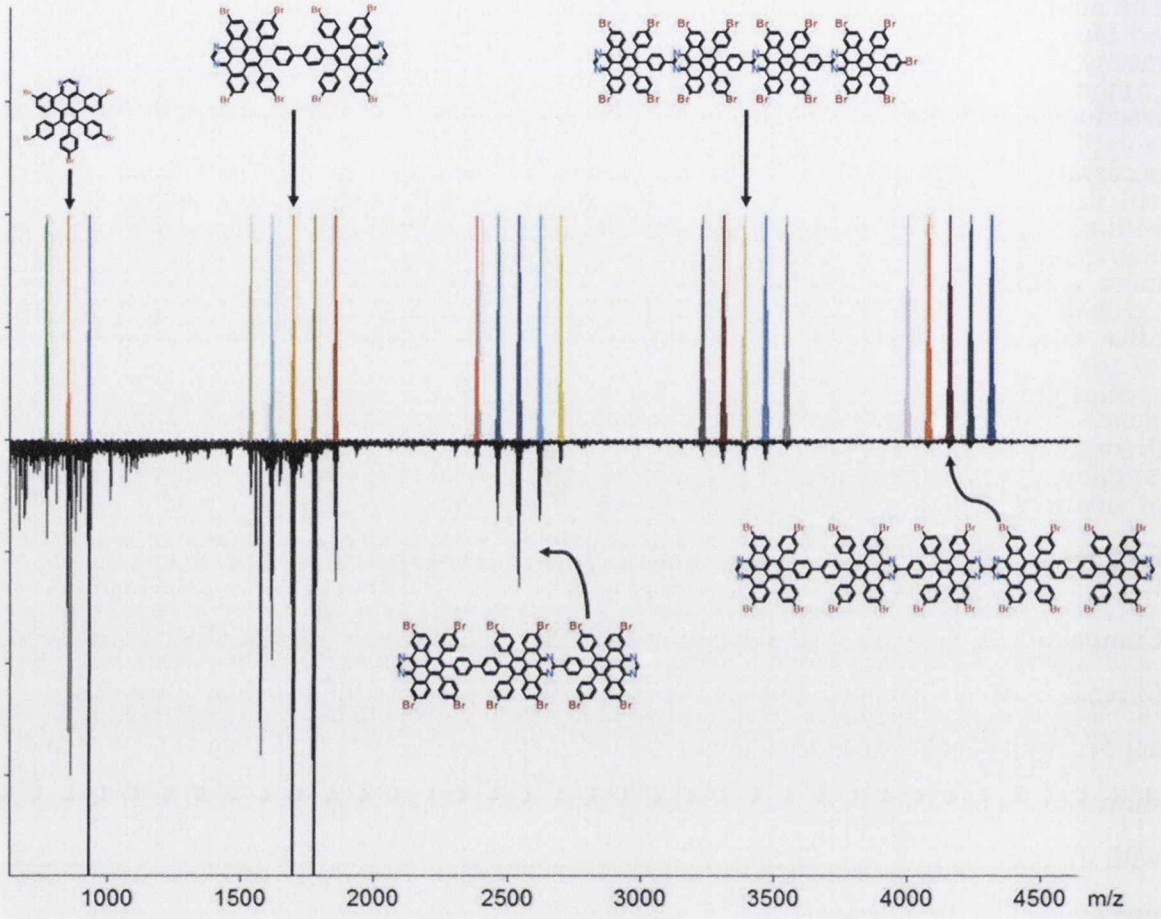

Figure 3.29: Mass spectrum of ***22****, achieved by direct laser desorption. Coloured lines represent isotopic models, separated by 79.9 amu. The central peak in each envelope is represented by the structures, which exist as the* $[M+H]^+$ *ions of the species shown.*

The presence of five brominated rings on the periphery serves as a useful point of reference. For example, the envelope centred at 1692 m/z shows the most abundant peak corresponding to $C_{80}H_{38}Br_8N_4$. The envelope at 2538 m/z corresponds to a trimeric species but interestingly the most abundant peak relates to a $C_{120}H_{56}Br_{18}N_4$ formula. This indicates that at each iteration from dimer onwards substitution likely occurs on a pyrimidine ring. This observation becomes extremely important in assessing preliminary surface polymerisation in Section 3.7.5. Interestingly, a higher-order "envelope of peaks" exists within each species' spectral region, comprising a series of isomeric envelopes,

each differing by 79.9 mass units. The origin of this observation is explored in Figure 3.30, showing in greater detail the peaks resulting from the trimeric species, centred at 2550 m/z. In all of the cases the resulting isotopic envelope is made up of multiple species, which all vary by 79.9 mass units, corresponding to varying number of bromine substituents. From dimer to pentamer and beyond, the spread of peaks can be rationalised by some of the possible permutations presented. As the propagation of growth is increased for the higher degree polymerisations, there exists a greater number of patterns which may exist, caused by a combination of linear or dendritic growth patterns. This is an interesting observation, which has implications for the results presented in Section 3.7.5

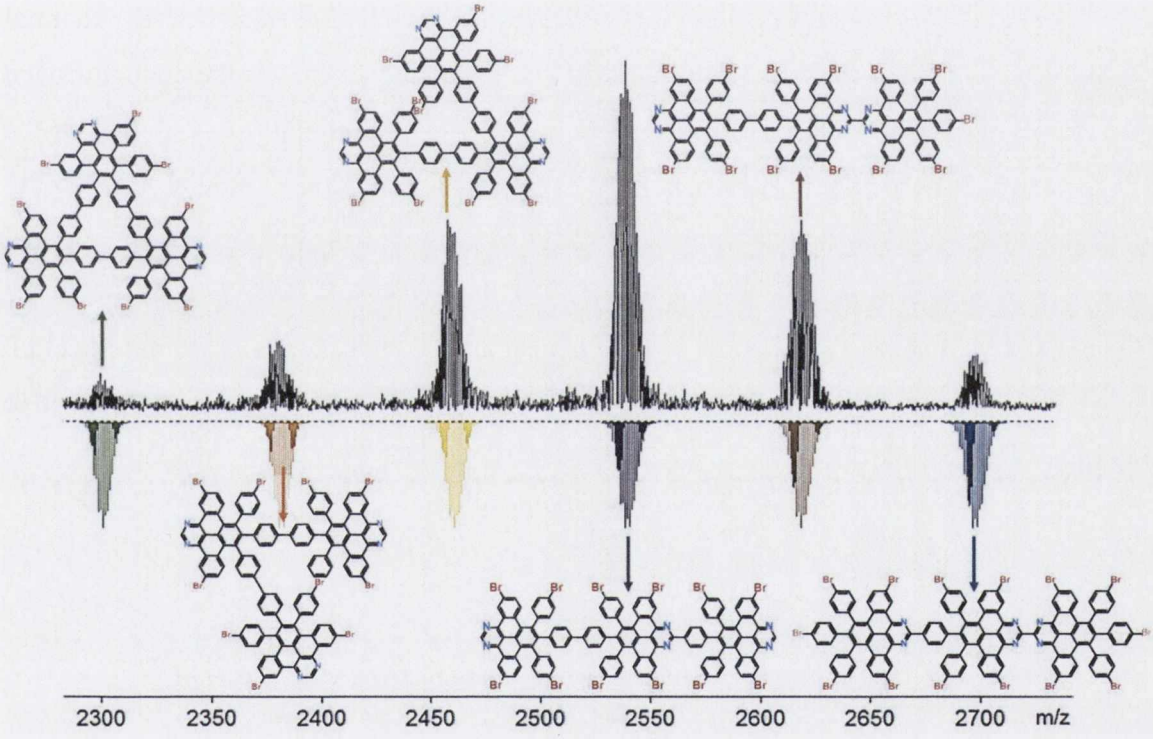

Figure 3.30: Enlarged area of mass spectrum upon irradiation of ***22****, focused on the trimeric region. Inset are possible structures and corresponding isotopic models for the observed patterns which exist as* $[M+H]^+$.

Further assessment of these nitrogen-substituted molecules would prove extremely interesting. In particular, elemental composition would support the postulations presented here. With such low nitrogen content at approximately 3 at.% throughout, a return to XPS studies unfortunately yielded no additional information. As before, the disappearance of bromine across a range of different samples could be identified, but the relatively low percentage nitrogen content made it very difficult to draw conclusions about its

environment. The use of solution based chemistry with mercury vapour lamps yielded useful results on small scale samples which allowed for analysis by NMR. However, to accumulate a greater knowledge of the potential for these molecules to form well-defined nanostructures it was necessary to turn to UHV surface studies.

3.7.5 On-surface Deposition and Growth

The reactivity of the molecules shown hitherto served as a very useful yet imprecise method to glean more information about their ultimate use and application, to generate specifically tailored structures. Ultimately, to exhaust the full potential of these molecules, as substituted precursors to nitrogen doped nanostructures, it was necessary to return to surface based methods. Numerous attempts within this body of work to deposit polyphenylene molecules in a homogeneous and reproducible manner by thermal evaporation had proved fruitless. Relatively low degradation temperatures of nitrogen substituted polyphenylenes restricted common evaporation techniques, as shown in the TGA analysis (Figure 3.31). However, with even partial cyclisation, the thermal stability of these types of molecules is dramatically increased with the onset of thermal degradation increasing from approximately 180 °C in the polyphenylene to 280 °C in the 1/3 substituted analogue (**4**) (shown in red). This added stability had a profound effect on the ability to thermally evaporate and deposit these types of molecules onto reactive substrates, such as Au (111).

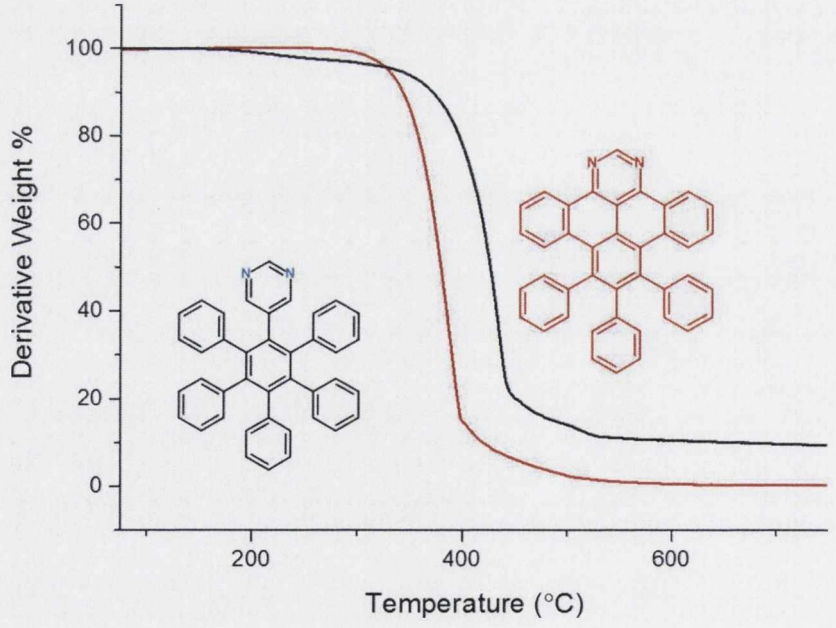

*Figure 3.31: TGA analysis of **1** and **4** with heating at 10 °C per minute under N_2.*

For dipyrimidyl compounds, a similar trend is seen in thermal stability upon cyclisation. **8** for example is seen to be thermally stable to above 450 °C, considerably higher than its uncyclised precursor, as seen in Figure 3.32.

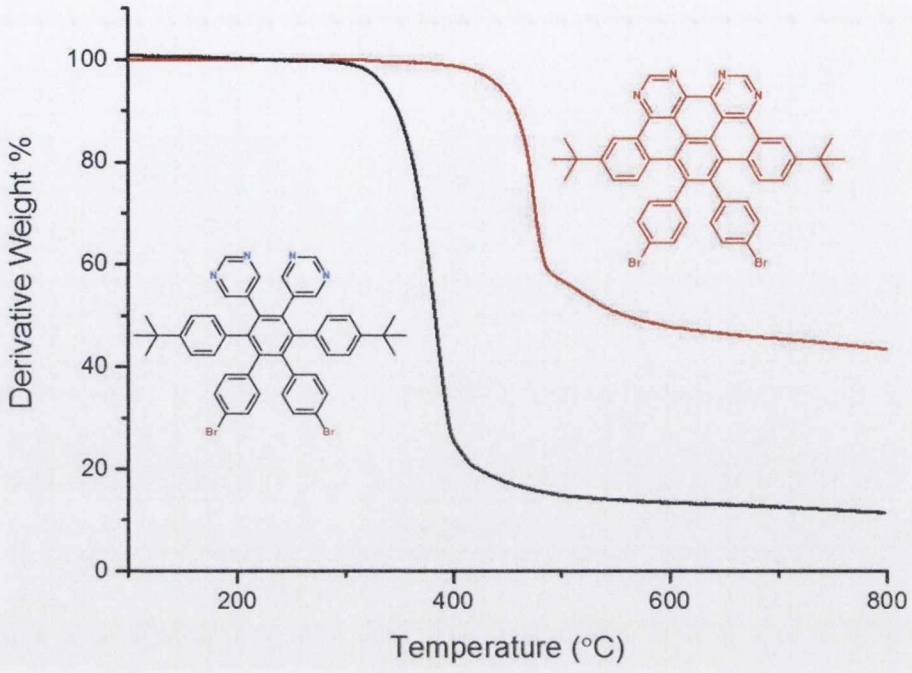

*Figure 3.32: TGA analysis of **7** and **8** with heating at 10 °C per minute under N_2.*

The presence of *tertiary*-butyl substituents serve to increase the stability and ease of processability. If surface reactions were achieved, the presence of only two bromine substituents would result in a relatively straight-forward growth pattern, potentially forming zig-zag nanoribbons. Evaporation at 250 °C, with a pressure of 2 x 10^{-9} mbar, resulted in the successful deposition of **8** on to a Au(111) surface. For the first time, a molecule of this nature was successfully deposited intact *via* thermal evaporation. Optimisation of conditions eventually resulted in a relatively homogeneous coverage. The reactive substrate was then heated from room temperature to 400 °C and any subsequent reaction monitored using scanning tunnelling microscopy (STM). Fascinatingly, dehalogenation was seen to occur and the molecules aligned into rows, as seen in Figure 3.33 (a). Good ordering is seen on the molecular level which does confirm that partially fused molecules of this nature can be deposited and aligned on a surface. Previous attempts to evaporate molecules of this nature with full peripheral *tertiary*-butyl substitution indicated that loss of the alkyl moieties was likely. This lead us to believe that steric hindrance from these substituents would not cause a problem, but rather serve as a useful synthetic advantage. In reality, Figure 3.33 (b) shows that it is likely such a postulation was incorrect as closer inspection appears to point to the formation of dimeric

species between adjacent molecules, but that any further formation of larger species is hindered. Most likely this is as a cause of steric hindrance from the alkyl substituents, which remain intact upon evaporation (as supported in Figure 3.32). Further heating of the substrate has no effect on the well-ordered dimeric species.

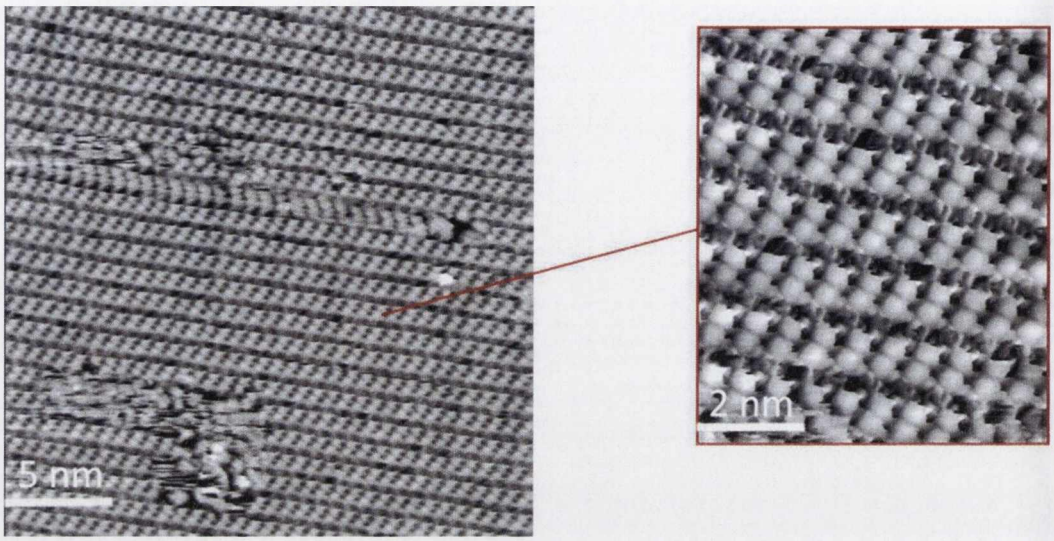

*Figure 3.33: STM images of **8** deposited on a Au(111) surface and heated to 200 °C.*

To achieve more successful deposition and growth, the precursor molecule would need to possess relatively simple halogen substitution to lead to predictable results. In addition, the aforementioned thermal stability would be a prerequisite. Figure 3.34 shows the most practical choice in **20**. This molecule results from a well optimised synthetic route and TGA analysis shows good stability above the range needed for evaporation. The first onset of mass-loss occurs from 310 - 480 °C and accounts for 57% of the sample weight. This compares with onset temperatures of 350 °C and 360 °C for the Br_4 (**21**) and Br_5 (**22**) analogues. The remaining mass loss occurs gradually up to 700 °C. Although greater thermal stability and proven reactivity has been demonstrated for the more substituted counterparts, the ability of a lower degree of substitution to limit the potential permutations, as observed by MALDI, served as a valid reason for beginning with this molecule. It was also expected that the formation of longer chains would only be made possible through substitution at both opposing sides of the molecule. Sterically, substitution from the central phenyl ring would potentially curve the formed chain into a direction which may ultimately restrict further growth. From LDI-initiated formation it was expected that the formation of long molecular chains may be made possible only through a zig-zag framework of approaching molecules, not overlooking the potential for

new C-C bond formation to any of the three unsubstituted rings, as alluded to in the previous section.

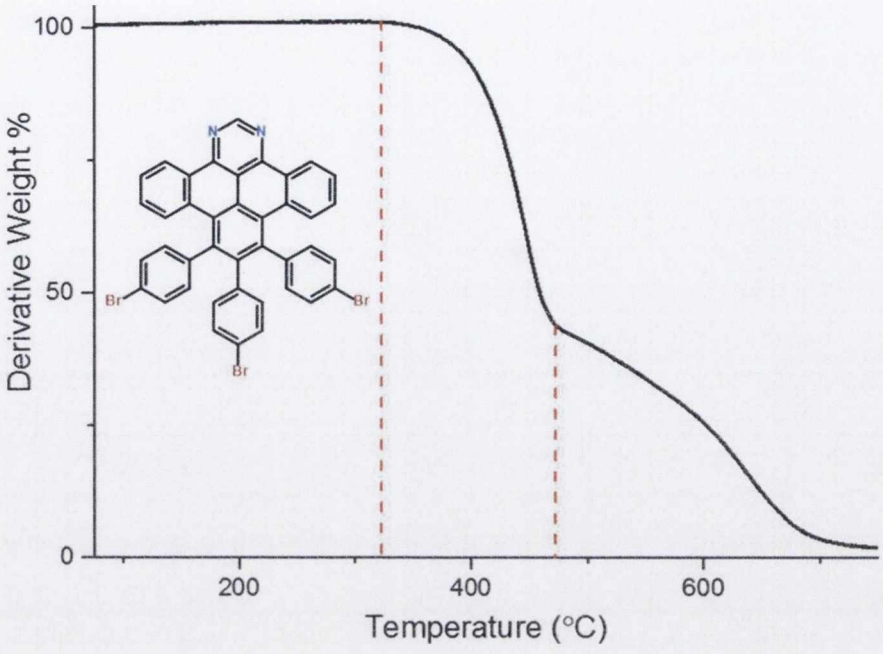

*Figure 3.34: TGA analysis of **20** with heating at 10 °C per minute under N_2.*

As before, thermal evaporation was eventually optimised at approximately 250 °C. Similarly, the molecules were seen to be deposited, intact, on to the reactive gold surface.

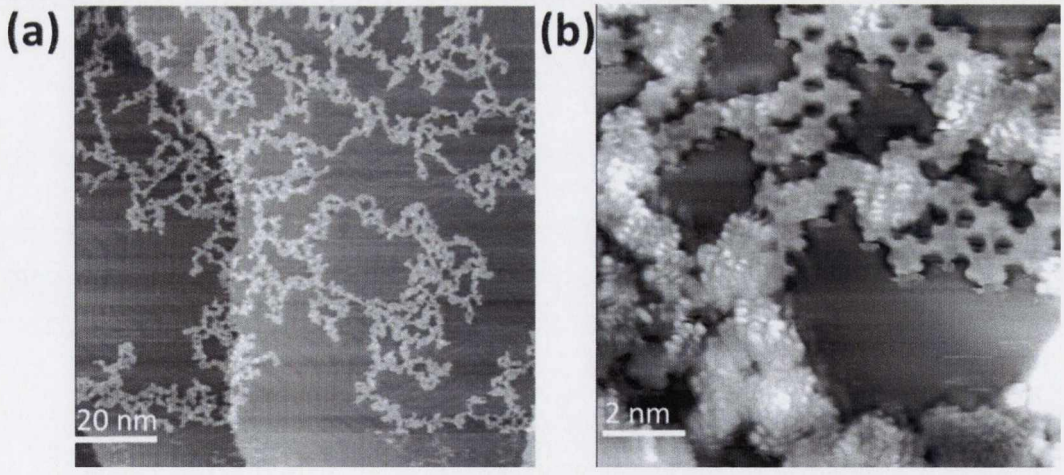

*Figure 3.35: STM images of **20** deposited on a Au(111) surface and heated to (a) 200 °C and (b) 400 °C.*

Figure 3.35 (a) shows the initial growth, upon heating the substrate to 200 °C. STM images clearly depict the formation of long, meandering ribbons of molecules of varying thicknesses which appear to vary from two molecules wide, to thicker frameworks. Some

chains are seen to grow in one direction for up to 400 nm, while other propagations fold back on themselves and eventually terminate. The less-than predictable nature of growth results in quite a porous formation. The ability to direct the size and shape of these pores would result in fascinating properties. To date, ribbon formation has not offered this form of molecular mesh, most likely due to the linear nature of substitution available to this point. Upon heating to 400 °C fascinating behaviour can be observed, as seen at higher magnification in Figure 3.35 (b). A range of different growth patterns can be identified, predominantly formed by the zig-zag approach of molecules. Figure 3.36 (a) shows one such pattern. It clearly depicts the early stages of growth of a double-armchair ribbon. The nature of formation shows that some molecules must also exhibit bond formation to the dibenzoperimidine core. This points to the existence of C-C bond formation, not only at C-Br positions but also possible C-H activation. Although common for intramolecular cyclodehydrogenation, this has not been commonly observed in intermolecular situations. Figure 3.36 (b) shows an instance in which the growth of two parallel chains is hindered by the introduction of a molecule in a varying pattern. This adds a kink to the ribbon, thereby hindering further growth in that direction.

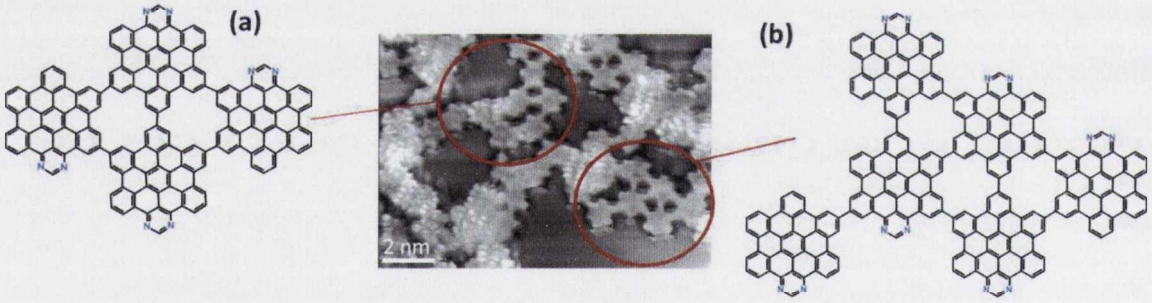

*Figure 3.36: STM images of **20** deposited on a Au(111) surface and heated to 400 °C; (a) formation of a two-molecule wide nanoband; (b) example of deviation from straight nanoband propagation.*

Although exhibiting obvious pitfalls in the formation of homogeneous coverage or predictable nanoribbon formation, the deposition of **20** served as a watershed case within and without of the Draper group research. These promising results are the culmination of five year's work towards using selectively substituted nitrogen-containing molecules for the formation of large nano-frameworks. On a wider level, the results offer three distinct areas of progress which have never been seen before;

i. wide nanobands, moving towards 2D ribbons

ii. double-sided nitrogen substitution, offering the prospect of complete N-substitution at the bay area

iii. coronene-sized voids in the interior.

The development of this methodology could yield very exciting results if the formation of architectures could be tailored, either by limiting the degree of halogen substitution or by blocking the potential for C-H activation. If this is achieved it could result in nanobands with intriguing properties. The potential to form wide armchair bands consisting of a very polar exterior with approximately 1 nm non-polar voids in the centre would prove very exciting. In addition, relatively minor synthetic alterations could be used to propagate growth to wider dimensions. Ultimately this could prove attractive in the fabrication of nanoscale devices. The eventual goal of these formations is not only to garner attention on a microscale platform, but also to highlight potential as scalable routes to form macro sized surfaces which hold catalytic application. As endeavours are being made by chemical means to photolytically incorporate nitrogen-substituted molecules of this nature into pre-existing carbon substrates such as carbon black, it was also necessary to begin preliminary catalytic tests. Such measurements of this type, on single molecule precursors, had never been trialled in this manner, as the understanding of the nature of encapsulation of such small molecules within ink-blends left a lot to be desired to date.

3.7.6 Preliminary Catalytic Testing

Section 3.3 discusses potential uses of materials such as the ones presented here for catalytic purposes in fuel cells. The use of electocatalysts for automotive purposes has made inroads to widespread commercialisation in the past few years, with the use of PEM cells. Unfortunately, these improvements still remain focused on a small range of materials, very limited types of cell formation and even more specific types of testing. Notwithstanding such limitations, the development of catalysts could offer improvements to degradation from automotive cycling. As previously mentioned, most catalytic materials for this application use platinum group-metal (PGM) alloys on high surface-area carbon. Dispersion of nanosized metal particulates is aided by the carbon substrate, which also allows for the transport of reactants and products throughout the electrode, resulting in good electrical conductivity. Incorporating nitrogen-substituted materials into carbon substrates would require these compounds to be exposed to highly corrosive conditions, including positive electrode potentials and low pH. Such an environment in fuel cell stacks has resulted in a very particular methodology for electrochemical testing of

potential catalytic materials. Catalytic testing of pyrimidyl substituted compounds for use in this regard would best follow industrially accepted practices for testing, if their potential application was ever to be realised. Whether these materials could be incorporated as molecular blends or through chemical reaction into carbon substrates it is necessary to begin preliminary testing through industrial collaboration.

For industrial processes thin film electrodes are normally fabricated from inks which contain catalyst, water, isopropanol and an ionomer such as Nafion™. By sonication, thin-films suitable for rotating-disc-electrochemistry (RDE) can be prepared. Formulation of these inks and the production of thin-films can be extremely time consuming. Although the presence of ionomer is not necessarily essential to proton conduction, its presence can help in binding particles to the glassy-carbon disk. To initiate catalytic testing on the compounds presented herein, **4** was chosen as a suitable single-molecule comparator. It would serve as a useful example of this family of molecules.

Preparation of inks, in the absence of PGM materials would allow for assessment of any innate catalytic activity in the N-substituted material. Dispersion of **4** in an isopropanol solution and blending with Nafion allowed for deposition on to a glassy carbon rotating-disk electrode. Using an MSR rotator, linear sweep voltammetry was performed at a scan rate of 5 mVs^{-1}, a rotational rate of 1600 rpm and in 0.1 M H_2SO_4. At voltages between 0.15 and 1.2 V it was possible to use cyclic voltammetry to investigate the Oxygen Reduction Reaction (ORR) and Hydrogen Oxidation Reaction (HOR), by sparging the electrodes with an O_2 and H_2 flow respectively. It is clear from Figure 3.37 that no catalytic activity is seen with respect to the glassy carbon background.

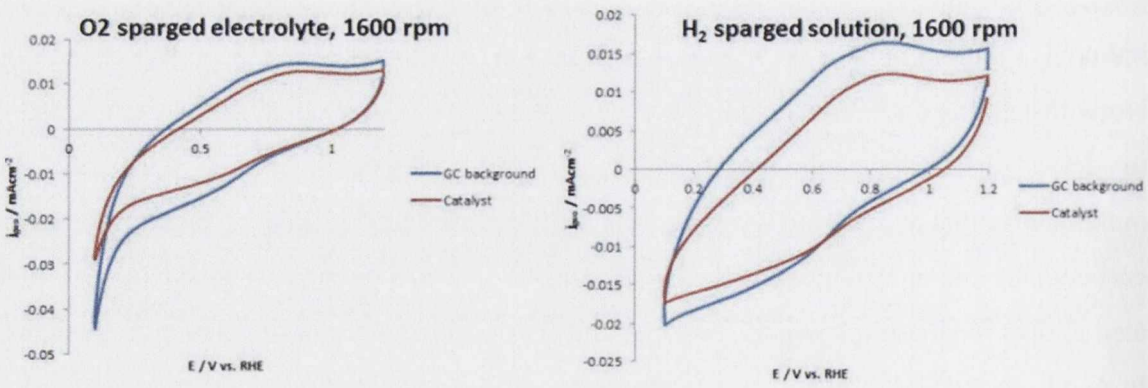

*Figure 3.37: RDE voltammogramms of **4** at scan rate of 5 mVs^{-1}, a rotational rate of 1600 rpm and in 0.1 M H_2SO_4.*

As outlined, it is likely that any enhanced catalytic activity from N-substituted materials in the presence of traditional catalysts of this nature may operate either *via* polarity changes induced as a result of the nitrogen atom, or by potential coordination to metal sites. Unfortunately, for a range of industrial processing reasons testing of catalytic abilities is seldom carried out in alkaline media, favouring non-absorbing acidic electrolytes such as dilute acidic solutions. In acidic media any enhanced catalytic activity created by the presence of the nitrogen lone-pair would obviously be negated upon protonation of the nitrogen atoms. At relatively low loading of active material it is likely that a large proportion of the pyrimidine rings would be protonated. Also, for a molecule of this nature, exhibiting C-N coordination sites, any stabilisation of metallic particles by the protonated species would be minimal. Preparation is currently underway to continue ORR measurements on these molecules in alkaline media. In addition, single molecule precursors with N-N type coordination, such as **8** could also show promise in this regard. These may yet serve to confirm an innate catalytic activity for these compounds, before their influence on metal-containing systems is assessed.

3.8 Conclusion and Future Work.

3.8.1 Conclusion

The work presented herein has shown exciting results from both a synthetic and materials perspective. The extension of syntheses from Chapter 2 enabled the first instance of controllable, peripheral substitution on polyaromatics of this form. The new bromination method allowed for the formation of a family of three substituted polyaromatics. The use of *in situ* NMR studies meant that optimisation of the reaction was possible, with a significant increase in relative yields. Separation using column chromatography allowed for complete characterisation of the three compounds by NMR, mass spectrometry and elemental analysis. It was also possible to characterise the more symmetric Br_3 and Br_5 products using single-crystal XRD. Partially-fused, polyphenylenes with nitrogen substitution have provided a solution to a synthetic obstacle which has alluded synthetic chemists for several years. Using this novel route to develop nanoribbon feedstocks was a natural progression.

The extension of this work to begin a preliminary nanomaterials study was ahead of the research trend. As mentioned, current larger-scale nitrogen substitution techniques are unspecific. Approaches such as plasma treatment, electrothermal reactions with ammonia and CVD have low controllability, poor nitrogen-substitution capabilities and are

ultimately limited by scale-up. The preliminary work shown here, originally for IHBC and subsequently for more complex systems, shows huge potential across a range of scales. The use of a simple monosubstituted compound such as IHBC, to probe the scope of reactivity, allowed for a range of characterisation techniques on both the molecular and surface science level to be carried out. Variation of the ionising source from e-beam to tuneable UV irradiation gave scope to characterise the outcomes of a simple binary system. Characterisation of these outcomes *in situ*, either by XPS or MALDI mass spectrometry was extremely fortuitous. These simple investigations have paved the way for development of procedures using single-molecule precursors of this nature across an expansive range of scales. For small-scale nanoribbon formation the compounds shown exhibit the first successful thermal evaporation of this family, from countless attempts over nearly a decade of work. Ribbon formation and cyclodehydrogenation, while crude and unpredictable, holds massive potential for the enormous family of compounds developed. On a larger scale, probing low energy UV irradiation to initiate polymeric formations on molecules with higher degrees of substitution has already lead to embryonic work which holds positive outcomes for the future.

Initial ORR and HOR rotating-disc electrode experiments are a useful way of screening molecules by predicting trends in fuel cell operation. Replicating industrial testing methodologies, while applicable for industrial integration may serve as an unnecessary complication for assessing the activity of these molecules. Gas diffusion in the ORR is integral to the efficiency of the reaction. As a cause of this, film formation and surface coverage on a glassy carbon electrode is very important to movement of the reactant and product between the active material and electrolyte. Ultimately, depositing catalyst-loaded inks onto electrodes can provide misleading results. The catalytic inactivity observed herein could potentially be as a result of poor dispersion of the molecules within the ink, non-uniform film deposition or a fundamental limitation caused by easily protonated nitrogen-containing rings in a low pH environment. Quantifying the loading of such a small organic molecule within an ionomer would also prove extremely difficult. To assess any molecules of this nature will require a more fundamental approach to testing. This can be achieved by drop casting or spin coating of the molecules directly on to glassy carbon electrodes. Testing in both alkaline and acidic media will provide more information on activity before integration into inks, either physically or chemically. Current work, surrounding the photolytic attachment of such molecules to sputtered carbon surfaces, with quantitative analysis made possible using XPS, may hold a solution to these

problems. This may answer the anomaly of published results for nitrogen doped surfaces in acidic media.

3.8.2 Future Work

Future developments from this work will follow three distinct pathways;

i. synthetic developments,
ii. small-scale surface growth
iii. large-scale substrate modification

Current research following on from the discoveries outlined here has adopted the same manner of introducing nitrogen substitution, focusing on disubstituted symmetric acetylenes. While this could introduce 2 or 4 nitrogen atoms per molecule, the limited nature of halogen substitution restricts the orientation of achievable super-structures. The Draper Group remains one of the few groups globally who concentrate on different modes of nitrogen-substitution, owed primarily for the necessity to provide different coordination environments for transition metal complexes. This synthetic expertise can allow for the synthesis of molecules which contain more than one peripheral nitrogen environment. This proficiency to control nitrogen substitution and peripheral halogenation alike is an extremely valuable tool. The reliance of current synthetic procedures on substitution *via* Diels-Alder reaction results in substitution being forced to the outermost regions of nanostructures. This precludes the possibility of substitution at the interior of such molecules. The achievability of complete substitution at the bay areas or the creation of highly polar voids in large formations would prove extremely interesting. These molecules would be of benefit not only for surface-controlled growth and cyclodehydrogenation, but may also allow for interesting photochemistry to be performed, as a method for functionalising existing carbon substrates.

Figure 3.38 shows the two proposed structures which would bring interesting developments in the formation of nanoribbons. The structure shown in Figure 3.38 (a) if successful would herald a new departure for the growth of nanoribbons in this area. A brominated phenanthroline platform would result in bond formation at this fused portion, thereby resulting in bipy-like substitution at the interior of any generated ribbons. Similarly, Figure 3.38 (b) would offer a similar functionality, while in addition offering the more common substitution pattern on the outside. This would potentially result in the generated structure shown in Figure 3.38 (c). If polymerisation and cyclodehydrogenation

in this manner were possible it would result in exciting possibilities of higher percentages of nitrogen-doping in ribbons complete substitution of the peripheries with both N-N and C-N coordination sites.

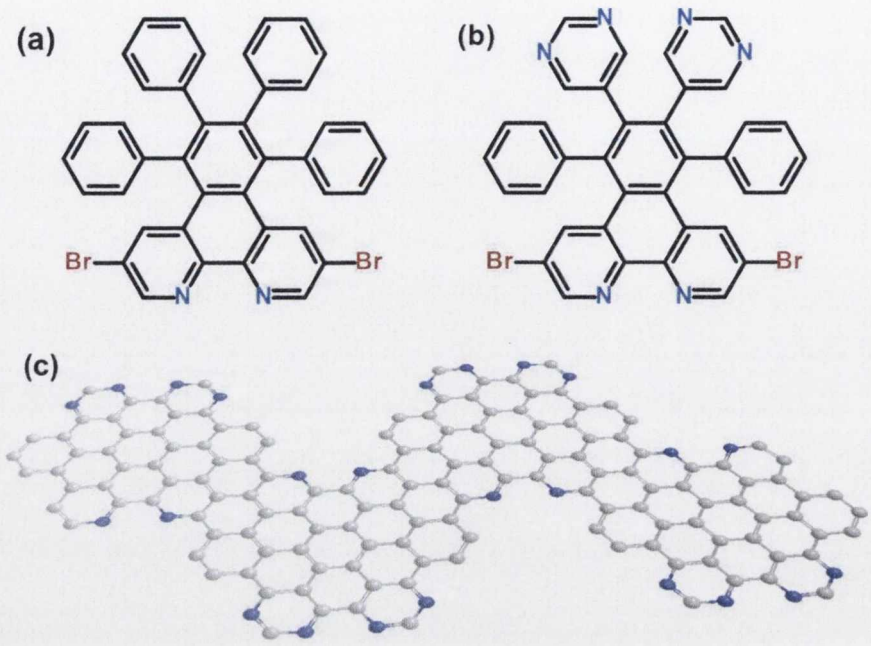

Figure 3.38: Proposed structures for future work: (a) 3,10-dibromo-5,6,7,8-tetraphenylbenzo[f][1,10]phenanthroline; (b) 3,10-dibromo-5,8-diphenyl-6,7-di(pyrimidin-5-yl)benzo[f][1,10]phenanthroline; (c) depicts potential nanoribbon growth and cyclodehydrogenation from precursor molecule in (b).

The two proposed structures shown in Figure 3.38 not only represent the possibility for small-scale surface reactions but also hold much potential for the photochemical functionalization of carbon substrates. Initial results show the promising nature of using brominated phenanthroline-based polyphenylenes as feedstocks for the functionalization of carbon surfaces. Using relatively low-energy U.V. light, as outlined previously it is possible to form reactive species which functionalise the carbon. This has currently proven successful for smaller species, which can be very accurately monitored using Raman and XPS. The introduction of slightly larger polyphenylenes will bring the added possibility of further functionality and coordination. This would signify the prospect of chemically functionalising carbon supports on a relatively large scale. While not necessarily offering the controllability for UHV on-surface growth it may offer an achievable method to chemically marry nitrogen-doped substrates with the current industrial methods for fuel cell fabrication.

3.9 References

(1) Navigant Research. *Stationary Fuel Cells*; 2014.

(2) U.S. Department of Energy. Energy Incentive Programs http://energy.gov/eere/femp/energy-incentive-programs (accessed Oct 1, 2014).

(3) Fuel Cell Today; Matthey, J. **2013**.

(4) Goswami, Y.; Kreith, F. *Energy Conversion*; CRC Press, 2007.

(5) Wieckowski, A.; Norskov, J. *Fuel Cell Science: Theory, Fundamentals, and Biocatalysis*; John Wiley & Sons, 2014.

(6) Yu, J.; Yi, B.; Xing, D.; Liu, F.; Shao, Z.; Fu, Y.; Zhang, H. *Phys. Chem. Chem. Phys.* **2003**, *5*, 611–615.

(7) Andrew, D.; Larminie, J. *Fuel Cell Systems Explained, 2nd Edition - James Larminie, Andrew Dicks*; Wiley.

(8) Williams, M. V.; Begg, E.; Bonville, L.; Kunz, H. R.; Fenton, J. M. *J. Electrochem. Soc.* **2004**, *151*, A1173.

(9) Pukrushpan, J. T.; Stefanopoulou, A. G. *IEEE Control Syst. Mag.* **2004**, *24*, 30–46.

(10) Arthur D. Little. *Progress Report for Fuel Cells for Transportation*; 2001.

(11) Sealy, C. *Mater. Today* **2008**, *11*, 65–68.

(12) *PEM Fuel Cell Electrocatalysts and Catalyst Layers*; Zhang, J., Ed.; Springer London: London, 2008.

(13) Antolini, E.; Giorgi, L.; Cardellini, F.; Passalacqua, E. *J. Solid State Electrochem.* **2001**, *5*, 131–140.

(14) Markovic, N. *Surf. Sci. Rep.* **2002**, *45*, 117–229.

(15) Jasinski, R. *Nature* **1964**, *201*, 1212–1213.

(16) Chen, Z.; Higgins, D.; Yu, A.; Zhang, L.; Zhang, J. *Energy Environ. Sci.* **2011**, *4*, 3167.

(17) Charreteur, F.; Jaouen, F.; Dodelet, J.-P. *Electrochim. Acta* **2009**, *54*, 6622–6630.

(18) Bashyam, R.; Zelenay, P. *Nature* **2006**, *443*, 63–66.

(19) Srivastava, D.; Menon, M.; Daraio, C.; Jin, S.; Sadanadan, B.; Rao, A. *Phys. Rev. B* **2004**, *69*, 153414.

(20) Jaouen, F.; Marcotte, S.; Dodelet, J.-P.; Lindbergh, G. *J. Phys. Chem. B* **2003**, *107*, 1376–1386.

(21) Faubert, G.; Côté, R.; Dodelet, J. P.; Lefèvre, M.; Bertrand, P. *Electrochim. Acta* **1999**, *44*, 2589–2603.

(22) Bron, M.; Radnik, J.; Fieber-Erdmann, M.; Bogdanoff, P.; Fiechter, S. *J. Electroanal. Chem.* **2002**, *535*, 113–119.

(23) Maiyalagan, T.; Viswanathan, B.; Varadaraju, U. V. *Electrochem. commun.* **2005**, *7*, 905–912.

(24) Wang, C.-H.; Shih, H.-C.; Tsai, Y.-T.; Du, H.-Y.; Chen, L.-C.; Chen, K.-H. *Electrochim. Acta* **2006**, *52*, 1612–1617.

(25) Shao, Y.; Liu, J.; Wang, Y.; Lin, Y. *J. Mater. Chem.* **2009**, *19*, 46.

(26) Xiong, W.; Du, F.; Liu, Y.; Perez, A.; Supp, M.; Ramakrishnan, T. S.; Dai, L.; Jiang, L. *J. Am. Chem. Soc.* **2010**, *132*, 15839–15841.

(27) Xue, Y.; Wu, B.; Jiang, L.; Guo, Y.; Huang, L.; Chen, J.; Tan, J.; Geng, D.; Luo, B.; Hu, W.; Yu, G.; Liu, Y. *J. Am. Chem. Soc.* **2012**, *134*, 11060–11063.

(28) Brun, N.; Wohlgemuth, S. A.; Osiceanu, P.; Titirici, M. M. *Green Chem.* **2013**, *15*, 2514.

(29) Kinoshita, K. *J. Electrochem. Soc.* **1990**, *137*, 845.

(30) Kim, H.; Lee, W.; Yoo, D. *Electrochim. Acta* **2007**, *52*, 2620–2624.

(31) Groves, M. N.; Chan, A. S. W.; Malardier-Jugroot, C.; Jugroot, M. *Chem. Phys. Lett.* **2009**, *481*, 214–219.

(32) Wohlgemuth, S.-A.; Fellinger, T.-P.; Jäker, P.; Antonietti, M. *J. Mater. Chem. A* **2013**, *1*, 4002.

(33) Yang, Z.; Nie, H.; Chen, X.; Chen, X.; Huang, S. *J. Power Sources* **2013**, *236*, 238–249.

(34) Walch, S.; Dhanda, A.; Aryanpour, M.; Pitsch, H. *J. Phys. Chem. C* **2008**, *112*, 8464–8475.

(35) Wiggins-Camacho, J. D.; Stevenson, K. J. *J. Phys. Chem. C* **2009**, *113*, 19082–19090.

(36) Ismagilov, Z. R.; Shalagina, A. E.; Podyacheva, O. Y.; Ischenko, A. V.; Kibis, L. S.; Boronin, A. I.; Chesalov, Y. A.; Kochubey, D. I.; Romanenko, A. I.; Anikeeva, O. B.; Buryakov, T. I.; Tkachev, E. N. *Carbon N. Y.* **2009**, *47*, 1922–1929.

(37) Podyacheva, O. Y.; Ismagilov, Z. R. *Catal. Today* **2014**.

(38) Yu, Y.-X. *Phys. Chem. Chem. Phys.* **2013**, *15*, 16819–16827.

(39) Zhang, L.; Xia, Z. *J. Phys. Chem. C* **2011**, *115*, 11170–11176.

(40) Lin, Z.; Song, M.; Ding, Y.; Liu, Y.; Liu, M.; Wong, C. *Phys. Chem. Chem. Phys.* **2012**, *14*, 3381–3387.

(41) Jeon, I.-Y.; Yu, D.; Bae, S.-Y.; Choi, H.-J.; Chang, D. W.; Dai, L.; Baek, J.-B. *Chem. Mater.* **2011**, *23*, 3987–3992.

(42) Lu, Y.-F.; Lo, S.-T.; Lin, J.-C.; Zhang, W.; Lu, J.-Y.; Liu, F.-H.; Tseng, C.-M.; Lee, Y.-H.; Liang, C.-T.; Li, L.-J. *ACS Nano* **2013**, *7*, 6522–6532.

(43) Lv, R.; Li, Q.; Botello-Méndez, A. R.; Hayashi, T.; Wang, B.; Berkdemir, A.; Hao, Q.; Elías, A. L.; Cruz-Silva, R.; Gutiérrez, H. R.; Kim, Y. A.; Muramatsu, H.; Zhu, J.; Endo, M.; Terrones, H.; Charlier, J.-C.; Pan, M.; Terrones, M. *Sci. Rep.* **2012**, *2*, 586.

(44) Qu, L.; Liu, Y.; Baek, J.-B.; Dai, L. *ACS Nano* **2010**, *4*, 1321–1326.

(45) Zhang, C.; Fu, L.; Liu, N.; Liu, M.; Wang, Y.; Liu, Z. *Adv. Mater.* **2011**, *23*, 1020–1024.

(46) Feng, L.; Chen, Y.; Chen, L. *ACS Nano* **2011**, *5*, 9611–9618.

(47) Deng, D.; Pan, X.; Yu, L.; Cui, Y.; Jiang, Y.; Qi, J.; Li, W.-X.; Fu, Q.; Ma, X.; Xue, Q.; Sun, G.; Bao, X. *Chem. Mater.* **2011**, *23*, 1188–1193.

(48) Dieter A. Schluter, Craig Hawker, J. S. *Synthesis of Polymers: New Structures and Methods*; Wiley -VCH, 2012.

(49) Yokoyama, T.; Yokoyama, S.; Kamikado, T.; Okuno, Y.; Mashiko, S. *Nature* **2001**, *413*, 619–621.

(50) Takada, M.; Tada, H. *Chem. Phys. Lett.* **2011**, *514*, 94–97.

(51) Theobald, J. A.; Oxtoby, N. S.; Phillips, M. A.; Champness, N. R.; Beton, P. H. *Nature* **2003**, *424*, 1029–1031.

(52) Grill, L.; Dyer, M.; Lafferentz, L.; Persson, M.; Peters, M. V; Hecht, S. *Nat. Nanotechnol.* **2007**, *2*, 687–691.

(53) Hipps, K. W.; Scudiero, L.; Barlow, D. E.; Cooke, M. P. *J. Am. Chem. Soc.* **2002**, *124*, 2126–2127.

(54) Hecht, S. *Angew. Chemie Int. Ed.* **2003**, *42*, 24–26.

(55) Hla, S.-W.; Bartels, L.; Meyer, G.; Rieder, K.-H. *Phys. Rev. Lett.* **2000**, *85*, 2777–2780.

(56) Yang, X.; Dou, X.; Rouhanipour, A.; Zhi, L.; Räder, H. J.; Müllen, K. *J. Am. Chem. Soc.* **2008**, *130*, 4216–4217.

(57) Matena, M.; Riehm, T.; Stöhr, M.; Jung, T. A.; Gade, L. H. *Angew. Chem. Int. Ed. Engl.* **2008**, *47*, 2414–2417.

(58) Perepichka, D. F.; Rosei, F. *Science* **2009**, *323*, 216–217.

(59) Gutzler, R.; Walch, H.; Eder, G.; Kloft, S.; Heckl, W. M.; Lackinger, M. *Chem. Commun. (Camb).* **2009**, 4456–4458.

(60) Walch, H.; Gutzler, R.; Sirtl, T.; Eder, G.; Lackinger, M. *J. Phys. Chem. C* **2010**, *114*, 12604–12609.

(61) Kimura, N.; Takamuku, S. **1995**, *1*, 8023–8024.

(62) Otero, G.; Biddau, G.; Sánchez-Sánchez, C.; Caillard, R.; López, M. F.; Rogero, C.; Palomares, F. J.; Cabello, N.; Basanta, M. A.; Ortega, J.; Méndez, J.; Echavarren, A. M.; Pérez, R.; Gómez-Lor, B.; Martín-Gago, J. A. *Nature* **2008**, *454*, 865–868.

(63) Cai, J.; Ruffieux, P.; Jaafar, R.; Bieri, M.; Braun, T.; Blankenburg, S.; Muoth, M.; Seitsonen, A. P.; Saleh, M.; Feng, X.; Müllen, K.; Fasel, R. *Nature* **2010**, *466*, 470–473.

(64) Bronner, C.; Stremlau, S.; Gille, M.; Brauße, F.; Haase, A.; Hecht, S.; Tegeder, P. *Angew. Chemie* **2013**, *52*, 4422–4425.

(65) Pinardi, A. L.; Otero-Irurueta, G.; Palacio, I.; Martinez, J. I.; Sanchez-Sanchez, C.; Tello, M.; Rogero, C.; Cossaro, A.; Preobrajenski, A.; Gómez-Lor, B.; Jancarik, A.; Stará, I. G.; Starý, I.; Lopez, M. F.; Méndez, J.; Martin-Gago, J. A. *ACS Nano* **2013**, *7*, 3676–3684.

(66) Pinardi, A. L.; Martin-gago, J. A. *ACS Nano* **2013**, 3676–3684.

(67) Cai, J.; Pignedoli, C. A.; Talirz, L.; Ruffieux, P.; Söde, H.; Liang, L.; Meunier, V.; Berger, R.; Li, R.; Feng, X.; Müllen, K.; Fasel, R. *Nat. Nanotechnol.* **2014**, *9*, 896–900.

(68) Zhang, Y.; Zhang, Y.; Li, G.; Lu, J.; Lin, X.; Du, S.; Berger, R.; Feng, X.; Müllen, K.; Gao, H.-J. *Appl. Phys. Lett.* **2014**, *105*, 023101.

(69) Delaney, C.; Perera, K. S. D.; Draper, S. M. *Pt Complexes of Novel Polypyridyl Ligands*; Trinity College Dublin, 2014.

(70) Pfaff, M.; Müller, P.; Bockstaller, P.; Müller, E.; Subbiah, J.; Wong, W. W. H.; Klein, M. F. G.; Kiersnowski, A.; Puniredd, S. R.; Pisula, W.; Colsmann, A.; Gerthsen, D.; Jones, D. J. *ACS Appl. Mater. Interfaces* **2013**, *5*, 11554–11562.

(71) Hla, S.; Meyer, G.; Rieder, K.-H. *Chem. Phys. Lett.* **2003**, *370*, 431–436.

(72) Murphy, F. A.; Draper, S. M. *J. Org. Chem.* **2010**, *75*, 1862–1870.

(73) Barth, G.; Linder, R.; Bryson, C. *Surf. Interface Anal.* **1988**, *11*, 307–311.

(74) Pinardi, A. Tailoring on-surface chemistry of (hetero) aromatics on transition metal surfaces, Universidad Autonoma De Madrid, 2013.

(75) Palma, C. *J. Am. Chem. Soc.* **2014**, *136*, 4651–4658.

4 Discotic Liquid Crystals

4.1 Introduction

As far back as 1839 Edmond Becquerel investigated the first photoelectrochemical phenomenon, in which two illuminated platinum electrodes immersed in a silver chloride solution produced an electrical current. This has become known as the Becquerel effect and is the basis for the photovoltaic phenomenon seen in solar cells. Solar cells, as we understand them today, were first introduced by Bell Labs in the 1950s. The first inorganic solar-cells were based on silicon and were subsequently modified in the following decade for incorporation into rockets. These technologies were based on classic crystalline semiconductors, in which the inorganic material absorbs a continuous spectrum of solar light and offers efficient transport of charge, coupled with wide conduction and valence bands. It was almost another thirty years before the advent of the first heterojunction device by Tang *et al.*, which was the tipping-point for such technologies, demonstrating that an efficiency of 1% was possible.[1] Subsequent years showed much publication on the use of organic dyes, polymers and C_{60} dyads or triads being used in heterojunction and bulk heterojunction cells, with efficiencies up to 5% demonstrated for all-carbon systems. The 1990s saw the introduction of a parallel direction of research, upon the reporting of dye-sensitized colloidal films of TiO_2 used in 'Grätzel Solar Cells'.[2] Grätzel cells were low cost and relatively high efficiency alternatives to the research at the time. Much work in this field since has concentrated on derivations of the photosensitizers used, with ruthenium (II) and osmium (II) complexes breaking previously-held records for solar conversion, under standard air-mass 1.5 irradiation.[3,4]

Although having lost some traction in the race for efficiencies over the last decade, organic photovoltaic (OPVs) have experienced somewhat of a renaissance in the past few years. This is owed to their low cost, low weight and high flexibility, and also to the recent ability to print a module in a continuous process. Recent research has shown that OPVs may actually hold considerable potential to disrupt other competing technologies through very low environmental impact and significantly shorter payback windows. The industry however has become incredibly reliant on efficiency as the sole metric for comparison. In this regard OPVs have continued a slow and steady improvement over the past 10 years, linked at least partially to the progression of processing technologies such as printing, coating and roll-to-roll deposition. Focused research and standardised testing protocols, established by the 'International Summit on Organic Photovoltaic Stability' (ISOS), have combined with recent improvements in design and stability to demonstrate

the viability of OPVs. Figure 4.1 illustrates the exponential rise in certified efficiencies, as published in 'Progress in Photovoltaics: Research and Applications' and collated by Sariciftci *et al.*[5] Due to the limitations imposed by some large-scale processing it must be remembered, as is the case with many technologies, that commercial modules in mass production ultimately yield lower efficiencies.

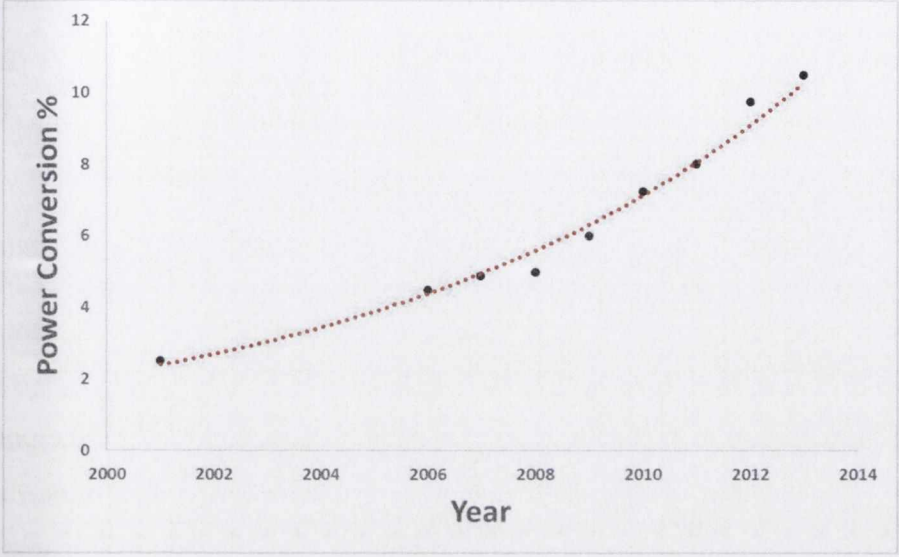

Figure 4.1: Maximum power conversion efficiencies of single-junction organic solar cells from 2001-2013.[5]

At an elementary level, OPV systems function through a four step process based on interactions between donor (D) and acceptor (A) portions, which account for the transport of holes and electrons respectively. Historically, effective donors have been made from conjugated polymers and acceptors from fullerene-type molecules. The absorption of a photon of light promotes an electron from the HOMO of the donor material, as seen in Figure 4.2 (**1**). Migration as an exciton, followed by charge separation generates an electron in the LUMO of the acceptor material (**2**). Subsequent movement of an electron to the cathode, balanced by movement of a hole to the anode (**3** + **4**) creates a current through an external circuit. Countless areas of development have been seen to affect the efficiency of the cell, such as light absorption, diffusion of the exciton, the nature of the D/A boundary and migration of the free negative charge through the acceptor material. The disordered nature of organic films can result in a propensity for charge recombination at this stage, thus greatly reducing the efficiency of currently transport.

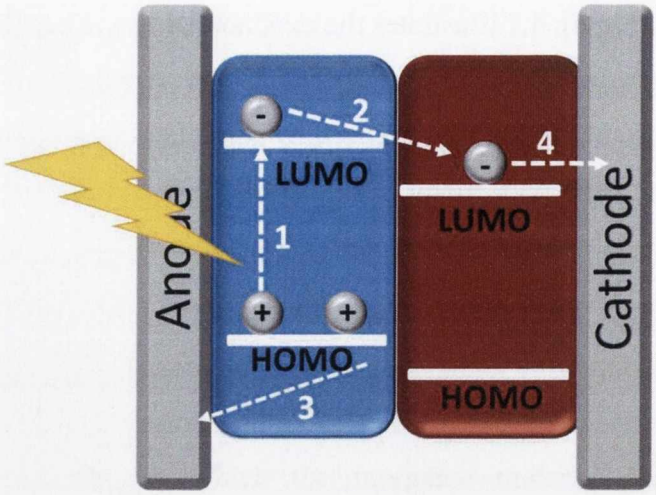

Figure 4.2: Simplified operation of an OPV; blue represents donor material, red represents acceptor material.

4.1.1 Development of Heterojunctions

For each of the steps shown in Figure 4.2 it is also possible to assess the potential for increasing efficiency in a four-fold manner: by increasing absorption, improving diffusion, inducing charge dissociation and inhibiting recombination. Organic materials can have absorption profiles which are quite narrow in their range. This profile can be reliant on the solid state absorption of the molecule and has a very complicated relationship with the absorption seen in solution. It is therefore possible to also improve efficiency by the addition of a dye, chosen because of its spectral overlap with the solar emission spectrum. Of great importance is the nature of these compounds' deposition within the cell. For a larger film thickness the presence of optical interference can prove detrimental to efficiency and operation. In accordance with Snell's law, the standing-wave at the interface of different layers can result in interference due to the variation of refractive index, if the wavelength of the incident light is larger than the thickness of the film it is incident upon. Upon generation of an exciton, the newly generated electron-hole pair remain localised on the donor molecule and rely on modes of transport (such as movement along a polymeric chain or hopping between thin layers of ionomers) to diffuse to the interface with an acceptor molecule. Minimising this distance has a direct influence on the time taken for the movement to occur. Ultimately this has a profound effect on the efficiency of the device, as exciton generation must occur within the diffusion length to the closest D/A interface. This is the basis for bulk-heterojunction systems, as for many polymeric structures intermixing on the nanoscale is required between donor and acceptor molecules.[6]

Separation of the charged pair in a heterojunction environment occurs only if the binding energy of the exciton is lower than the energy gap between both LUMO levels of donor and acceptor, otherwise the dissociative process is not energetically viable and the generation of free charges is not facilitated. The use of charge transport materials can prove integral to the migration of holes and electrons and can aid the dissipation and collection of charge within a cell. The ability to control and predict the deposition and morphology of molecules has always been a challenge for the materials chemist. In OPV devices, this morphology greatly impacts on the behaviour of an exciton at the D/A boundary. An endless number of blends of nanotubes, polymers and fibres have all been documented as potential matrices, but there is still no consensus on the ideal morphology at the nanoscale. Shown in Figure 4.3 are some orientations of heterojunctions that have been previously studied. Figure 4.3 (a) shows a very fine dispersion of D/A material which can optimise charge generation, but ultimately falls short in the transport of charge. A much improved morphology for charge-transport is seen in Figure 4.3 (b), but charge generation is dramatically reduced as it relies on the proximity of D/A molecules. Figure 4.3 (c) shows a situation which finds compromise between both of the previous arrangements. Practically, this system experiences limitations due to the intensive nature of generating such nano-patterns.

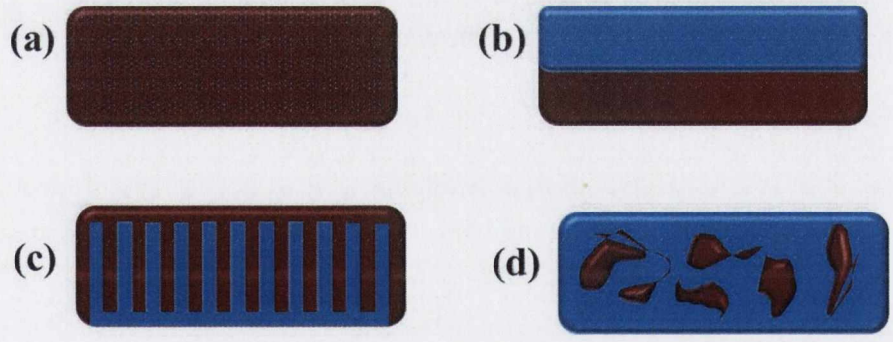

Figure 4.3: Common types of nanopattern seen in heterojunction systems: (a) dispersion; (b) bilayer stack; (c) ordered nanopattern; (d) real bulk heterojunction.

In reality, the morphology of commonly-used heterojunction D/A mixes is more likely to resemble that seen in Figure 4.3 (d). Research has also shown that intimate mixing, such as that seen in dyads and molecular double cables can lead to recombination and poor charge-carrier capabilities, most likely due to the exceptionally small mean-free path.[7] The varying effects of these nanopatterns reinforce the importance of mixing, morphology and coverage between donor and acceptor molecules within OPVs.

Discotic liquid crystals (DLCs) (a class of p-type semiconductor) can be used to great effect for OPV application, owing mainly to the ease of their solution processing and their self-organisation properties. The ability to self-assemble into hierarchical structures through supramolecular interactions is a vital characteristic in the control of molecular orientation. DLCs can efficiently transport charge between molecules aligned in stacks, while providing considerable insulation to inhibit charge losses. The ability to control their order at a range of length-scales, as represented in Figure 4.4, supports the potential for using them as semiconductors in a range of applications, from organic light-emitting diodes (OLEDs) to organic field-effect transistors (OFETs).[8]

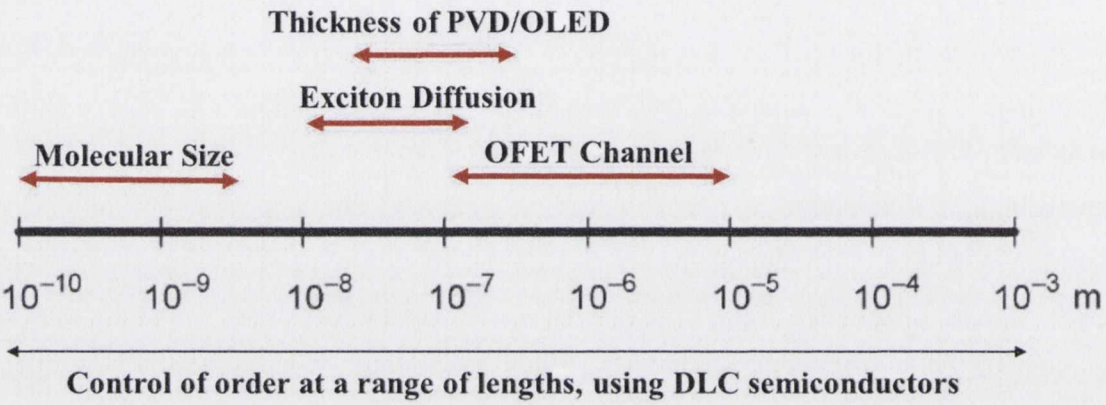

Figure 4.4: Usual lengths addressed in organic electronics which can be realised using discotic liquid crystals, as originally depicted by Geerts et al. [8]

In 2001, Schmidt-Mende reported 34% quantum efficiency and power efficiencies of 2% for the first liquid crystalline material; dodecyl substituted hexabenzocoronene, to be used as a hole-transporting layer in an OPV with perylene dye as the electron transporting layer.[9] This added yet another possibility to the suite of applications that can exploit the unique properties of liquid crystals, in addition to LEDs and OFETs. To fully understand the adaptation of this phenomenon to photovoltaic applications, it is necessary to understand the fascinating behaviour of these types molecules and the dramatic effect which molecular ordering has on their physical, photophysical, electrical and chemical properties.

4.2 Liquid Crystals

Liquid crystals (LCs) can be categorised under the headings of thermotropic and lyotropic. Thermotropic liquid crystals exhibit a phase transition that is temperature

dependent, while lyotropic liquid crystals display phase transitions that are dependent only on the presence of certain solvents.

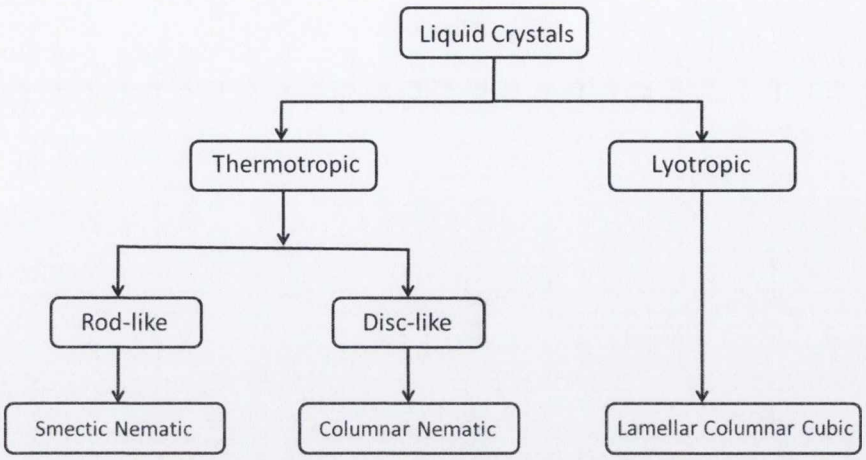

Figure 4.5: The classification of liquid crystals.

Within the sub-classification of thermotropic liquid crystals the majority of molecules exhibit a rod-like behaviour. These are termed 'calamitic', meaning rod-like, in order to distinguish them from the less common discotic class, in which molecules have a disc-like shape. The term 'mesophase' is used to define particular states of matter between solid and liquid, which for thermotropic LCs, such as calamitic and discotic, can be achieved by varying the temperature. This is represented in Figure 4.6, in which increasing temperature is seen to have an effect on the ordering of molecules.

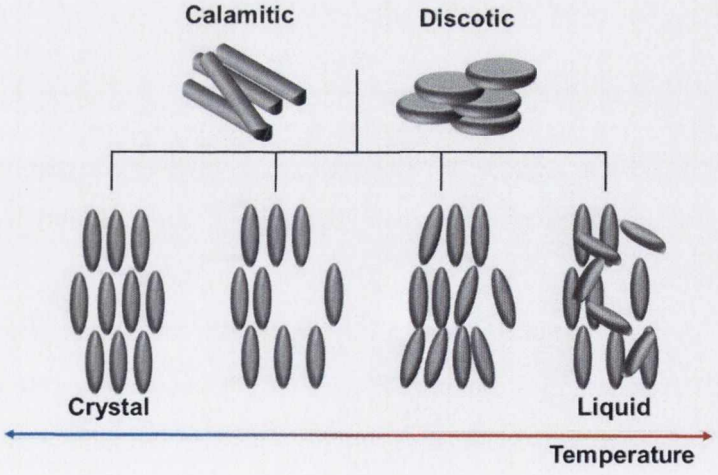

Figure 4.6: Representation of the mesophases seen in thermotropic liquid crystals.

4.3 Discotic Liquid Crystals.

Discotic Liquid Crystals (DLCs) display two different mesophases: nematic and columnar. Nematic LCs, of which there are several sub categories [some depicted in

Figure 4.7 (a) and (b)], tend only to exhibit an orientational order of molecules, but lack any distinct long-range order. Although the nematic columnar phase is characterised by columnar stacking, it displays only short range positional order and does not form two-dimensional lattices. Columnar mesophases, of which two of the most common types[10,11] are shown in Figure 4.7 (c) and (d), are classified into five distinct classes which all form two-dimensional lattices. Columar hexagonal, observed in the stacking of substituted phthalocyanines[12] is given its name due to the hexagonal packing of each molecular column. Columnar rectangular mesophases require the stacking of molecules in columns with packing in a rectangular unit. This mesophase has been observed in bis(hydrazinato) nickel(II) complexes which exhibit fascinating polymesomorphic transitions. In addition, the much less common chiral discotic nematic and nematic lateral phases also exist. Typical DLCs (of which more than several thousand exist) are large planar discs which, through non-covalent driven self-assembly, stack into columns and can exhibit intermolecular core distances of between 3.4 to 3.7 Å.

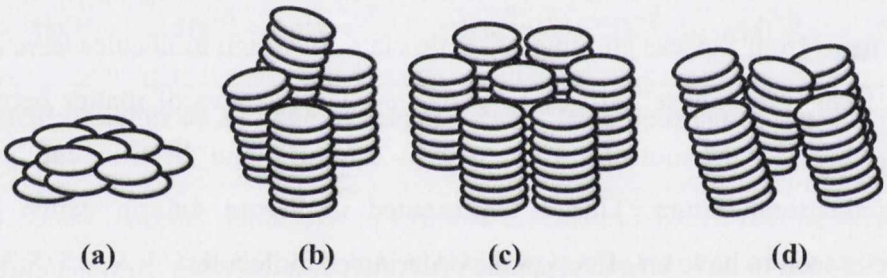

Figure 4.7: Examples of typical DLCs: (a) nematic discotic; (b) nematic columnar; (c) columnar hexagonal; (d) columnar rectangular.

The short distance between cores ensures a high electron wavefunction overlap between adjacent molecules. This large overlap is reflected in measured band widths of 1.1 eV[13] (1.0-1.4 eV for graphite) and high charge mobilities (μ) between 0.2 to 1.3 $cm^2\ V^{-1}\ s^{-1}$.[8] Alkyl substituted polyaromatics in particular have been shown to display some of the highest charge carrier mobilities observed for a DLC, in addition to the promising results obtained from their integration in bulk-heterojunction solar cells. These positive outcomes have resulted in much research on the varied substitution of such triphenylene, chrysene and coronene-like cores (shown in Figure 4.8) and their integration into functioning devices.[14,15]

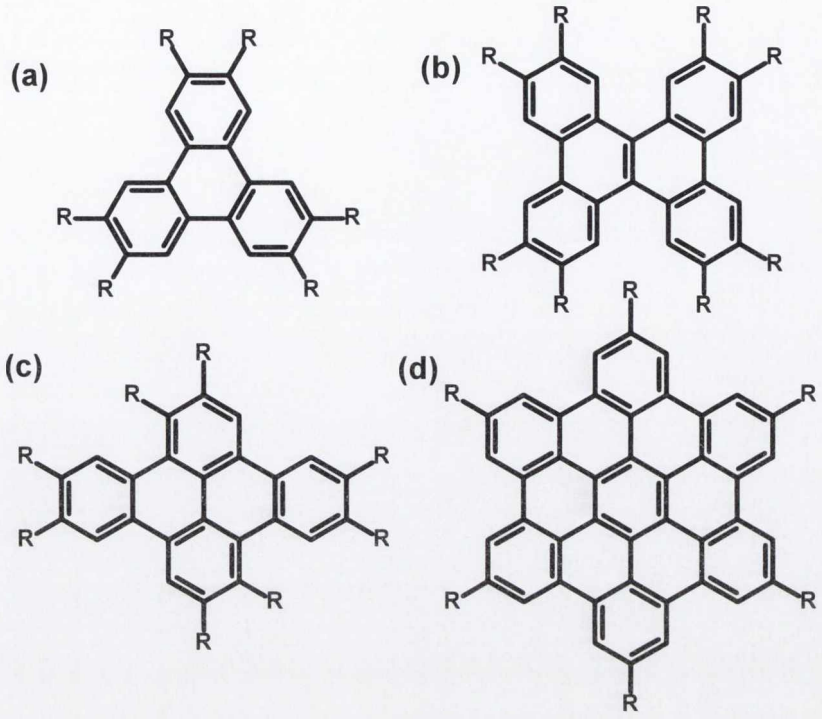

Figure 4.8: Examples of common DLC cores: (a) triphenylene; (b) dibenzochrysene; (c) dibenzopyrene; (d) hexabenzocoronene.

4.3.1 Processing and Characterisation

To successfully synthesise a range of substituted self-assembling DLCs it is necessary to consider several factors:

i. specific assembly of molecules in solution
ii. increased order in columnar mesophases
iii. modification of the all-carbon core to better stabilise hole transport
iv. substitution of the periphery with heteroatoms

Müllen *et al.* have been pioneers in successfully characterising C_{12}, C_{14} and C_{16} substituted HBC using solid-state nuclear magnetic resonance (SSNMR), atomic-force microscopy (AFM), pulse-radiolysis time-resolved microwave conductivity (PR-TRMC) and differential scanning calorimetry (DSC) analysis. These comprehensive methods of characterisation provide valuable information pertaining to the molecular packing and intra-columnar charge-carrier mobilities of the first generation of HBC based DLCs. The principal work, published in 1999, presented a HBC system with charge carrier mobility of >1 $cm^2\ V^{-1}s^{-1}$ for compounds which exhibited liquid crystalline behaviour at room temperature and high solubility in a range of organic solvents.[16,17] Substitution of the HBC with C_{14} alkyl chains showed the highest ever charge mobility measured for a DLC,

well in excess of the previous record held for hexahexylthiotriphenylene (0.1 $cm^2 V^{-1}s^{-1}$). All of the various substitutions showed high solubility in organic solvents, enabling easy processing, either by spin-coating or other solution-based methods, shown in Figure 4.9 (a). The ability to successfully deposit these materials *via* solution processing methods can prove extremely beneficial to their viability in many organic electronic devices.

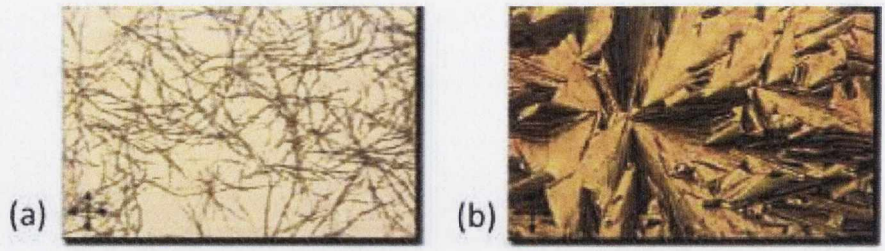

Figure 4.9: Polarised optical microscopy (POM) images of dodecyl substituted HBC reproduced from Kastler;[18] (a) from solution (tetrahydrofuran); (b) crystallization from the melt.

Solution processing has been shown to inhibit face-on stacking of the discs and to strongly promote the stacking of the molecules on their edges, as shown in Figure 4.10 (a). As charge transport occurs parallel to an insulating substrate in a FET, this is a property of much importance in the migration of charge.[19,20] This can be achieved using Langmuir-Blodgett film techniques,[21] zone-casting[22] and solution-casting onto polytetrafluoroethylene (PTFE).[21] In general, with substrates of a different polarity, an edge-on arrangement serves to minimise the surface contact of molecules. Work by Van de Craats *et al.* has recently found that processing HBC-based DLCs using the solution casting method on rubbed PTFE produces highly-ordered films, with molecules parallel to the orientation axis.[23] Face-on (homeotropic alignment) can be achieved by cooling certain DLCs from the melt (Figure 4.9 (b)).

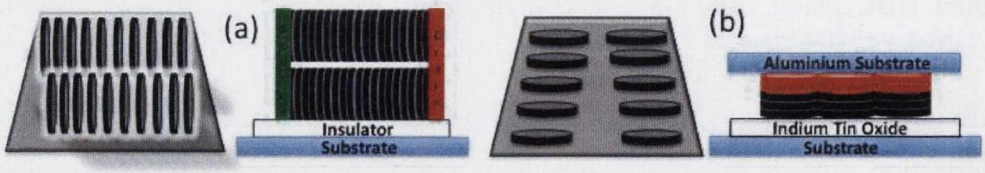

Figure 4.10: Representation of (a) a field-effect transistor (b) a photovoltaic device and the ideal arrangement of discotic molecules in each; "edge-on" for FETs and "face-on" for photovoltaic devices. Black discs represent DLC, red discs represent perylene diimide.

Mackenzie *et al.*[9] have documented the incorporation of HBC-PhC_{12} as a hole-transport layer in an organic thin layer solar-cell, using perylene diimide as the electron-transporting layer (Figure 4.10 b). Displaying external quantum efficiencies of 34%, these devices are comparable with some of the best results ever seen for organic photovoltaic devices. In addition to the methods of characterisation for DLCs already mentioned, two other useful methods which are commonplace in liquid-crystal characterisation require some description.

4.3.1.1 Small Angle Neutron Scattering (SANS)

Neutrons behave with both a wave and particle nature and can interact with other nuclei either *via* nuclear or magnetic scattering. A beam of neutrons can be scattered elastically by a single nucleus. If the nucleus is treated as a single point and any energy exchange disregarded, then the scattering of the neutron beam as a function of interaction potential can be achieved. This in turn means that we can represent the disruption of the beam, with respect to a point nucleus in terms of degree of scattering as shown in Figure 4.11, thereby providing information about the distance between the nucleus and neutron (r), which is in the range of 1 Å.

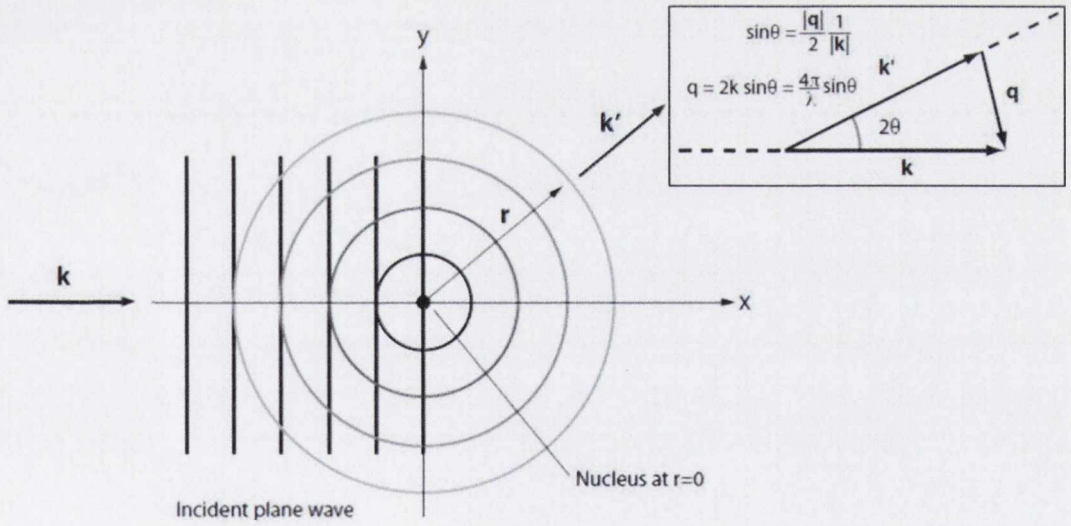

Figure 4.11: Depiction of elastic neutron scattering. Reproduced with edits from Jackson.[24]

It is possible however to apply these considerations to lengths which are much longer than just an atomic radius. By applying scattering length density as a function of distance from one molecule to another it is possible to deal with a macroscopic cross section across a whole sample, this is known as Small Angle Neutron Scattering (SANS). These

measurements analyse neutrons scattered into the small angle region and are therefore used to study order on the nanoscale. Macroscopic cross sections are collected as a function of the scattering vector (q) and are normally presented as a 1-dimensional scattering pattern, as shown in Figure 4.12. This allows for contrasting of relative scattering and can therefore give much information about the scattering of neutrons per unit length. By using the Fourier transform of the scattering length density it is possible to interpret the data to analyse the shape and form of particles. Applying a structure factor, such as the core-shell cylindrical model shown in Figure 4.12 (inset), this method can be used to calculate scattering with respect to a cylindrical form factor of length L and radius R. This serves to very accurately give information about the behaviour of the columnar packing of disc-like molecules over a range of temperatures; a technique ideally suited to discotic thermotropic liquid crystals.

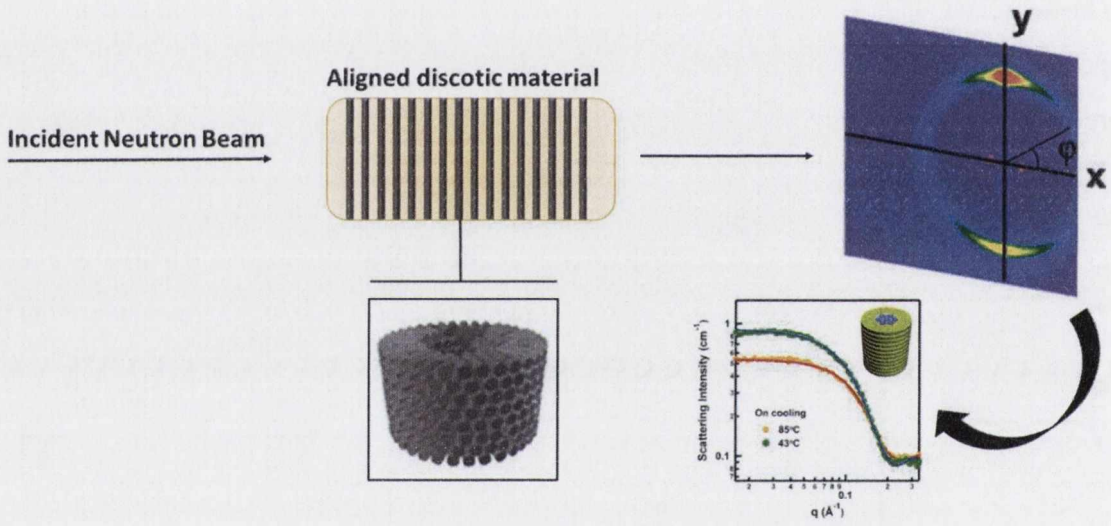

Figure 4.12: Simplified schematic for the irradiation of an aligned discotic material with a neutron beam, showing the profile of scattered neutrons and resulting curves with a theoretical form factor model. Inset shows behaviour of C_{12}HBC, measured by Choi et al.[25]

4.3.1.2 Polarising Optical Microscopy

Liquid crystals are also birefringent - they exhibit two types of refraction dependent on the manner in which light is incident upon them, with respect to the unit vector n (the 'director'). When unpolarised light is incident on a birefringent sample it means that its two elements travel at different velocities and therefore result in a difference of phase. This is represented in Figure 4.13. This phenomenon can be used as a tool for the analysis

of liquid crystal samples: using polarisers, light can be aligned to angles between both fast and slow components of the sample.

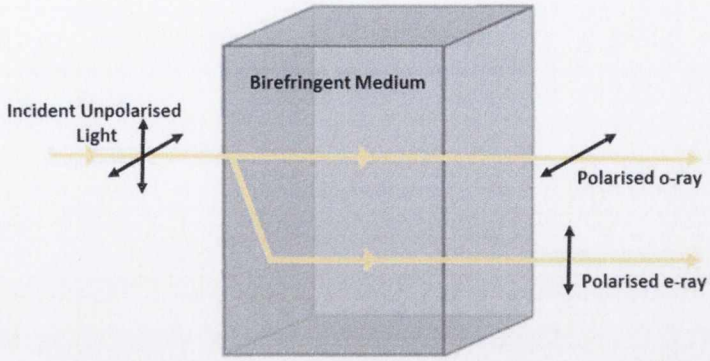

Figure 4.13: Light travelling through a birefringent material, taking on two possible pathways.

Upon passing through the first polariser, light is linearly polarised. Once this light is incident upon a birefringent sample it splits into two orthogonal beams, as indicated in Figure 4.13; one parallel to the fast axis and one to the slow. These orthogonally polarised beams exhibit different refractive indices and therefore one beam is retarded with respect to the other, as seen in Figure 4.14. After passing through a second polariser, resulting dark and bright regions will be created, depending on the orientation of incident light from the first polariser. Therefore, for a liquid crystal sample, a resulting image is generated which can be used to map areas of varying thickness and birefringence, shown in Figure 4.14.

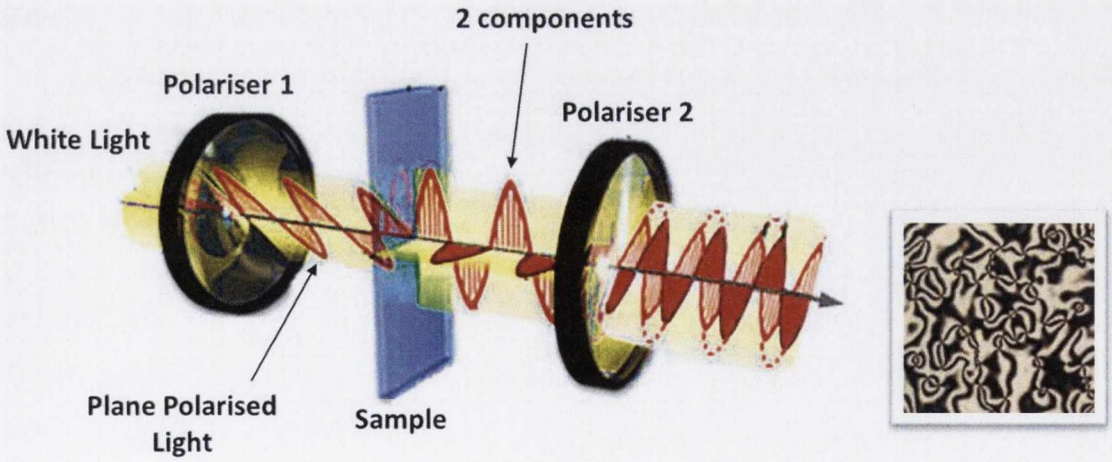

Figure 4.14: Simplified diagram of polarised light microscopy on a liquid-crystal sample. Inset shows image of a nematic liquid crystal using crossed polarizers. Reproduced with edits from Nikon MicroscopyU.[26]

A combination of polarising optical microscopy (POM) and temperature variation is an extremely useful tool for the analysis of DLC samples. This technique, known as variable temperature polarising microscopy allows for analysis of transition temperatures in thermotropic liquid crystals, as a phase change from anisotropic to isotropic stops the birefringent phenomenon.

4.3.2 Synthetic Strategies

In addition to physical approaches for imposing different forms of molecular ordering on DLCs, it is also possible to strategically control long range ordering by relatively simple synthetic changes to the shape, size and nature of substitution on the all-carbon polyaromatic core. The first example of this was carried out by Van de Craats and Warman.[27] From PRTMC studies of various core sizes, they predicted a relationship between 1-dimensional charge mobility and the size of the discotic core. Interestingly, it is also noted that, although the nature of alkyl substitution affects the mesophase transition temperatures, it is seen to have no notable effect of charge mobility. $\Sigma\mu_{1D}$, the sum of mobility of holes (μ_+) and electrons (μ_-) is calculated from Equation 4.1, in which 'n' is the number of carbon atoms in the aromatic core. By definition, this also states that for a core that moves to infinite size, the charge mobility approaches 3 $cm^2V^{-1}s^{-1}$, as is the case for graphite. From a fundamental basis, this approximate relationship is in line with predictions about increasing core size, as larger polyaromatic cores would be expected to increase orbital overlap with adjacent molecules. An increase in cohesive forces would also improve interactions with adjacent molecules and ultimately minimise disorder.

Equation 4.1: The empirical relationship, Suggested by Van de Craats and Warman relating one-dimensional charge carrier mobilities to the size of an aromatic core.[27]

$$\Sigma\mu_{1D} = 3e\left(\frac{-83}{n}\right)$$

$\Sigma\mu_{1D}$ -one dimensional charge mobility
n – number of atoms within the core

In a similar manner, the application of semi-classical Marcus Theory has also been used to garner information about the relationship between the transport of charge *via* the hopping mechanism and other properties of the organic semiconductor. Marcus Theory proposes a rate of hopping between molecules which serves to accurately model the transport of charge in semi-ordered arrays. This theoretical description suggests that the movement of charges between adjacent discs is reliant on the overlap of HOMO and LUMO orbitals, and the reorganisation energy between charged or neutral species. This

would mean that high rates of transfer would require small values of reorganisation energy, combined with a maximum possible transfer integral between molecules. When simplified, the findings show a direct relationship between hopping frequency and charge mobility perpendicular to the stacks (see Equation 4.2). Most important is the inverse proportionality between the hopping rate and distance between adjacent molecules (*d*), represented in Einstein's relation.

Equation 4.2: Relationship between the hopping rate from disc to disc and interdisc distance.

$$v = \frac{k_B T \mu_{II}}{ed^2}$$

v – hopping rate
d – distance between adjacent discs
k_B – Boltzmann constant
T – Temperature
μ_{II} –Charge-carrier mobility

Both of these findings show the importance of disc size and the minimisation of the intermolecular distances, and have formed the basis for most of the synthetic advances made in DLCs over the past decade. As a result, DLC research moved from the smaller triphenylene-based structures to the larger hexabenzocoronene (HBC). HBC could serve as a larger, flat and highly-conjugated core, which could be easily modified with respect to substitution, symmetry and size. A larger disc will result in stronger π-π interactions and ultimately behave as graphitic subunits. Geerts *et al.* succeeded in providing a useful practical study of extended HBC-like molecules of sizes 24-132 aromatic carbons, some of which are presented in Figure 4.15.[8] It is worth noting that for larger PAH cores, above approximately 60 carbon atoms, the crude experimental approximation in Equation 4.1 fails to accurately predict $\Sigma\mu_{1D}$ and appears to deviate from core size alone, as shown for Figure 4.15 (c). This is reported to be a result of the effects of increasing π-π overlap, twinned with a decrease in average charge density. In addition to these substantial findings, work has also shown that insulation of the core with an additional phenyl ring acting as a bridge to the alkyl chain has a large effect on the thermotropic behaviour of the DLC. This results in liquid-crystalline behaviour over a range from -78 °C to 192 °C. Such a broad temperature range for LC mesophases still remains a much sought-after property for prospective compounds. This additional insulation also proved beneficial to the half-life ($t_{1/2}$) of the charge carrier, which was much longer than that for the hexagonal columnar (D_h) phase of any of the compounds without the phenyl bridge. Although size

and symmetry have played a significant role in the development of DLCs to this point, there still exists quite a body of work which has focused on the improvement of liquid-crystalline behaviour, transition temperature and phase morphology. One such strand of research has focused on the inclusion of heteroatoms into DLCs.

Compound	Atoms in Core	λ_{max}(nm)	$\Sigma\mu_{1D}$($cm^2V^{-1}s^{-1}$)	
			Found	Calculated
a	24	331	0.1	0.09
b	60	410	0.23	0.75
c	96	462	0.2	1.26

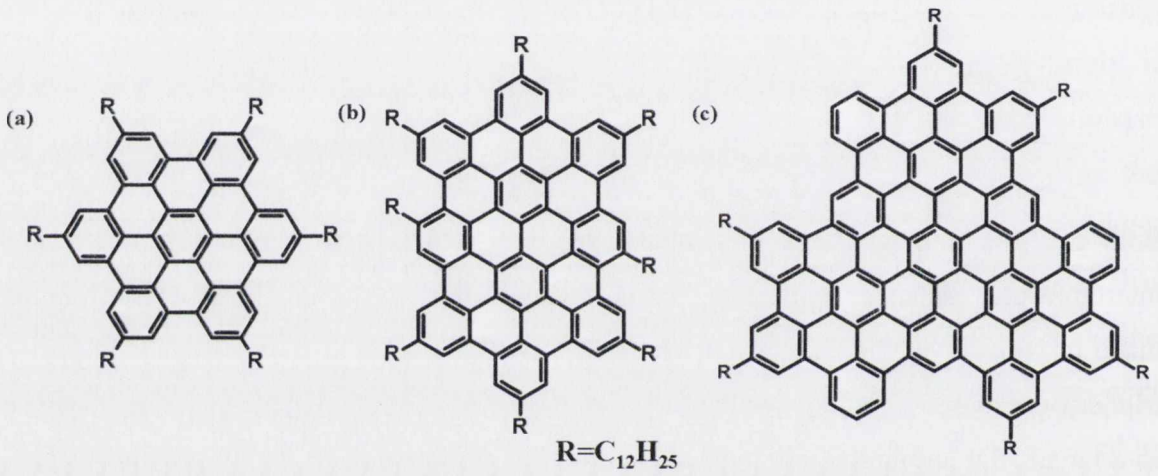

Figure 4.15: Comparison of three extended HBC cores with respect to core-size and charge mobility.

4.3.3 Heteroatoms in hexabenzocoronene-based discotic liquid crystals

The advantage of introducing heteroatoms to DLCs is threefold:

(1) directly affecting the semiconducting nature of the DLC (integration of electron donors and acceptors)
(2) presenting the possibility of a molecular double-cable, giving two charge transfer pathways within the stacked molecules
(3) lowering symmetry and stabilising the mesophases by disfavouring crystallisation.

A noteworthy example is the substituted triphenylene derivative, shown in Figure 4.16 (a), synthesised by Gearba *et al.*[28] It shows highly-efficient intermolecular H-bonding, which results in a very short 3.18 Å interdisc distance. Introduction of heteroatoms to HBC derivatives may be achieved *via* variation of both connecting groups and side-chains. The preparation of halogenated species using a bottom-up synthesis is the starting platform for the synthesis of many triarylamine-substituted derivatives. The compound shown in Figure 4.16 (b) exhibits liquid crystalline mesophases above 90 °C and charge carrier mobilities above 0.2 cm^2 V^{-1} s^{-1}.[29] Using the same synthetic starting-point, intriguing amphiphilic derivatives can also be synthesised. Attaching alkyl and oligoether chains to the core promotes interdigitation between the chains and discs, thereby creating large nanotubes comprising *ca.* 50,000 molecules which inhibit the formation of multilayer structures in polar solvents.[30] In the past decade, the work of Williams *et al.* with low-symmetry nitrogen-containing benzo triphenylene derivatives[31,32] and that of Würthner[33] and Langhals[34] incorporating peripheral perylene diimide dyes into DLCs, all reinforce the potential of successfully synthesising nitrogen-doped DLCs with competitive charge-mobility carrying properties. Molecules bearing electron withdrawing groups, such as NO_2 and CN are seen to exhibit D_h mesophases over particularly broad temperature ranges, while those substituted with electron-donating groups melt directly from crystalline state to isotropic liquid. As the π-π stacking of these disc-like molecules can be directly affected by the minimisation of repulsive forces (seen upon the addition of electron-withdrawing groups) it is easily rationalized that stabilisation is observed upon the addition of nitrogen atoms in the core. The structural features mentioned hitherto result in high charge carrier mobilities and liquid crystalline behaviour over a wide temperature range. This offers much promise for the application of heteroatom-substituted planar graphene fragments in field-effect transistors, PV cells and various other molecular electronic devices.

Compound	Core Size	Number of derivative compounds	$\Sigma\mu_{1D}(cm^2V^{-1}s^{-1})$		Phase Transition Temperature (°C)	
			Discotic (D_h)	Crystalline(K)	K-D	D-Iso
a	18	4	0.04	0.08	20	250
b	42	3	0.26-0.38	1.13	90	120
c	24	4	0.11	1.3	178	292
d	34	3	0.15-0.21	0.24	53	>200
e	29	1	0.24	0.24	113	161
f	40	16	0.042-0.27	0.67	97	300

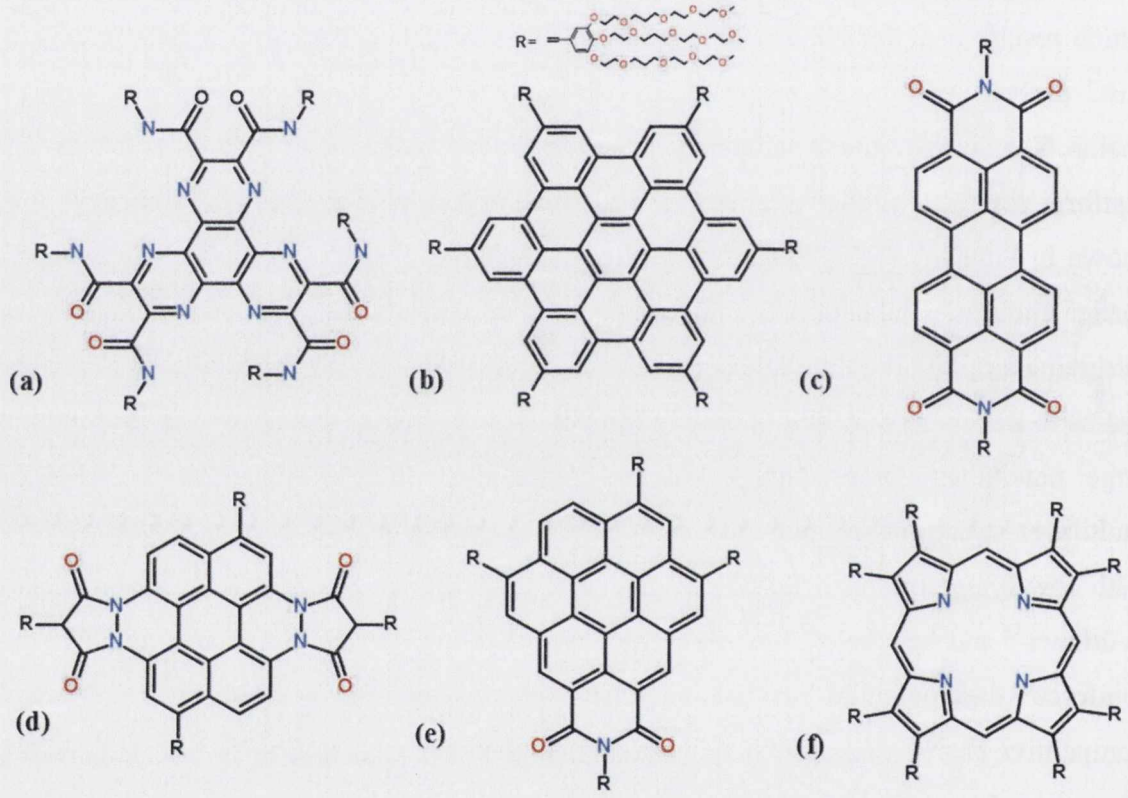

Figure 4.16: Some examples DLCs containing heteroatom substitution, the table provides a comparison of charge mobilities and phase transition temperatures.

The following sections continue the synthetic investigation of substituted nitrogen-containing polyaromatic cores. In addition to the extremely close packing of diaza and tetraaza molecules shown in previous chapters, other members of the nitrogen heterosuperbenzene (NHSB) family have been shown to stack in a columnar fashion in solution. In the solid-state the molecules arrange in a helical nature due the polarity of the nitrogen substitution. This is best represented by the synchrotron molecular structure of NHSB, in which the nitrogen atoms (represented by spheres) are rotated through adjacent

molecules, to form a helical pattern through the stack. Figure 4.17 (a) shows the packing in the crystal lattice, with chloroform and water solvent molecules present. Figure 4.17 (b) shows a simplified representation with the removal of the *tertiary*-butyl substituents, allowing for the helical stacking of the molecule to be clearly observed. Alkyl substitution of such cores has been shown to restrict rotation of the core and raise the barrier to dynamic disorder. The permanent dipole in these pyrimidyl substituted molecules was expected to lock the molecules in such a rotation, resulting in a head-to-tail intermolecular arrangement. The electron mobility between adjacent molecules may well be improved as a result of the overlap between pyrimidyl and aromatic frontier orbitals from molecule to molecule. Additionally, the inclusion of nitrogen atoms will also bring a range of desirable qualities, such as thermal stability and efficient photoluminescence.

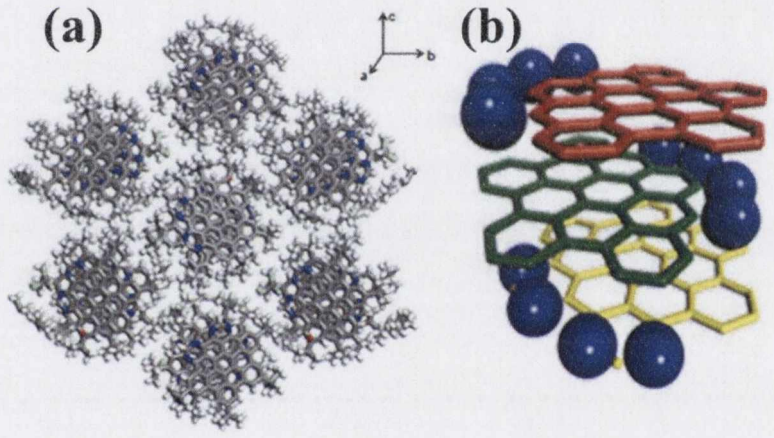

Figure 4.17: (a) Synchrotron structure of NHSB depicting the helical nature of packing; (b) packing of adjacent moelcules, tertiary-butyl substituents and hydrogen atoms removed for clarity. Reproduced with edits from Lankage.[35]

4.4 Aims and Goal

Recent work within the Draper group has taken well-documented synthetic strategies for NHSB and developed these methodologies to incorporate dodecyl chains around the periphery of the doped graphene fragment, C_{12}NHSB (Figure 4.18 b).[36,37] This compound heralds a new departure for HBC-based DLCs, with the introduction of a dipole-moment in the molecule and the possibility of n-type semiconducting properties. In addition to increased solubility this molecule also offers the possibility of metal coordination, resulting in a dual-functional material that may both efficiently harvest light through the MLCT while also behaving like a molecular wire, through the stacking of aromatic cores.

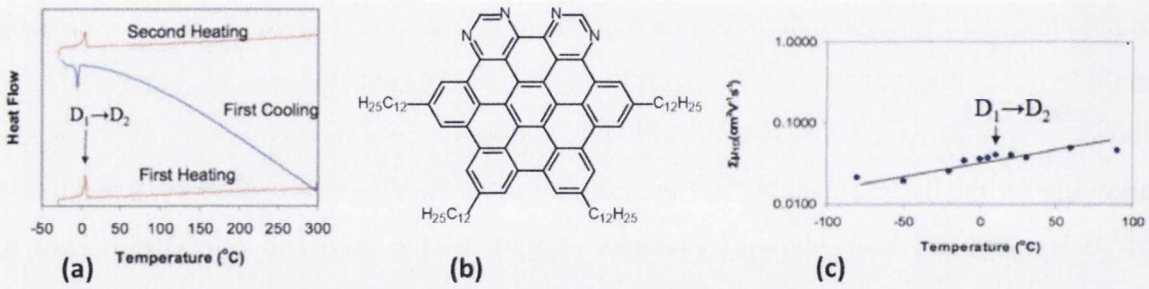

Figure 4.18: (a) Differential scanning calorimetry (DSC) trace for C_{12}NHSB; (b) C_{12}NHSB synthesised by Draper et al.; (c) Charge mobility of C_{12}NHSB as a function of temperature.

C_{12}-NHSB shows promising thermal stability, comparable with that reported for many all carbon systems. Decomposition is seen to occur at 470 °C and is attributed to the loss of dodecyl substituents. DSC analysis, as seen in Figure 4.18 (a), shows a phase transition at 5 °C, which exhibits an enthalpy change indicative of a conformational change within the mesophase (20 kJ mol^{-1}) and exhibits no other phase changes detected in the temperature window. Crystalline to liquid crystalline enthalpy changes are observed with a much larger enthalpy change (60-70 kJ mol^{-1}). Pulse-radiolysis time-resolved microwave conductivity (PR-TRMC) measurements of C_{12}NHSB (Figure 4.18 (c)) provided intriguing results. As is expected of discotic materials at phase transition temperatures, no sudden drop of charge mobility from maximum to minimum conductance is observed at 5 °C. This supports the assertion that the compound is liquid crystalline at all temperatures. The only other compound that exhibits this behaviour at room temperature is the phenyl insulated all-carbon analogue HBC-PhC_{12}. The charge-carrying mobility of C_{12}NHSB however, measured to be 0.05 cm^2 V^{-1} s^{-1} remains drastically lower. As a conclusion to this previous work, it is likely that the electron-rich nitrogen atoms inhibit efficient overlap of HOMO and LUMO orbitals of neighbouring molecules within the column, leading to an overall loss of conductivity and decreased close-packing. To this point however, the synthesis of this molecule has been achieved in a manner similar to other nitrogen-containing polyphenylenes, as outlined in Chapter 1. This route is ultimately hampered by some low yielding synthetic steps, in particular the introduction of the alkyl substitution and the altered reactivity as a result.

This works aims to address the shortcomings of pyrimidyl-substituted DLCs, through three distinct synthetic routes:

- Redevelopment of the synthetic route to C_{12}NHSB

- Synthesis of other nitrogen-containing analogues to counteract the effect of increased polarity, with a view to increasing intramolecular close-packing.

- Development of a new synthetic methodology to yield other derivatives, allowing for variation in the range of alkyl side-chains.

As seen in the synthesis of HBC, Mullen *et al.* have developed extremely effective routes for the formation of highly symmetric PAHs. These methodologies allow for substitution of a symmetric acetylene, followed by cyclotrimerisation to yield the polyphenylene precursor. The synthesis of the lower-symmetry nitrogen-containing analogue, however, requires bottom-up synthesis through an eight-step synthetic pathway, as discussed in Chapter 1. It is hoped that by developing and tailoring novel routes to these new compounds, inroads will be made in the development of new N-doped cores which may exhibit increased reduced conductivity losses and close-packing. These molecules offer an excellent platform for new research in the field of tuneable luminescent materials with a host of possibilities in opto-electronic devices.

4.5 Results and Discussion

4.5.1 Synthesis

A new synthesis for two alkyl substituted cyclopentadienones was developed. As outlined in Chapter 1, the synthesis of substituted cyclopentadienones is achieved *via* a two-fold Knoevenagel reaction between a suitable 1,3-diphenyl-2-propanone and 1,2-diphenylethane-1,2-dione. To begin, a new synthetic pathway for 1,2-bis(4-dodecylphenyl)ethane-1,2-dione (**27**) was planned. This route, as outlined in Scheme 4.1, involved a McMurry coupling reaction between two molecules of 4-bromobenzaldeyde in the presence of zinc powder and $TiCl_4$, furnishing *trans*-4,4'-dibromostilbene in high yield. Subsequent Negishi coupling, using $NiCl_2$(dppp) in catalytic amounts and dodecylmagnesium bromide allowed for the introduction of dodecyl chains. Bromination across the double bond was achieved using Br_2 in chloroform. The resulting off-white crystalline solid was subjected to reflux in potassium *tert*-butoxide and *tert*-butanol overnight which, *via* an elimination reaction, yielded the symmetric aryl acetylene **26**.

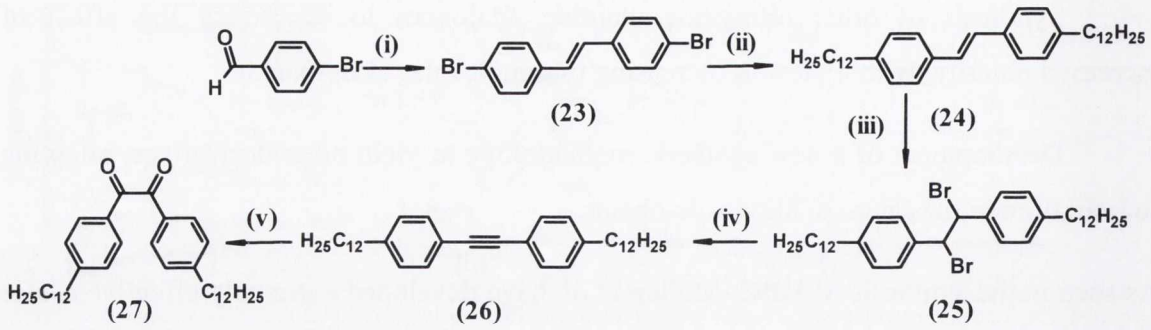

Scheme 4.1: Revised synthetic route for the synthesis of ***27****: (i) Zn, $TiCl_4$, THF, -10 °C, 6 h (82%); (ii) dodecylmagnesiumbromide, $NiCl_2$(dppp), diethyl ether, RT, 24 h (93%); (iii) Br_2, $CHCl_3$, RT, 18 h (85%); (iv) potassium tert-butoxide, tert-butanol, reflux, 20 h (74%); (v) I_2, DMSO, 155 °C, 18 h, (71%).*

Previously **27** had been synthesised *via* the lithiation of bromododecylbenzene, but poor yields and difficulty of purification meant that the oxidation of the substituted arylacetylene, shown in Scheme 4.1 (v), proved much more viable. Reacting the acetylene with iodine in dimethylsulfoxide (DMSO) at 155 °C overnight gave **27** as a pale yellow solid, in yields above 70%. The second constituent part of a substituted cyclopentadienone is the substituted 1,3-diphenyl-2-propanone, the synthesis of which is outlined in Scheme 4.2. Dodecyl benzylbromide was synthesised from the reaction of dodecylbenzene with paraformaldehyde and hydrobromic acid in acetic acid, following the method of St. Clair *et al.*[38] The solution was refluxed for 4 days to give **28**, in particularly low yield (<20%). Variation of reaction conditions such as time, temperature and concentration of reactants in the synthesis of **28** all showed no discernible effect on the yield, yet the commercial availability of the starting materials allowed the inefficient reaction to remain moderately feasible.

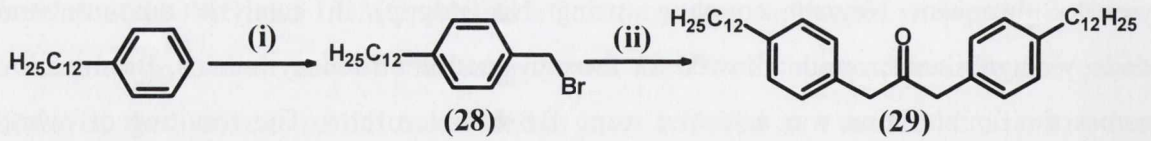

Scheme 4.2: Synthetic pathway for the formation of ***29****: (i) HBr, paraformaldehyde, glacial acetic acid, 75 °C, 4 d (14%); (ii) $Fe(CO)_5$, CH_2Cl_2/H_2O, reflux, 20 h (62%).*

Maintaining a rigorously inert atmosphere has the most profound effect of all on the success of the reaction in Scheme 4.2 (i). Unless carried out under a fully inert atmosphere the reaction is seen to favour the *meta*-substituted product. Using a much documented iron pentacarbonyl coupling in a biphasic system with tetrabutylammonium

hydrogensulfate as phase-transfer catalyst,[39] the diaryl-2-propanone derivative **29** was synthesised from **28** in moderate yield. A subsequent two-fold Knoevenagel condensation between **27** and **29** using KOH in ethanol,[40] yielded the cyclopentadienone **30** as a viscous purple oil (Scheme 4.3).

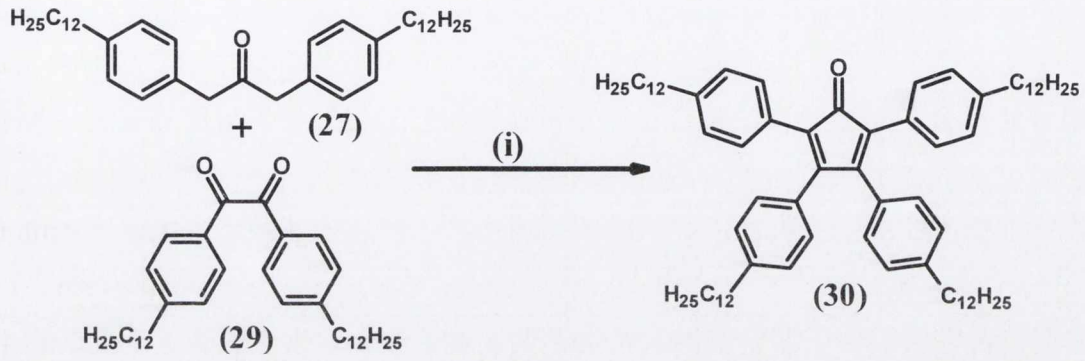

*Scheme 4.3: Synthesis of **30**: (i) KOH, C_2H_5OH, reflux, 5 min (42%).*

The synthesis of a nitrogen-containing analogue of $HBCPhC_{12}$ would also require a substituted cyclopentadienone analogue of **30**. This was approached in a similar manner to that outlined in Scheme 4.3. Starting from commercially available 4-bromobiphenyl, dodecyl substitution was achieved on a large scale and, as before, the substituted benzylbromide (**34**) was synthesised with ease. The next step however, to synthesise the biphenyl substituted 1,3-diphenyl-2-propanone was not successful, under similar conditions to **30**. Ultimately, this hampered the synthesis of a phenyl-insulated cyclopentadienone of this nature. Although, the second constituent part (1,2-bis-(4'-dodecyl-biphenyl-4-yl)-ethane-1,2-dione (**37**)) was obtained in high yield and purity, *via* a three-step route from the Friedel-Crafts acylation of 4-bromobiphenyl shown in Scheme 4.4, a different approach was still required.

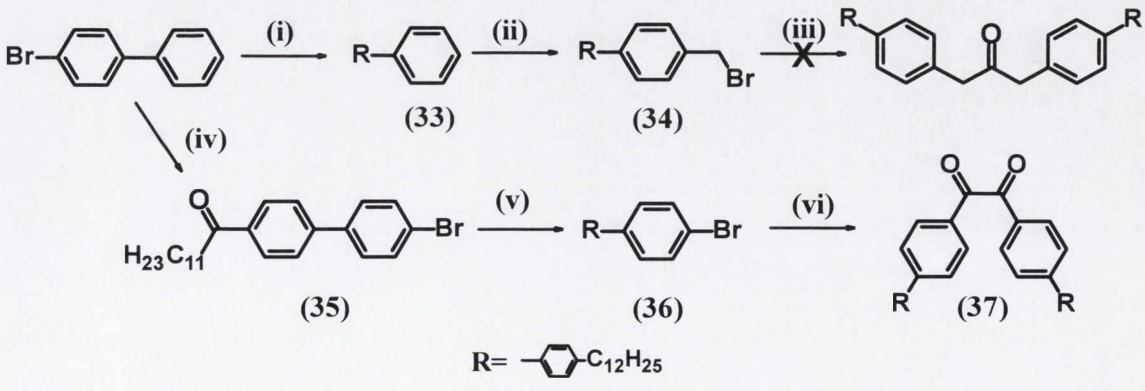

*Scheme 4.4: Synthetic route to **37**: (i) dodecylmagnesiumbromide, $NiCl_2$(dppp), diethyl ether, RT, 3 d, (57%); (ii) paraformaldehyde, HBr, glacial acetic acid, 4 days, 75 °C*

(15%); (iii) NaOH, benzyltriethylammonium chloride, $Fe(CO)_5$, CH_2Cl_2/H_2O, reflux, 15-24 h; (iv) dodecanoyl chloride, $AlCl_3$, carbon disulfide, 45 °C, 2h, (85%); (v) hydrazine hydrate, KOH, triethylene glycol, 2 h, reflux (58%); (vi) n-BuLi, THF, dimethylbenzene-1,4-diamine, -78 °C, 18 h (53%).

A solution to the problem experienced in Scheme 4.4 (iii) could be potentially addressed by coupling alkyl substituents directly to a brominated 1,3-diaryl acetone, but there existed another significant hurdle in the synthetic procedure which warranted an overall change of direction. Although successful synthesis of the cyclopentadienone analogues could provide a useful platform for the introduction of heteroatoms to form substituted polyphenylenes, *via* [2+4] Diels-Alder cycloadditions with an appropriate acetylene. This would require the synthesis of an asymmetric pyrimidyl acetylene, shown in Scheme 4.5. To achieve this, dodecanoyl bromobenzene was synthesised from the Friedel-Crafts acylation of bromobenzene, to yield (**32**), followed by a Wolff-Kisher reduction of the ketone, following a literature procedure.[41] The final step of this procedure (iii) also proved to be unsuccessful. Using a range of conventional Sonogashira methods, the reaction was extensively repeated, yet remained unfruitful. Modifying the synthetic method by varying solvent, temperature, time and catalyst all failed to yield any success. On further investigation it became apparent that Sonogashira coupling reactions involving alkyl-substituted aryl halides in the literature were limited to a small number of examples.

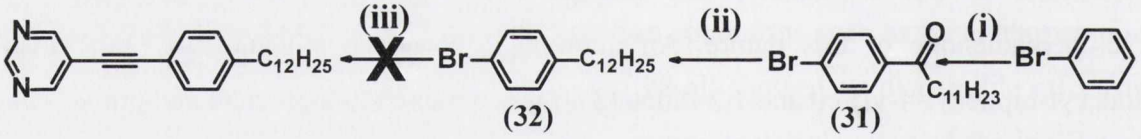

Scheme 4.5: Attempted synthetic route to dodecylphenyl pyrimidyl acetylene: (i) dodecanoyl chloride, $AlCl_3$, 50 °C, 2h, (64%); (ii) hydrazine hydrate, KOH, triethylene glycol, reflux, 2 h (65%); (iii) 5-bromopyrimidine, $Pd(PPh_3)_2Cl_2$, CuI, Et_3N, DMF, 55 °C 1-24 h and $Pd(PPh_3)_2Cl_2$, CuI, Et_3N, DMF, 110-125 °C, 20 min-200 min.

This left two conceivable solutions in the synthesis of such an asymmetric acetylene: 1) develop a method, other than Sonogashira coupling to yield a terminal acetylene, directly attached to 4-phenyldodecane. Following deprotection this may be coupled to bromopyrimidine or 2) begin with commercially available starting materials, synthesise the halo-substituted asymmetric acetylene, concluding with one of a myriad of Kumada-like couplings to attach a dodecyl chain.

Route 1 could be approached *via* the method of Corey and Fuchs by converting 4-dodecylbenzaldehyde to a 3-dibromomethylidene derivative. This could be followed by lithiation and subsequently, a Johnson-like Claisen rearrangement species would undergo an elimination reaction to yield 1-ethynyl-4-phenyldodecane. Although a very elegant synthesis, this failed to provide an efficient methodology.

Route 2, beginning with commercially available 1-bromo-4-ethynylbenzene, and making use of highly-efficient microwave synthesis, allowed for the synthesis of **38** in high yield, with a total reaction time of 4 h. Pure product was isolated *via* trituration, removing the need for laborious chromatographic techniques.

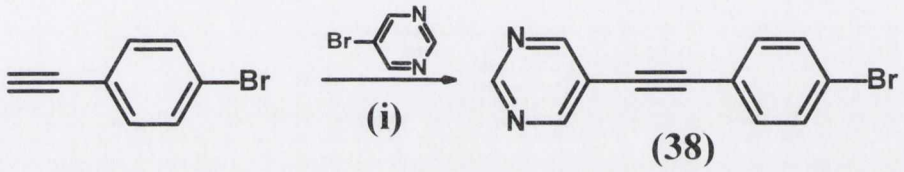

(38)

*Scheme 4.6: Synthetic route to **38**: (i) $Pd(PPh_3)_2Cl_2$, CuI, Et_3N, $\mu\lambda$, 125 °C, 50 min (63%).*

The ability to synthesise **38** provided three possible routes for the formation of a penta-substituted diazapolyphenylene;

1. Direct cycloaddition of **38** with a dodecyl-substituted cyclopentadienone, followed by coupling of an alkyl chain to the singly brominated ring.
2. Alkyl coupling directly to **38**, subsequently followed by cycloaddition with a dodecyl-substituted cyclopentadienone.
3. Cycloaddition **38** to a similarly brominated cylopentadienone, followed by complete alkyl coupling at the five peripheral positions.

Although [4+2] cycloaddition between **38** and a dodecyl-substituted cyclopentadienone such as **30** was successful, the subsequent purification and characterisation of the dodecyl-substituted polyphenylene, in the absence of field desorption mass spectrometry limited the viability of this route. It was thought to be more feasible to develop a new pathway to the chosen product, which optimised the direct route (**3**) shown above, beginning with cheap and commercially available starting-materials and allowing for full characterisation of a series of polyphenylenes, prior to attachment of the long alkyl chains. If successful, this route would also offer a much more accessible means to the C_{12}NHSB analogue mentioned previously. This would ensure that a large proportion of syntheses were centred on high yielding steps and could draw on the ample experience

within the Draper group for the purification and characterisation of such products. This would serve to circumvent any obstacles in the purification and characterisation caused by presubstitution of the starting materials. This method would yield new novel polyphenylenes which could be synthesised through a series of high-yielding steps. Substitution may be introduced directly, using either Pd- or Ni-catalysed Kumada coupling, creating a comparator to C_{12}NHSB by using a selection of long-chain alkylmagnesium bromides. Substitution, in the form of additional ring insulation, may also be introduced through Suzuki coupling using a suitably substituted phenyldodecane boronic acid.

4.6 A New Approach

4.6.1 Synthesis of a tetrabrominated precursor

For comprehensive characterisation by usual liquid crystal methods it was necessary to develop a synthesis which could be scaled-up by a suitable degree. As the synthesis of substituted polyphenylenes can be increased to 1 g proportions, this would provide a very feasible synthetic route. In a similar fashion to other Diels-Alder reactions encountered in this thesis, the acetylene and cyclopentadienone were heated to 250 °C using benzophenone as a high boiling point solvent. The crude product was subjected to column chromatography and elution with dichloromethane allowed for the removal of solvent and unreacted starting materials. Increasing the polarity using methanol 1-4% yielded the product **42** as an off-white crystalline solid.

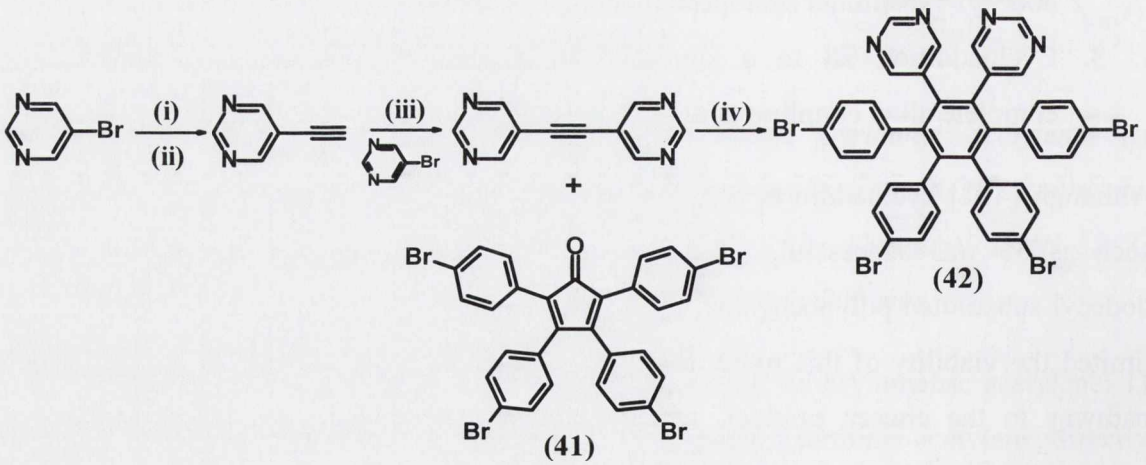

Scheme 4.7: Synthetic pathway for the formation of ***42****: (i) $Pd(PPh_3)_2Cl_2$, CuI, Et_2NH, RT, 5 h (56%); (ii) NaOH, toluene, reflux, 2 h (45%); (iii) $Pd(PPh_3)_2Cl_2$, CuI, Et_3N, DMF, 55 °C, 2 h (34%); (iv) benzophenone, 250 °C, 4 h (52%).*

42 was characterised using NMR spectroscopy, mass spectrometry and elemental analysis. A combination of 1D and 2D experiments (as shown in Figure 4.19) were used to fully assign the structure. NOE experiments allowed for direct identification of each pendant phenyl ring: irradiation of the pyrimidine singlet at 8.18 ppm, corresponding to the α-protons, allowed for identification of the adjacent phenyl signals *via* through-space interactions. In a similar fashion the assignment of the remaining phenyl ring was also possible.

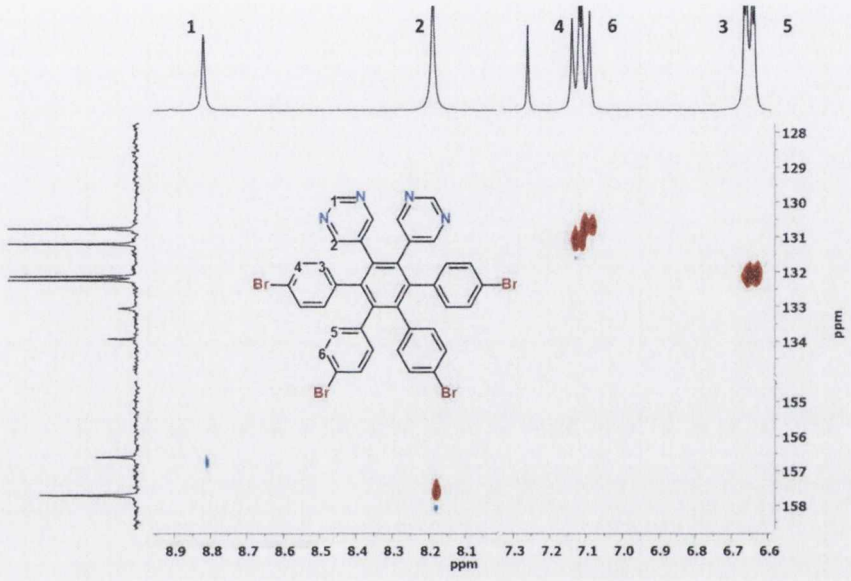

Figure 4.19: 2D HSQC of ***42*** *($CDCl_3$, 100.6 MHz, RT) with assignment of ^1H NMR signals.*

Crystals of **42** suitable for single crystal X-ray diffraction studies were prepared by slow evaporation of a dichloromethane/methanol mixture. Poor quality data resulted in a less than ideal data set. **42** crystallised in the monoclinic $P2_1/c$ space group, with one molecular unit and three molecules of water in the unit cell. As seen in Figure 4.20 (c), the molecules were seen to pack in a classic herring-bone motif with solvent molecules present in the voids. Both pyrimidine rings were observed to interdigitate with the pendant phenyl rings of its nearest neighbour, influenced by the weak interactions seen between the carbon atoms in the 1-position of the pyrimidyl rings with the bromine atom substituted in the *para* position of the pendant phenyl rings.

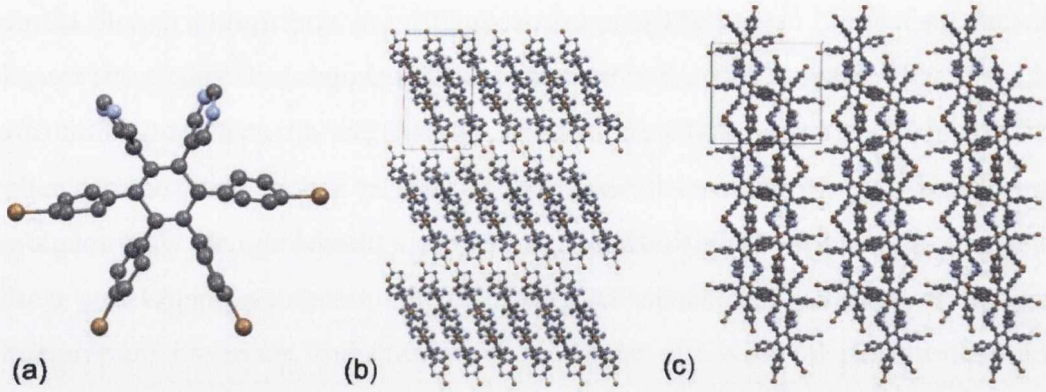

Figure 4.20: Crystal structure of ***42*** *showing (a) unit cell (b) packing, viewed along b-axis (c) packing, viewed along c-axis. Hydrogen atoms and solvent molecules removed for clarity; orange: bromine, blue: nitrogen.*

As discussed in Chapter 2, cyclodehydrogenation of halogenated polyphenylenes has posed problems for synthetic chemists. Likewise, **42** was unreactive under $FeCl_3$ conditions. Recent publications herald the use of 2,3-dichloro-5,6-dicyano-p-benzoquinone (DDQ) under acidic conditions as a potential solution to this problem. **42** did not react under these conditions. This unreactive response towards cyclodehydrogenation has been a feature of all the brominated species presented herein. Had cyclodehydrogenation been possible on the halogenated platform, it would have allowed alkyl coupling to remain the final step in the synthetic procedure. Success in this regard would have proved a useful method in circumventing the pitfalls seen previously in these syntheses, when dodecyl substituents are in place. Using Kumada coupling, however, it was possible to couple alkyl chains to all four pendant phenyl rings. [1,1′-bis(diphenylphosphino)ferrocene]dichloropalladium ([$PdCl_2$(dppf)]), as a catalyst for the reaction of primary and secondary alkyl Grignard reagents with organic halides, was first presented by Hayashi *et al.* The ability of this catalyst to provide good yields and selectivity proves very important in the presence of multiple coupling sites and has been shown to offer good results in this regard.[41] Generation of the reagent *in situ* from phenyldodecane using 1,1' –bis(diphenylphosphino)ferrocene]dichloropalladium ($PdCl_2$(dppf)) as catalyst generated the polyphenylene **43** in good yield.

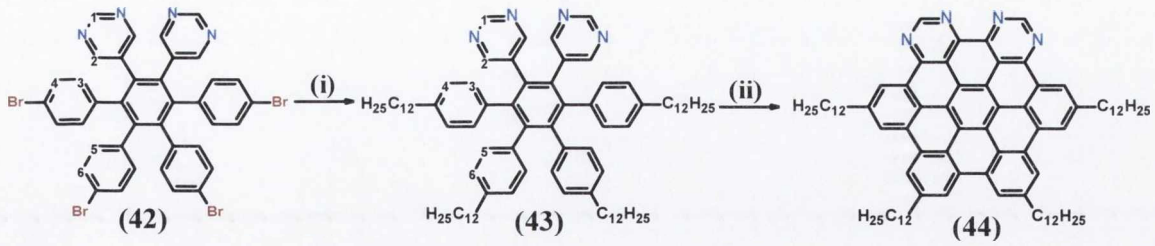

*Scheme 4.8: Procedure for the synthesis of **43** and **44**: (i) $Pd(dppf)Cl_2$, tetrahydrofuran, $C_{12}H_{25}MgBr$, reflux 12 h; (ii) $FeCl_3$, CH_3NO_2, RT, 4h.*

The lack of consistent fragmentation pathways in solution-state mass spectrometry resulted in NMR assignment being the only trustworthy method of characterisation. In a manner similar to the brominated precursor, full assignment of **43** could be achieved with ease as shown in Figure 4.21, owing greatly to the retention of the C_2 axis of symmetry. A marginal shift is seen in the pyrimidyl signals between both compounds. A global TOCSY experiment can be used to initially assess the various spin systems. A better understanding of assignment can then be gleaned from NOE experiments using linear-field gradient pulses, an example of which is outlined in red in Figure 4.21. This provides a useful means by which to interpret through-space interactions from H2 on the pyrimidine ring to the adjacent phenyl signals resulting from H3 and H4. An upfield shift is observed for H4 and H6 upon dodecyl substitution which, when adjacent to the bromine atoms, were seen to be deshielded by the greater electronegativity. Substitution with alkyl chains negates this effect and the signals are shifted closer to the overall phenyl signals. As in many C_{12}-substituted polyphenylenes of this nature, both sets of alkyl chains, although inequivalent, appear as three sets of overlapped signals in the aliphatic region. At δ = 2.36 ppm the benzylic protons appear as a multiplet, integrating for 8 protons. A multiplet centred on δ = 1.26 ppm accounts for most of the alkyl protons, apart from the terminal methyl groups which appear as a triplet at δ = 0.9 ppm with a coupling constant of J = 5.9 Hz. HMBC and HSQC experiments also allow for full assignment of the ^{13}C signals. A minor shift is again seen on the pyrimidyl ring with C1 and C2 moving from 157.7 to 157.9 and 156.6 to 155.6 respectively. As expected, a more significant change is observed for the aromatic ^{13}C signals. An upfield shift of approximately 1 ppm is seen for both C3 and C5 and for C4 and C6 a more considerable move from δ = 131.2 - 127.4 ppm and δ = 130.8 - 126.6 ppm is observed. The full assignment is collated in Table 4.1.

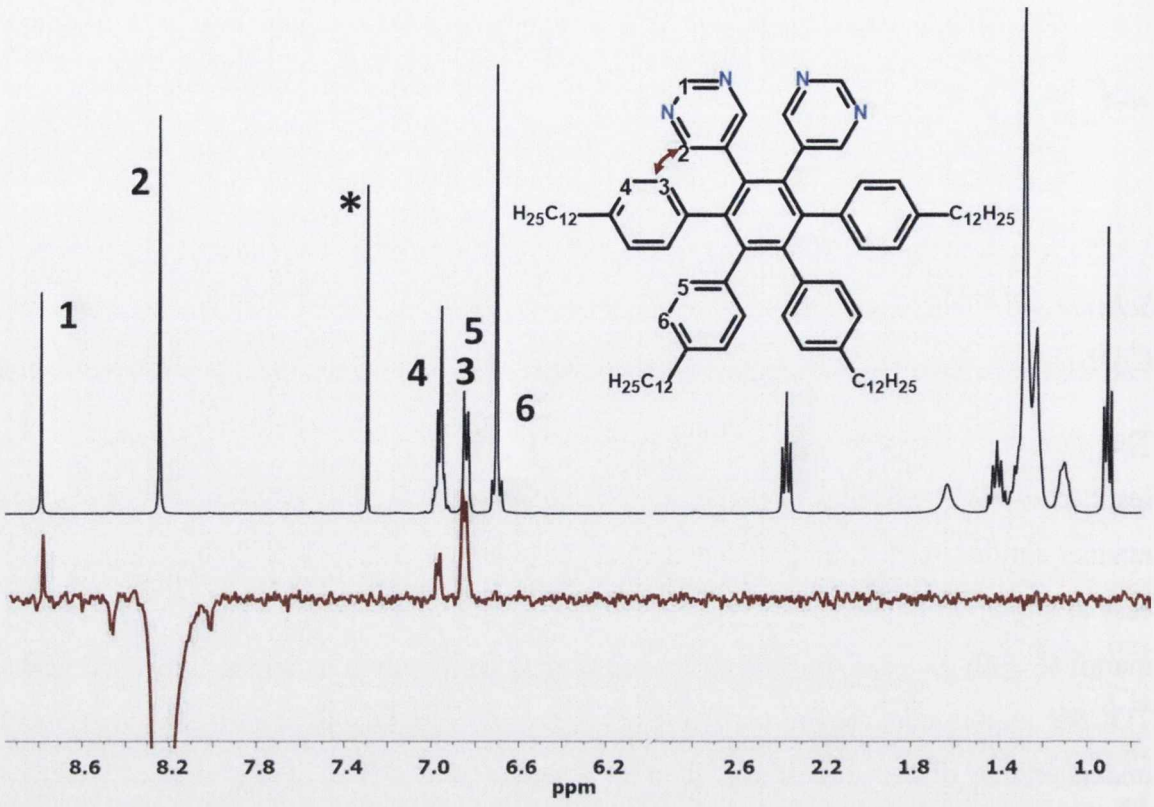

*Figure 4.21: Assignment of ^1H NMR signals of **43** in $CDCl_3$ at room temperature (400 MHz). Asterisk denotes $CDCl_3$ solvent peak. Red trace shows NOE response upon irradiation of $\delta = 8.20$ ppm.*

*Table 4.1: ^1H-NMR data for relevant proton signals of **42** and **43** ($CDCl_3$, RT, 600 MHz).*

Proton	H1	H2	H3	H4	H5	H6
42 (ppm)	8.82	8.18	6.65	7.12	6.5	7.10
43 (ppm)	8.79	8.25	6.96	6.70	6.69	6.68

Cyclodehydrogenation to form **44** using a $FeCl_3/CH_3NO_2$ system was achieved as before with much success. Stirring for 4 hours, followed by quenching and extraction with dichloromethane yielded a brown oil which was purified by column chromatography. Using a toluene/methanol eluent system the fully cyclised product was isolated as a waxy brown solid. NMR assignment and mass spectrometry analysis were used to fully

characterise the product. This method of synthesis showed improved yields for almost every step of the reaction. The use of brominated precursors not only proves beneficial for structures which were not synthetically possible by commonly-used pre substitution methods, but also as a much more feasible, efficient and easily characterised alternative. Increasing the scale of the synthesis of **44** allowed for further methods of characterisation which are discussed in Section 4.7. These add to our understanding of the behaviour of **44** and its assessment as a potential DLC contender.

4.6.2 Synthesis of a pentabrominated precursor

Success in the synthesis of a pentabrominated polyphenylene was also eventually achieved by developing on the methodology shown in Section 4.6.1, starting from 4-bromobenzyl bromide and 4-bromobenzaldehyde, as shown in Scheme 4.9.

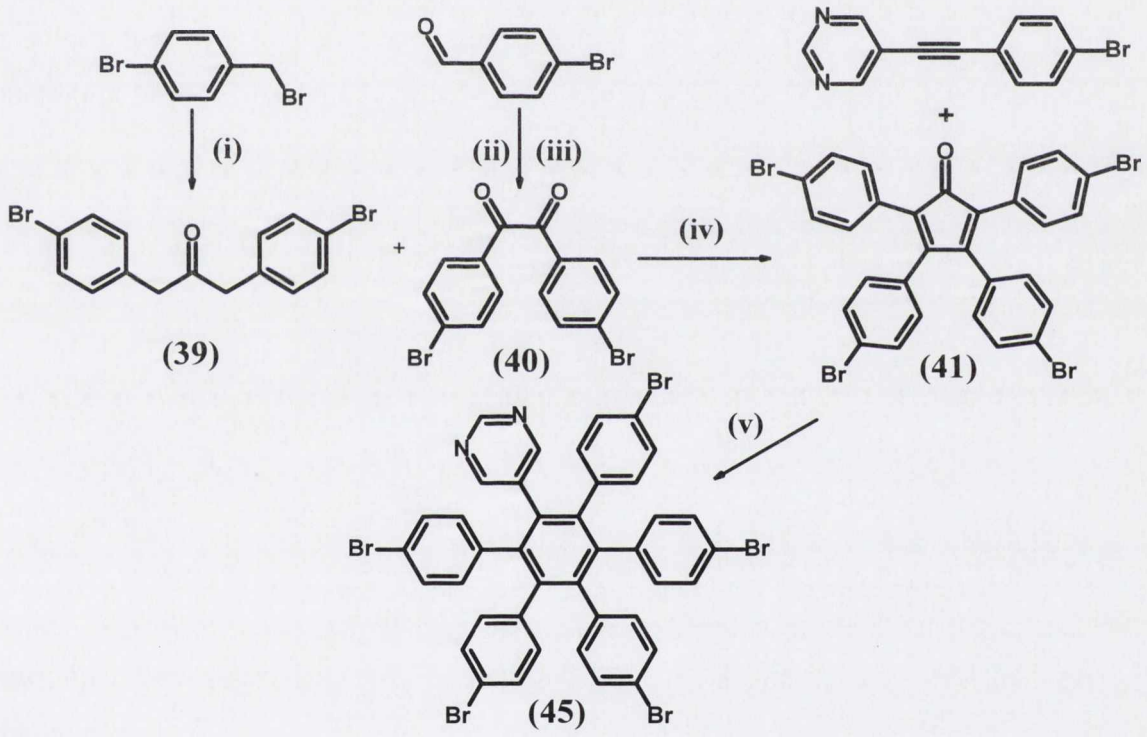

Scheme 4.9: The synthetic route to ***45****: (i) $Fe(CO)_5$, Bu_4NHSO_4, $Ca(OH)_2$, reflux, 18 h (63%); (ii) thiamine hydrochloride, H_2O, 10% NaOH, 65 °C 12 h (47%); (iii) NH_4NO_3, $Cu(OAc)_2.H_2O$, CH_3COOH, reflux, 2 h (82%); (iv) KOH, ethanol, reflux, 5 min; (v) benzophenone, 250 °C, 6 h (70%).*

As before, the substituted diphenylpropan-2-one was synthesised using $Fe(CO)_5$. 4,4'-dibromobenzil was synthesised *via* the oxidation of the substituted benzoin intermediate using ammonium nitrate. The 4,4'-dibromobenzoin precursor was synthesised using a classic benzoin condensation, nucleophilically catalysed using thiamine hydrochloride

(Vitamin B12). The tetrabromo substituted tetracyclone, as in **41**, was synthesised using a Knoevenagel condensation, and the target-polyphenylene was precipitated using methanol in high yield and purity. Slow evaporation of a dichloromethane/methanol mix produced crystals which were suitable for single crystal X-ray analysis.

The structure of **45** was solved in the P $2_1/n$ space group, with Z = 4. The final anisotropic refinement converged at R_1 = 6.89%, for the observed data and wR_2 = 16.34% for all data. The goodness-of-fit was 1.066. The largest peak in the final difference electron density synthesis was 1.936 $e^-/Å^3$ and the largest hole was -1.733 $e^-/Å^3$. The lower occupancy ring system was modelled with restraints (FLAT, EADP, DFIX) and then refined to convergence. One CH_2Cl_2 solvent molecule was half occupied and disordered over an inversion centre. Figure 4.22 shows the molecular structure and packing motif of **45**. The dichloromethane solvent molecules shown in Figure 4.22 prove integral to the crystal packing of the polyphenylene. Interactions between the chlorine atoms from the solvent molecule and bromine atoms from the pendant phenyl rings (3.572 Å) play an important role in the packing of the molecules, shown along the b axis in Figure 4.22.

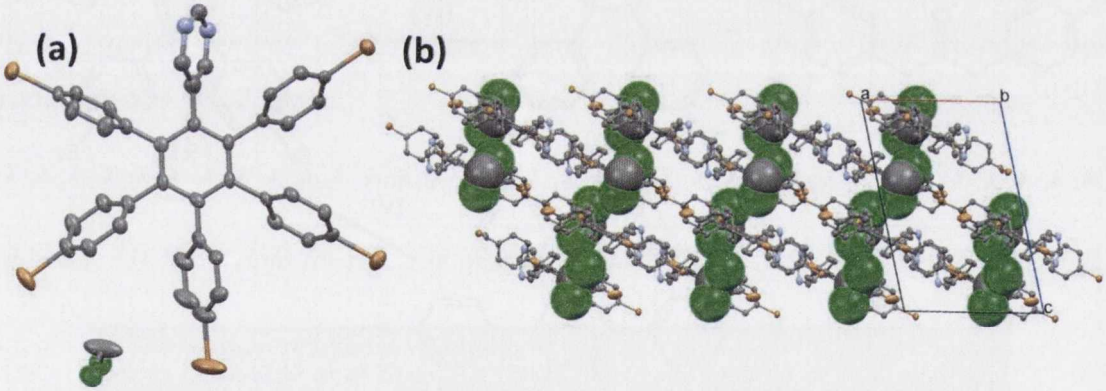

*Figure 4.22 Representation of the crystal structure of **45**: (a) unit cell with one dichloromethane solvent molecule; (b) packing, viewed along the b-axis. Hydrogen atoms are removed for clarity; orange: bromine, blue: nitrogen, green: chlorine.*

Similar to **43**, cyclodehydrogenation of this pentabrominated species either using $FeCl_3$ or DDQ also proved unfruitful and it was therefore necessary to carry out alkyl substitution directly on the polyphenylene. Unlike **43** however, the quest for a suitable mode of coupling proved complicated as $PdCl_2$(dppf) produced very low-yielding results. Traditional Kumada reaction catalysts, such as $NiCl_2$(dppe) and $NiCl_2$(dppp), as used in the less complex systems, were unsuccessful for such compounds with higher degrees of halogenation. After countless attempts, with variation of catalysts, solvents and reaction

conditions, $PdCl_2$(dppf) was returned as the catalyst, resulting in low yielding dodecyl substitution across all five positions, to give the polyphenylene **46**. Fechtenkotter has shown that, for similar polybrominated polyphenylenes, partially alkylated side-products are formed and that the variation of concentration, temperature and catalytic loading had no discernible effect on the yield of the desired product or the elimination of side products.[42] Purification using column chromatography with dichloromethane: methanol (5%) resulted in successful isolation of **46** as a brown waxy solid. NMR characterisation proved complicated as increased substitution at the periphery most likely caused a significant deshielding of the pyrimidyl signals, in addition to a significant increase of stacking between molecules in the solution phase. This results in considerably broad and convoluted peaks, but full assignment is presented in Chapter 5. Subsequent cyclodehydrogenation of **46** proved unfruitful using $FeCl_3$ in nitromethane. Success in this regard will ultimately be limited by the preceding reaction and the ability to generate larger quantities of the uncyclised polyphenylene. This would ensure that the progress of cyclodehydrogenation could be assessed, as partially cyclised products cannot be characterised *via* mass spectrometry.

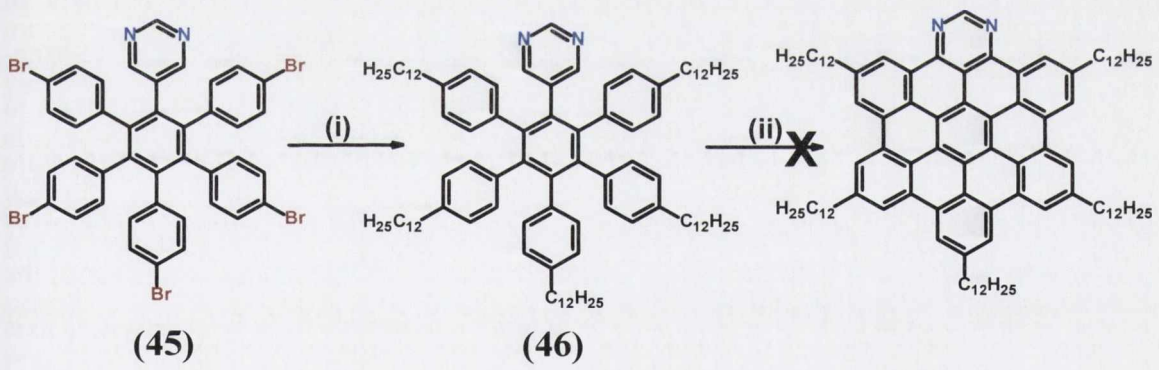

(45) **(46)**

Scheme 4.10: Procedure for the synthesis of ***46*** *and attempted cyclodehydrogenation thereof: (i) Pd(dppf)Cl_2, tetrahydrofuran, $C_{12}H_{25}MgBr$, reflux 12h; (ii) $FeCl_3$, CH_3NO_2, RT, 4h.*

4.6.3 An alternative nitrogen substitution pattern

Running concurrently with attempts to synthesise tetra- and penta-substituted platforms was a third approach which was hoped would yield a trisubstituted analogue. As outlined in Chapter 1, attempting to confer a different substitution pattern onto symmetrical nitrogen-substituted analogues may also be achieved using cyclotrimerisation. Scheme 4.11 shows the synthesis of a new polyphenylene (**47**) with triangular symmetry, which

may lead to discotic-helical (D_h) stacking between cores, as seen in recent triazine-based discoveries.[43]

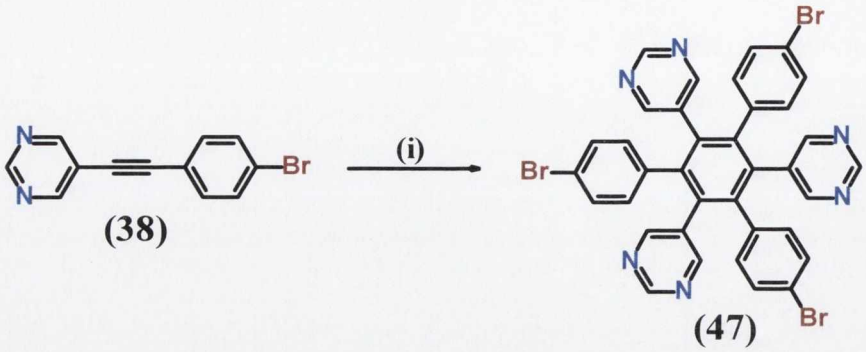

*Scheme 4.11: Cyclotrimerisation of **38** to synthesise **47**: (i) $Co_2(CO)_8$, dioxane, 115 °C, 24 h (30%).*

The helicity of a stack influences the intermolecular spacing and can have a profound effect on substituent chains and their interactions with neighbouring stacks.[44] Using cobalt octocarbonyl the cyclotrimerisation of **38** was successfully achieved, yielding the symmetric polyphenylene as the major product. The blue axes, shown in the Figure 4.23 (b) inset depict the C_{3v} symmetry evident in the cylotrimerised product, however in practice such high symmetry is not exhibited in solution for ^{1}H-NMR, due to ring-locking. Variable temperature measurements in dimethyl-D_6 sulfoxide, normally help to overcome the barrier for free-rotation (80 °C). In this case however higher temperature spectra exhibited more pronounced signals. In total, four different ring systems were exhibited by the molecule. Significantly hindered rotation of the pendant rings about the central benzene is evident. Such a locked orientation creates a lower symmetry C_{2v} axis within the molecule (shown in red). Using ROESY experiments a full assignment of this phenomenon was made possible, as shown in Figure 4.23 (b). In a similar manner to polyphenylenes **42** and **45**, **47** brings the opportunity to investigate the effect of substitution patterns on the behaviour of nitrogen-containing discotic liquid crystals. All these routes serve to compensate for the possible lack of insulation caused by the nitrogen atoms present in the periphery, while also attempting to reap the benefits of N-doping the graphene fragment at the core.

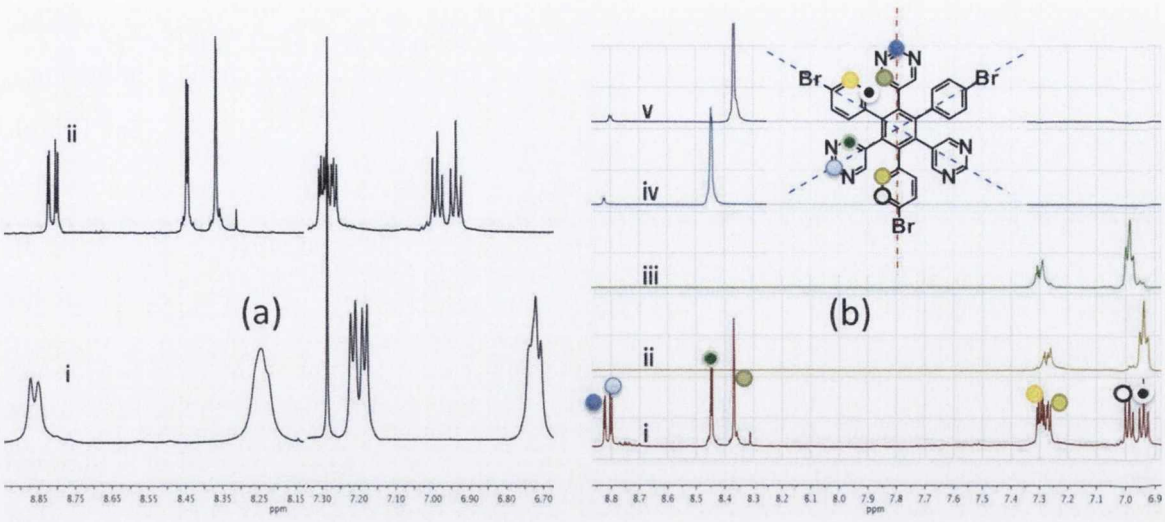

*Figure 4.23: (a) ^{1}H-NMR of **47** in (i) chloroform-D and (ii) dimethyl-D_6 sulfoxide (80 °C); (b) Selective ROE experiments of **47**.*

While interesting from a synthetic viewpoint, successful isolation of symmetric isomers from cyclotrimerisations of this manner, as outlined in Chapter 2, is ultimately statistically limited by the formation of a threefold excess of asymmetric isomer. This, combined with extremely low-yielding coupling reactions as outlined in Section 4.6.2 meant that the ultimate feasibility of this route was also hampered by extremely poor yielding reactions. Recently, other research groups have also encountered similar pitfalls, attributed to low-yielding coupling reactions. Using field-desorption mass spectrometry, which is renowned for its ability to ionise hydrocarbons of this nature without fragmentation, Fechtenkotter *et al.* successfully monitored coupling reactions at hexa-substituted polyphenylenes.[42] They noted the formation of multiple partially-substituted products, which could not be separated using column chromatography owed to the similar chemical properties of the analogues. Interestingly, although complete alkylation was shown to be unsuccessful it was also noted that dehalogenation was shown to have occurred. This most likely points to *in situ* quenching of the Grignard reagent responsible for the Kumada coupling within the dry ethereal solvent. Although the synthesis of the tri and penta-substituted molecules did not provide fruitful results, there remained a wide range of information which could be gleaned from the study of **44**.

4.7 Further Characterisation

As described in Section 4.4, **44** has been previously seen to exhibit some very peculiar liquid crystalline properties. In particular, it has been found to have no identifiable transition from discotic-crystalline phase transition in an accessible temperature range.

Differential Scanning Calorimetry (DSC) measurements show that the only discernible phase transition occurs at 5 °C and appears to correspond most likely to a discotic-discotic change. Charge mobility studies support this finding and appear to infer that liquid-crystalline behaviour is retained across the temperature range. The lack of an accessible crystalline phase (K-phase) results in an extremely low charge mobility. The ability of SANS to probe small-angle scattering of neutrons would allow for investigation of the nanoscale behaviour of **44** and may allow for assessment of the relationship between scattering intensity and angle. This in turn allows for characterisation of the long-range order at a given temperature. Performing SANS on a 2.5 wt.% solution of **44** in deuterated tetrahydrofuran unfortunately showed that the compound appeared to be fully dissolved or consisting of very small aggregates and therefore displayed no apparent long-range order, as shown in Figure 4.24. At 25 °C the compound showed clear isotropic behaviour. This is most apparent at high q with a very low signal to noise ratio and overall a particularly low scattering intensity. Choi *et al.* have modelled the analogous C_{12}HBC above the discotic-isotropic temperature (Figure 4.25). Using a cylindrical core-shell model (shown in the inset) the graph shows that in the isotropic state an aggregate of that form factor would show low scattering intensity which decreases further with increasing q. This confirms that in Figure 4.24, the SANS data for **44** represents small aggregates dispersed in d-THF rather than any large crystalline aggregates.

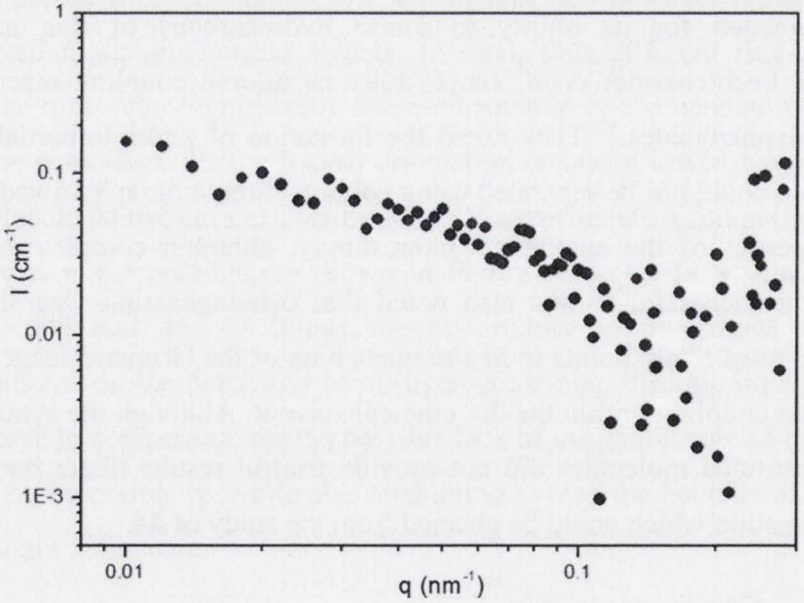

*Figure 4.24: SANS data of **44** at RT in deuterated tetrahydrofuran and 2.5 wt%.*

Comparison with previously studied systems shows that the true liquid crystalline behaviour exhibited by C_{12}HBC, as measured by Choir *et al.* can be observed at 5.5 wt%

in toluene and is shown in Figure 4.26.[25] The scattering data shows that at 45 °C, C_{12}HBC exhibits defined crystalline aggregates with columnar packing.

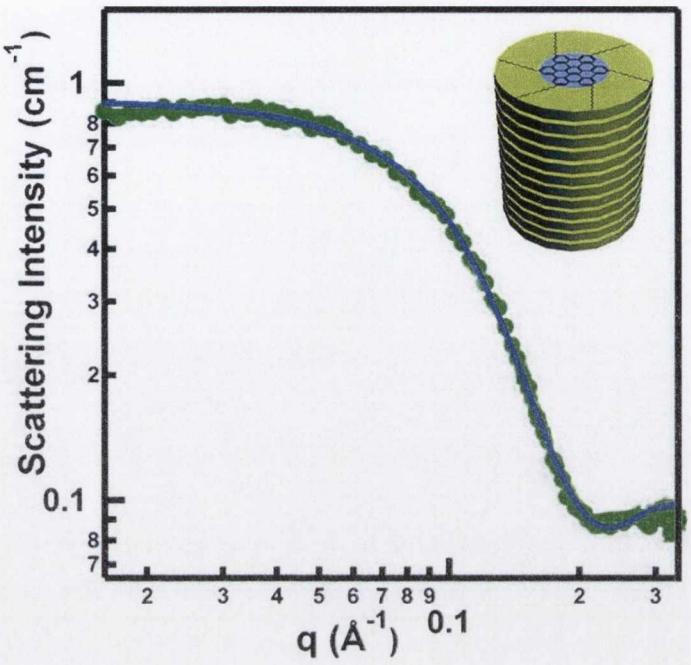

Figure 4.25: SANS data for C_{12}HBC in deuterated p-*xylene at 43 °C, as measured by Choi et al., fitted with a core-shell cylindrical form factor model, showing isotropic behaviour.*[25]

In the low q region the data for C_{12}HBC almost perfectly mirrors Porod's Law, which describes the asymptotic fitting of scattering intensity behaving proportionally to q^{-4}. The nature of packing at this temperature is supported by a POM study in the same temperature region, shown in Figure 4.26. At this temperature the molecule shows needle-like structures with an obvious birefringence, confirming that the molecules order in a columnar liquid-crystalline manner. At higher temperature (above the discotic-isotropic clearing temperature) no aggregation can be identified and birefringence is seen to disappear. In comparison then, it is reasonable to conclude that at 2.5 wt% **44** does not show any long range crystalline behaviour. It is likely that this could be as a result of the low concentration or indeed a function of temperature, although the DSC data presented previously would suggest that the molecule should be in discotic phase at room temperature.

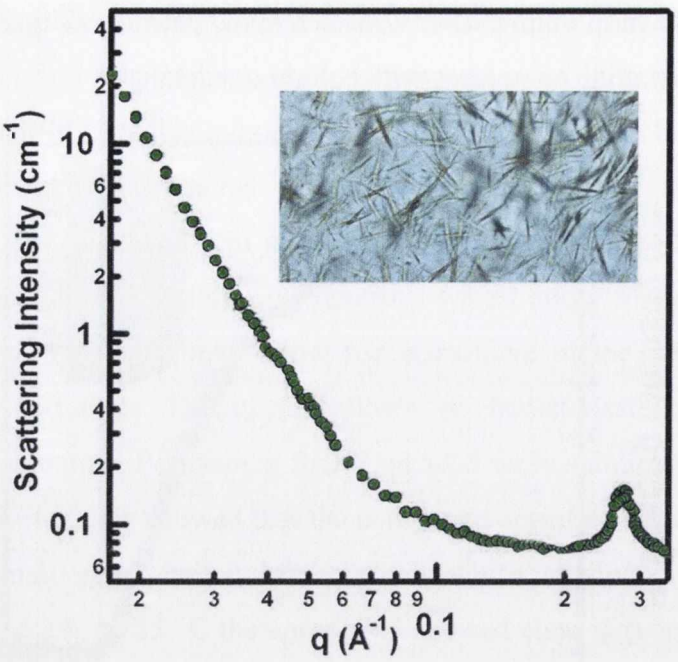

Figure 4.26: SANS intensity plot of C_{12}HBC at 45 °C upon heating in deuterated p-xylene. Inset shows POM image in p-xylene at 50 °C (concentration 1.1 wt%). Reproduced with edits from Choi et al.[25]

To glean more information about the behaviour of **44** and its apparent anomalies (namely the difficulty in finding clear crystalline or isotropic transitions) it was necessary to turn to POM. Using variable temperature facilities it was possible to not only investigate liquid-crystalline behaviour but also to amass more knowledge about the thermotropic nature of the molecule. At room temperature in the solid state the molecule exhibits well defined needle-like structures which show an obvious birefringence and indicate order in a columnar phase. Interestingly, upon heating no change whatsoever is observed to either the birefringence or visible aggregation. This infers that the conclusion from DSC and PR-TRMC measurements, which showed that no discotic-isotropic or discotic-crystalline phase changes can be identified over the 110 °C range from -80 °C to 90 °C is indeed correct. Also thought-provoking is that the ability to observe the POM to 0 °C, in Figure 4.27 again indicates that **44** most likely never reaches a fully crystalline phase in this temperature range. The retention of the small needle-like aggregates observed supports the DSC information which is indicative of a conformational change within the mesophase This would also support the proposal that the lack of an accessible crystalline phase is the reason why such a low charge mobility value was measured for this compound, as charge mobility values in the discotic phase are dramatically lower than in the crystalline phase.

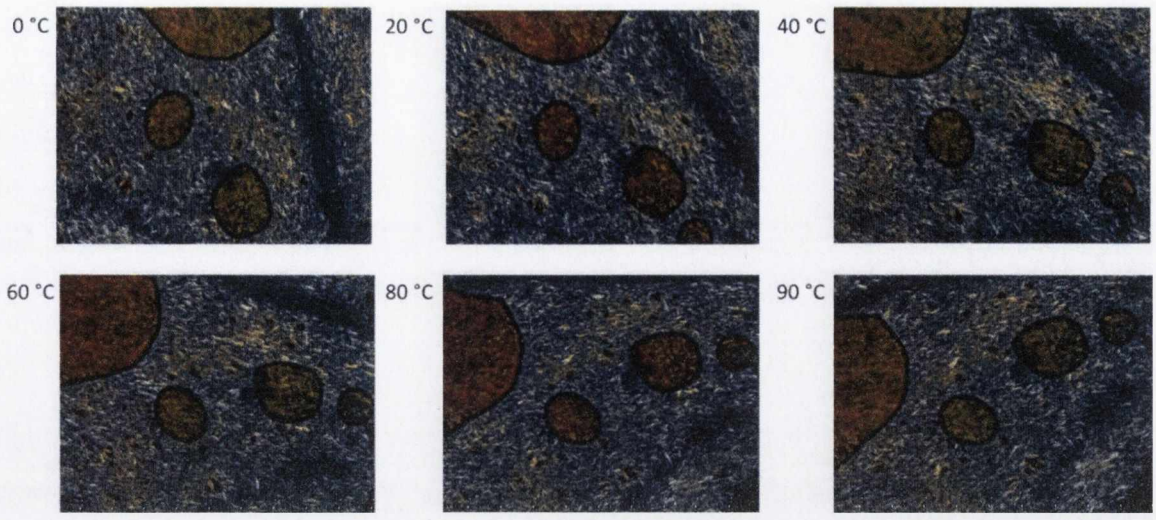

*Figure 4.27: POM images of **44** in the solid state at varying temperatures.*

This phenomenon has been seen previously in hexabenzocoronenes with dodecylphenyl substituents, in which columnar liquid-crystalline phases are seen from room temperature to 600 °C. Surprisingly, materials which exhibit a wide phase-width, extremely low crystalline-discotic and an extremely high discotic-isotropic phase transitions have never been observed to date. For example, substituents such as dovetail alkyl moieties serve to lower both discotic and isotropic clearing temperatures in a similar fashion, but a substance in which clearing temperatures at both extremes are inaccessible remains an anomaly. The confirmation of such interesting liquid crystalline behaviour shown here warrants the need for extension of this new synthetic route to encompass the diaza-substituted molecules previously attempted. As seen in Chapter 2, a single pyrimidyl substitution can result in extremely close packing between molecules. In an alkyl substituted molecule of the same nature this could result in increased electronic mapping between adjacent molecules and may reduce shortcomings in charge mobility as a result of polarity. Additionally, an extra dodecyl chain could increase insulation between neighbouring columns.

4.8 Conclusion and Future Work

By developing new methods and adopting other useful strategies, this chapter has presented three novel polyphenylene platforms, with ample scope for the development of a family of nitrogen-substituted discotic liquid crystals. Optimisation of these methodologies offers a very promising opportunity to develop these precursors using a range of substituents to directly address the previous shortcomings in the charge mobility of C_{12}NHSB. Preliminary results show that coupling reactions leave a lot to be desired.

The target compounds, which were successfully synthesised were also characterised using NMR, mass spectrometry, IR spectroscopy and melting-point techniques. A new synthetic procedure furnished **44** in relatively high yields, with further characterisation affording interesting results. POM has also given a greater insight into the nature of these types of substituted molecules with respect to temperature, supporting previous data which has shown a broad anisotropic range and a low temperature crystalline-discotic transition.

4.8.1 Future Work

The future of the work in this chapter will need to be driven by a more thorough characterisation of the materials' bulk morphology and further development of the new pathways for synthesis presented here. To date there still exists only a small body of work from within the Draper group investigating the introduction of heteroatoms into the core of alkyl-substituted hexabenzocoronenes. An understanding of whether head-to-tail or homeotropic intra-columnar arrangements will dominate is still not known. To begin, SANS characterisation will need to be revisited at higher concentrations. Although 5.5 %wt concentration would require 50-100 mg of fully cyclised product it would provide ample information about the long range order of these molecules with respect to temperature. Increased concentrations, although severely limited by the scalability of the cyclisation reaction, would increase the potential for aggregation and long-range ordering.

The use of hot-stage POM proved a very useful tool in the confirmation of birefringent needle-like structures across the 0-90 °C region. A welcome addition to this study would be the use of a controllable low-temperature stage. Such a system may allow for the confirmation of a transition to the crystalline phase. This would serve an important purpose in adding another quantitative element to the assessment of heteroatom substitution in DLCs. The introduction of high resolution SSNMR and mass spectrometry facilities offer new means of characterisation which are likely to have a profound effect on the progression of synthetic routes. Using in-house thermogravimetric analysis, differential scanning calorimetry and hot-stage polarising microscopy would provide ample information regarding the liquid crystalline behaviour of possible materials. Through a current collaborative effort, small-angle neutron scattering and intracolumnar charge-mobility measurements will offer the most pertinent information about the viability of any target compounds in the field of organic electronics.

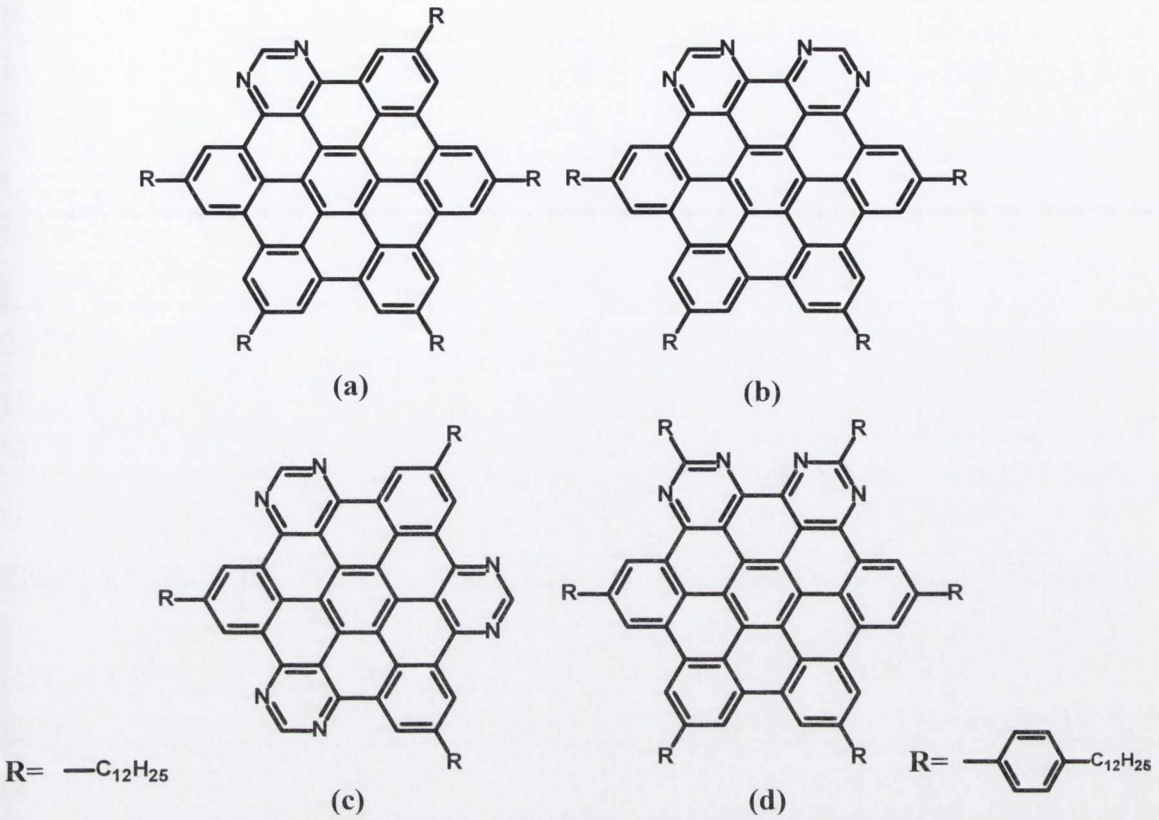

Figure 4.28: Selection of proposed structures to address shortcomings of C_{12}NHSB seen hitherto.

Synthetically, the completion of this work would hope to achieve the library of compounds outlined in Figure 4.28. The compounds shown in Figure 4.28 (a), (b) and (c) represent a continuation on the body of work presented here. Figure 4.28 (d) however is representative of another possible route which may also be taken concurrently. The novel methodology that this work attempts to introduce is the insertion of a range of substituents that promote liquid-crystallinity between the nitrogen motifs at the periphery of the C_{12}NHB analogues. This can be achieved, as shown in Scheme 4.12, using the method of Hughes *et al.*[45] Progression of n-alkyl substitution on the pyrimidine ring can yield the polyphenylene depicted in Scheme 4.12. Despite the background achievements, the synthesis of this molecule is challenging. A positive outcome would serve to establish the balance between the perturbation of long-range order due to the presence of heteroatoms and the positive effects of a number of alkyl substituents. Alkyl substitution of the new brominated polyphenylenes presented in this work presents a wonderful opportunity for a new range nitrogen-containing discotic liquid crystals, with varied ligand capabilities. It is hoped that these molecules, would serve to increase insulation of the cores and thereby

promote more efficient intramolecular close packing. If achieved, this offers new alternatives for low-cost and efficient organic semiconductors.

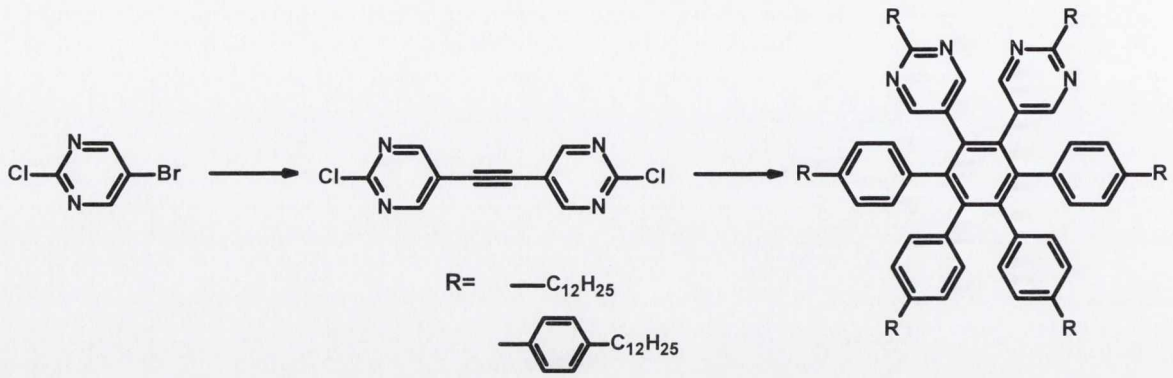

Scheme 4.12: Possible development of 2-chloro-5-bromopyrimidine, offering novel substitution at the periphery of C_{12}NHSB.

4.9 References

(1) Tang, C. W. *Appl. Phys. Lett.* **1986**, *48*, 183.

(2) O'Regan, B.; Grätzel, M. *Nature* **1991**, *353*, 737–740.

(3) Kuang, D.; Klein, C.; Ito, S.; Moser, J. E.; Humphry-Baker, R.; Evans, N.; Duriaux, F.; Grätzel, C.; Zakeeruddin, S. M.; Grätzel, M. *Adv. Mater.* **2007**, *19*, 1133–1137.

(4) Swetha, T.; Reddy, K. R.; Singh, S. P. *Chem. Rec.* **2015**, *15*, 457–474.

(5) Scharber, M. C.; Sariciftci, N. S. *Prog. Polym. Sci.* **2013**, *38*, 1929–1940.

(6) Poelking, C.; Andrienko, D. *J. Am. Chem. Soc.* **2015**.

(7) Mohamad, D. K.; Fischereder, A.; Yi, H.; Cadby, A. J.; Lidzey, D. G.; Iraqi, A. *J. Mater. Chem.* **2011**, *21*, 851–862.

(8) Sergeyev, S.; Pisula, W.; Geerts, Y. H. *Chem. Soc. Rev.* **2007**, *36*, 1902–1929.

(9) Schmidt-Mende, L.; Fechtenkötter, A.; Müllen, K.; Moons, E.; Friend, R. H.; MacKenzie, J. D. *Science* **2001**, *293*, 1119–1122.

(10) Barberá, J.; Elduque, A.; Giménez, R.; Oro, L. A.; Serrano, J. L. *Angew. Chemie Int. Ed. English* **1996**, *35*, 2832–2835.

(11) Destrade, C.; Foucher, P.; Gasparoux, H.; Tinh, N. H.; Levelut, A. M.; Malthete, J. *Mol. Cryst. Liq. Cryst.* **1984**, *106*, 121–146.

(12) Sauer, T. *Macromolecules* **1993**, *26*, 2057–2063.

(13) Crispin, X.; Cornil, J.; Friedlein, R.; Okudaira, K. K.; Lemaur, V.; Crispin, A.; Kestemont, G.; Lehmann, M.; Fahlman, M.; Lazzaroni, R.; Geerts, Y.; Wendin, G.; Ueno, N.; Brédas, J.-L.; Salaneck, W. R. *J. Am. Chem. Soc.* **2004**, *126*, 11889–11899.

(14) Van de Craats, A. M.; Stutzmann, N.; Bunk, O.; Nielsen, M. M.; Watson, M.; Mullen, K.; Chanzy, H. D.; Sirringhaus, H.; Friend, R. H. *Adv. Mater.* **2003**, *15*, 495–499.

(15) Pisula, W.; Menon, A.; Stepputat, M.; Lieberwirth, I.; Kolb, U.; Tracz, A.; Sirringhaus, H.; Pakula, T.; Müllen, K. *Adv. Mater.* **2005**, *17*, 684–689.

(16) Craats, A. M. van de; Warman, J. M.; Fechtenkötter, A.; Brand, J. D.; Harbison, M. A.; Müllen, K. *Adv. Mater.* **1999**, *11*, 1469–1472.

(17) Fechtenkotter, A.; Saalwachter, K.; Harbison, M. A.; Müllen, K.; Spiess, H. W. *Angew. Chemie-International Ed.* **1999**, *38*, 3039–3042.

(18) Kastler, M. PhD Thesis, 2006.

(19) Kopitzke, J.; Wendorff, J. H. *Chemie unserer Zeit* **2000**, *34*, 4–16.

(20) Dimitrakopoulos, C. D.; Malenfant, P. R. L. *Adv. Mater.* **2002**, *14*, 99–117.

(21) Reitzel, N.; Hassenkam, T.; Balashev, K.; Jensen, T. R.; Howes, P. B.; Kjaer, L. K.; Fechtenkötter, A.; Tchebotareva, N.; Ito, S.; Müllen, L. K.; Bjørnholm, T. *Chemistry* **2001**, *7*, 4894–4901.

(22) Tracz, A.; Jeszka, J. K.; Watson, M. D.; Pisula, W.; Müllen, K.; Pakula, T. *J. Am. Chem. Soc.* **2003**, *125*, 1682–1683.

(23) Ohta, K.; Hatsusaka, K.; Sugibayashi, M.; Ariyoshi, M.; Ban, K.; Maeda, F.; Naito, R.; Nishizawa, K.; Van de Craats, A. M.; Warman, J. M. *Mol. Cryst. Liq. Cryst.* **2003**, *397*, 25–45.

(24) Jackson, A. *Introduction to Small-Angle Neutron Scattering and Neutron Reflectometry*; 2008.

(25) Kim, H.-S.; Lee, J.-H.; Kim, T.-H.; Okabe, S.; Shibayama, M.; Choi, S.-M. *J. Phys. Chem. B* **2011**, *115*, 7314–7320.

(26) Nikon MicroscopyU. Nikon MicroscopyU | Polarized Light Microscopy https://www.microscopyu.com/articles/polarized/birefringenceintro.html (accessed Jul 7, 2015).

(27) Van de Craats, A. M.; Warman, J. M.; Mullen, K.; Geerts, Y.; Brand, J. D. *Adv. Mater.* **1998**, *10*, 36.

(28) Gearba, R. I.; Lehmann, M.; Levin, J.; Ivanov, D. A.; Koch, M. H. J.; Barberá, J.; Debije, M. G.; Piris, J.; Geerts, Y. H. *Adv. Mater.* **2003**, *15*, 1614–1618.

(29) Wu, J.; Li, J.; Kolb, U.; Müllen, K. *Chem. Commun. (Camb).* **2006**, 48–50.

(30) Hill, J. P.; Jin, W.; Kosaka, A.; Fukushima, T.; Ichihara, H.; Shimomura, T.; Ito, K.; Hashizume, T.; Ishii, N.; Aida, T. *Science* **2004**, *304*, 1481–1483.

(31) Foster, E. J.; Jones, R. B.; Lavigueur, C.; Williams, V. E. *J. Am. Chem. Soc.* **2006**, *128*, 8569–8574.

(32) Foster, E. J.; Babuin, J.; Nguyen, N.; Williams, V. E. *Chem. Commun. (Camb).* **2004**, 2052–2053.

(33) Würthner, F. *Chem. Commun.* **2004**, 1564–1579.

(34) Langhals, H. *Helv. Chim. Acta* **2005**, *88*, 1309–1343.

(35) Lankage, B. S. PhD Thesis, Trinity College Dublin, 2010.

(36) Roberts, D. J. PhD Thesis, Trinity College Dublin, 2009.

(37) Delaney, C. MSc. Thesis, Trinity College Dublin, 2011.

(38) Van der Made, A. W.; Van der Made, R. H. *J. Org. Chem.* **1993**, *58*, 1262–1263.

(39) Tanguy, G.; Weinberger, B.; des Abbayes, H. *Tetrahedron Lett.* **1984**, *25*, 5529–5532.

(40) Grummit, O.; Johnson, J. *Org. Synth.* **1955**, *3*, 86.

(41) Ito, S.; Wehmeier, M.; Brand, J. D.; Kubel, C.; Epsch, R.; Rabe, J. P.; Müllen, K. *Chem. Eur. J.* **2000**, *6*, 4327–4342.

(42) Fechtenkötter, A. PhD Thesis, 2001.

(43) Lee, H.; Kim, D.; Lee, H.-K.; Qiu, W.; Oh, N.-K.; Zin, W.-C.; Kim, K. *Tetrahedron Lett.* **2004**, *45*, 1019–1022.

(44) Fontes, E.; Heiney, P.; de Jeu, W. *Phys. Rev. Lett.* **1988**, *61*, 1202–1205.

(45) Hughes, G.; Wang, C.; Batsanov, A. S.; Fern, M.; Frank, S.; Bryce, M. R.; Perepichka, I. F.; Monkman, A. P.; Lyons, B. P. *Org. Biomol. Chem.* **2003**, *1*, 3069.

5 Experimental

5.1 General Methods

Unless stated, all reactions were performed under argon using standard Schlenk techniques. All solvents were distilled using appropriate drying agents and degassed prior to use. Flash chromatography was performed using silica gel (Fluka 60) as the stationary phase; all separations were carried out in air. Chemicals were purchased from Sigma-Aldrich Chemical Ltd. and were used without further purification. The starting materials, 5-ethynylpyrimidine, 1,2-di(pyrimidin-5-yl)ethyne, 5-((4-(tert-butyl)phenyl)ethynyl)pyrimidine, 2,3,4,5-tetrakis(4-(tert-butyl)phenyl)cyclopenta-2,4-dien-1-one, 2,5-dimethyl-3,4-diphenylcyclopenta-2,4-dien-1-one, 4b-hydroxy-5,7-diphenyl-4b,5-dihydro-6H-cyclopenta[f][1,10]phenanthrolin-6-one,7,9-bis(4-(tert-butyl)phenyl)-8H-cyclopenta[a]acenaphthylen-8-one, were synthesised *via* published synthetic procedures, developed by Draper *et al.*[1] 5-(phenylethynyl)pyrimidine and compounds **1** and **3** were prepared using procedures modified from Gourdon *et al.*[2] Compound **2** and 5-((3,4,5-trimethoxyphenyl)ethynyl)pyrimidine were prepared using the procedure of Wijesinghe *et al.*[3] Iodo- HBC was synthesised using the procedure of Roberts *et al.*[4] Microwave synthesis was performed using a CEM Discover 300 W multimode microwave, in 35 mL vessels, at constant power.

Electrospray mass spectra were recorded on a micromass LCT TOF electrospray mass spectrometer. MALDI-TOF mass spectra were recorded on a Waters MALDI-QTOF Premier spectrometer using a α-cyano-4-hydroxy cinnamic acid or trans-2-[3-(4-tert-Butylphenyl)-2-methyl-2-propenylidene] malononitrile (DCTB) matrix. Accurate mass spectra were recorded against Leucine Enkephalin (555.62 g mol^{-1}) or [Glu1]-Fibrinopeptide B (1570.6 g mol-1) and reported to within 5 ppm.

NMR spectra were recorded in $CDCl_3$, CD_2Cl_2, CD_3OD and C_2D_2OS with (i) a Bruker Avance DPX-400 MHz spectrometer at the following frequencies: 400.13 MHz for ^1H and 100.6 MHz for ^{13}C (ii) an AV-400 MHz spectrometer at 400.23 MHz for ^1H and 100.6 MHz for ^{13}C or (iii) an AV-600 MHz spectrometer at 600.13 MHz for ^1H and 150.9 MHz for ^{13}C. The signals for ^1H and ^{13}C were referenced to TMS at $\delta = 0.00$, coupling constants were recorded in hertz (Hz) to one decimal place. All 2-D ^1H and ^{13}C spectra were recorded using a Bruker Avance 400 MHz spectrometer or an AV-600 MHz spectrometer and were employed to assign ^1H and ^{13}C peaks. Homonuclear correlation spectroscopy was performed using TOCSY or ^1H-^1H COSY experiments and

heteronuclear correlation spectroscopy was performed using HSQC, HMQC or HMBC (long-range experiments).

Melting points were determined on a Griffin Melting Point apparatus. IR analysis was recorded in solid form using a PerkinElmer Spectrum 100 FTIR spectrometer with a Universal ATR accessory. Elemental Analysis was performed on a Carlo Erba 1006 automatic analyser at University College Dublin by Ms. Ann Connolly.

Thermogravimetric analysis (TGA) analysis was performed using a Perkin Elmer Pyris 1 under a flow of Nitrogen, at a heating rate of 10 °C/min using ceramic crucible pans.

High resolution transmitting electron microscopy (HRTEM) was performed using a double aberration-corrected JEOL 2200MCO instrument. The instrument was operated at 80 keV with spherical aberration set to 3 μm. Samples were drop-cast onto an ultrathin carbon support (<3 nm) which was supported by a copper TEM grid (Agar Scientific, S186-4) and baked at 60 °C in a vacuum for 5 hours.

Scanning Tunnelling Microscopy (STM) was performed by Dr. Marek Knorr at the University of Muenster, using a Createc LTSTM incorporated in an ultra-high vacuum system. Chamber temperature was maintained at 4K or 77K with a typical pressure of 4.3 x 10^{-9} mbar.

X-ray photoelectron spectroscopy (XPS) characterization was performed on an ultra-high vacuum system (Omicron) at 1×10^{-10} mbar base pressure, equipped with a monochromatized Al Kα source (1486.6 eV) and a multichannel array detector. Spectra were recorded with an analyser resolution of 0.5 eV at 45° take-off angle. Samples were then irradiated with a 5 eV flux charge neutralising gun for 30 minutes. Spectra were recorded post-irradiation in the same manner as before. Peaks were fitted to Voigt functions after Shirley background correction was performed, using commercial software (Igor Pro).[5,6]

Small angle neutron scattering (SANS) was carried out by Prof. Rachel Evans on the LOQ beamline at the ISIS Pulsed Neutron Source (STFC Rutherford Appleton Laboratory, Didcot, U.K.).[7] A simultaneous q-range of ~0.009–0.24 $Å^{-1}$ was achieved using an incident wavelength range of 2.2–10 Å separated by time-of-flight and employing an instrument set up of L1 = L2 = 4.1 m. The sample was prepared in deuterated tetrahydrofuran. Each raw scattering data set was corrected for the detector

efficiencies, sample transmission and background scattering and subsequently converted to scattering cross-section data ($\partial\Sigma/\partial\Omega$ *vs.* q) using the instrument-specific software. The data was placed on an absolute scale (cm^{-1}) using the scattering from a standard sample (a solid blend of hydrogenated and perdeuterated polystyrene) in accordance with established procedures.[8] The sample was placed in a quartz cuvette (Hellma) of 1 mm path length and maintained at 25.0 ± 0.5 °C throughout the measurements.

Polarising Optical Microscopy (POM) was performed by Prof. Sujarit Dhara in the University of Hyderabad India, using an Olympus BX51 optical polarising microscope. By fixing the sample and polariser in the crossed-position the stage was heated using a Mettler-Toledo temperature controller. Samples were prepared in the solid state and applied directly to a glass microscope slide.

Crystal data are summarised in tables in the Annex. Selected bond lengths and angles are given in the discussion. The single crystal analysis was performed by Dr. Tom McCabe in Trinity College with a Rigaku Saturn-724 CCD diffractometer or Dr. Brendan Twamley with a Bruker SMART APEX CCD diffractometer, using graphite monochromated Mo-Kα (λ=0.71073Å) radiation at the temperature given in tables. Data integration and reduction was carried out using Bruker Saint+ Version 6.45 software and corrected for absorption and polarization effects using SADABS version 2.10 software. Space group determination, structure solution and refinement were obtained using Shelxtl* version 6.14 software. *Software Reference Manual, version 5.625, Bruker Analytical X-Ray systems Inc., Madison, WI 2001. Sheldrick, G.M. SHELXTL, An Integrated System for Data Collection, Processing, Structure Solution and Refinement, Bruker Analytical X-Ray Systems Inc., Madison, WI, 2001. All the non-hydrogen atoms were refined anistropically, and the hydrogen atoms were fixed from the residual electron density using appropriate HFIX commands. Intermolecular interactions were computed using the PLATON program. Absolute structure determinations were based on the Flack parameter. The functions minimised were $\Sigma w(F_o^2 - F_c^2)$, with $w = [\sigma^2(F_o^2) + (aP)^2 + bP]^{-1}$, where $P = [\max(F_o)^2 + 2F_c^2]/3$.

5.2 Experimental Procedures

5.2.1 Synthesis of 5-(4',5',6'-triphenyl-[1,1':2',1''-terphenyl]-3'-yl)pyrimidine (1)

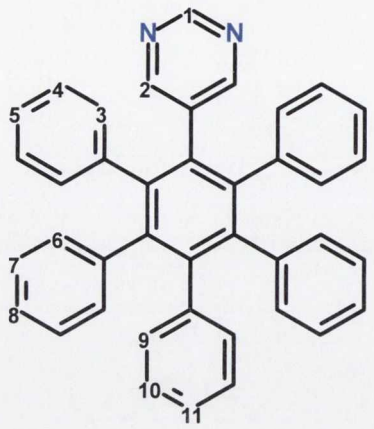

5-(phenylethynyl)pyrimidine (325 mg, 1.8 mmol), tetraphenylcyclopentadione (525 mg; 1.4 mmol) and benzophenone (1 g) were placed in a round bottom flask (10 mL). The mixture was heated under nitrogen to 300 °C for 4 hours. The product was then precipitated using dichloromethane and methanol to give a white solid.

Yield: 249 mg; 70 %.

^{1}H NMR (400 MHz, $CDCl_3$) δ 8.70 (s, 1H, **1**), 8.20 (s, 2H, **2**), 6.96 (d, 5H), 6.92 (m, 25 H, **3-11**) ppm.

^{13}C NMR (101 MHz, $CDCl_3$) δ 157.4 (2C, **2**), 155.7 (1C, **1**), 141.9 (1C, C_Q), 140.8 (2C, C_Q), 140.3 (2C, C_Q), 139.8 (1C, C_Q), 139.6 (2C, C_Q), 139.1 (1C, C_Q), 138.8 (2C, C_Q), 132.4 (1C, C_Q), 131.1 (4C, **3**), 131.0 (4C, **6**), 127.2 (4C, **4**), 126.62 (4C, **7**), 126.5 (3C, **10**, **11**), 126.0 (2C, **5**), 125.5 (2C, **8**), 125.4 (2C, **9**) ppm.

HRMS (m/z) calculated for $[C_{40}H_{28}N_2+H]^+$ 537.2331, found 537.2324.

IR (υ_{max}/cm^{-1}): 3026 (C-H), 1578 (C=C), 1550, 1498, 1442, 1393, 1186, 1157, 1073, 816, 779 (C-H bend), 739.

m.p. > 300 °C.

5.2.2 Synthesis of 2,3,4,5-tetrakis(4-tert-butylphenyl)-6-(3,4,5-trimethoxyphenyl)1-(5-pyrimidyl)-benzene (2)

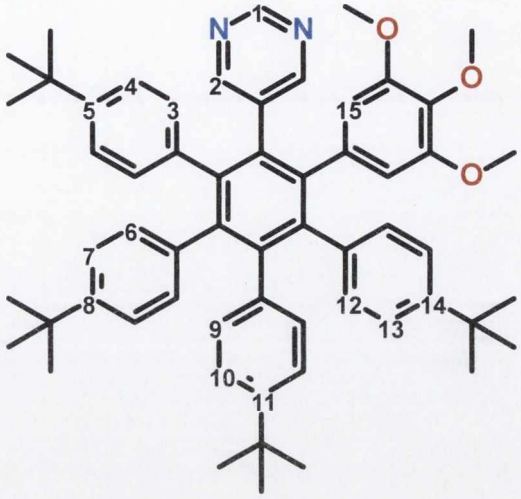

5-((3,4,5-trimethoxyphenyl)ethynyl)pyrimidine (90 mg, 0.32 mmol), 2,3,4,5-tetra(tert-butylphenyl)cyclopentadien-1-one (190 mg, 0.31 mmol) and benzophenone (500 mg) were heated at 300 °C for 3 hours. Purification by column chromatography using dichloromethane as eluent removed benzophenone. Subsequent elution with a CH_2Cl_2: CH_3OH (2%) mixture yielded the product, which was recrystallised from dichloromethane and methanol to give white crystals.

Yield: 946 mg; 69 %.

^{1}H NMR (400 MHz, $CDCl_3$) δ 8.82 (s, 1H, **1**), 8.34 (s, 2H, **2**), 6.95 (d, J = 8.1 Hz, 2H, 7/10), 6.92 (d, J = 7.7 Hz, 2H, **13**), 6.87 (d, J = 7.7 Hz, 2H, **4**), 6.85 (d, J = 7.0 Hz, 2H, **7/10**), 6.73 (d, J = 8.5 Hz, 2H, **12**), 6.71 (d, J = 7.8 Hz, 3H, **6/9**), 6.68 (d, J = 7.7 Hz, 2H, **3**), 6.66 (d, J = 7.4 Hz, 2H, **6/9**), 6.02 (s, 2H, **14**), 3.70 (s, 3H, -C**H**$_3$O), 3.43 (s, 6H, -C**H**$_3$O), 1.15 (s, 18H, ^{t}**Bu**), 1.12 (s, 18H, ^{t}**Bu**) ppm.

^{13}C NMR (151 MHz, $CDCl_3$) δ 157.80 (2C, **2**), 154.9 (1C, **1**), 152.0 (C_Q), 148.7 (C_Q), 148.1 (C_Q), 147.89 (C_Q), 147.8 (C_Q), 142.4 (C_Q), 141.5 (C_Q), 140.9 (C_Q), 140.8 (C_Q), 140.0 (C_Q), 137.3 (C_Q), 137.1 (C_Q), 136.9 (C_Q), 136.4 (C_Q), 136.3 (C_Q), 135.6 (C_Q), 134.7 (C_Q), 132.1 (C_Q), 131.1 (2C, **6/9**), 130.8 (2C, **12**), 130.7 (2C, **3**), 130.6 (2C, **6/9**), 124.0 (2C, **7/10**), 123.6 (2C, **13**), 123.3 (2C, **4**), 123.2 (2C, **7/10**), 109.9 (2C, **15**), 60.9 (1C,-**C**OCH$_3$), 55.9 (2C,-**C**OCH$_3$), 34.2 (1C, ,-CO**C**H$_3$), 34.1 (1C,-CO**C**H$_3$), 34.0 (1C,-CO**C**H$_3$), 33.9 (3C, ^{t}**Bu**), 31.2 (3C, ^{t}**Bu**), 31.1 (3C, ^{t}**Bu**), 31.1 (3C, ^{t}**Bu**) ppm.

HRMS (m/z) calculated for $[C_{59}H_{66}N_2O_3+H]^+$ 817.5152; found 817.5161.

IR (υ_{max}/cm^{-1}): 3031 (C-H), 2986, 2920, 2870, 1600, 1504 (C=N), 1408 (C=C), 1198, 1236, 845, 776.

m.p. : 260-263 °C.

5.2.3 Synthesis of 5-(4,4''-di-tert-butyl-4',5',6'-tris(4-(tert-butyl)phenyl)-[1,1':2',1''-terphenyl]-3'-yl)pyrimidine (3)

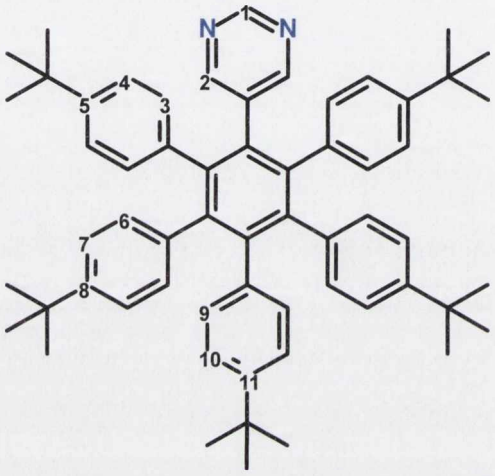

5-((4-(tert-butyl)phenyl)ethynyl)pyrimidine (400 mg, 1.69 mmol), 2,3,4,5-tetra(tert-butylphenyl)cyclopentadien-1-one (1.04, 1.7 mmol) and benzophenone (750 mg) were heated under nitrogen at 300 °C for 3 hours. Purification by column chromatography using dichloromethane as eluent yielded the product, which was recrystallised from dichloromethane and methanol to give an off-white solid.

Yield: 946 mg; 69 %.

^{1}H NMR (400 MHz, $CDCl_3$) δ 8.70 (s, 1H, **1**), 8.24 (s, 2H, **2**), 6.92 (d, J = 8.2 Hz, 4H, **4**), 6.88 – 6.81 (m, 6H, **7**, **10**), 6.71 (m, 6H, **3**, **9**), 1.59 (s, 18H, **^{t}Bu**), 1.12 (s, 18H, **^{t}Bu**) ppm.

^{13}C NMR (101 MHz, $CDCl_3$) δ 157.58 (2C, **2**), 154.4 (1C, **1**), 148.1 (2C, C_Q), 147.34 (2C, C_Q), 141.7 (2C, C_Q), 14.1 (2C, C_Q), 137.0 (2C, C_Q), 136.6 (2C, C_Q), 136.8 (2C, C_Q), 130.52 (4C, **3**), 130.33 (6C, **6**, **9**) 123.49 (4C, **4**), 122.74 (6C, **7**, **10**), 33.71 (3C, C_Q), 33.61 (3C, C_Q), 30.69 (9C, **^{t}Bu**), 30.66 (6C, **^{t}Bu**), 29.25 (1C, C_Q) ppm.

HRMS (m/z) calculated for $[C_{60}H_{68}N_2+H]^+$ 817.5461; found 817.5461.

IR (υ_{max}/cm^{-1}): 3010 (C-H), 2875, 1560, 1440, 1290 (CH_3 bend), 860, 780.

m.p. : 273-276 °C.

5.2.4 Synthesis of 8,9,10-triphenyltribenzo[e,gh,j]perimidine (4)

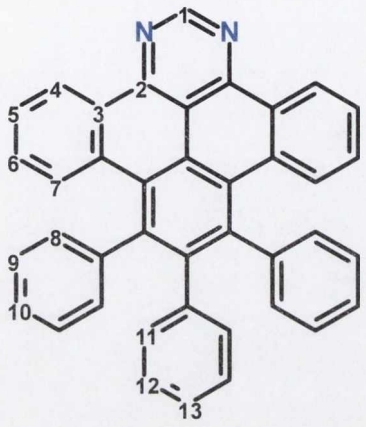

5-(4',5',6'-triphenyl-[1,1':2',1''-terphenyl]-3'-yl)pyrimidine (200 mg, 0.372 mmol) and bromine (6.23 g, 39 mmol) were heated to 90 °C in toluene (20 mL) for 2 hours in a pressure tube. The product precipitated directly from the reaction mixture as a white crystalline powder.

Yield: 168 mg, 85%.

^{1}H NMR (600 MHz, $CDCl_3$) δ 9.82 (s, 1H, **1**), 9.46 (d, J = 8.0 Hz, 2H, **4**), 7.74 (d, J = 8.5 Hz, 2H, **7**), 7.65 (t, J = 7.4 Hz, 2H, **5**), 7.33 – 7.25 (m, 2H, **6**), 7.22 – 7.19 (m, 6H, **9**, **10**), 7.16 – 7.11 (m, 4H, **8**), 6.95-6.91 (m, 3H, **12**, **13**), 6.84 (d, J = 7.2 Hz, 2H, **11**) ppm.

^{13}C NMR (151 MHz, $CDCl_3$) δ 155.2 (1C, **1**), 153.0 (2C, **2**), 144.3 (2C, C_Q), 142.6 (2C, C_Q), 139.9 (2C, C_Q), 139.8 (1C, C_Q), 134.1 (2C, C_Q), 131.6 (2C, **11**), 131.2 (4C, **7**), 129.7 (2C, **7**), 129.2 (2C, **6**), 128.2 (2C, **10**), 127.2 (2C, **5**), 127.1 (2C, C_Q), 126.7 (4C, **9**), 126.4 (1C, **13**), 125.5 (2C, **12**), 125.4 (2C, **4**), 123.8 (2C, C_Q), 114.8 (1C, C_Q) ppm.

HRMS (m/z) calculated for $[C_{40}H_{24}N_2 + H]^+$ 533.2018, found 533.2015.

Elemental Analysis: calculated for $C_{40}H_{24}N_2$: C, 90.20; H, 4.54; N, 5.26. Found: C, 86.47; H, 4.36; N, 4.98.

IR (υ_{max}/cm^{-1}): 3025 (C-H), 1963, 1550, 1442, 1421, 1393, 1186, 1158, 909, 779, 739, 696.

m.p. > 300 °C.

5.2.5 Synthesis of 13-(tert-butyl)-8,9,10-tris(4-(tert-butyl)phenyl)-4,6-dimethoxytribenzo[e,gh,j]perimidin-5-ol (5)

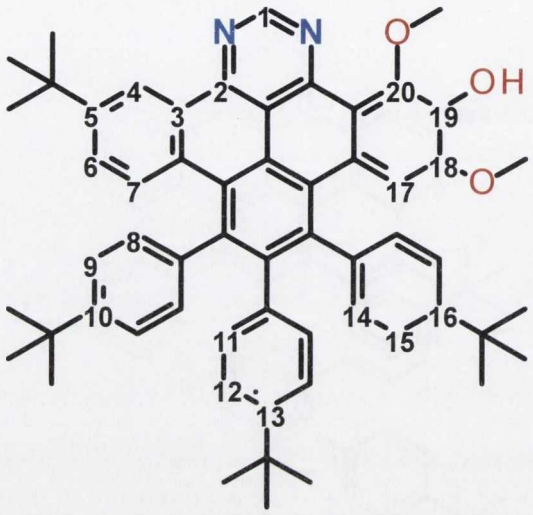

5-(4-(tert-butyl)-4',5',6'-tris(4-(tert-butyl)phenyl)-3",4",5"-trimethoxy-[1,1':2',1"-terphenyl]-3'-yl)pyrimidine (34 mg, 4 mmol) and bromine (6.23 g, 39 mmol) were heated to 90 °C in toluene (20 mL) at for 2 hours. The crude product was collected by filtration and was recrystallized from dichloromethane and methanol to yield pale yellow crystals.

Yield: 34 mg, 90%.

^{1}H NMR (600 MHz, $CDCl_3$) δ 15.63 (s, 1H, -O**H**), 9.62 (s, 1H, **1**), 9.51 (s, 1H, **4**), 7.87 (d, J = 9.0 Hz, 1H, **7**), 7.41 (s, 1H, **17**), 7.36 (dd, J = 9.0, 2.1 Hz, 1H, **6**), 7.19 (d, J = 8.4 Hz, 2H, **9**), 7.18 (d, J = 8.4 Hz, 2H, **15**) 7.02 (d, J = 9.8 Hz, 2H, **14**), 7.01 (d, J = 9.8 Hz, 2H, **8**), 6.83 (d, J = 8.2 Hz, 2H, **12**), 6.56 (d, J = 8.2 Hz, 2H, **11**), 4.05 (s, 3H,-C**H**$_3$O), 3.19 (s, 3H, -C**H**$_3$O), 1.48 (s, 9H, **^{t}Bu**), 1.30 (s, 9H, **^{t}Bu**), 1.22 (s, 9H, **^{t}Bu**), 1.19 (s, 9H, **^{t}Bu**) ppm.

^{13}C NMR (151 MHz, $CDCl_3$) δ 154.4 (1C, C_Q), 154.2 (1C, C_Q), 154.1 (2C, **2**), 151.4 (1C, **1**), 150.0 (1C, C_Q), 149.4 (1C, C_Q), 148.8 (1C, C_Q), 147.6 (1C, C_Q), 145.4 (1C, C_Q), 140.5 (1C, C_Q), 139.7 (1C), 139.5 (1C, C_Q), 139.2 (1C, C_Q), 137.1 (1C, C_Q), 135.2 (1C, C_Q), 132.0 (1C, C_Q), 131.3 (2C, **11**), 131.0 (2C, C_Q), 130.6 (2C, **14**), 130.4 (2C, **8**), 129.3 (1C, **7**), 127.3 (1C, **6**), 126.7 (1C, C_Q), 125.0 (2C, **8**), 124.7 (2C, **9**), 122.7 (1C, C_Q), 122.6 (2C, **12**), 121.2 (1C, **4**), 113.6 (1C, C_Q), 110.0 (1C, C_Q), 105.4 (1C, **17**), 60.6 (1C, -**C**H$_3$O),

55.0 (1C, -CH_3O), 34.8 (1C, C_Q), 34.3 (1C, C_Q), 34.2 (1C, C_Q), 33.9 (1C, C_Q), 31.2 (3C, **^{t}Bu**), 31.1 (3C, **^{t}Bu**), 31.0 (3C, **^{t}Bu**), 31.0 (3C, **^{t}Bu**) ppm.

HRMS (m/z) calculated for $[C_{58}H_{61}N_2O_3+H]^+$ 833.4682, found 833.4615.

IR (υ_{max}/cm^{-1}): 2958 (O-H stretch), 1581, 1565, 1456 (C=C), 1424 (O-H bend), 1140, 1118, 1080, 824, 785 (C-H), 654.

m.p. > 300 °C.

5.2.6 Synthesis of 5,13-di-tert-butyl-8,9,10-tris(4-(tert-butyl)phenyl)tribenzo[e,gh,j]perimidine (6)

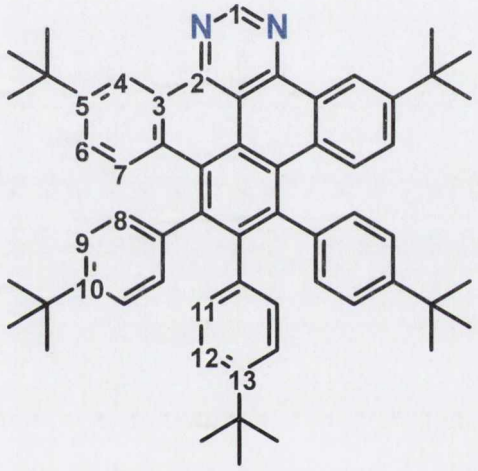

5-(4,4''-di-tert-butyl-4',5',6'-tris(4-(tert-butyl)phenyl)-[1,1':2',1''-terphenyl]-3'-yl)pyrimidine (47 mg, 0.057 mmol) and bromine (6.23 g, 39 mmol) were heated to 90 °C in toluene (20 mL) for 2 hours. The crude product was collected and was recrystallized from dichloromethane and methanol to yield colourless crystals.

Yield: 33 mg, 70%.

^{1}H NMR (400 MHz, $CDCl_3$) δ 9.85 (s, 1H, **1**), 9.51 (s, 2H, **4**), 7.85 (d, *J* = 9.0 Hz, 2H, **7**), 7.35 (d, J = 9.0 Hz, 2H, **6**), 7.18 (d, *J* = 7.9 Hz, 4H, **9**), 7.02 (d, *J* = 7.9 Hz, 4H, **8**), 6.84 (d, *J* = 7.9 Hz, 2H, **12**), 6.60 (d, *J* = 7.9 Hz, 2H, **11**), 1.49 (s, 18H, **^{t}Bu**), 1.30 (s, 18H, **^{t}Bu**), 1.16 (s, 9H, **^{t}Bu**) ppm.

^{13}C NMR (151 MHz, $CDCl_3$) δ 153.43 (1C, **1**), 150.0 (1C, C_Q), 149.34 (2C, C_Q), 147.68 (2C, C_Q), 145.1 (1C, C_Q), 141.8 (1C, C_Q), 140.07 (2C, C_Q), 139.4 (2C, C_Q), 137.3 (2C, C_Q), 135.5 (1C, C_Q) 132.3 (1C, C_Q), 132.2 (2C, C_Q), 131.14 (2C, **11**), 130.61 (4C, **8**),

129.52 (2C, **7**), 127.2 (2C, C_Q) 126.80 (2C, **6**), 124.80 (4C, **9**), 122.75 (2C, **12**), 121.39 (2C, **4**), 115.2 (2C, C_Q), 34.97 (2C, C_Q), 34.4 (2C, C_Q), 34.1 (1C, C_Q), 31.4 (6C, **^{t}Bu**), 31.3 (6C, **^{t}Bu**), 31.27 (3C, **^{t}Bu**) ppm.

HRMS (m/z) calculated for $[C_{60}H_{64}N_2+ H]^+$ 813.5148, found 813.5149.

IR (υ_{max}/cm^{-1}): 2963, 1580, 1544, 1465 (C=N), 1372, 1284, 1250, 1148, 850.

m.p. > 300 °C.

5.2.7 Synthesis of 5,5'-(4-bromo-6'-(4-bromophenyl)-4''-(tert-butyl)-5'-(4-(tert-butyl)phenyl)-[1,1':2',1''-terphenyl]-3',4'-diyl)dipyrimidine (7)

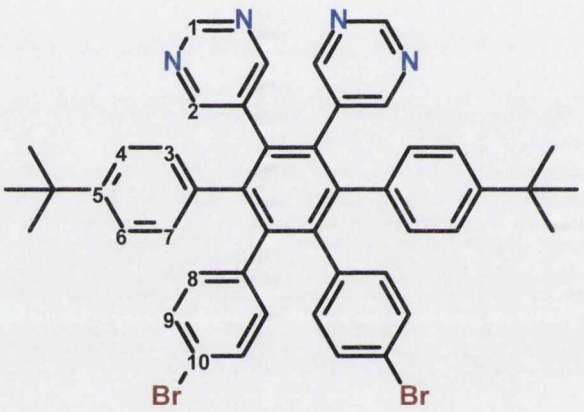

1,2-di(pyrimidin-5-yl)ethyne (250 mg; 1.36 mmol) and 3,4-bis(4-bromophenyl)-2,5-bis(4-(tert-butyl)phenyl)cyclopenta-2,4-dien-1-one (800 mg; 1.22 mmol) were heated in a round bottom flask at 280 °C for 3 hours under argon. After cooling, crystallisation directly from the reaction mixture using methanol produced colourless crystals.

Yield: 0.840 g, 85%.

^{1}H NMR (400 MHz, $CDCl_3$) δ 8.81 (s, 2H, **1**), 8.22 (s, 4H, **2**), 7.06 (d, J = 8.5 Hz, 4H, **8**), 6.99 (d, J = 8.3 Hz, 4H, **3**), 6.70 (m, 8H, **9**, **4**), 1.16 (s, 18H, **^{t}Bu**) ppm.

^{13}C NMR (101 MHz, $CDCl_3$) δ 157.9 (4C, **2**), 156.1 (2C, **1**), 149.8 (2C, **5**), 141.7 (2C, C_Q), 141.2 (2C, C_Q), 138.1 (2C, C_Q), 134.9 (2C, C_Q), 133.7 (2C, C_Q), 133.7 (2C, C_Q) 132.5 (4C, **8**), 130.7 (4C, **3**), 130.2 (4C, **9**), 124.6 (4C, **4**), 120.3 (2C, **10**), 34.3 (2C, **5**), 31.1 (6C, **^{t}Bu**) ppm.

HRMS (ESI) (m/z) calculated for $[C_{46}H_{40}N_4Br_2+ H]^+$ 807.1693, found 807.1697.

Elemental Analysis: calculated for $C_{46}H_{40}Br_2N_4$: C, 68.32; H, 4.99; N, 6.93. Found: C, 68.48; H, 4.82; N, 6.76.

IR (υ_{max}/cm^{-1}): 2974, 1446, 1548 (C=N), 1398, 1276, 1051, 751, 698 (C-Br), 637.

m.p. >300 °C.

5.2.8 Synthesis of 15,16-bis(4-bromophenyl)-3,12-di-tert-butyl-5,7,8,10-tetraazatribenzo[fg,ij,rst]pentaphene (8)

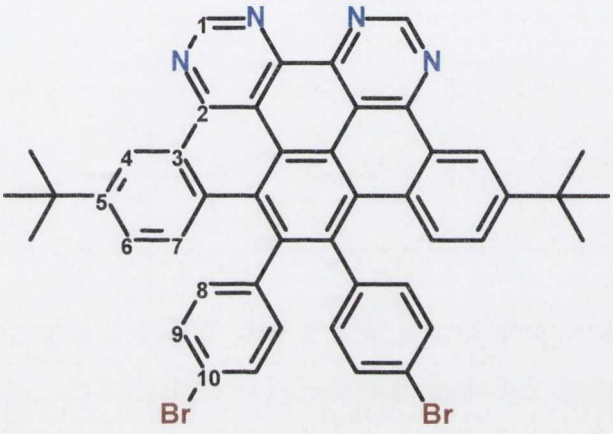

1,2-dipyrimidyl-3,6-bis-(4-tert-butylphenyl)-4,5-bis-(4-bromo-phenyl)benzene (100 mg, 0.12 mmol) and bromine (6.23 g, 39 mmol) were heated in a pressure-tube with toluene (10 mL) at 90 °C for 2 hours. The dark red suspension was filtered and recrystallised from dichloromethane and methanol to yield a bright yellow solid.

Yield: 69 mg, 70%.

^{1}H NMR (600 MHz, $CDCl_3$) δ 10.09 (s, 2H, **1**), 9.62 (d, J = 2.2 Hz, 2H, **4**), 7.66 (d, J = 8.9 Hz, 2H, **7**), 7.52 – 7.48 (m, 6H, **6**, **9**), 7.14 – 7.00 (m, 4H, **8**), 1.53 (s, 18H, **^{t}Bu**) ppm.

^{13}C NMR (151 MHz, $CDCl_3$) δ 156.4 (2C, **1**), 154.4 (2C, **2**), 151.3 (2C, C_Q), 150.6 (2C, C_Q), 140.9 (2C, C_Q), 140.4 (2C, C_Q), 132.8 (4C, **8**), 131.5 (4C, **9**), 131.1 (2C, C_Q), 130.2 (2C, C_Q), 128.8 (2C, **7**), 128.5 (2C, **6**), 127.1 (2C, C_Q), 122.2 (4C, **4**), 121.5 (2C, C_Q), 121.0 (2C, **10**), 35.0 (2C, **5**), 31.1 (6C, **^{t}Bu**) ppm.

HRMS (m/z) calculated for $[C_{46}H_{35}N_4Br_2 + H]^+$ 801.1228, found 801.1239.

Elemental Analysis: calculated for $C_{46}H_{34}N_4Br_2$: C, 68.84 H, 4.27; N, 6.98. Found: C, 66.31; H, 4.27; N, 6.98.

IR (υ_{max}/cm^{-1}): 3355, 2955, 1557, 1528, 1487, 1362 (CH_3 bend), 1258 (C=N), 1069, 1012, 831, 680 (C-Br).

m.p. >300 °C.

5.2.9 Synthesis of 5,5'-(5',6'-bis(4-bromophenyl)-[1,1':4',1''-terphenyl]-2',3'-diyl)dipyrimidine (9)

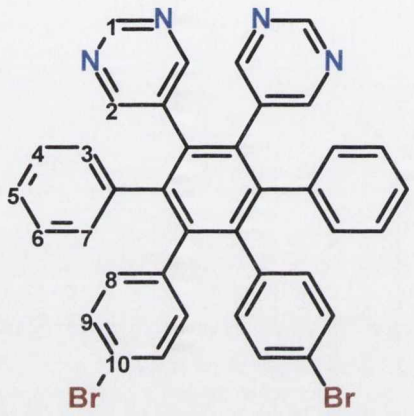

Dipyrimidyl acetylene (295 mg; 1.62 mmol) and 3,4-bis(4-bromophenyl)-2,5-diphenylcyclopenta-2,4-dien-1-one (800 mg; 1.47 mmol) were heated in a round bottom flask at 280 °C for 3 hours. After cooling, crystallisation directly from the reaction mixture using methanol produced white crystals.

Yield: 820 mg, 80%.

^{1}H NMR (400 MHz, CDCl3) δ 8.79 (s, 2H, **1**), 8.23 (s, 4H, **2**), 7.09 (m, 2H, **5**), 7.00 (m, 4H, **3**), 6.81 (m, 4H), 6.71 (d, J = 8.1 Hz, 4H, **9**) ppm.

^{13}C NMR (151 MHz, $CDCl_3$) δ 157.8 (4C, **2**), 156.3 (2C, **1**), 141.8 (2C, C_Q), 141.2 (2C, C_Q), 138.0 (2C, C_Q), 137.9 (2C, C_Q), 133.8 (2C, C_Q), 133.5 (2C, C_Q), 132.3 (4C, **9**), 130.8 (4C, **4**), 130.4 (4C, **8**), 127.9 (4C, **3**), 126.9 (2C, **5**), 120.6 (2C, **10**) ppm.

HRMS (m/z) calculated for $[C_{38}H_{25}Br_2N_4 + H]^+$: 695.0446, found 695.0448.

IR (υ_{max}/cm^{-1}): 2990 (C-H), 1454, 1509, 1366, 1277, 1151, 760, 689 (C-Br), 688.

m.p. >300 °C.

5.2.10 Synthesis of 15,16-bis(4-bromophenyl)-5,7,8,10-tetraazatribenzo[fg,ij,rst]pentaphene (10)

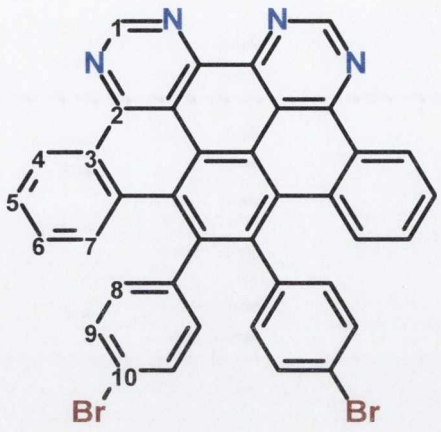

5,5'-(5',6'-bis(4-bromophenyl)-[1,1':4',1"-terphenyl]-2',3'-diyl)dipyrimidine (100 mg, 0.14 mmol) and bromine (6.23 g, 39 mmol) were heated in a pressure-tube with toluene (10 mL) at 90 °C for 2 hours. The dark red suspension was filtered and recrystallised from dichloromethane and methanol to yield a dark red solid.

Yield: 63 mg, 65%.

^{1}H NMR (600 MHz, $CDCl_3$) δ 10.15 (s, 2H, **1**), 9.54 (d, J = 8.4 Hz, 2H, **4**), 7.80 (m, 2H, **7**), 7.75 (m, 2H, **5**), 7.47 (m, 6H, **6**, **8**), 7.11 (d, J = 7.7 Hz, 4H, **9**) ppm.

^{13}C NMR (151 MHz, $CDCl_3$) δ 156.8 (2C, **1**), 154.4 (2C, **2**), 140.9 (2C, C_Q), 140.7 (2C, C_Q), 133.6 (2C, C_Q), 133.2 (4C, **9**), 132.9 (2C, C_Q) 131.7 (4C, **8**), 130.7 (2C, **6**), 129.2 (2C,**7**), 128.8 (2C, C_Q), 128.3 (2C,**5**), 127.7 (2C, C_Q), 126.2 (2C, **4**), 121.8 (2C, C_Q), 121.3 (2C, C_Q), 117.0 (2C, C_Q) ppm.

HRMS (m/z) calculated for $[C_{38}H_{18}Br_2N_4 + H]^+$: 688.9976, found 688.9971.

Elemental Analysis: calculated for $C_{38}H_{18}Br_2N_4$: C, 66.11; H, 2.63; N, 8.12. Found: C, 55.62; H, 1.84; N, 5.80.

IR (υ_{max}/cm^{-1}): 3355 (C=C), 2955, 1557, 1528, 1487, 1362, 1258, 1069, 1012, 831, 680 (C-Br), 771.

m.p. >300 °C.

5.2.11 Synthesis of 5,5'-(7,10-bis(4-(tert-butyl)phenyl)fluoranthene-8,9-diyl)dipyrimidine (11)

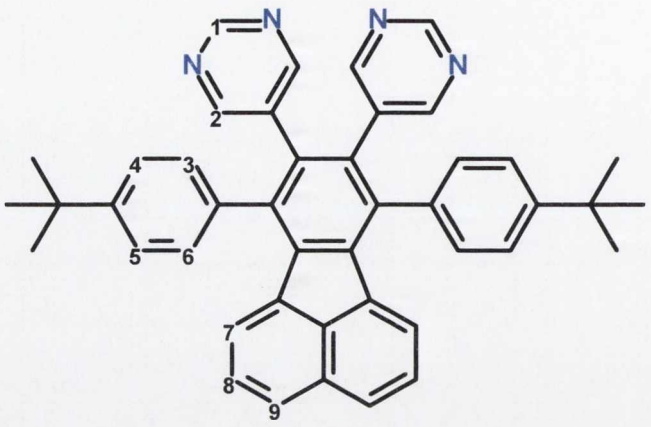

1,2-di(pyrimidin-5-yl)ethyne (59 mg, 0.320 mmol), 7,9-di-(4-*tert*-butylphenyl)-8H-cyclopenta[l]acenaphthylen-8-one (150 mg, 0.320 mmol) and benzophenone (750 mg) were heated to reflux for 2.5 h. Column chromatography using diethyl ether as eluent gave the product in high purity as a white solid.

Yield: 120 mg, 59 %.

^{1}H NMR (400 MHz, $CDCl_3$) δ 8.81 (s, 2H, **1**), 8.35 (s, 4H, **2**), 7.78 (d, 2H, J = 8.0; **9**), 7.41 (d, 4H, J = 8.2 Hz, **4**), 7.35 (dd, 2H, J = 7.0 Hz, J = 8.0 Hz, **8**), 7.22 (d, 4H, J = 8.2 Hz, **3**), 6.71 (d, 2H, J = 7.0 Hz, **7**), 1.36 (s, 18H, **^{t}Bu**) ppm.

^{13}C NMR (151 MHz, $CDCl_3$) 157.5 (2C, **1**), 155.7 (2C, **2**), 150.6 (2C, C_Q), 138.0 (2C, C_Q), 137.3 (2C, C_Q), 135.0 (2C, C_Q), 134.3 (2C, C_Q), 134.2 (2C, C_Q), 132.8 (2C, C_Q), 132.7 (2C, C_Q), 129.2 (2C, C_Q), 128.9 (4C, **3**), 127.4 (2C, **9**), 127.0 (2C, **8**), 125.4 (4C, **4**), 123.6 (2C, **7**), 34.2 (2C, C_Q), 31.3 (6C, **^{t}Bu**) ppm.

HRMS (m/z) calculated for $[C_{44}H_{38}N_4 + H]^+$: 623.3175, found 623. 3179.

IR (υ_{max}/cm^{-1}): 2954, 1579 (C=C), 1548, 1513, 1462, 1402, 1362, 1267, 1185, 1118, 1014, 916, 827, 775, 730.

m.p. >300 °C.

5.2.12 Synthesis of 6,15-di-tert-butyl-8,10,11,13-tetraazadibenzo[fg,ij]fluorantheno[7,8,9,10-rst]pentaphene (12)

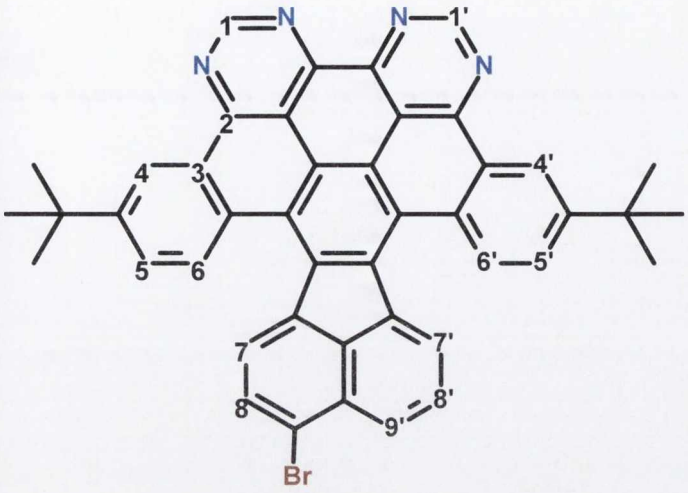

5,5'-(7,10-bis(4-(tert-butyl)phenyl)fluoranthene-8,9-diyl)dipyrimidine (**11**) (100 mg, 0.16 mmol) and bromine (6.23 g, 39 mmol) were heated in a pressure-tube with toluene (10 mL) at 90 °C for 4 hours. The dark red suspension was filtered and recrystallised from dichloromethane and methanol to yield a dark red solid.

Yield: 49 mg, 44 %.

^{1}H NMR (600 MHz, $CDCl_3$) δ 10.16 (s, 2C, **1**, **1'**), 9.59 (s, 1H, **4**), 9.45 (s, 1H, **4'**), 8.22-8.16 (m, 1H, **5'/5**), 8.11-8.02 (m, 1H, **9'**), 7.83 (d, J = 7.4 Hz, 1H, **5'/5**), 7.72-7.68 (m, 1H, **6'/6**), 7.61 (d, J = 7.0 Hz, 1H, **6'/6**), 7.51 (t, J = 7.4 Hz, 1H, **8**), 7.42 (d, J = 7.8 Hz, 1H, **8'**), 7.41 (d, J = 7.8 Hz, 1H, **7'**), 7.08 (d, J = 7.4 Hz, 1H, **7**) ppm.

^{13}C NMR (151 MHz, $CDCl_3$) δ 156.8 (1C, **1**), 156.62 (1C, **1'**), 150.72 (2C, C_Q), 147.02 (2C, C_Q), 144.75 (2C, C_Q), 143.89 (2C, C_Q), 143.08 (1C, C_Q), 142.94 (1C, C_Q), 140.04 (1C, C_Q), 138.58 (1C, C_Q), 137.63 (1C, C_Q), 135.35 (1C, C_Q), 133.12 (1C, C_Q), 132.38 (2C, C_Q), 131.18 (1C, C_Q), 130.81 (1C, **7'**), 130.68 (1C, **7**), 130.13 (2C, **5'/5**), 129.02 (1C, **4'**), 128.9 (1C, **8'**), 128.80 (2C, **6'/6**), 128.7 (1C, **9'**) 128.28 (2C, **5'/5**), 128.0 (1C, **8**), 126.98 (1C, C_Q), 123.86 (1C, **4**), 118.74 (2C, **C-Br**), 35.7 (1C, C_Q), 31.6 (1C, C_Q), 29.7 (3C, **^{t}Bu**), 22.19 (3C, **^{t}Bu**) ppm.

HRMS (m/z) calculated for $[C_{44}H_{31}BrN_4 + H]^+$: 695.1810, found 695.1823.

Elemental Analysis: calculated for C, 75.97; H, 4.49; N, 8.05. Found: C, 76.58; H, 4.39; N, 7.54.

m.p. >300 °C.

5.2.13 Synthesis of 4,4'-(4,4''-di-tert-butyl-5',6'-bis(4-(tert-butyl)phenyl)-[1,1':2',1''-terphenyl]-3',4'-diyl)dipyridine (13)

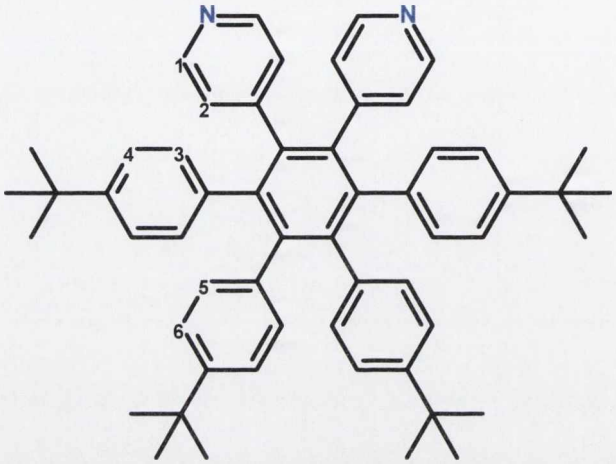

A mixture of 2,3,4,5-tetrakis(4-(tert-butyl)phenyl)cyclopenta-2,4-dien-1-one (400 mg, 0.66 mmol), 1,2-di(pyridin-4-yl)ethyne (150 mg, 0.83 mmol) and benzophenone (750 mg) was heated to 280 °C for 3 hours. After cooling, crystallisation using dichloromethane/methanol yielded the product as a pale brown solid.

Yield: 306 mg, 61 %.

^{1}H NMR (400 MHz, $CDCl_3$) δ 8.20 (d, J = 5.0 Hz, 4H, **1**), 6.92 (d, J = 8.3 Hz, 4H, **2**), 6.86 (m, 8H, **4**, **6**), 6.7 (d, J = 8.7 Hz, 4H, **5**), 6.66 (d, J = 8.3 Hz, 4H, **3**), 1.12 (s, 18H, **^{t}Bu**), 1.11 (s, 18H, **^{t}Bu**) ppm.

^{13}C NMR (101 MHz, $CDCl_3$) δ 149.6 (2C, C_Q), 148.8 (2C, C_Q), 148.1 (2C, C_Q), 147.6 (4C, **1**), 142.3 (2C, C_Q), 140.3 (2C, C_Q), 136.8 (2C, C_Q), 136.3 (2C, C_Q), 136.2 (2C, C_Q), 130.7 (8C, **3**, **5**), 126.6 (4C, **4**), 123.8 (4C, **2**), 123.3 (4C, **6**), 34.2 (2C, C_Q), 34.1 (2C, C_Q), 31.1 (12C, **^{t}Bu**) ppm.

HRMS (m/z) calculated for $[C_{56}H_{60}N_2 + H]^+$: 761.4835, found 761.4805.

Elemental Analysis: calculated for $C_{56}H_{60}N_2$: C, 88.37; H, 7.95; N, 3.68. Found: C, 88.02; H, 7.80; N, 3.72.

IR (υ_{max}/cm^{-1}): 2962 (C-H), 2867, 1722, 1597 (C=C), 1363 (CH_3 bend), 1269, 1107, 828, 678

m.p. >300 °C.

5.2.14 Synthesis of 4,4'-(3',6'-dimethyl-[1,1':2',1''-terphenyl]-4',5'-diyl)dipyridine (14)

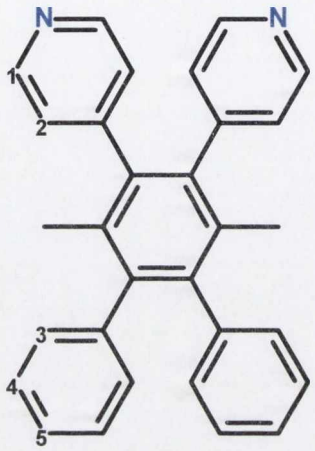

A mixture of 2,5-dimethyl-3,4-diphenylcyclopenta-2,4-dien-1-one (350 mg, 1.4 mmol), 1,2-di(pyridin-4-yl)ethyne (270 mg, 1.5 mmol) and benzophenone (750 mg) was heated to 280 °C for 2.5 hours. The product was purified by column chromatography. CH_2Cl_2 was firstly used to elute benzophenone, at which point a CH_2Cl_2:CH_3OH (1:1) mixture recovered the product as an off-white solid.

Yield: 381 mg, 65%

^{1}H NMR (400 MHz, CD_3CN) δ 8.63 (s, 4H, **1**), 7.81 (d, J = 6.0 Hz, 4H, **2**), 7.25 (t, 4H, J = 7.48 Hz, **4**), 7.19 (t, J = 7.3 Hz, 2H, **5**), 7.09 (d, J = 6.9 Hz, 4H, **3**), 1.79 (s, 6H, -C**H**$_3$) ppm.

^{13}C NMR (101 MHz, $CDCl_3$) δ 158.1 (2C, C_Q), 143.2 (2C, C_Q), 140.6 (4C, **1**), 139.3 (2C, C_Q), 133.8 (2C, C_Q), 130.9 (2C, C_Q), 129.3 (4C, **3**), 128.6 (4C, **2**), 127.4 (4C, **4**), 126.2 (4C, **5**), 18.1 (2C, -**C**H_3) ppm.

HRMS (m/z) calculated for $[C_{30}H_{24}N_2 + H]^+$: 413.2012, found 413.2032.

IR (υ_{max}/cm^{-1}): 2919 (C-H), 1684, 1634, 1602, 1501, 1634, 1422, 1325 (CH_3 bend), 1071, 1111, 766, 705.

m.p. >300 °C.

5.2.15 Synthesis of 6-(4-(tert-butyl)phenyl)-5,8-diphenyl-7-(pyrimidin-5-yl)benzo[f][1,10]phenanthroline (15)

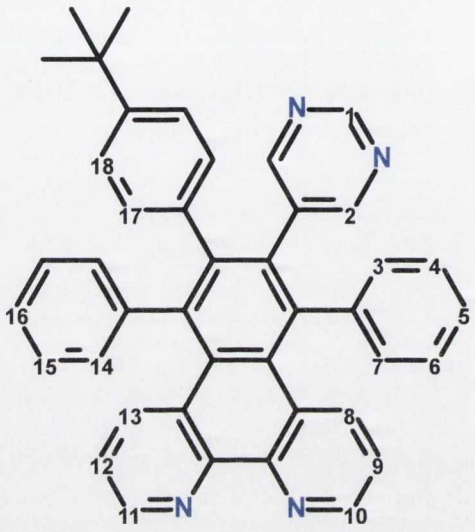

A mixture of 4b-hydroxy-5,7-diphenyl-4b,5-dihydro-6H-cyclopenta[f][1,10]phenanthrolin-6-one (400 mg, 0.66 mmol), 1,2-di(pyridin-4-yl)ethyne (150 mg, 0.83 mmol) and benzophenone (750 mg) was heated to 280 °C for 3 hours. The reaction mixture was purified by column chromatography using 5% methanol in dichloromethane as eluent. Crystallisation using dichloromethane/methanol yielded the product as an off-white solid.

Yield: 88 mg, 42 %.

^{1}H NMR (400 MHz, $CDCl_3$) δ 8.95 (br s, 2H, **10**, **11**), 8.78 (s, 1H, **1**), 8.09 (s, 2H, **2**), 7.86 (dd, J = 8.6, 1.3 Hz, 2H, **8**/**13**), 7.85 (dd, J = 7.5, 1.5 Hz, 1H, **8**/**13**) 7.25-7.10 (m, 12H, **9**/**12**, H_{Ph}), 7.00 (d, J = 8.3 Hz, 1H, **18**), 6.64 (d, J = 8.3 Hz, 2H, **17**), 1.20 (s, 9H, **^{t}Bu**) ppm.

^{13}C NMR (151 MHz, $CDCl_3$) δ 141.1 (1C, C_Q), 140.9 (1C, C_Q), 140.5 (1C, C_Q), 138.5 (1C, C_Q), 138.2 (1C, C_Q), 136.5 (1C, **8**), 136.0 (1C, **13**), 134.8 (1C, C_Q), 134.2 (1C, C_Q), 133.8 (1C, C_Q), 131.2 (2C), 131.0 (2C), 130.4 (2C), 130.3 (2C), 129.0 (2C), 128.8 (1C), 128.0 (1C), 127.3 (1C), 127.0 (1C, C_Q), 126.6 (1C), 126.6 (1C), 125.6 (1C), 125.4 (1C), 123.9 (2C), 121.0 (1C, **9**), 121.0 (1C, **12**) ppm.

HRMS (m/z) calculated for $[C_{42}H_{32}N_4 + H]^+$: 593.2705, found 593.2719.

Elemental Analysis: calculated for $C_{42}H_{32}N_4$: C, 81.19; H, 5.27; N, 8.94. Found: C, 81.69; H, 5.21; N, 8.74.

IR (υ_{max}/cm^{-1}): 1555 (C=N), 1415 (C=C), 1373 (CH_3), 766, 742, 706.

5.2.16 Synthesis of 13-(tert-butyl)-16-phenylbenzo[7',8']quinazolino[4',5',6':9,10,1]phenanthro[2,3-f][1,10]phenanthroline (16)

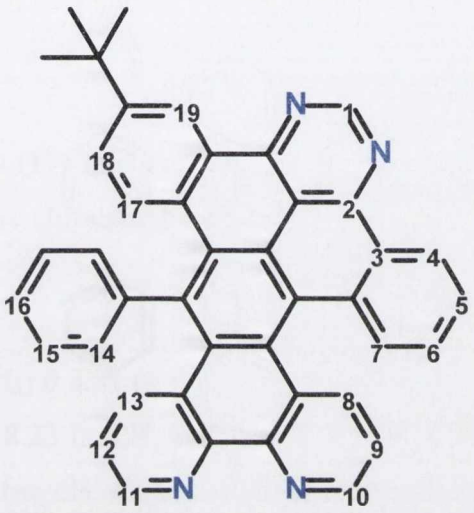

6-(4-(tert-butyl)phenyl)-5,8-diphenyl-7-(pyrimidin-5-yl)benzo[f][1,10]phenanthroline (**15**) (55 mg, 0.085 mmol) and bromine (6.23 g, 39 mmol) were heated in a pressure-tube with toluene (10 mL) at 90 °C for 2 hours. The dark red suspension was filtered and recrystallised from dichloromethane and methanol to yield an orange solid.

Yield: 29 mg, 60 %.

^{1}H NMR (600 MHz, $CDCl_3$) δ 10.03 (s, 1H, **1**), 9.70 (d, 1H, **19**), 9.64 (s, 1H, **4**), 9.45 (s, 2H, **10**, **11**), 8.81 (m, 2H, **8**, **13**), 8.49 (s, 2H, **9**, **12**), 7.94 (s, J = 8.0 Hz 2H, **18**), 7.82 (d, J = 8.0 Hz, 2H, **17**), 7.76 (m, 3H, **14**, **16**), 7.69 (m, 2H, **5**, **7**), 7.49 (d, J = 9.0 Hz, 2H, **15**), 7.42 (d, J = 6.2 Hz, 1H, **6**) ppm.

^{13}C NMR (151 MHz, $CDCl_3$) δ 155.9 (1C, **1**), 154.5 (1C, **2**), 152.7 (1C, **4**), 151.0 (1C, C_Q), 150.2 (1C, C_Q), 146.4 (1C, C_Q), 142.3 (2C, **8**, **13**), 137.0 (1C, C_Q), 133.0 (1C, C_Q), 132.2 (2C, **15**), 132.0 (1C, C_Q), 131.9 (1C, C_Q), 131.5 (1C, C_Q), 130.8 (1C, C_Q), 130.6 (1C, **5**/**7**), 130.2 (2C, **8**, **13**), 130.0 (1C, **5**/**7**), 129.7 (2C, **9**, **12**), 129.4 (1C, C_Q), 129.2 (1C, C_Q), 128.8 (3C, **14**/**16**), 128.4 (1C, **18**), 128.1 (1C, **17**), 127.0 (1C, **6**), 125.8 (2C, **10**, **11**),

125.2 (1C, **19**), 125.0 (1C, C_Q), 124.4 (1C, C_Q), 124.3 (1C, C_Q), 123.6 (1C, C_Q), 123.0 (1C, C_Q), 31.1 (3C, **^{t}Bu**), 29.5 (1C, C_Q) ppm.

HRMS (m/z) calculated for $[C_{42}H_{29}N_4 + H]^+$: calculated 589.2392, found 589.2390.

m.p. >300 °C.

5.2.17 Synthesis of 5,5',5''-(5'-phenyl-[1,1':3',1''-terphenyl]-2',4',6'-triyl)tripyrimidine (17)

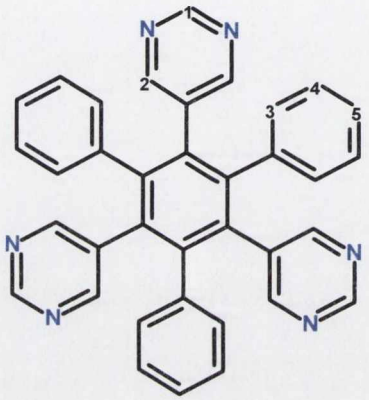

5-pyrimidinephenylacetylene (250 mg, 1.39 mmol) was dissolved in dioxane (7 mL). Dicobalt octacarbonyl (88 mg, 0.26 mmol) was added, and the solution refluxed for 48 hours under argon. The reaction mixture was cooled to room temperature and the solvent was removed *in vacuo*. The desired product was purified by preparative-plate chromatography using dichloromethane:methanol (5%) as eluent with the symmetric fraction (**17**) being collected firstly.

Yield: 22 mg, 15.6 %

^{1}H NMR (600 MHz, $CDCl_3$) δ 8.73 (s, 3H, **1**), 8.23 (s, 6H, **2**), 7.04 (m, J = 7.9 Hz, 9H, **4**, **5**), 6.87 (d, J = 6.6 Hz, 6H, **3**) ppm.

^{13}C NMR (151 MHz, $CDCl_3$) δ 157.5 (6C, **2**), 155.9 (3C, **1**), 142.8 (3C, C_Q), 137.2 (3C, C_Q), 133.8 (3C, C_Q), 133.5 (3C, C_Q) 130.2 (6C, **3**), 128.1 (6C, **4**), 127.3 (3C, **5**) ppm.

HRMS (m/z) calculated for $[C_{36}H_{24}N_6 + H]^+$: 541.2135, found 541.2134.

m.p. >300 °C.

5.2.18 Synthesis of 5,5',5''-(5'-phenyl-[1,1':2',1''-terphenyl]-3',4',6'-triyl)tripyrimidine (18)

From the same reaction as (**17**) this asymmetric isomer could be isolated as the second fraction from the preparative chromatography plate.

Yield: 35 mg, 25 %

^{1}H NMR (400 MHz, $CDCl_3$) δ 8.81 (s, 1H, **1'**), 8.80 (s, 1H, **1''**), 8.73 (s, 1H, **1**), 8.28 (s, 2H, **2'**), 8.27 (s, 2H, **2''**), 8.23 (s, 2H, **2**), 7.08-7.03 (m, 3H, **5'**, **5''**, **5**), 7.01 – 6.97 (m, 6H, **3'**, **3''**, **3**), 6.90 – 6.84 (m, 6H, **4'**, **4''**, **4**) ppm.

^{13}C NMR (101 MHz, $CDCl_3$) δ 157.8 (2C, **2'**, **2''**), 1575 (1C, **2**), 156.5 (1C, **1'**), 156.4 (1C, **1''**), 156.0 (1C, **1**), 143.4 (1C, C_Q), 142.4 (1C, C_Q), 142.2 (1C, C_Q), 138.1 (1C, C_Q), 137.8 (1C, C_Q), 137.4 (1C, C_Q), 135.5 (1C, C_Q), 135.0 (1C, C_Q), 134.0 (1C, C_Q), 133.8 (1C, C_Q), 133.4 (1C, C_Q), 133.2 (1C, C_Q), 131.0 (4C, **4'**, **4''**), 130.6 (2C, **4**), 128.4 (2C, **5'**, **5''**), 127.8 (2C, **3'**), 127.8 (2C, **3''**), 127.6 (1C, **5**), 127.0 (2C, **3**) ppm.

HRMS (m/z) calculated for $[C_{36}H_{24}N_6 + H]^+$: 541.2135, found 541.2134.

m.p. >300 °C.

5.2.19 Synthesis of 1,3,9,11,12,14-hexaazadibenzo[fg,ij]triphenyleno[1,2,3,4-rst]pentaphene (19)

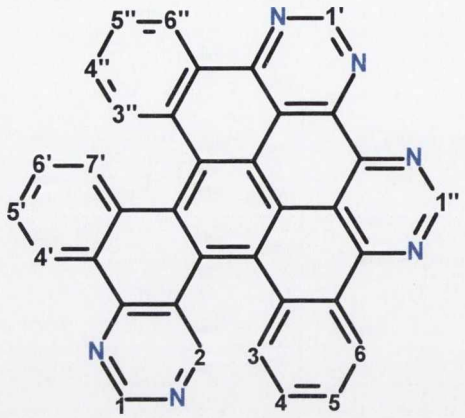

5,5',5''-(5'-phenyl-[1,1':2',1''-terphenyl]-3',4',6'-triyl)tripyrimidine (20 mg, 0.027 mmol) and bromine (6.23 g, 39 mmol) were heated in a pressure-tube with toluene (10 mL) at 90 °C for 2 hours. The orange suspension was filtered to yield dark orange crystals.

Yield: 12 mg, 84 %.

^{1}H NMR (600 MHz, MeOD) δ 9.66 (s, 1H, **1''**), 9.56 (s, 1H, **2**), 9.42 (d, *J* = 7.0 Hz, 2H, **6**), 9.27 (d, *J* = 7.5 Hz, 1H, **6''**), 9.17 (d, *J* = 8.0 Hz, 2H, **3**), 9.13 (s, 1H, **1'**), 8.79 (s, 1H, **1**), 8.35 (d, *J* = 8.5 Hz, 1H, **3''**), 8.02 (t, *J* = 7.1 Hz, 1H, **5**), 7.98 (t, *J* = 7.7 Hz, 1H, **4**), 7.75 (t, *J* = 7.7 Hz, 1H, **5''**), 7.68 (d, *J* = 7.5 Hz, 1H, **4'**), 7.64 (d, *J* = 7.9 Hz, 1H, **7'**), 7.57 (t, *J* = 7.4 Hz, 1H, **5'**), 7.43 (t, *J* = 7.7 Hz, 1H, **4''**), 7.33 (t, *J* = 7.7 Hz, 1H, **6'**) ppm.

^{13}C NMR (151 MHz, MeOD) δ 157.2 (1C, C_Q), 156.9 (1C, C_Q), 156.8 (1C, C_Q), 154.7 (1C, **1''**), 154.3 (1C, **1'**), 154.1 (1C, C_Q), 151.2 (1C, C_Q), 149.0 (1C, **2**), 147.8 (1C, C_Q), 144.7 (1C, C_Q), 143.0 (1C, C_Q), 141.9 (1C, **1**), 140.5 (1C, C_Q), 136.9 (1C, C_Q), 136.7 (1C, C_Q), 135.9 (1C, C_Q), 133.9 (1C, C_Q), 133.2 (1C, C_Q), 132.8 (1C, C_Q), 132.5 (1C, C_Q), 131.9 (1C, C_Q), 131.6 (1C, **5**), 131.0 (1C, C_Q), 130.9 (1C, **4**), 130.8 (1C, **5'**), 130.0 (1C, **3''**), 129.9 (1C, **4''**), 129.0 (1C, **6''**), 128.6 (1C, **6'**), 128.0 (1C, **3**), 127.6 (1C, C_Q), 127.2 (1C, **6**), 126.7 (1C, **6''**), 125.8 (1C, **7'**), 125.6 (1C, **4'**), 116.4 (1C, C_Q) ppm.

HRMS (m/z) calculated for $[C_{36}H_{16}\ N_6 + H]^+$: 533.1515, found 541.1512.

IR (υ_{max}/cm^{-1}): 2953 (C-H), 2253, 2127, 1660, 1540 (C=N), 1050, 1023, 1001, 822, 760, 615

m.p. >300 °C.

5.2.20 Synthesis of 8,9,10-tris(4-bromophenyl)tribenzo[e,gh,j]perimidine (20)

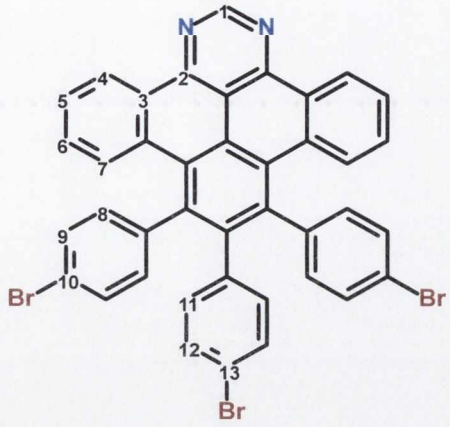

5-(4',5',6'-triphenyl-[1,1':2',1''-terphenyl]-3'-yl)pyrimidine (**1**) (200 mg, 0.372 mmol) and bromine (6.23 g, 39 mmol) were stirred for 25 minutes. The crude product was then precipitated using dichloromethane and methanol. Purification on SiO_2 using dichloromethane:hexane (8:2) yielded the product as a pale-yellow solid.

Yield: 227 mg, 80 %.

^{1}H NMR (600 MHz, $CDCl_3$) δ 9.80 (s, 1H, **1**), 9.46 (s, 2H, **4**), 7.69 (d, J = 7.2 Hz, 2H, **5**), 7.67 (d, J = 8.8 Hz, 2H,**7**), 7.38 (d, J = 8.1 Hz, 2H, **6**), 7.39 (d, J = 8.1 Hz, 4H, **9**), 7.16 (d, J = 7.7 Hz, 2H, **12**), 6.98 (d, J = 7.7 Hz, 4H, **8**), 6.68 (d, J = 8.2 Hz, 2H, **11**) ppm.

^{13}C NMR (151 MHz, $CDCl_3$) δ 154.9 (1C, **1**), 152.7 (2C, **2**), 142.4 (2C, C_Q), 140.9 (2C, C_Q), 138.3 (1C, C_Q), 138.1 (1C, C_Q), 133.4 (2C, C_Q), 132.8 (2C, **11**), 132.5 (4C, **8**), 131.6 (4C, **9**), 129.9 (2C, **12**), 129.4 (4C, **6**, **7**), 127.6 (2C, **5**), 127.3 (2C, C_Q), 125.6 (2C, **4**), 123.9 (2C, C_Q), 121.2 (2C, **10**), 120.3 (1C, **13**), 114.3 (2C, C_Q) ppm.

HRMS (m/z) calculated for $[C_{40}H_{22}N_2Br_3 + H]^+$ 766.9327, found 766.9333.

Elemental Analysis: calculated for $C_{40}H_{21}Br_3N_2$: C, 62.45 ; H, 2.75; N, 3.64. Found: C, 59.29; H, 2.32; N, 3.32.

IR (υ_{max}/cm^{-1}): 3045 (C-H), 1588, 1559 (C=N), 1540, 1488, 1388, 1305, 1126, 1103, 1068, 1010, 960, 851, 740, 695, 682 (C-Br).

m.p. >300 °C.

5.2.21 Synthesis of 5-bromo-8,9,10-tris(4-bromophenyl)tribenzo[e,gh,j]perimidine (21)

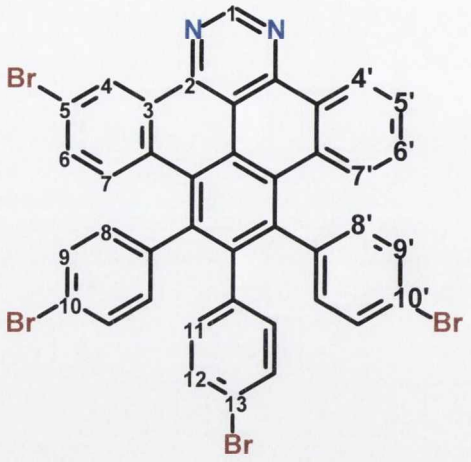

5-(4',5',6'-triphenyl-[1,1':2',1''-terphenyl]-3'-yl)pyrimidine (**1**) (162 mg; 0.3019 mmol) and bromine (5 mL) were placed in a round bottom flask (10 mL). The mixture was stirred at room temperature for 90 minutes. The crude product was purified by column chromatography using dichloromethane as eluent. The product was recrystallized using dichloromethane and methanol yielding a yellow solid

Yield: 41 mg, 23 %.

^{1}H NMR (400 MHz, $CDCl_3$) δ 9.82 (s, 1H, **1**), 9.59 (d, *J* =2.2 Hz, 1H, **4**), 9.45 (d, *J* = 7.8 Hz, 1H, **4'**), 7.71 (t, *J* = 7.4 Hz, **5'**), 7.69 (d, *J* =8.2 Hz, 4H, **7'**), 7.50 (d, *J* =8.2, 1H, **7**), 7.45 (d, *J* =8.2, 1H, **6**), 7.40-7.35 (m, 5H, **9**, **9'**, **6'**), 7.17 (d, *J* = 8.2 Hz, 2H, **11**), 6.98 (d, *J* = 8.1, 2H, **8**), 6.96 (d, *J* = 8.2 Hz, 2H, **8'**), 6.67 (d, *J* = 8.1 Hz, 2H, **12**) ppm.

^{13}C NMR (101 MHz, $CDCl_3$) δ 155.4 (2C, C_Q), 152.7 (1C, C_Q), 151.3 (1C, C_Q), 142.3 (1C, C_Q), 140.5 (1C, C_Q), 140.3 (1C, C_Q), 138.0 (1C, C_Q), 137.9 (1C, C_Q), 137.6 (1C, C_Q), 133.0 (1C, C_Q), 132.4 (2C, **12**), 132.2 (2C, **8'**), 132.1 (2C, **8**), 131.9 (1C, **6**), 131.7 (1C, C_Q), 131.6 (1C, C_Q), 131.5 (2C, **9'**), 131.3 (2C, **9**), 130.6 (1C, 7), 130.1 (1C, C_Q), 129.8 (2C, **11**), 129.1 (2C, **6**, **7'**), 127.7 (1C, **4**), 127.3 (1C, **5'**), 127.1 (1C, C_Q), 126.4 (1C, C_Q), 125.1 (1C, **4'**), 122.0 (1C, C_Q), 121.1 (1C, C_Q), 121.0 (1C, C_Q), 120.0 (1C, C_Q), 114.3 (1C, , C_Q) ppm.

HRMS (m/z) calculated for $[C_{40}H_{20}Br_4N_2 + H]^+$ 844.8438, found 844.8412.

Elemental Analysis: calculated for $C_{40}H_{20}Br_4N_2$: C, 56.64, H, 2.38, N, 3.30. Found C, 55.76, H, 2.06, N, 3.09.

IR (υ_{max}/cm^{-1}): 3039 (C-H), 1575 (C=N), 1539, 1508, 1439 (C=C), 1384, 1254, 1176, 1099, 1072, 1011, 814, 761, 733, 695 (C-Br).

m.p. >300 °C.

5.2.22 Synthesis of 5,13-dibromo-8,9,10-tris(4-bromophenyl)tribenzo[e,gh,j]perimidine (22)

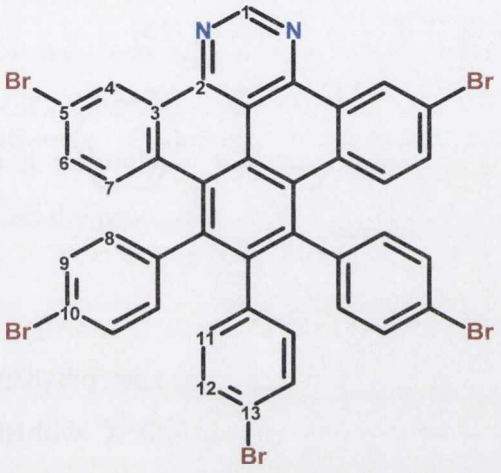

5-(4',5',6'-triphenyl-[1,1':2',1''-terphenyl]-3'-yl)pyrimidine (**1**) (200 mg, 0.372 mmol) and bromine (6.23 g, 39 mmol) were refluxed in $CHCl_3$ for 3 hours. The crude product was then precipitated using dichloromethane and methanol. Purification by column chromatography using dichloromethane:hexane (8:2) as eluent yielded the product as a pale-yellow solid.

Yield: 171 mg, 50 %.

^{1}H NMR (600 MHz, $CDCl_3$) δ 9.81 (s, 1H, **1**), 9.59 (s, 1H, **4**), 7.51 (d, J = 9.0 Hz, 2H, **7**), 7.45 (d, J = 8.9 Hz, 2H, **6**), 7.41 (d, J = 7.4 Hz, 4H, **9**), 7.17 (d, J = 7.4 Hz, 2H, **12**), 6.96 (d, J = 7.7 Hz, 4H, **8**), 6.66 (d, J = 7.5 Hz, 2H, **11**) ppm.

^{13}C NMR (151 MHz, $CDCl_3$) δ 155.7 (1C, **1**), 151.9 (2C, **2**), 142.7 (2C, C_Q), 140.4 (2C, C_Q), 138.1 (2C, C_Q), 137.9 (2C, C_Q), 132.7 (2C, **11**), 132.4 (2C, **9**), 132.3 (2C, **8**), 132.00 (2C, **7**), 131.9 (2C, C_Q), 130.8 (2C, **6**), 130.2 (2C, **11**), 128.6 (2C, C_Q), 128.1 (2C, **3**), 126.9 (2C, C_Q), 123.8 (2C, C_Q), 122.4 (2C, **5**), 121.6 (2C, **10**), 120.5 (1C, **13**), 114.8 (2C, C_Q) ppm.

HRMS (m/z) calculated for $[C_{40}H_{19}N_2Br_5 + H]^+$ 922.7521, found 922.7538.

Elemental Analysis: calculated for $C_{40}H_{19}Br_5N_2$: C, 51.82; H, 2.07; N, 3.02. Found: C, 50.86; H, 1.80; N, 2.76.

IR (υ_{max}/cm^{-1}): 3039 (C-H), 1896, 1573, 1538, 1488 (C=C), 1072, 1012, 970 (C-H), 846, 819, 796, 696, 677 (C-Br).

m.p. >300 °C.

5.2.23 Synthesis of *trans*-4, 4'-dibromostilbene (23)

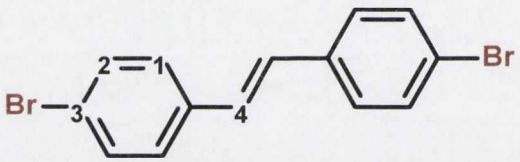

Titanium tetrachloride (16.5 mL, 151 mmol) and zinc powder (19.9 g, 30 mmol) were added slowly to dry tetrahydrofuran (300 mL) at -10 °C with stirring. To this, a solution of 4-bromobenzaldehyde (10.0 g, 54 mmol) in dry tetrahydrofuran (150 mL) was added and the mixture was refluxed for 6 hours. After cooling, the reaction mixture was quenched with saturated $NaHCO_3$ solution and extracted with ethyl acetate. The organic layer was then washed with brine and water (3 x 50 mL) and dried over $MgSO_4$. Recrystallisation from hexane yielded the product as a white crystalline solid.

Yield: 7.5 g, 82 %.

^{1}H NMR ($CDCl_3$) δ 7.41 (d, 4H, J = 8.5 Hz, **1**), 7.29 (d, 4H, J = 7.9 Hz, **2**), 6.94 (s, 2H, **4**) ppm.

^{13}C NMR ($CDCl_3$) δ: 135.9 (2C, C_Q), 131.9 (4C, **1**), 128.1 (2C, **4**), 128.0 (4C, **2**), 121.7 (2C, **3**) ppm.

IR (υ_{max}/cm^{-1}): 1585 (C=C), 1489, 1405, 1074, 1006, 970, 948, 820, 713, 615 (C-Br).

m.p. : 182-185 °C.

5.2.24 Synthesis of 4, 4'-didodecyl-*trans*-stilbene (24)

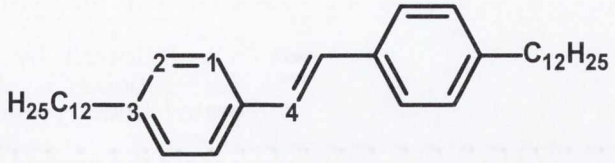

To a solution of *trans*-4, 4'-dibromostilbene (**23**) (7.45 g, 22 mmol) and $NiCl_2$(dppp) (0.48 g, 0.89 mmol) in diethylether (60 mL), dodecymagnesiumbromide (50 mL, 1 M in diethylether, 0.5 mol) was slowly added. The reaction mixture was stirred for 3 days, at which point 2 M HCl (150 mL) was added. The organic layer was the collected, dried over $MgSO_4$ and the solvent evaporated *in vacuo*. The crude product was then dissolved in dichloromethane, filtered through a short silica plug. Removing the solvent under reduced pressure precipitated the product as a white solid.

Yield: 10.6 g, 93 %.

^{1}H NMR (600 MHz, $CDCl_3$) δ 7.44 (d, 4H, J = 8.0 Hz, **1**), 7.18 (d, 4H, J = 8.0 Hz, **2**), 7.07 (s, 2H, **4**), 2.63 (t, 4H, J = 7.5 Hz, -CH dodecyl), 1.5-1.1 (m, 40H, -CH dodecyl), 0.91 (t, 6H, J = 7.0 Hz, -CH dodecyl) ppm.

^{13}C NMR (151 MHz, $CDCl_3$) δ 142.0 (2C, C_Q), 134.5 (2C,C_Q), 128.3 (4C, **1**), 127.2 (2C, **4**), 125.9 (4C, **2**), 35.3 (-CH dodecyl), 31.5 (-CH dodecyl), 31.0 (-CH dodecyl), 29.2 (-CH dodecyl), 29.2 (-CH dodecyl), 29.2 (-CH dodecyl), 29.1 (-CH dodecyl), 28.9 (-CH dodecyl), 28.9 (-CH dodecyl), 22.3 (-CH dodecyl), 13.7 (-CH dodecyl) ppm.

IR (υ_{max}/cm^{-1}): 2917 (-CH dodecyl), 2848 (-CH dodecyl), 1480, 948, 857, 966, 840, 722.

m.p. : 79-81 °C.

5.2.25 Synthesis of 4,4'-didodecyldiphenylacetylene (26)

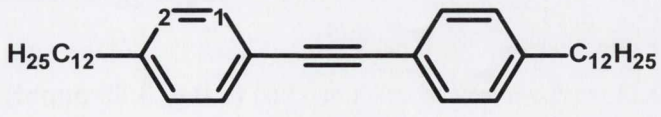

To a solution of 4,4'-didodecyl-trans-stilbene (**24**) (10 g, 19.4 mmol) in chloroform (120 mL), bromine (1 mL, 19.6 mmol) was added. The solution was stirred at room temperature overnight and was then washed with aqueous sodium sulfite and water. The product was dried over $MgSO_4$ and the solvent evaporated in vacuo. The solid was then redissolved in *tert*-butanol (180 mL) and potassium-*tert*-butoxide (25 g, 223 mmol)

added. The reaction mixture was heated to reflux for 24 hours. After allowing the reaction mixture to cool to room temperature it was extracted with methyl-*tert*-butyl ether. The organic phase was then washed with 2 M HCl, followed by a saturated sodium bicarbonate solution. The solvent was the evaporated under reduced pressure and the crude product recrystallised from boiling toluene to yield the desired product.

Yield: 7.4 g, 81 %.

^{1}H NMR (600 MHz, $CDCl_3$) δ 7.36 (d, 4H, J = 8.0 Hz, **1**), 7.07 (d, 4H, J = 8.0 Hz, **2**), 2.53 (t, 4H, J = 7.5 Hz, -CH dodecyl), 1.53-1.19 (m, 40H, -CH dodecyl), 0.81 (t, 6H, J = 6.9 Hz, -CH dodecyl) ppm.

^{13}C NMR (151 MHz, $CDCl_3$) δ 143.3 (2C, C_Q), 131.4 (4C, **1**), 128.4 (4C, **2**), 120.6 (2C, C_Q), 89.0 (2C, -**C**≡C-), 36.0 (-CH dodecyl), 32.0 (-CH dodecyl), 31.3 (-CH dodecyl), 29.7 (-CH dodecyl), 29.7 (-CH dodecyl), 29.6 (-CH dodecyl), 29.5 (-CH dodecyl), 29.4 (-CH dodecyl), 29.3 (-CH dodecyl), 22.7 (-CH dodecyl), 14.2 (-CH dodecyl) ppm.

IR (υ_{max}/cm^{-1}): 2918 (-CH dodecyl), 2847 (-CH dodecyl), 1461, 961, 840, 818, 723.

m.p. : 53-56 °C.

5.2.26 Synthesis of 4,4'-didodecylbenzil (27)

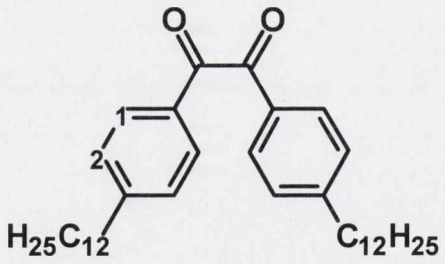

A solution of 4,4'-didodecyldiphenylacetylene (**26**) (2.0 g, 3.88 mmol) and iodine (0.49 g, 1.92 mmol), dissolved in dimethyl sulfoxide (100 mL) was stirred at 155 °C for 24 hours. After cooling, the reaction mixture was washed with a sodium thiosulphate solution (200 mL) and extracted with dichloromethane (3 x 50 mL). The organic phase was washed with water and dried over $MgSO_4$. After evaporation of the solvent the crude was purified by column chromatography on silica (petroleum ether/dichloromethane 3:1). Recrystallisation from acetone yielded the product as pale yellow crystals.

Yield: 3.52 g, 42 %.

^{1}H NMR (600 MHz, $CDCl_3$) δ 7.90 (d, 4H, *J* = 8.5 Hz, **1**), 7.32 (d, 4H, *J* = 8.5 Hz, **2**), 2.70 (t, 4H, *J* = 7.7 Hz, -CH dodecyl), 1.7-1.2 (m, 40H, -CH dodecyl), 0.90 (t, 6H, *J* = 7.0 Hz, -CH dodecyl) ppm.

^{13}C NMR (151 MHz, $CDCl_3$) δ 194.1 (2C, -**C**O), 150.6 (2C, C_Q), 130.4 (2 C, C_Q), 129.6 (4C, **1**), 128.6 (4C, **2**), 35.8 (-CH dodecyl), 31.5 (-CH dodecyl), 30.6 (-CH dodecyl), 29.2 (-CH dodecyl), 29.2 (-CH dodecyl), 29.1 (-CH dodecyl), 29.0 (-CH dodecyl), 28.9 (-CH dodecyl), 28.8 (-CH dodecyl), 22.3 (-CH dodecyl), 13.7 (-CH dodecyl) ppm.

IR (υ_{max}/cm^{-1}): 2916 (-CH dodecyl), 2850 (-CH dodecyl), 1666 (-C=O), 1605, 1466, 1172, 1218, 880, 772, 617.

m.p. : 45-47 °C

5.2.27 Synthesis of 4-bromomethyldodecylbenzene (28)

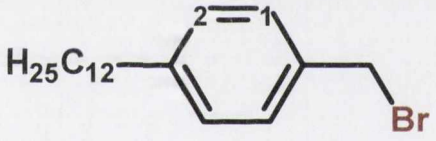

Phenyldodecane (14.60 g, 59.11 mmol) and paraformaldehyde (1.82 g, 60.57 mmol) were dissolved in glacial acetic acid (100 mL). Hydrobromic acid (40 mL, 33 % in acetic acid) was then added after 5 minutes. The solution was heated at 80 °C for 96 hours, quenched with water and extracted using dichloromethane. After drying over $MgSO_4$ the organic layer was filtered over celite and evaporated to dryness to yield an oily residue. Subjecting the crude material to column chromatography using petroleum ether as eluent the product was obtained as a white crystalline powder.

Yield: 9.6 g, 14 %.

^{1}H NMR (600 MHz, $CDCl_3$) δ 7.33 (d, 2H, *J* = 8.0 Hz, **1**), 7.17 (d, 2H, *J* = 8.0 Hz, **2**), 4.52 (s, 2H, -C**H**$_2$), 2.61 (t, 2H, *J* = 7.8 Hz, -CH dodecyl), 1.68-1.24 (m, 20H, -CH dodecyl), 0.91 (t, 3H, *J* = 7.0 Hz, -CH dodecyl) ppm.

^{13}C NMR (151 MHz, $CDCl_3$) δ 143.0 (1C, C_Q), 134.5 (1C, C_Q), 128.5 (2C, **1**), 128.4 (2C, **2**), 35.3 (1C, -**C**H_2), 33.4 (-CH dodecyl), 31.5 (-CH dodecyl), 30.9 (-CH dodecyl), 29.2 (-

CH dodecyl), 29.2 (-CH dodecyl), 29.1 (-CH dodecyl), 28.9 (-CH dodecyl), 28.9 (-CH dodecyl), 22.3 (-CH dodecyl), 13.7 (-CH dodecyl) ppm.

IR (υ_{max}/cm^{-1}): 2916 (-CH dodecyl), 2848 (-CH dodecyl), 1461, 834, 772, 725.

m.p. : 42-43 °C

5.2.28 Synthesis of 1,3-bis(4-dodecylphenyl)-propan-2-one (29)

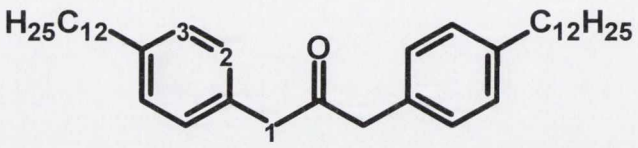

Calcium hydroxide (3.2 g, 44.2 mmol), tetrabutylammonium hydrogensulphate (67 mg, 0.29 mmol) and 1-(bromomethyl)-4-dodecylbenzene (**28**) (3 g, 8.84 mmol) were dissolved in 1:1 dichloromethane:water (200 mL) and bubbled with argon to degas for 20 minutes. Iron pentacarbonyl (865 mg, 0.6 mL, 4.6 mmol) was then added and the reaction stirred for 18 hours under argon. The reaction mixture was then oxidised in air for 2 hours and acidified with HCl (2 M). The aqueous layer was then extracted with dichloromethane, again washed with HCl (2 M), deionised water, dried over $MgSO_4$ and the solvent evaporated under reduced pressure. The resulting solid was purified by column chromatography. Elution with petroleum ether yielded the desired product as white crystals.

Yield: 3.0 g, 62 %.

^{1}H NMR (600 MHz, $CDCl_3$) δ 7.15 (d, 4H, J = 7.8 Hz, **2**), 7.09 (d, 4 H, J = 8.0 Hz, **3**), 3.71 (s, 4H, **1**), 2.62 (t, 4H, J = 7.6 Hz), 1.6-1.3 (m, 40H, -CH dodecyl), 0.94 (t, 6H, J = 6.8 Hz, -CH dodecyl) ppm.

^{13}C NMR (151 MHz, $CDCl_3$) δ 204.7 (1C, -**C**O), 140.6 (2C, C_Q), 129.4 (2C, C_Q), 128.8 (4C, **2**), 128.8 (4C, **3**), 48.7 (2C, **1**), 35.6 (-CH dodecyl), 31.9 (-CH dodecyl), 30.5 (-CH dodecyl), 29.7 (-CH dodecyl), 29.7 (-CH dodecyl) 29.6 (-CH dodecyl), 29.6 (-CH dodecyl), 29.4 (-CH dodecyl), 22.8 (-CH dodecyl), 14.2 (-CH dodecyl) ppm.

IR (υ_{max}/cm^{-1}): 2917 (-CH dodecyl), 2849 (-CH dodecyl), 1715(-C=O), 1519, 1466, 1059, 822, 721.

m.p. : 71-72 °C.

5.2.29 Synthesis of tetra(4-dodecyl-phen-1-yl)cyclopentadienone (30)

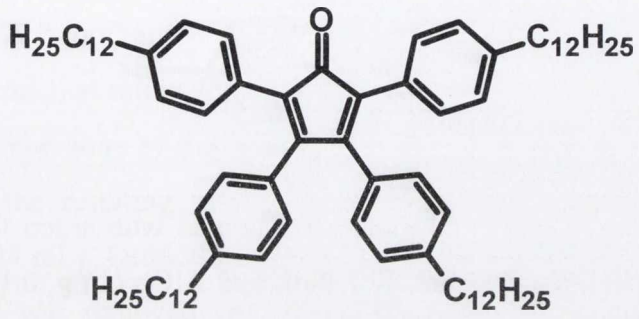

Potassium hydroxide (150 mg, 2.67 mmol) in ethanol (2 mL) was added to a refluxing solution of 1,2-bis(4-dodecylphenyl)ethane-1,2-dione (**27**) (500 mg, 0.91 mmol) and 1,3-bis(4-dodecylphenyl)propan-2-one (**29**) (480 mg, 0.87 mmol) in ethanol (20 mL). After 5 minutes the reaction mixture was cooled to 0 °C for 30 minutes at which point the solvent was decanted off. The viscous oil was subjected to column chromatography; elution with dichloromethane/hexane (9:1) yielded the product as a purple waxy solid.

Yield: 406 mg, 42%.

^{1}H NMR (600 MHz, $CDCl_3$) δ 7.18 (d, 4H, J = 8.3 Hz, -CH Ar), 7.06 (d, 4H, J = 8.3 Hz, -CH Ar), 6.97 (d, 4H, J = 8.0 Hz, -CH Ar), 6.83 (d, 4H, J = 8.0 Hz, -CH Ar), 2.57 (m, 8 H, -CH dodecyl), 1.6-1.1 (m, 80H, -CH dodecyl), 0.91 (t, 12H, J = 6.7 Hz, -CH dodecyl) ppm.

^{13}C NMR (151 MHz, $CDCl_3$) δ 200.9 (1C, -**C**O), 154.0 (2C, C_Q), 143.0 (2C, C_Q), 141.9 (2C, C_Q), 130.5 (2C, C_Q), 129.8 (4C, -CH Ar), 129.2 (4C, -CH Ar), 128.2 (2C, C_Q), 127.8 (4C, -CH Ar), 127.7 (4C, -CH Ar), 124.5 (2C, C_Q), 35.7 (-CH dodecyl), 35.6 (-CH dodecyl), 31.8 (-CH dodecyl), 31.0 (-CH dodecyl), 30.9 (-CH dodecyl), 29.6 (-CH dodecyl), 29.5 (-CH dodecyl), 29.5 (-CH dodecyl), 29.4 (-CH dodecyl), 29.4 (-CH dodecyl), 29.2 (-CH dodecyl), 29.2 (-CH dodecyl), 29.2 (-CH dodecyl), 29.0 (-CH dodecyl), 22.5 (-CH dodecyl), 13.9 (-CH dodecyl) ppm.

IR (υ_{max}/cm^{-1}): 2924 (-CH dodecyl), 2843 (-CH dodecyl), 1715 (-C=O), 1519, 1466, 1059, 822, 721.

m.p. : 45-46 °C.

5.2.30 Synthesis of 4-bromododecananoylbenzene (31)

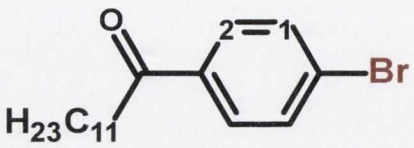

Bromobenzene (31.3 g, 21 mL, 0.2 mol) was bubbled with argon for 20 min. To this, dodecanoyl chloride (21.9 g, 23.4 mL, 0.1 mol) and $AlCl_3$ (16 g, 0.12 mol) were added. The reaction mixture was heated to 50 °C for 2 hours at which point it was poured on to ice water and extracted with dichloromethane. The organic phase was then washed with 2 M HCl, then brine and dried over $MgSO_4$. After the removal of solvent the product was recrystallised from ethanol, yielding white crystals.

Yield: 21.8 g, 64%.

^{1}H NMR (400 MHz, $CDCl_3$) δ 7.89 (d, 2H, *J* = 9.0 Hz, **1**), 7.66 (d, 2H, *J* = 9.0 Hz, **2**), 2.94 (t, 2H, *J* = 7.5 Hz, -CH dodecyl), 1.74 (q, 2H, *J* = 7.4 Hz, -CH dodecyl), 1.21 - 1.42 (m, 18H, -CH dodecyl), 0.91 (t, 3H, *J* = 6.8 Hz, -CH dodecyl) ppm.

^{13}C NMR (101 MHz, $CDCl_3$) δ 199.6 (1C, -**C**O), 135.8 (1C, C_Q), 131.9 (2C, **1**), 129.6 (2C, **2**), 128.0 (1C, **C**-Br), 38.6 (-CH dodecyl), 31.9 (-CH dodecyl), 29.6 (-CH dodecyl), 29.5 (-CH dodecyl), 29.5 (-CH dodecyl), 29.3 (-CH dodecyl), 28.7 (-CH dodecyl), 24.3 (-CH dodecyl), 22.7 (-CH dodecyl), 14.1 (-CH dodecyl) ppm.

IR (υ_{max}/cm^{-1}): 2916 (-CH dodecyl), 2848 (-CH dodecyl), 1715 (-C=O), 1519, 1465, 1059, 822, 720.

m.p. : 62-65 °C.

5.2.31 Synthesis of 4-bromododecylbenzene (32)

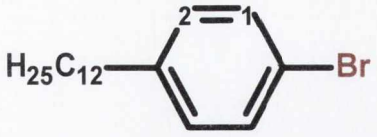

A mixture of 1-(4-bromophenyl)dodecan-1-one (**31**) (14.65 g, 43.19 mmol), hydrazine hydrate (6.29 mL, 129 mmol) and potassium hydroxide (9.67 g, 172 mmol) was heated in ethylene glycol (70 mL), at reflux for 2 h. The mixture was then distilled at atmospheric pressure until the temperature of the reaction mixture exceeded 210 °C. After cooling to room temperature, the resulting mixture was poured into water and acidified using hydrochloric acid (25 mL). Extraction was carried out using DCM and after drying over $MgSO_4$ the solvent was removed *in vacuo*. Purification was achieved using column chromatography with petroleum ether as eluent. The product was isolated as a colourless oil.

Yield: 9.13 g, 65%.

^{1}H NMR (400 MHz, $CDCl_3$) δ 7.42 (d, 2H, J = 9.0 Hz, **1**), 7.08 (d, 2H, J = 8.0 Hz, **2**), 2.59 (t, 2H, J = 7.5 Hz, -CH dodecyl), 1.62 - 1.30 (m, 20H, -CH dodecyl), 0.92 (t, 3H, J = 7.5 Hz) ppm.

^{13}C NMR (101 MHz, $CDCl_3$) δ 131.2 (1C, C_Q), 130.3 (2C, **1**), 128.5 (2C, **2**), 128.0 (1C, C-Br), 35.4 (-CH dodecyl), 32.0 (-CH dodecyl), 31.4 (-CH dodecyl), 29.7 (-CH dodecyl), 29.6 (-CH dodecyl), 29.5 (-CH dodecyl), 29.4 (-CH dodecyl), 29.2 (-CH dodecyl), 24.2 (-CH dodecyl), 22.7 (-CH dodecyl), 14.2 (-CH dodecyl) ppm.

m.p. : 18-20 °C.

5.2.32 Synthesis of 4-dodecyl-biphenyl (33)

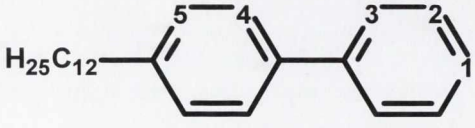

Bromobiphenyl (12 g, 55 mmol) and $NiCl_2$dppp (1 g, 1.8 mmol) were dissolved in distilled tetrahydrofuran (150 mL). To this, dodecylmagnesium bromide (60 mL, 60 mmol, 1 M solution) was added slowly. The reaction mixture was stirred at room

temperature for 48 hours. The reaction was then quenched using HCl (150 mL, 2 M HCl) and extracted using diethyl ether (3 x 50 mL). The solution was filtered through a 2 cm silica plug and the solvent removed *in vacuo*. Recrystallisation from cold hexane gave the desired product.

Yield: 9.6 g, 57 %.

^{1}H NMR (400 MHz, $CDCl_3$) δ 7.66 (d, 2H, J = 8.0 Hz, **3**), 7.59 (d, 2 H, J = 8.0 Hz, **4**), 7.51 (t, 2H, J = 7.6 Hz, **2**), 7.40 (t, 1H, J = 7.5 Hz, **1**), 7.32 (d, 2H, J = 8.7 Hz, **5**) 2.59 (t, 2H, J = 7.5 Hz, -CH dodecyl), 1.62 – 1.31 (m, 20H, -CH dodecyl), 0.92 (t, 3H, J = 7.5 Hz) ppm.

^{13}C NMR (101 MHz, $CDCl_3$) δ 142.2 (1C, C_Q), 141.3 (1C, C_Q), 138.6 (1C, C_Q), 128.9 (2C, **2**), 128.8 (2C, **5**), 127.0 (4C, **3**, **4**), 127.0 (1C, **1**), 35.7 (-CH dodecyl), 32.0 (-CH dodecyl), 29.8 (-CH dodecyl), 29.7 (-CH dodecyl), 29.6 (-CH dodecyl), 29.5 (-CH dodecyl), 22.8 (-CH dodecyl), 14.2 (-CH dodecyl) ppm.

IR (υ_{max}/cm^{-1}): 2915 (-CH dodecyl), 2847 (-CH dodecyl), 1487, 1462, 1006, 841, 760, 748, 722, 685.

m.p. : 42-43 °C.

5.2.33 Synthesis of 4-dodecyl-4'bromobiphenyl (34)

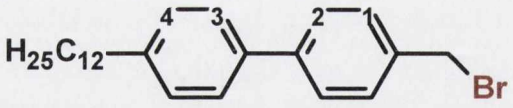

4-dodecyl-biphenyl (3.75 g, 22.3 mmol) and paraformaldehyde (2.26 g, 24 mmol) were dissolved in glacial acetic acid (150 mL). Hydrobromic acid (12 mL, 33% in acetic acid) was then added after 5 minutes. The solution was then heated at 70 °C for 3 days, quenched with water and extracted using dichloromethane. After drying over $MgSO_4$ the organic layer was filtered over celite and evaporated to dryness to yield an oily residue. After the product was subjected to column chromatography, using petroleum ether as eluent, a white crystalline product was obtained.

Yield: 873 mg, 15 %.

^{1}H NMR (400 MHz, $CDCl_3$) δ 7.62 (d, 2H, *J* = 9.0 Hz, **1**), 7.50 (d, 2H, *J* =8.0 Hz, **2/3**), 7.46 (d, 2H, **2/3**), 7.29 (d, 2H, *J* = 9.0 Hz, **4**), 3.74 (s, 2H, -C**H**$_2$), 2.69 (t, 2H, *J* = 7.5 Hz, -CH dodecyl), 1.62 - 1.3 (m, 20H, -CH dodecyl), 0.93 (t, 3H, *J* = 7.5 Hz, -CH dodecyl) ppm.

^{13}C NMR (101 MHz, $CDCl_3$) δ 128.4 (2C, **1**), 128.3 (2C, **2/3**), 127.0 (2C, C_Q), 126.8 (2C, **2/3**), 126.6 (2C, **4**), 35.3 (-CH dodecyl), 32.3 (-CH dodecyl), 31.6 (-CH dodecyl), 31.2 (-CH dodecyl), 29.4 (-CH dodecyl), 29.4 (-CH dodecyl), 29.4 (-CH dodecyl), 22.4 (-CH dodecyl), 17.6 (-CH dodecyl), 14.24 (-CH dodecyl) ppm.

IR (υ_{max}/cm^{-1}): 2917 (-CH dodecyl), 2848 (-CH dodecyl), 1487, 1463, 1006, 823, 735, 761, 749, 680 (C-Br).

m.p. : 33-35 °C.

5.2.34 Synthesis of 4-dodecanoyl-4'-bromobiphenyl (35)

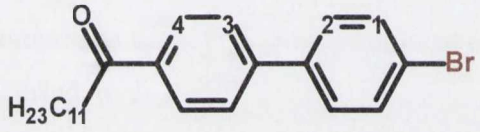

4-bromophenyl (20 g, 21 mL, 85 mmol) was dissolved in CS_2 and bubbled with argon for 20 min. To this, dodecanoyl chloride (25 g, 26.75 mL, 85 mmol) and $AlCl_3$ (14.5 g, 108 mmol) were added. The reaction mixture was heated to 45 °C overnight, at which point it was poured on to ice water and extracted with chloroform. After the removal of solvent the product was recrystallised from ethanol, yielding white crystals.

Yield: 35.3 g, 85%.

^{1}H NMR (400 MHz, $CDCl_3$) δ 8.05 (d, 2 H, *J* = 8.0 Hz, **1**), 8.66 (d, 2 H, *J* = 8.0 Hz, **2**), 7.62 (d, 2 H, *J* = 8.0 Hz, **4**), 7.52 (d, 2 H, *J* = 8.0 Hz, **3**), 3.00 (t, 2 H, *J* = 7.5 Hz, -CH dodecyl), 1.78 (m, 2 H, -CH_2 dodecyl), 1.47 - 1.22 (m, 16 H, -CH dodecyl), 0.91 (t, 3 H, *J* = 6.85 Hz) ppm.

^{13}C NMR (101 MHz, $CDCl_3$) δ 199.7 (1C, -**C**O), 143.8 (1C, C_Q), 138.4 (1C, C_Q), 135.6 (1C, C_Q), 131.6 (2C, **1**), 128.4 (2C, **2/3**), 128.3 (2C, **2/3**), 126.6 (2C, **4**), 122.1 (1C, **C**-Br), 38.3 (-CH dodecyl), 31.4 (-CH dodecyl), 29.2 (-CH dodecyl), 29.1 (-CH dodecyl), 29.0 (-CH dodecyl), 28.9 (-CH dodecyl), 28.8 (-CH dodecyl), 24.3 (-CH dodecyl), 22.3 (-CH dodceyl), 13.7 (-CH dodecyl) ppm.

m.p. : 62-65 °C.

5.2.35 Synthesis of 4-bromo-4'-dodecyl-1,1'-biphenyl (36)

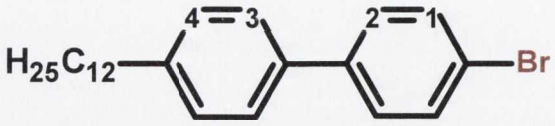

A mixture of (**35**) (17.80 g, 64 mmol), hydrazine hydrate (18 mL, 37 mmol) and potassium hydroxide (15.5 g, 172 mmol) was heated in ethylene glycol (20 mL) at reflux for 6 h. The mixture was then distilled at atmospheric pressure until the temperature of the reaction mixture exceeded 210 °C. After cooling to room temperature, the resulting mixture was poured into water and acidified using hydrochloric acid (25 mL). Extraction was carried out using DCM and after drying over $MgSO_4$ the solvent was removed *in vacuo*. Purification was achieved using column chromatography with hexane as eluent. The product was isolated as a colourless oil.

Yield: 15.1 g, 58 %.

^{1}H NMR (400 MHz, $CDCl_3$) δ 7.59 (d, 2H, J = 8.0 Hz, **1**), 7.53 (d, 2H, J = 8.0 Hz, **2**), 7.49 (d, 2H, J = 8.0 Hz, **3**), 7.31 (d, 1H, J = 8.0 Hz, **4**), 2.69 (t, 2H, J = 7.5 Hz, -CH dodecyl), 1.7- 1.32 (m, 20H, -CH dodecyl), 0.96 (t, 3H, J = 7.5 Hz, -CH dodecyl) ppm.

^{13}C NMR (101 MHz, $CDCl_3$) δ 142.2 (1C, C_Q), 139.6 (1C, C_Q), 136.8 (1C, C_Q), 131.4 (2C, **1**) 128.6 (2C, **4**), 128.1 (2C, **2/3**), 128.0 (2C, **2/3**), 120.7 (1C, **C**-Br), 35.2 (-CH dodecyl), 31.5 (-CH dodecyl), 29.3 (-CH dodecyl), 29.3 (-CH dodecyl), 29.2 (-CH dodecyl), 29.1 (-CH dodecyl), 28.9 (-CH dodecyl), 22.3 (-CH dodceyl), 13.8 (-CH dodecyl) ppm.

IR (υ_{max}/cm^{-1}): 2916 (-CH dodecyl), 2848 (-CH dodecyl), 1481, 1462, 1078, 1389, 1078, 1000, 806, 785, 623 (C-Br).

m.p. : 41-43 °C.

5.2.36 Synthesis of 1,2-bis(4'-dodecyl-[1,1'-biphenyl]-4-yl)ethane-1,2-dione (37)

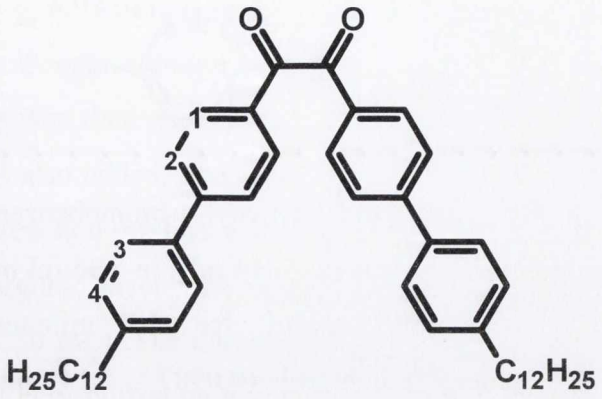

n-BuLi (1 mL, 2.5 M, 15.5 mmol) was added to (**36**) (5 g, 15.36 mmol) in tetrahydrofuran (60 mL) and stirred -78 °C for 90 minutes. At that point the solution was added *via* cannula to a suspension of 1,4-dimethylpiperazine-2,3-dione (0.99 g, 6.91 mmol) in tetrahydrofuran (60 mL) also at -78 °C. The reaction was allowed to warm to room temperature and was stirred for 18 hours. Hydrochloric acid (2 M) was used to quench the reaction and using dichloromethane the organic phase was separated, washed with HCl (2 M), deionised water and dried over $MgSO_4$. After removal of solvent *in vacuo* the resulting solid was purified by column chromatography on silica using a dichloromethane: petroleum ether (3:1) yielded a yellow viscous product.

Yield: 3.17 g, 53 %.

^{1}H NMR (400 MHz, $CDCl_3$) δ 8.09 (d, 4H, J = 8.5 Hz, **1**), 7.76 (d, 4H, J = 8.5 Hz, **2**), 7.58 (d, 4H, **3**), 7.32 (d, J = 7.7 Hz, 4H, **4**) 2.69 (t, 4H, J = 7.7 Hz, -CH dodecyl), 1.71-1.29 (m, 40 H, -CH dodecyl), 0.92 (t, 6H, J = 7.0 Hz, -CH dodecyl) ppm.

^{13}C NMR (101 MHz, $CDCl_3$) δ 194.1 (2C, -**C**O), 147.1 (2C, C_Q), 143.0 (2C, C_Q), 137.3 (2C, C_Q), 131.4 (2C, **1**), 131.0 (2C, **4**), 130.1 (4C, C_Q), 128.7 (4C, **2**) 126.9 (4 C, **3**), 126.7 (4C, C_Q), 35.2 (-CH dodecyl), 31.5 (-CH dodecyl), 31.0 (-CH dodecyl), 29.2 (-CH dodecyl), 29.2 (-CH dodecyl), 29.1 (-CH dodecyl), 29.0 (-CH dodecyl), 28.9 (-CH dodecyl), 28.8 (-CH dodecyl), 22.3 (-CH dodecyl), 13.8 (-CH dodecyl) ppm.

IR (υ_{max}/cm^{-1}): 2916 (-CH dodecyl), 2849 (-CH dodecyl), 1667 (-C=O), 1601, 1468, 1182, 881, 813, 718.

m.p. : 112-114 °C

5.2.37 Synthesis of 6-(bromophenylethynyl) pyrimidine (38)

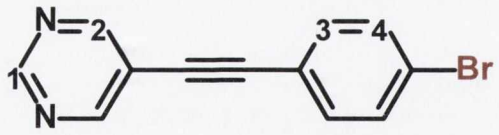

Bromopyrimidine (1.3 g, 8.17 mmol) and 1-ethynyl-4-bromobenzene (1.3 g, 7.18 mmol) were added to a mixture of DMF: $NHEt_2$ (2: 5, 14 mL) in a 35 ml microwave vessel. The solution was then bubbled with argon for 10 minutes at which point bis(triphenylphosphine)palladium(II) dichloride (0.0987 g, 0.14 mmol) and copper iodide (0.064 g, 0.34 mmol) were added and the vessel sealed. The reaction mixture was heated in a microwave at 120 °C for 15 minutes. After cooling, the reaction mixture was quenched onto HCl (100 mL, 1 M), extracted with diethyl ether and washed with water (3x100 mL). The organic phase was dried over $MgSO_4$ and concentrated *in vacuo*. The product was precipitated using cold methanol. Recrystallisation from hexane yielded the product as a pale yellow solid.

Yield: 1.02 g, 55%.

^{1}H NMR (400 MHz, $CDCl_3$) δ 9.17 (s, 1H, **1**), 8.89 (s, 2H, **2**), 7.56 (d, 2H, J = 7.5 Hz, **4**), 7.45 (d, 2H, J = 8 Hz, **3**) ppm.

^{13}C NMR (101 MHz, $CDCl_3$) δ 158.2 (2C, **1**), 156.2 (1C, **2**) 131.6 (2C, **4**), 132.8 (2C, **3**), 131.4 (1C, C_Q), 123.5 (1C, **C**-Br), 119.2 (1C, C_Q), 120.2 (1C, C_Q), 94.8 (1C, **C**≡C), 82.9 (1 C, **C**≡**C**) ppm.

HRMS (m/z) calculated for $[C_{12}H_7BrN_2]^+$: 257.9793, found 257.9792.

IR (υ_{max}/cm^{-1}): 1541, 1482, 1412, 1067, 1183, 1009 (C=N), 904, 713, 631 (C-Br).

m.p. : 55-58 °C.

5.2.38 Synthesis of 1,3-bis(4-bromophenyl)propan-2-one (39)

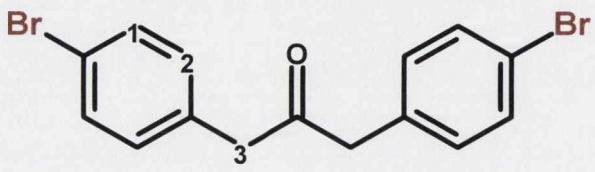

A mixture containing calcium hydroxide (4.25 g, 75.35 mmol) and tetrabutylammonium hydrogensulfate (2.35 g, 6.93 mmol) in dichloromethane and water (1 : 1, 250 mL), was degassed by bubbling nitrogen through it for 20 min. 1-bromo-4-benzyl bromide (6.18 g, 5.0 mL, 27.21 mmol) was then added. To this solution iron pentacarbonyl (2.5 g, 1.73 mL, 12.76 mmol) was also added. The reaction was stirred, under nitrogen, for 24 h. By bubbling with air the reaction mixture was then oxidised for 1 h and acidified with a 10% HCl (90 mL). The organic layer was separated and the aqueous layer extracted with dichloromethane (3 x 50 mL). The combined extracts were then dried over $MgSO_4$ and the solvent removed. Recrystallisation from methanol gave the product as a white solid.

Yield: 3.15 g, 63%.

^{1}H NMR (400 MHz, $CDCl_3$) δ 7.48 (d, 2H, J = 8.0 Hz, **1**), 7.05 (d, 2 H, J = 8.0 Hz, **2**), 3.72 (t, 2 H, J = 7.5 Hz, **3**) ppm.

^{13}C NMR (101 MHz, $CDCl_3$) δ 204.6 (1C, -**C**O), 132.6 (2C, C_Q), 131.9 (4C, **1**), 131.2 (4C, **2**), 121.4 (2C, -**C**Br), 48.5 (2C, -**C**H_2) ppm.

HRMS (m/z) calculated for $[C_{15}H_{11}OBr_2]^+$: 364.9177, found *m/z* 364.9194.

IR (υ_{max}/cm^{-1}): 1710 (-C=O), 1415, 1485, 1339, 1055, 1071, 828, 791, 729, 667 (C-Br).

m.p. : 63-66 °C.

5.2.39 Synthesis of 4,4'-dibromobenzil (40)

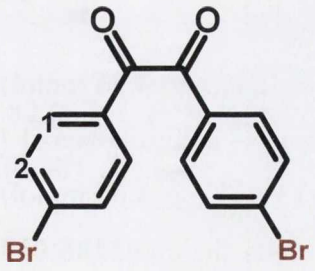

Thiamin hydrochloride (5 g, 20 mmol) was dissolved distilled water (5 mL) and ethanol (100 mL. The solution was cooled to below -5 °C, at which point a 10% NaOH solution was used to adjust the pH of the reaction mixture to pH 9. At this point, 4-bromobenzaldehyde (20 g, 108 mmol) was added and the solution heated to 65 °C for 15 h. After cooling, the precipitate was filtered and washed with cold water and methanol.

Recrystallisation from ethanol yielded a mixture of benzoin and benzyl. This solid was dissolved in acetic acid (6 mL) and to the solution, NH_4NO_3 (135 mg, 1.69 mmol), and $Cu(OAc)_2.H_2O$ (31.4 mg, 0.17 mmol) were added. The mixture was heated to reflux for 2.5 h and after cooling the precipitate was filtered and washed with water and ethanol to yield pale yellow crystals.

Yield: 400 mg, 82%.

^{1}H NMR (400 MHz, $CDCl_3$) δ 7.86 (d, 2H, J = 9.0 Hz, **1**), 7.70 (d, 2H, J = 9.0 Hz, **2**) ppm.

^{13}C NMR (101 MHz, $CDCl_3$) δ 192.7 (2C, **C**-O), 132.5 (4C, **1**), 131.5 (2C, C_Q), 131.3 (4C, **2**), 130.8 (2C, **C**-Br) ppm.

HRMS (m/z) calculated for $[C_{14}H_8Br_2O_2+H]^+$: 926.7856, found 926.7893.

m.p. : 220-222 °C

5.2.40 Synthesis of 2,3,4,5-tetrakis-(4'-bromo)-cyclopenta-2,4-dienone (41)

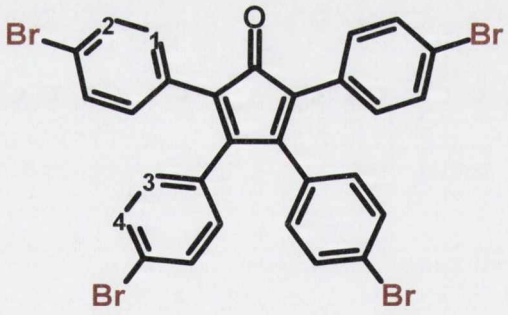

A solution of potassium hydroxide (245 mg, 4.36 mmol) in ethanol (5 mL) was added in two parts to a refluxing solution of 4,4'-dibromobenzil **(40)** (1.6 g, 4.35 mmol) and 1,3-bis(4-bromophenyl)propan-2-one **(39)** (1.6 g, 4.35 mmol) in ethanol (20 mL) and refluxed for 15 min. The reaction mixture was the cooled to 0 °C, at which point the precipitate was collected and washed with cold ethanol to yield the product as a dark red solid.

Yield: 1.97 g, 65 %.

^{1}H NMR (400 MHz, $CDCl_3$) δ 7.43 (d, 2H, J = 9.0 Hz, **2**), 7.39 (d, 2H, J = 8.0 Hz, **2**), 7.09 (d, 2H, J = 7.5 Hz, **1**), 6.81 (d, 2H, J = 8.0 Hz, **4**) ppm.

^{13}C NMR (101 MHz, $CDCl_3$) δ 199.2 (1C, -**C**O), 153.2 (2C, C_Q), 131.8 (4C, **2**), 131.6 (8C, **2**, **1**), 131.1 (2C, C_Q), 130.9 (4C, **4**), 128.9 (2C, C_Q), 125.0 (2C, C_Q), 123.6 (2C, -**C**Br), 122.5 (2C, -**C**Br) ppm.

IR (υ_{max}/cm^{-1}): 1710 (-C=O), 1481, 1072, 1008, 850, 838, 805, 784, 662 (C-Br).

m.p. >300 °C.

5.2.41 Synthesis of 1,2 di(2,5-pyrimidyl)-3,4,5,5-tetra-(4-bromophenyl)benzene (42)

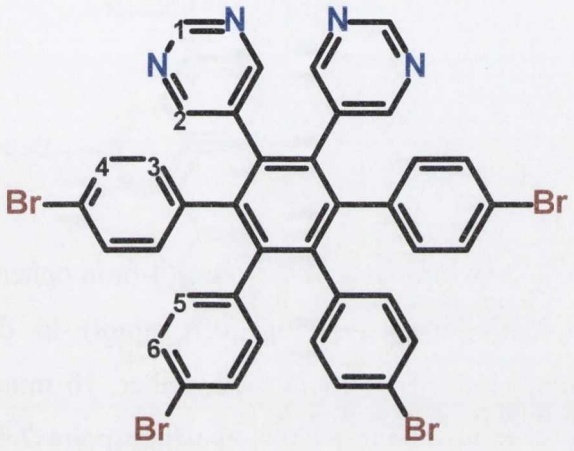

Dipyrimidyl acetylene (160 mg, 0.87 mmol) and 2,3,4,5-tetrakis-(4'-bromo)-cyclopenta-2,4-dienone (**41**) (400 mg, 0.57 mmol) were added to benzophenone (500 mg) in a 25 cm^3 round bottom flask and heated to 250 °C for 4 hours. After cooling, the reaction mixture was dissolved in dichloromethane (2 mL) and purified by column chromatography using dichloromethane: methanol (4%) as eluent. Recrystallisation from hexane yielded the product as a pale brown solid.

Yield: 273 mg, 56%.

^{1}H NMR (400 MHz, $CDCl_3$) δ 8.82 (s, 2H, **1**), 8.18 (s, 4H, **2**), 7.12 (d, 4H, J = 8.7 Hz, **4**), 7.10 (d, 4 H, J = 8.7 Hz, **6**), 6.65 (d, 4H, J = 8.7 Hz, **3**), 6.50 (d, 4H, J = 8.7 Hz, **5**) ppm.

^{13}C NMR (101 MHz, $CDCl_3$) δ 157.7 (4C, **2**), 156.6 (2C, **1**), 141.5 (2C, C_Q), 140.9 (2C, C_Q), 137.4 (2C, C_Q), 136.9 (2C, C_Q), 134.0 (2C, C_Q), 132.3 (4C, **5**), 132.2 (4C, **3**) 131.2 (4C, **4**), 130.8 (4C, **6**), 121.5 (2 C, **C**-Br), 120.9 (2 C, **C**-Br) ppm.

HRMS (m/z) calculated for $[C_{38}H_{22}N_4Br_4+H]^+$: 850.8656, found 850.8679.

IR (υ_{max}/cm^{-1}): 2916 (C-H), 2849, 1666, 1601, 1882, 1462 (C=N), 881, 813, 619 (C-Br).

m.p. >300 °C.

5.2.42 Synthesis of 5,5'-(4,4''-didodecyl-5',6'-bis(4-dodecylphenyl)-[1,1':2',1''-terphenyl]-3',4'-diyl)dipyrimidine (43)

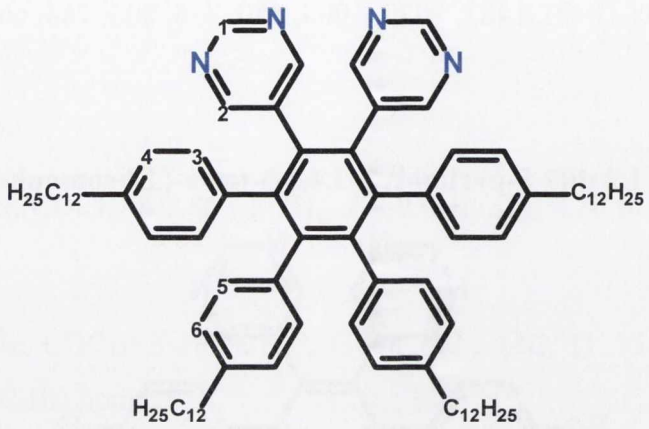

To a solution of 1,2-di(2,5-pyrimidyl)-3,4,5,5-tetra-(4-bromophenyl)benzene (**42**) (400 mg, 0.47 mmol) and $PdCl_2$(dppf) (70 mg, 0.1 mmol) in diethylether (60 mL), dodecylmagnesiumbromide (10 mL, 1 M in diethylether, 10 mmol) was slowly added. The reaction mixture was refluxed for 3 days, at which point 2 M HCl (150 mL) was added. The organic layer was then collected, dried over $MgSO_4$ and the solvent evaporated *in vacuo*. The crude product was then purified by column chromatography using dichloromethane: methanol (5%) as eluent. Removing the solvent under reduced pressure yielded the product as a white solid.

Yield: 256 mg, 45%.

^{1}H NMR (400 MHz, $CDCl_3$) δ 8.79 (s, 2H, **1**), 8.24 (s, 4H, **2**), 6.95 (d, J = 7.3 Hz, 4H, **4**), 6.87 – 6.82 (m, 4H, **3**), 6.71 (d, J = 8.8 Hz, 4H, **5**), 6.69 (d, J = 8.8 Hz, 4H, **6**), 2.37 (t, J = 7.5 Hz, 8H, -CH dodecyl), 1.47 – 1.05 (m, 80H, -CH dodecyl), 0.91 (t, J = 6.8 Hz, 12H, -CH dodecyl) ppm.

^{13}C NMR (101 MHz, $CDCl_3$) δ 158.0 (4C, **2**), 156.0 (2C, **1**), 143.0 (2C, C_Q), 141.0 (2C, C_Q), 140.2 (2C, C_Q), 139.0 (2C, C_Q), 136.5 (2C, C_Q), 134.0 (2C, C_Q), 131.1 (4C, **3**), 130.8 (4C, **5**), 127.5 (4C, **4**), 126.9 (4C, **6**), 126.4 (2C, C_Q), 120.7 (2C, C_Q), 35.3 (8C, -CH dodecyl), 31.9 (-CH dodecyl), 31.1 (-CH dodecyl), 29.7 (-CH dodecyl), 29.6 (-CH dodecyl), 29.5 (-CH dodecyl), 29.4 (-CH dodecyl), 28.8 (-CH dodecyl), 22.7 (-CH dodecyl), 14.1 (12C, -CH dodecyl) ppm.

IR (υ_{max}/cm^{-1}): 3100, 2980 (C-H alkyl), 2154, 1620 (C=C), 1545 (C=N), 944.

m.p. : 74-78 °C

5.2.43 Synthesis of tetra-peri-dodecyl-benzo-di-peri-(pyrimidine)-coronene (44)

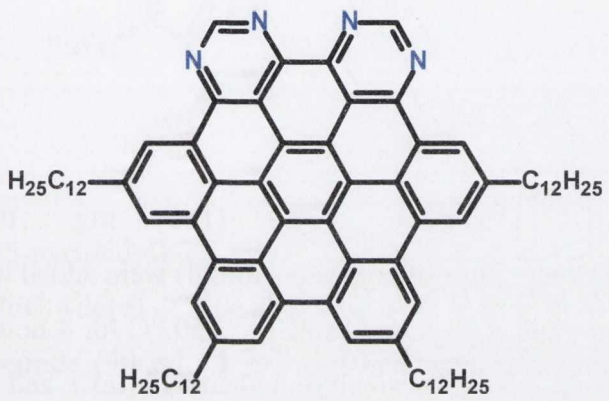

To a solution of 5,5'-(4,4''-didodecyl-5',6'-bis(4-dodecylphenyl)-[1,1':2',1''-terphenyl]-3',4'-diyl)dipyrimidine (**43**) in dichloromethane (40 mL), iron(III) chloride in nitromethane (5 mL) was added *via* cannula. The mixture was stirred overnight, with a stream of nitrogen bubbled through the solution, at which point it was quenched with methanol. After stirring in water (50 mL) for 4 hours, followed by extraction into dichloromethane and drying over $MgSO_4$, the solvent was removed *in vacuo*. The crude brown oil was subjected to column chromatography with toluene: methanol (2%) which yielded a light-brown waxy solid.

Yield: 20 mg, 21 %.

^{1}H NMR (400 MHz, $CDCl_3$) δ 9.22 (br. s, 10H,), 2.34 (t, J = 7.5 Hz, 8H, -CH dodecyl), 1.65 – 1.33 (m, 80H, -CH dodecyl), 0.91 (t, J = 6.8 Hz, 12H, -CH dodecyl) ppm.

APCI-MS (m/z) calculated for $[C_{86}H_{110}N_4+H]^+$: 1199.8809, found 1199.8790.

5.2.44 Synthesis of 1-(2,5-pyrimidyl)-2,3,4,5,6-penta(4-bromophenyl)benzene (45)

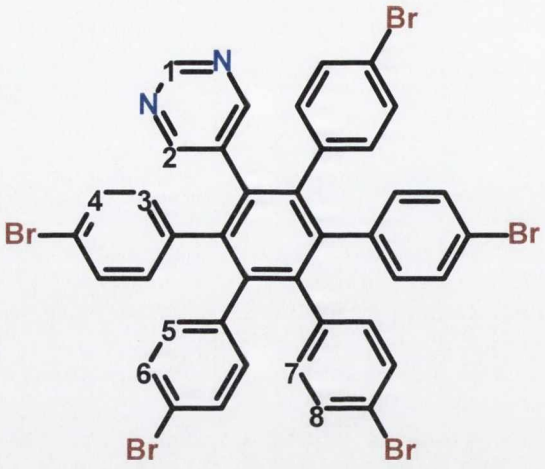

6-(bromophenylethynyl) pyrimidine (**38**) (160 mg, 0.61 mmol) and tetrabromocylopentadienone (**30**) (400 mg, 0.57 mmol) were added to benzophenone (500 mg) in a 25 cm^3 round bottom flask and heated to 250 °C for 4 hours. After cooling, the reaction mixture was dissolved in dichloromethane (2 mL) and purified by column chromatography (4% dichloromethane:methanol). Recrystallisation from hexane yielded the product as a pale brown solid.

Yield: 375 mg, 70%.

^{1}H NMR (400 MHz, $CDCl_3$) δ 8.80 (s, 1H, **1**), 8.16 (s, 2H, **2**), 7.12 (m, 10H, **4**, **6**, **8**), 6.66 (m, 10 H, **3**, **5**, **7**) ppm.

^{13}C NMR (101 MHz, $CDCl_3$) δ 157.6 (2C, **2**), 156.0 (1C, **1**) 140.2 (2C, C_Q), 140.0 (2C, C_Q), 137.9 (1C, C_Q), 137.8 (2C, C_Q), 137.4 (2C, C_Q), 133.5 (1C, C_Q), 132.4 (4C, **4**), 132.34 (6C, **6**, **8**), 131.0 (6C, **3**, **5**), 130.6 (2C, C_Q), 130.6 (2C, **7**), 122.1 (2C, **C**-Br), 120.7 (2 C, **C**-Br), 120.7 (1 C, **C**-Br) ppm.

HRMS (m/z) calculated for $[C_{40}H_{24}N_2Br_5+H]^+$: 926.7856, found 926.7893.

IR (υ_{max}/cm^{-1}): 1490 (C=C), 1386, 1071, 1009, 828, 769, 630 (C-Br).

m.p. >300 °C

5.2.45 Synthesis of 5-(4,4''-didodecyl-4',5',6'-tris(4-dodecylphenyl)-[1,1':2',1''-terphenyl]-3'-yl)pyrimidine (46)

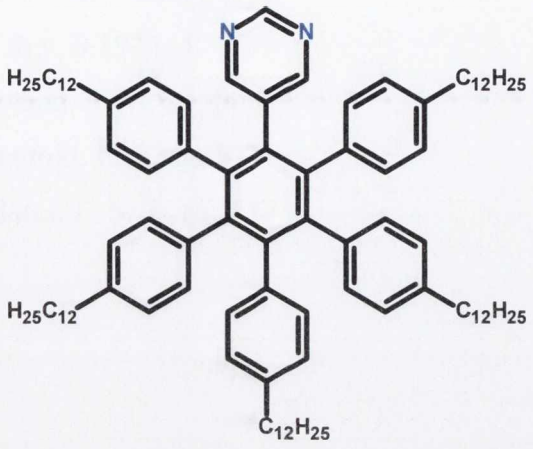

To a solution of 1-(2,5-pyrimidyl)-2,3,4,5,6-penta(4-bromophenyl)benzene (**45**) (210 mg, 0.22 mmol) and $PdCl_2$(dppf) (110 mg, 0.16 mmol) in diethylether (40 mL), dodecylmagnesiumbromide (30 mL, 1 M in diethylether, 30 mmol) was slowly added. The reaction mixture was refluxed for 3 days, at which point 2 M HCl (150 mL) was added. The organic layer was then collected, dried over $MgSO_4$ and the solvent evaporated *in vacuo*. The crude product was then purified by column chromatography using dichloromethane: methanol (5%) as eluent. Removing the solvent under reduced pressure yielded the product as a brown solid.

Yield: 15 mg, 5%.

^{1}H NMR (400 MHz, $CDCl_3$) δ 8.38 (s, 1H), 8.12 (s, 2H), 7.92 (s, 4H), 7.38 (m, 16H), 2.37 – 2.14 (m, 10H), 1.70 – 1.04 (m, 100H), 0.91 (s, 15H) ppm.

^{13}C NMR (101 MHz, $CDCl_3$) δ 145.08 (2C, -CH pyrimidyl), 142.0 (1C, -CH pyrimidyl), 135.1 (4C, -CH Aryl), 134.8 (4C, -CH Aryl), 134.6 (2C, C_Q), 131.3 (2C, C_Q) 131.25 (2C, C_Q), 130.2 (2C, C_Q) 128.72 (4C, -CH Aryl), 128.6 (2C, -CH Aryl), 128.5 (2C, -CH Aryl), 128.49 (4C, -CH Aryl), 128.3 (4C, C_Q), 128.11 (4C, C_Q), 127.8 (1C, C_Q), 44.02 (-CH dodecyl), 32.83 (-CH dodecyl), 32.38 (-CH dodecyl), 30.21 (-CH dodecyl), 29.66 (-CH dodecyl), 29.44 (-CH dodecyl), 29.36 (-CH dodecyl), 29.23 (-CH dodecyl), 29.01 – 28.85 (-CH dodecyl), 25.75 (-CH dodecyl), 24.37 (-CH dodecyl), 22.70 (-CH dodecyl), 14.13 (-CH dodecyl) ppm.

m.p. : 42-44 °C

5.2.46 Synthesis of 1,3,5-tri(3-bromophenyl)-2-4-6(2,5-pyrimidyl)benzene (47)

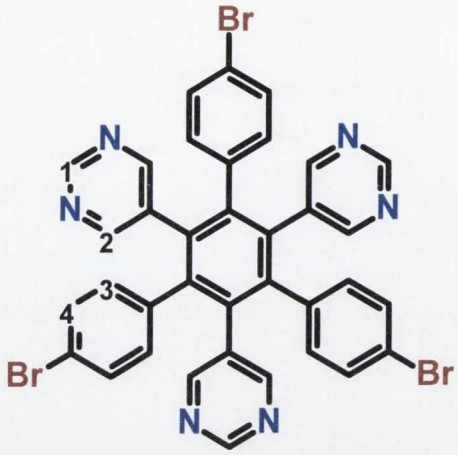

1-bromo-4-ethynylpyrimidine (**38**) (129 mg, 0.5 mmol) was dissolved in dioxane (10 mL). To this dicobalt octacarbonyl (25.6 mg, 0.075 mmol) was added and the solution refluxed at 115 °C for three days. The solution was then cooled to room temperature and the solvent removed under reduced pressure. The product was then purified by column chromatography using dichloromethane: methanol (4%).

Yield: 70 mg, 54%.

^{1}H NMR (400 MHz, $CDCl_3$) δ 8.82 (m, 3H, **1**), 8.44 (m, 6H, **2**), 7.29 (m, 6H, **4**), 6.99 (m, 6H, **3**) ppm.

^{13}C NMR (101 MHz, $CDCl_3$) 157.4 (6C, **2**), 157.0 (3C, **1**), 142.0 (3C, C_Q), 136.3 (3C, C_Q), 135.4 (3C, C_Q), 132.0 (6C, **3**), 131.6 (3C, C_Q), 131.0 (6C, **4**), 122.2 (3C, **C**-Br) ppm.

IR (υ_{max}/cm^{-1}): 2902, 2823, 1567 (C=N), 1443 (C=C), 757, 624 (C-Br).

HRMS (m/z) calculated for $[C_{36}H_{21}N_6Br_3+H]^+$: 774.9456, found 774.9448.

m.p. >300 °C

5.3 References

(1) Draper, S. M.; Gregg, D. J.; Madathil, R. *J. Am. Chem. Soc.* **2002**, *124*, 3486–3487.

(2) Nagarajan, S.; Barthes, C.; Gourdon, A. *Tetrahedron* **2009**, *65*, 3767–3772.

(3) Wijesinghe, L. P.; Lankage, B. S.; Ó Máille, G. M.; Perera, S. D.; Nolan, D.; Wang, L.; Draper, S. M. *Chem. Commun. (Camb).* **2014**, *50*, 10637–10640.

(4) Roberts, D. J.; Nolan, D.; Ó Máille, G. M.; Watson, G. W.; Singh, A.; Ledoux-Rak, I.; Draper, S. M. *Dalt. Trans.* **2012**, *41*, 8850.

(5) Shirley, D. *Phys. Rev. B* **1972**, *5*, 4709–4714.

(6) Proctor, A.; Sherwood, P. M. A. *Anal. Chem.* **1982**, *54*, 13–19.

(7) Heenan, R. K.; Penfold, J.; King, S. M. *J. Appl. Crystallogr.* **1997**, *30*, 1140–1147.

(8) Wignall, G. D.; Bates, F. S. *J. Appl. Crystallogr.* **1987**, *20*, 28–40.

6 Annex

6.1 Crystal Data

*Table 6.1 Crystal data and structure refinement for **4**.*

Identification code	tcd24_sq	
Empirical formula	$C_{40}H_{24}N_2$	
Formula weight	532.61	
Temperature	100(2) K	
Wavelength	0.71073 Å	
Crystal system	Triclinic	
Space group	$P\bar{1}$	
Unit cell dimensions	a = 9.9837(11) Å	α= 114.3132(19)°.
	b = 12.3004(13) Å	β= 95.279(2)°.
	c = 14.6640(15) Å	γ = 90.120(2)°.
Volume	1632.5(3) $Å^3$	
Z	2	
Density (calculated)	1.083 Mg/m^3	
Absorption coefficient	0.063 mm^{-1}	
F(000)	556	
Crystal size	0.130 x 0.130 x 0.060 mm^3	
Theta range for data collection	1.818 to 27.572°.	
Index ranges	$-12 \leq h \leq 13$, $-15 \leq k \leq 16$, $-19 \leq l \leq 19$	
Reflections collected	28083	
Independent reflections	7496 [R(int) = 0.0430]	
Completeness to theta = 25.242°	99.8 %	
Absorption correction	Semi-empirical from equivalents	
Max. and min. transmission	0.7456 and 0.7064	
Refinement method	Full-matrix least-squares on F^2	
Data / restraints / parameters	7496 / 0 / 380	
Goodness-of-fit on F^2	0.924	
Final R indices [I>2sigma(I)]	R1 = 0.0528, wR2 = 0.1437	
R indices (all data)	R1 = 0.0876, wR2 = 0.1557	
Largest diff. peak and hole	0.884 and -0.217 $e.Å^{-3}$	

Table 6.2 Crystal data and structure refinement for ***6****.*

Identification code	tcd172_sq	
Empirical formula	$C_{60}H_{64}N_2$	
Formula weight	813.13	
Temperature	100(2) K	
Wavelength	1.54178 Å	
Crystal system	Monoclinic	
Space group	C2/c	
Unit cell dimensions	a = 31.9866(12) Å	α= 90°.
	b = 9.5056(4) Å	β= 100.381(2)°.
	c = 34.2688(13) Å	γ = 90°.
Volume	10248.9(7) $Å^3$	
Z	8	
Density (calculated)	1.054 Mg/m^3	
Absorption coefficient	0.451 mm^{-1}	
F(000)	3504	
Crystal size	0.250 x 0.070 x 0.070 mm^3	
Theta range for data collection	2.622 to 62.358°.	
Index ranges	-36≤h≤34, -10≤k≤10, -39≤l≤38	
Reflections collected	55520	
Independent reflections	8025 [R(int) = 0.0540]	
Completeness to theta = 62.358°	98.6 %	
Absorption correction	Semi-empirical from equivalents	
Max. and min. transmission	0.7522 and 0.6537	
Refinement method	Full-matrix least-squares on F^2	
Data / restraints / parameters	8025 / 1458 / 1148	
Goodness-of-fit on F^2	1.041	
Final R indices [I>2σ(I)]	R1 = 0.0517, wR2 = 0.1444	
R indices (all data)	R1 = 0.0722, wR2 = 0.1607	
Largest diff. peak and hole	0.347 and -0.207 $e.Å^{-3}$	

Table 6.3 Crystal data and structure refinement for ***8****.*

Identification code	tcd131t_sq	
Empirical formula	$C_{46}H_{34}Br_2N_4$	
Formula weight	802.59	
Temperature	100(2) K	
Wavelength	0.71073 Å	
Crystal system	Triclinic	
Space group	P-1	
Unit cell dimensions	a = 7.1844(7) Å	α= 114.067(4)°.
	b = 16.9591(17) Å	β= 97.740(5)°.
	c = 18.2000(19) Å	γ = 101.895(4)°.
Volume	1921.0(3) $Å^3$	
Z	2	
Density (calculated)	1.388 Mg/m^3	
Absorption coefficient	2.148 mm^{-1}	
F(000)	816	
Crystal size	0.260 x 0.040 x 0.030 mm^3	
Theta range for data collection	1.373 to 23.083°.	
Index ranges	$-7\leq h\leq 7$, $-18\leq k\leq 18$, $-19\leq l\leq 19$	
Reflections collected	5338	
Independent reflections	5338 [R(int) = 0.1836]	
Completeness to theta = 23.083°	99.0 %	
Absorption correction	Semi-empirical from equivalents	
Max. and min. transmission	0.7449 and 0.5663	
Refinement method	Full-matrix least-squares on F^2	
Data / restraints / parameters	5338 / 30 / 477	
Goodness-of-fit on F^2	1.057	
Final R indices [$I>2\sigma(I)$]	R1 = 0.0986, wR2 = 0.2105	
R indices (all data)	R1 = 0.1609, wR2 = 0.2391	
Extinction coefficient	0.0107(15)	
Largest diff. peak and hole	1.456 and -1.238 $e.Å^{-3}$	

Table 6.4 Crystal data and structure refinement for ***12****.*

Identification code	tcd151	
Empirical formula	$C_{45}H_{33}BrCl_2N_4$	
Formula weight	780.56	
Temperature	100(2) K	
Wavelength	0.71073 Å	
Crystal system	Monoclinic	
Space group	$P2_1/n$	
Unit cell dimensions	a = 18.8112(11) Å	α= 90°.
	b = 7.4994(4) Å	β= 91.628(3)°.
	c = 25.0964(14) Å	γ = 90°.
Volume	3539.0(3) $Å^3$	
Z	4	
Density (calculated)	1.465 Mg/m^3	
Absorption coefficient	1.353 mm^{-1}	
F(000)	1600	
Crystal size	0.220 x 0.100 x 0.020 mm^3	
Theta range for data collection	1.335 to 25.415°.	
Index ranges	$-22 \leq h \leq 22$, $-9 \leq k \leq 9$, $-29 \leq l \leq 30$	
Reflections collected	50843	
Independent reflections	6482 [R(int) = 0.1562]	
Completeness to theta = 25.242°	99.9 %	
Absorption correction	Numerical	
Max. and min. transmission	1.0000 and 0.8462	
Refinement method	Full-matrix least-squares on F^2	
Data / restraints / parameters	6482 / 16 / 497	
Goodness-of-fit on F^2	1.051	
Final R indices [I>2σ(I)]	R1 = 0.0962, wR2 = 0.2164	
R indices (all data)	R1 = 0.1694, wR2 = 0.2487	
Extinction coefficient	0.0060(9)	
Largest diff. peak and hole	0.999 and -1.583 $e.Å^{-3}$	

Table 6.5 Crystal data and structure refinement for ***14****.*

Identification code	tcd55	
Empirical formula	C30 H24 N2	
Formula weight	412.51	
Temperature	100(2) K	
Wavelength	1.54178 Å	
Crystal system	Orthorhombic	
Space group	$P 2_1 2_1 2_1$	
Unit cell dimensions	a = 8.907(2) Å	α= 90°.
	b = 11.134(3) Å	β= 90°.
	c = 22.778(6) Å	γ = 90°.
Volume	2258.9(10) $Å^3$	
Z	4	
Density (calculated)	1.213 Mg/m^3	
Absorption coefficient	0.542 mm^{-1}	
F(000)	872	
Crystal size	0.200 x 0.150 x 0.150 mm^3	
Theta range for data collection	3.881 to 69.189°.	
Index ranges	$-10 \leq h \leq 10$, $-13 \leq k \leq 13$, $-26 \leq l \leq 27$	
Reflections collected	23403	
Independent reflections	4205 [R(int) = 0.0294]	
Completeness to theta = 67.679°	99.9 %	
Absorption correction	Semi-empirical from equivalents	
Max. and min. transmission	0.7532 and 0.7126	
Refinement method	Full-matrix least-squares on F^2	
Data / restraints / parameters	4205 / 0 / 291	
Goodness-of-fit on F^2	1.011	
Final R indices [I>2sigma(I)]	R1 = 0.0279, wR2 = 0.0748	
R indices (all data)	R1 = 0.0283, wR2 = 0.0753	
Absolute structure parameter	0.16(11)	
Largest diff. peak and hole	0.111 and -0.156 $e.Å^{-3}$	

*Table 6.6 Crystal data and structure refinement for **16**.*

Identification code	tcd200	
Empirical formula	$C_{43}H_{36}N_4O$	
Formula weight	624.76	
Temperature	100(2) K	
Wavelength	1.54178 Å	
Crystal system	Triclinic	
Space group	Pī	
Unit cell dimensions	a = 9.1242(4) Å	α= 112.3203(19)°.
	b = 12.5691(6) Å	β= 93.941(2)°.
	c = 16.3622(7) Å	γ = 102.9904(19)°.
Volume	1666.54(13) $Å^3$	
Z	2	
Density (calculated)	1.245 Mg/m^3	
Absorption coefficient	0.586 mm^{-1}	
F(000)	660	
Crystal size	0.180 x 0.150 x 0.120 mm^3	
Theta range for data collection	2.963 to 69.025°.	
Index ranges	$-11\leq h\leq 10$, $-15\leq k\leq 15$, $-19\leq l\leq 19$	
Reflections collected	30820	
Independent reflections	6092 [R(int) = 0.0617]	
Completeness to theta = 67.679°	99.4 %	
Absorption correction	Semi-empirical from equivalents	
Max. and min. transmission	0.7531 and 0.6649	
Refinement method	Full-matrix least-squares on F^2	
Data / restraints / parameters	6092 / 3 / 459	
Goodness-of-fit on F^2	1.052	
Final R indices [I>2σ(I)]	R1 = 0.0572, wR2 = 0.1595	
R indices (all data)	R1 = 0.0695, wR2 = 0.1708	
Largest diff. peak and hole	0.440 and -0.542 $e.Å^{-3}$	

*Table 6.7 Crystal data and structure refinement for **20**.*

Identification code	tcd94	
Empirical formula	$C_{41}H_{21}DBr_3Cl_3N_2$	
Formula weight	889.69	
Temperature	100(2) K	
Wavelength	0.71073 Å	
Crystal system	Triclinic	
Space group	$P\bar{1}$	
Unit cell dimensions	a = 7.2200(2) Å	α= 78.2477(10)°.
	b = 14.3748(4) Å	β= 87.9428(10)°.
	c = 16.9537(4) Å	γ = 87.2994(10)°.
Volume	1720.14(8) $Å^3$	
Z	2	
Density (calculated)	1.718 Mg/m^3	
Absorption coefficient	3.786 mm^{-1}	
F(000)	876	
Crystal size	0.240 x 0.160 x 0.063 mm^3	
Theta range for data collection	1.448 to 30.117°.	
Index ranges	$-10\leq h\leq 10$, $-20\leq k\leq 20$, $-23\leq l\leq 23$	
Reflections collected	103702	
Independent reflections	10120 [R(int) = 0.0259]	
Completeness to theta = 25.242°	100.0 %	
Absorption correction	Semi-empirical from equivalents	
Max. and min. transmission	0.7891 and 0.4877	
Refinement method	Full-matrix least-squares on F^2	
Data / restraints / parameters	10120 / 3 / 458	
Goodness-of-fit on F^2	1.092	
Final R indices [I>2sigma(I)]	R1 = 0.0386, wR2 = 0.1093	
R indices (all data)	R1 = 0.0465, wR2 = 0.1131	
Extinction coefficient	n/a	
Largest diff. peak and hole	1.603 and -1.214 $e.Å^{-3}$	

Table 6.8 Crystal data and structure refinement for ***42***

Identification code	Br_4 Polyphen	
Empirical formula	C_{152} H_{20} Br_{16} N_{16}	
Formula weight	3456.24	
Temperature	293(2) K	
Wavelength	0.71073 Å	
Crystal system	monoclinic	
Space group	P21/c	
Unit cell dimensions	a = 20.377(4) Å	α= 90°.
	b = 18.654(4) Å	β= 90.83(3)°.
	c = 11.886(2) Å	γ = 90°.
Volume	4517.5(15) $Å^3$	
Z	1	
Density (calculated)	1.270 Mg/m^3	
Absorption coefficient	3.593 mm^{-1}	
F(000)	1648	
Crystal size	0.4 x 0.3 x 0.3 mm^3	
Theta range for data collection	1.48 to 31.22°.	
Index ranges	-28<=h<=28, -26<=k<=25, -11<=l<=16	
Reflections collected	43516	
Independent reflections	13049 [R(int) = 0.1556]	
Completeness to theta = 31.22°	88.9 %	
Refinement method	Full-matrix least-squares on F^2	
Data / restraints / parameters	13049 / 0 / 402	
Goodness-of-fit on F^2	2.122	
Final R indices [I>2sigma(I)]	R1 = 0.3858, wR2 = 0.7077	
R indices (all data)	R1 = 0.4322, wR2 = 0.7333	
Largest diff. peak and hole	4.833 and -1.464 $e.Å^{-3}$	

Table 6.9 Crystal data and structure refinement for ***45****.*

Identification code	tcd165	
Empirical formula	$C_{41.50}H_{25.75}Br_5Cl_{3.25}N_2$	
Formula weight	1067.15	
Temperature	100(2) K	
Wavelength	0.71073 Å	
Crystal system	Monoclinic	
Space group	$P2_1/n$	
Unit cell dimensions	a = 11.6640(5) Å	α= 90°.
	b = 18.9361(7) Å	β= 102.7949(17)°.
	c = 18.2197(7) Å	γ = 90°.
Volume	3924.3(3) $Å^3$	
Z	4	
Density (calculated)	1.806 Mg/m^3	
Absorption coefficient	5.375 mm^{-1}	
F(000)	2076	
Crystal size	0.160 x 0.090 x 0.050 mm^3	
Theta range for data collection	1.572 to 25.499°.	
Index ranges	$-14 \leq h \leq 14$, $-22 \leq k \leq 22$, $-22 \leq l \leq 22$	
Reflections collected	98059	
Independent reflections	7301 [R(int) = 0.0928]	
Completeness to theta = 25.242°	100.0 %	
Absorption correction	Numerical	
Max. and min. transmission	0.9628 and 0.6496	
Refinement method	Full-matrix least-squares on F^2	
Data / restraints / parameters	7301 / 6 / 483	
Goodness-of-fit on F^2	1.066	
Final R indices [I>2σ(I)]	R1 = 0.0689, wR2 = 0.1412	
R indices (all data)	R1 = 0.1170, wR2 = 0.1634	
Largest diff. peak and hole	1.936 and -1.733 $e.Å^{-3}$	